# A 'Concentrate-&-Degrade' Technique for Cost Effective Adsorption and Degradation of Per-and Polyfluoroalkyl Substances in Water

by

Yangmo Zhu

A dissertation submitted to the Graduate Faculty of
Auburn University
in partial fulfillment of the
requirements for the Degree of
Doctor of Philosophy

Auburn, Alabama
August 6, 2022

Keywords: PFAS, Adsorbent, Photocatalysis, Concentrate and destroy, Optimization, Field Water

Approved by

Dr. Dongye Zhao, Chair, Engineering Alumni Council Endowed Professor of Civil and Environmental Engineering
Dr. Mark Barnett, Professor of Civil and Environmental Engineering
Dr. Natalie Cápiro, Assistant Professor of Civil and Environmental Engineering
Dr. Xinyu Zhang, Associate Professor of Chemical Engineering
Dr. Dengjun Wang, Assistant Professor of Aquatic Chemistry

**Abstract**

The overarching goal of this research is to develop and test a new class of carbon-photocatalyst composites for enhanced adsorption and destruction of per- and polyfluoroalkyl substances (PFAS) in water and field water. PFAS are ubiquitous in water, due to their widespread applications in various industrial and consumer products, and health concerns. Yet, a cost-effective technology has been lacking for the degradation of PFAS due to their resistance to conventional treatment. Thus, we developed a novel 'Concentrate-&-Destroy' technology, using adsorptive photocatalysts for enhanced removal of PFAS from water.

Metal-doped AC-supported titanate nanotubes (M/TNTs@AC) were synthesized based on commercial activated carbon (ACs) and titanium oxide ($TiO_2$), through a one-step facial alkaline hydrothermal process followed by proper metal doping and calcination. The material synthesis was optimized at varying AC mass contents, under different hydrothermal conditions, by doping various metals ions, and by varying calcination temperatures. Based on the experimental results, the highest photocatalytic mineralization efficiency of pre-sorbed perfluorooctane sulfonic acid (PFOS) was up to 66.2% using the 2 wt.% Ga/TNTs@Filtrosorb-400® granular activated carbon composite photocatalyst synthesized under the optimum parameters, 50 wt.% of Filtrosorb-400® granular activated carbon, 130 ℃ of hydrothermal temperature, 72 h of hydrothermal duration, and 550 ℃ of calcination temperature. The superior photoactivity of Ga/TNTs@AC is attributed to the oxygen vacancies, which not only suppressed recombination of the $e^-/h^+$ pairs, but also facilitated $O_2^{\bullet-}$ generation. Both $h^+$ and $O_2^{\bullet-}$ played critical roles in the PFOS degradation, which starts with cleavage of the sulfonate group and converts it into perfluorooctanoate (PFOA) that is then decarboxylated and defluorinated following the stepwise defluorination mechanism.

In addition, we used Ga/TNTs@AC for enhanced removal of PFAS from field water. Seven PFAS were detected in the field water, with the most predominant PFAS being PFOS. Ga/TNTs@AC (3 g/L) was able to remove ~98% of PFOS (spiked at 100 µg/L) from filed water within 10 min and offered large adsorption capacity. Subsequently, 35.5% of pre-concentrated PFOS (100 µg/L) on Ga/TNTs@AC (3 g/L) was degraded, with the defluorination rate of 25.8%. However, addition $Fe^{3+}$ added in the system increased PFOS degradation to 80.4%, corresponding with the mineralization of 70.0%. The superior photoactivity is attributed to the concurrent complexes, including the $Fe^{3+}$ complex with DOM and the complex between $Fe^{3+}$ and PFOS. Additionally, acidic condition is favorable for not only PFOS adsorption in field water onto Ga/TNTs@AC, but also PFOS degradation in the presence of $Fe^{3+}$.

GenX, the ammonium salt of hexafluoropropylene oxide dimer acid, has been used as a replacement for perfluorooctanoic acid. Due to its widespread uses, GenX has been detected in waters around the world amid growing concerns about its persistence and adverse health effects. Thus, we developed an adsorptive photocatalyst by depositing a small amount (3 wt.%) of bismuth (Bi) onto TNTs@AC (Bi/TNTs@AC), and tested the material for adsorption and subsequent *solid-phase* photodegradation of GenX. Bi/TNTs@AC at 1 g/L was able to adsorb GenX (100 µg/L, pH 7.0) within 1 h, and then degrade 70.0% and mineralize 42.7% of pre-sorbed GenX under UV (254 nm) in 4 h. The efficient degradation also regenerated the material, allowing for repeated uses without chemical regeneration.

Overall, the adsorptive photocatalysts and the 'Concentrate-&-Destroy' strategy represent a significant advancement in the treatment of PFAS. The new materials hold the promise to treat some of the most challenging contaminants in water in a more cost-effective manner.

## Acknowledgments

It's my honor to get the help and support of my committee members, family, and friends to finish my Ph.D. dissertation.

I would like to express my special appreciation and thanks to my major advisor, Dr. Dongye Zhao. He has been a tremendous mentor for me. He is a great scientist, who has rigorous attitude, genius ideas, and diligence. I really appreciate his support, continuous encouragement, patience, and guidance in accomplishing my career goals. Without his lenient and patient guidance, I couldn't have my current achievements. To be a scientist like him is the goal of my life. I thank him for everything he has done for me.

I gratefully acknowledge Drs. Mark Barnett, Natalie Cápiro, and Xinyu Zhang for their serving on my dissertation committee, for their valuable time and insightful advice on various research problems. It has been a great privilege and honor to work with them. I am extending my heartfelt thanks to Dr. Dengjun Wang, serving as the university reader. Sincere appreciation is also extended to Dr. Melissa Boersma for her analytical assistance, Dr. Wen Liu, Dr. Tianyuan Xu, and Dr. Zongsu Wei for their inspiration and kind supports; and thank Auburn University for providing the learning opportunity and comfortable learning and living environment. Special thanks are extended to my fellow students for their great friendship, helps, and research advice.

Finally, I am extremely grateful to my parents for their love, prayers, caring and sacrifices for educating and preparing me for my future. Without their love, support, and encouragement, I would not have been capable of completing this study.

# Table of Contents

## List of Tables

xi

## List of Figures

xiii

**Chapter 1. General Introduction**

**1.1. Background**

Per- and polyfluoroalkyl substances (PFAS) have emerged as a major contamination concern worldwide. For nearly 80 years, PFAS have been widely used in every-day consumer products such as food packaging, pesticides, waterproof fabrics, carpets, non-stick cookware, masking tape, and firefighting foams (Rahman et al. 2014). A latest study reported that PFAS were detected in 43 out of 44 tap water samples from 31 states in the US, with total PFAS concentrations ranging from <1 to 186 ng/L (Sydney Evans 2020). Human exposure to PFAS has been linked to cancer, elevated cholesterol, immune suppression, and endocrine disruption (Li et al. 2019). Health concerns in the early 2000s prompted manufacturers in Europe and North America to phase out perfluorooctanoic acid (PFOA) and (PFOS) (Land 2015). However, the past widespread uses and the high persistency of these chemicals have left a legacy of persisting water contamination. In addition, these legacy PFAS are still being used in other countries. A recent survey revealed that drinking water supplies for 6 million U.S. residents exceeded the United States Environmental Protection Agency's (EPA) lifetime health advisory (70 ng/L) for the sum of PFOA and PFOS (Hu et al. 2016).

Multiple actions have been taken since 2000 to limit the production and environmental release of long-chain PFAS, including the replacement of the long-chain PFAS with shorter-chain analogues, such as perfluorohexanedulfonic acid (PFHxS) and perfluoroether carboxylic acids (PFECAs) (Bao et al. 2018; Wang et al. 2013). Hexafluoropropylene oxide dimer acid (HFPO−DA), also known as perfluoro-2-propoxypropanoic acid (PFPrOPrA) belongs to the class of PFECAs. Its ammonium salt is a substitute chemical for PFOA with a trade name GenX used

as a processing aid in the production of fluoropolymers. However, the detection of HFPO-DA poses a new challenge to the scientific community because of the potential adverse effects to human health. GenX has been detected in river water downstream of fluorochemical plants in The Netherlands, Germany, China, and United States with the highest concentration of 812, 86.1, 3100, and 4500 ng/L, respectively (Gebbink et al. 2017; Heydebreck et al. 2015; Sun et al. 2016) .

Conventional biological wastewater treatment processes, such as activated sludge, anaerobic digestion, and trickling filtration, are not effective in degrading PFAS owing to their strong and stable carbon-fluorine bonds. Other treatment technologies have been investigated to remove and/or degrade PFAS in contaminated water, including adsorption by activated carbon (AC) or ion exchange resins, membrane filtration, chemical, and electrochemical oxidation/reduction, photochemical decomposition, sonolysis, and incineration (Hori et al. 2005; Ross et al. 2018; Vecitis et al. 2008). However, conventional adsorbents (AC and ion exchange resins) are much less effective for treating short-chain PFAS. Moreover, the regeneration of the spent adsorbents requires costly and toxic chemical solvents such as methanol, which also generates large amounts of regenerant waste residual. In recent years, photocatalytic degradation has attracted growing attention due to its relatively high transformation efficiency of PFAS and easier operation (Cambié et al. 2016; Schneider et al. 2014; Wang et al. 2017). However, the current photocatalytic treatment has been limited to directly treating a large volume of water using energy-intensive photo-irradiation, resulting in high energy cost and generation of harmful byproducts in the treated water. Therefore, our group proposed and tested a novel 'Concentrate-&-Destroy' strategy using a new class of adsorptive photocatalysts for potentially more cost-effective degradation and mineralization of PFAS in water (Xu et al. 2020; Zhu et al. 2021). First, PFAS are concentrated from large volumes of contaminated water onto a much smaller volume of an adsorptive

photocatalyst, a composite composed of a carbonaceous material and a photocatalyst. Subsequently, the pre-concentrated PFAS are efficiently degraded or defluorinated under solar or UV irradiation, which also regenerates the material without invoking a chemical solvent and salts. This strategy utilizes low-cost adsorption approach to treat low-concentration PFAS in large volumes of water, which not only facilitates the subsequent photodegradation efficiency, but also reduces the energy input for the photodegradation and prevents the secondary contamination issues compared to the conventional approach of treating the bulk water.

## 1.2. Objectives

The overarching goal of this research is to develop and test a new class of carbon-photocatalyst composites for enhanced adsorption and destruction of PFAS in water. The specific objectives are to:

1) Synthesize and test gallium-doped carbon-modified titanate nanotubes (Ga/TNTs@AC) and test the material for adsorption and destruction of PFOS,

2) Prepare and optimize Ga/TNTs@AC by using various commercial ACs and photocatalysts and by optimizing the synthesis conditions, and elucidate how material characteristics relate to PFOS photodegradation,

3) Test the AC-photocatalyst composites for selective adsorption of target PFAS under field water conditions and subsequently degrade the PFAS under UV irradiation,

4) Examine the effect of water matrix on PFAS adsorption and photodegradation, and explore engineered means to enhance the photocatalytic mineralization of pre-sorbed PFAS,

5) Prepare and test bismuth-doped carbon-modified titanate nanotubes (Bi/TNTs@AC) for adsorption and photocatalytic degradation of GenX,

6) Elucidate the adsorption and photocatalytic mechanisms.

## 1.3. Organization

This dissertation includes six chapters. Except for **Chapter 1** (General Introduction) and **Chapter 6** (Conclusions and Suggestions for Future Research), each chapter of this dissertation is formatted in the journal style of Water Research.

**Chapter 1** gives a general introduction of the background and the overall objectives of this dissertation. **Chapter 2** describes the synthesis, optimization, and testing of M/TNTs@AC under various synthesis conditions toward PFOS mineralization under UV irradiation, including the type and amount of doping metals on TNTs@AC, type and amount of ACs, hydrothermal reaction temperatures and duration, and calcination temperature. **Chapter 3** illustrates the effectiveness of Ga/TNTs@AC toward PFOS adsorption and *solid-phase* photodegradation rate. Based on the characterizations, the reaction mechanisms are explored. This chapter is based on the information that has been published in *Chemical Engineering Journal* (Zhu et al. 2021). **Chapter 4** presents a 'Concentrate-&-Destroy' strategy using a photo-regenerable adsorbent (Ga/TNTs@AC) for enhanced adsorption and photocatalytic degradation of PFAS in field water. **Chapter 5** investigates the GenX removal and photodegradation rate using Bi/TNTs@AC. This chapter is based on the information that has been published in *Water Research* (Zhu et al. 2022). **Chapter 6** gives some recommendations for future work.

## Chapter 2. Metal-Doped Carbon-Supported/Modified Titanate Nanotubes for Perfluorooctane Sulfonate Degradation in Water: Effects of Preparation Conditions and Parameter Optimization

Metal-doped AC-supported titanate nanotubes (M/TNTs@AC) have been shown promising for photocatalytic degradation of per- and polyfluoroalkyl substances (PFAS). However, the preparation recipe of these adsorptive photocatalysts have not yet been optimized in terms of type and portion of precursor materials and the metal dopants as well as synthesizing conditions. To address this knowledge gap, we prepared TNTs@AC based on a commercial $TiO_2$ and different activated carbons (ACs) at varying $TiO_2$:AC ratios and under different hydrothermal conditions. In addition, a suite of dopant metals ions, including $Fe^{3+}$, $Bi^{3+}$, $Ga^{3+}$, $In^{3+}$, $Co^{2+}$, $Cu^{2+}$, and $Mn^{2+}$, were compared to gauge their effect on the material photoactivity. Moreover, the effect of the calcination temperature was also tested. The photocatalytic performance of M/TNTs@AC was evaluated based on their effectiveness in the defluorination of the PFOS under 4-h UV irradiation with gallium doped TNTs@AC (Ga/TNTs@AC) showing the highest degradation efficiency. Subsequently, the preparation parameters were optimized by means of pre-sorbed PFOS defluorination. Five synthesis parameters, including carbon source, carbon mass content, hydrothermal treatment temperature and duration, and calcination were selected to investigate their effects on the photocatalytic activity of the resultant composites. Based on the experimental results, the highest photocatalytic mineralization efficiency of PFOS was up to 66.2% using the 2 wt.% Ga/TNTs@ Filtrosorb-400® granular activated carbon composite photocatalyst synthesized under the optimum parameters, 50 wt.% of Filtrosorb-400® granular activated carbon, 130 ℃ of hydrothermal temperature, 72 h of hydrothermal duration, and 550 ℃ of calcination temperature.

The catalysts were analyzed by X-ray diffraction, $N_2$ Brunauer-Emmett-Teller, UV-vis diffuse reflectance spectrometry, and photoluminescence. Material characterizations revealed that the superior photoactivity of 2%Ga/TNTs@AC prepared under the optimized conditions is attributed to the smaller pore size, pure crystallized anatase phase formed during the calcination, high UV light absorption, and oxygen defects induced by $Ga^{3+}$. The toxicity of the intermediates was predicted by the ecotoxicity analysis using ECOSAR software where the shorter-chain PFAS were less toxic than parent PFOS.

## 2.1. Introduction

There have been over 4000 PFAS listed in The Organization for Economic Co-operation and Development (OECD) Report, with around 256 PFAS or roughly 5.5% being considered commercially relevant (Buck et al. 2021; OECD 2018). Among the most widely used and detected PFAS are PFOS and PFOA. Due to their persistency, bioaccumulation, and ubiquitously distribution in aquatic environments, they were phased out in early 2000s in Europe and north America (Roth et al. 2021). Yet, these legacy chemicals remain being widely detected in aquatic systems and drinking water, which prompted EPA to have established a lifetime health advisory level at 70 ng/L for the sum of PFOA and PFOS.

Titanate nanotubes (TNTs), derived from $TiO_2$, offer some unique advantages such as high specific surface area (SSA), ion-exchange capability, and photocatalytic activity. However, the negative and hydrophilic surface of TNTs is unfavorable for adsorption and photocatalytic degradation of anionic PFAS such as PFOA and PFOS. To overcome this, we prepared an activated carbon (AC) supported/modified TNTs, namely TNTs@AC, through an alkaline hydrothermal method (Liu et al. 2016). To further enhance the specific interactions with PFOA and PFOS and the photocatalytic activity, we doped TNTs@AC with various photoactive metal oxides.

However, while such metal-doped TNTs@AC (or M/TNTs@AC) composites have demonstrated great potential for adsorption and photocatalytic degradation of anionic PFAS, the material preparation has not been systematically optimized. Information is lacking on the effects of precursor materials ($TiO_2$ and ACs), their relative contents, the type and amount of the dopant metals, the hydrothermal treatment conditions (temperature and duration), and calcination temperature. Understanding the effects of these factors will facilitate tuning and optimizing the material preparation to achieve best treatment performances according to the characteristics of the target PFAS.

As such, the overall goal of this study was to optimize M/TNTs@AC by using different dopant metals and various commercial ACs and by tuning the synthesis conditions. The material performance was evaluated based on defluorination (*i.e.*, conversion of fluorine in PFAS into fluoride) of PFOS pre-sorbed on the materials under 4-h UV irradiation. The specific objectives were to evaluate the effects of (1) the type and amount of doping metals on TNTs@AC, (2) type and amount of ACs, (3) hydrothermal reaction temperature and duration, (4) calcination temperature. In addition, we also evaluated the acute and chronic toxicity of the photodegradation byproducts.

## 2.2. Materials and methods

### 2.2.1. Chemicals

All chemicals were of analytical grade or higher. Nano-$TiO_2$ Degussa P-25 (80% anatase and 20% rutile) was purchased from Evonik Industries (Worms, Germany). Filtrosorb-400® granular activated carbon (GAC) (F400) was acquired from Calgon Carbon Corporation (PA, USA). Darco® granular activated charcoals with a mesh size of 4-12 (D4-12) and 20-40 (D20-40), and a Darco® G-60 (D60) were obtained from Sigma-Aldrich (St. Louis, MO, USA). Norit 1240 EN®

GAC (NAC1240) and HydroDarco® 820 (HD820) were purchased from Cabot Corporation (Boston, USA). **Table 2-1** provides salient properties of these materials. All materials were used as received. PFOS, anhydrous gallium(III) chloride, iron(III) chloride hexahydrate, copper(II) chloride anhydrous, cobalt(II) chloride hexahydrate, manganese(II) chloride tetrahydrate, bismuth(III) chloride, anhydrous indium(III) chloride, and sodium hydroxide were obtained from VWR International (Radnor, PA, USA). All solutions were prepared using deionized (DI) water (18.2 MΩ cm).

**Table 2-1.** Key physicochemical properties of various parent carbons.

| Sample | BET surface area ($m^2$/g) | Particle size (mm) | Pore volume ($cm^3$/g) |
|---|---|---|---|
| F400 | 1012.0 (Morlay et al. 2012) | 0.25-0.5 | 0.570 (Morlay et al. 2012) |
| D4-12 | 293.98±6.26 | 1.68-4.76 | 0.157 |
| D20-40 | 483.15±6.62 | 0.420-0.841 | 0.261 |
| NAC1240 | 828.23±20.42 | 0.420-1.68 | 0.429 |
| HD820 | 557.04±8.80 | 0.841-2.38 | 0.298 |
| D60 | 717.54±15.56 | <0.15 | 0.393 |

### 2.2.2. Preparation of M/TNTs@AC

M/TNTs@AC was synthesized based on our prior work (Zhu et al. 2021). First, TNTs@AC was prepared through a modified one-step hydrothermal method (Liu et al. 2016). Typically, 0.6, 0.8, 1.2, 1.8, or 2.4 g of F400 and 1.2 g of $TiO_2$ were mixed in 66.7 mL of a 10 M NaOH solution. According to the different F400 mass contents in the composite (mass of F400/total mass of $TiO_2$ and F400), the resulting materials were denoted as 33%, 40%, 50%, 60%, and 67% F400,

respectively. After magnetic stirring for 12 h, the mixture was transferred into a 100 mL Teflon reactor with a stainless-steel cover and heated at a controlled temperature in the range of 130-200 °C (to gauge the temperature effect) for 24-72 h (to test the reaction time effect). Upon cooling, the resulting solids (TNTs@AC) were separated upon gravity settling and washed with DI water until neutral pH, and then oven-dried at 105 °C. No fluoride was detected in the resulting material.

Subsequently, 1 g of dried TNTs@AC was dispersed in 80 mL DI water under continuous stirring, and then 4 mL of a metal solution (5 g/L as M) was added dropwise into the TNTs@AC suspension over a pH range of 4.0-6.0 (M = $Fe^{3+}$, $Bi^{3+}$, $Ga^{3+}$, $In^{3+}$, $Co^{2+}$, $Cu^{2+}$, or $Mn^{2+}$). After stirring for 3 h, which was sufficient for complete adsorption of the metals onto the TNTs, the particles were separated by removing the supernatant, and then oven-dried at 105 °C. Based on the initial and final concentrations of metal ions in the aqueous phase, >99.9% of M was taken up by TNTs/AC. In addition, <0.01 wt.% of Ti was dissolved in the supernatant during the M-doping. Finally, the solid particles were subjected to calcination at 350 °C-650 °C (to evaluate calcination temperature effect) with a temperature ramp of 10 °C/min and under a nitrogen flow of 100 mL/min. Based on the percentage mass content of M, the resulting composites were denoted as wt.%M/TNTs@AC.

The following synthesis conditions were varied: carbon source (D20-40, D4-12, NAC1240, HD820, D60, and F400), carbon mass contents as wt.% (33%, 40%, 50%, 60%, and 67% AC), hydrothermal treatment temperature (130, 150, 165, 180, and 200 °C); hydrothermal treatment time (24, 48, and 72 h), and calcination temperature (350, 450, 550, and 650 °C).

### 2.2.3. Characterization

Most promising materials were characterized to understand the relationship between material characteristics and the photocatalytic activity. The surface morphologies and microstructures were

26

characterized by scanning electron microscopy (SEM S-4800, Hitachi, Japan). The crystal phases

of the materials were identified through X-ray diffraction (XRD) analysis using a Rigaku Ultima

IV powder diffractometer (Tokyo, Japan) with Cu Kα radiation ($\lambda = 1.5418$ Å). XRD spectra

were collected between 5° to 80° two-theta angles with a 2 °/min scan speed. The $N_2$ Brunauer-

Emmett-Teller (BET) SSA and pore volume of the materials were analyzed by nitrogen

adsorption-desorption (Micromeritics ASAP 2460, USA). The photoluminescence (PL) spectra

were obtained on an FLS1000 photoluminescence spectrometer (Edinburgh Instruments, UK)

equipped with a xenon source at an excitation wavelength of 254 nm. The UV-vis diffuse

reflectance spectrometry (UV-DRS) analysis was performed on a Shimadzu UV-3600i Plus

spectrophotometer.

### 2.2.4. Adsorption and subsequent solid-phase photodegradation of PFOS

Adsorption test was performed in the dark using 40 mL high-density polypropylene (HDPE)

vials. The reaction was initiated by mixing 40 mL of a PFOS solution (100 µg/L) and 0.12 g of a

M/TNTs@AC, with the pH adjusted to $7.0 \pm 0.1$. The vials were then placed on a rotator (100

rpm) located in an incubator at 25 °C.

Upon PFOS adsorption equilibrium, nearly all PFOS (100 µg/L) in the solution was

transferred and pre-concentrated on the solid materials. Upon removal of the solution, the PFOS-

laden particles were transferred to a quartz-dish along with 10 mL of DI water, and then placed

into a quartz tray (OD×H = 6×1.5 cm) with a quartz cover. The photoreactor was then placed in a

Rayonet chamber UV-reactor (Southern New England Ultraviolet CO., Branford, CT, USA)

equipped with 16 RPR-2537 Å lamps. The light intensity was 210 W/m² at the edge (1.5 in or 3.81

cm to the nearest lamp) of the quartz tray and 128 W/m² at the center. The solids in the quartz

photo-reactor were manually shaken intermittently to facilitate the UV exposure (for large reactors,

the solid-liquid slurry can be stirred continuously as commonly practiced in photocatalytic processes). After 4-h UV irradiation, the mixtures were sacrificially filtered through a 0.22 µm polyether sulfone (PES) membrane (>99% PFOS recovery). Then, the liquid was collected for fluoride analysis. Duplicate experiments were carried out for each time point. Defluorination of PFOS was quantified based on the fluoride concentration in the aqueous phase. Fluoride adsorption on the solid phase sample during the photodegradation process was negligible. To confirm, the solid sample after the photodegradation was extracted using 20 mL of a 1 M NaOH solution. The extractant was then neutralized by a 2 M HCl solution to $7.0 \pm 0.5$ and then filtered with a 0.22 µm PES membrane. No fluoride was detected in the filtrate.

### 2.2.5. Chemical analysis

Aqueous $F^-$ was analyzed by ion chromatography (Dionex, CA, USA) equipped with an anion exchange column (Dionex Ionpac AS22) and an anion dynamically regenerated suppressor (ADRS 600, 4mm). The detection limit was $10.00 \pm 0.01$ µg/L. Dissolved metals in aqueous phase were determined on an inductively coupled plasma-optical emission spectroscopy (ICP-OES, 710-ES, Varian, USA).

### 2.3. Results and discussion

### 2.3.1. Effect of metal dopants on PFOS photodegradation

Based on our prior work, the photocatalytic activity of TNTs@AC can be strongly affected by the metal dopant. To optimize the type and amount of the metals, a suite of commonly used metal dopants was screened at an identical concentration of 2 wt.%, including $Mn^{2+}$, $Cu^{2+}$, $In^{3+}$, $Co^{2+}$, $Fe^{3+}$, $Bi^{3+}$, and $Ga^{3+}$. In all cases, the metal ions were first adsorbed onto TNTs@AC, and upon oven-drying, the composites were calcined at 550 °C under $N_2$. **Figure 2-1(a)** shows the XRD patterns of the synthesized samples doped with the different metals. The XRD patterns for

2%In/TNTs@AC, 2%Bi/TNTs@AC, 2%Fe/TNTs@AC, and 2%Ga/TNTs@AC nearly resembled one other, where the peaks at 25.3°, 37.8°, 48.0°, 53.9°, 55.0°, and 62.7° are indexed to the (101), (004), (200), (105), (211), and (204) planes of tetragonal anatase, respectively (JCPDS-ICDD No. 21-1272). Moreover, no typical diffraction peaks belonging to Ga were observed for 2%Ga/TNTs@AC, which agrees with the prior report that the presence of Ga altered the titanate lattice after the calcination and no evident diffraction for $Ga_2O_3$ was observed owing to the substitution of $Ti^{4+}$ by $Ga^{3+}$ (Zhu et al. 2021). However, a weak peak at 24.4° corresponding to $Na_2Ti_3O_7$ (JCPDS-ICDD No. 31-1392) was observed for 2%In/TNTs@AC and 2%Bi/TNTs@AC. Referring to 2%In/TNTs@AC, the anatase peaks significantly weakened compared to those for the others. For 2%Bi/TNTs@AC, two additional peaks emerged at 27.2° and 39.6° in 2%Bi/TNTs@AC sample, which are consistent with the JCPDS-ICDD No. 44-1246 representing metallic Bi. Notably, XRD patterns for the samples doped with divalent metal ions ($Mn^{2+}$, $Cu^{2+}$, and $Co^{2+}$) displayed more evident and new characteristic peaks at 24.4°, 31.7°, 32.7°, 43.9°, 45.5°, 47.6°, and 56.5° compared to those doped by trivalent metal ions ($In^{3+}$, $Fe^{3+}$, $Bi^{3+}$, and $Ga^{3+}$). The peaks at 24.4°, 31.7° and 43.9° are ascribed to sodium tri-titanate ($Na_2Ti_3O_7$), whereas those at 32.7°, 45.5°, 47.6°, and 56.5° correspond to $Na_{0.8}Ti_4O_8$ (JCPDS-ICDD No. 73-1400), suggesting the coexistence of $Na_2Ti_3O_7$ and $Na_{0.8}Ti_4O_8$ in 2%Mn/TNTs@AC, 2%Cu/TNTs@AC, and 2%Co/TNTs@AC (Chen et al. 2012). The formation of $Na_{0.8}Ti_4O_8$ might be owing to the dehydration of interlayered −OH from the titanate nanostructure, while $Na^+$ ions remain chemically bonded to [$TiO_6$] octahedral layers (Dostanić et al. 2019). As a consequence, the crystal anatase phase was formed when the samples were doped by the trivalent metals, while the anatase peak intensities decreased in the sequence of 2%Ga/TNTs@AC > 2%Fe/TNTs@AC > 2%Bi/TNTs@AC > 2%In/TNTs@AC. On the other hand, the divalent metal ions deposited on

TNTs@AC ($Mn^{2+}$, $Cu^{2+}$, and $Co^2$) facilitated the formation of the tri-titanate phase, where $Na_2Ti_3O_7$ and $Na_{0.8}Ti_4O_8$ were the dominant crystal structures. Generally, the tri-titanate phase was transformed into the anatase phase upon the calcination, leading to a greater photocatalytic activity due to the improved separation of photo-generated charge carriers (sodium tri-titanate has much lower photocatalytic activity than anatase owing to the sodium content in titanate and the higher bandgap value (3.7 eV for $Na_2Ti_3O_7$ and 3.2 eV for anatase)) (Haque et al. 2017; Vithal et al. 2013; Zhang et al. 2015). Besides, the anatase phase could facilitate light absorption (Wang et al. 2012b) (**Figure 2-1b**).

**Figure 2-1b** shows the UV-vis DRS spectra for the metal-doped TNTs@AC. All samples exhibited high light absorption in the UV range of 200-320 nm, where a slightly higher absorption intensity was observed for the materials doped with trivalent metals. Overall, the light absorption followed the order of $In^{3+} > Ga^{3+} > Co^{2+} > Fe^{3+} > Bi^{3+} > Mn^{2+} > Cu^{2+}$. Notably, all composites (except for Co/TNTs@AC) showed a sharp absorption edge at ~320-360 nm (Xu et al. 2014), where the introduction of $Fe^{3+}$ and $Mn^{2+}$ resulted in much lowest light absorbance. Thus, 2%Ga/TNTs@AC, the only one with a pure anatase phase as confirmed by XRD, exhibited the greatest light absorption throughout the UV and visible range (200-800 nm).

**Figure 2-2a** depicts the PL spectra of the various M/TNTs@AC composites. A prominent peak at ~358 nm was observed in the composites deposited with $Bi^{3+}$, $Fe^{3+}$, and $In^{3+}$, which can be ascribed to the emission of band gap transition related to the anatase structure of $TiO_2$ (Taieb et al. 2016). This result is in agreement with the XRD analysis confirming the anatase phase in the samples. A new PL peak was observed for Cu/TNTs@AC at 348 nm, which was from band edge emissions resulting from the electron-hole recombination of the free excitations in Cu/TNTs@AC (Jamila et al. 2020). In addition, the PL spectra for Ga/TNTs@AC exhibited a wide blue emission

PL peak at about 434 nm, which originated from the recombination of excited electrons trapped in the oxygen vacancies with the holes created above the valence band (Kim and Shim 2007; Vasanthi et al. 2019). The observation is in accord with the results reported by Zhu et al. (2021), though the peak associated with the Ga-induced oxygen vacancies occurred at ~550 nm. Nevertheless, this prominent peak at 434 nm was not observed for other materials, indicating that only Ga/TNTs@AC  generated the oxygen vacancies due to the embedded $Ga^{3+}$. The oxygen vacancies facilitate the adsorption of molecular $O_2$, which reacts with the photo-induced electrons and free electrons on the oxygen vacancies to generate $O_2^{\bullet-}$ and free up holes that are responsible for the enhanced solid-phase photocatalytic degradation of PFOS by 2%Ga/TNTs@F400 (Zhu et al. 2021).

**Figure 2-2b** compares the photocatalytic activities of the M/TNTs@AC composites doped with various metal when used for defluorination of pre-sorbed PFOS. After 4 h of UV-light irradiation, 2%Ga/TNTs@F400 and 2%Bi/TNTs@F400 clearly outperformed the other counterparts, with a PFOS mineralization of 66.2% and 60.3%, respectively. 2%Mn/TNTs@F400 was least effective with only 11.2% of PFOS defluorinated. Based on the defluorination rates, the photocatalytic activity for the materials followed the rank of 2%Ga/TNTs@F400 (66.2%) > 2%Bi/TNTs@F400 (60.3%) > ; > 2%Fe/TNTs@F400 (36.4%) > 2%Co/TNTs@F400 (33.1%) > 2%In/TNTs@F400 (30.3%) > 2%Cu/TNTs@F400 (18.4%) > 2%Mn/TNTs@F400 (11.2%). Taken together the observations from XRD analysis, PL, and UV-vis diffuse reflectance spectra, the superior photoactivity of Ga/TNTs@AC toward PFOS is attributed to: 1) the nearly 100% pure anatase phase in 2%Ga/TNTs@AC after the calcination, which is generally regarded as the more photochemically active phase of titania owing to the combined effect of lower rates of $e^-/h^+$ recombination and higher surface adsorptive capacity (Hurum et al. 2003); 2) the enhanced UV

light absorption; and 3) the generation of oxygen vacancies induced by the substitution of $Ti^{4+}$ by $Ga^{3+}$, facilitating the separation of the $e^-/h^+$ pairs and generation of $O_2^{\bullet-}$.



(a)                                        (b)
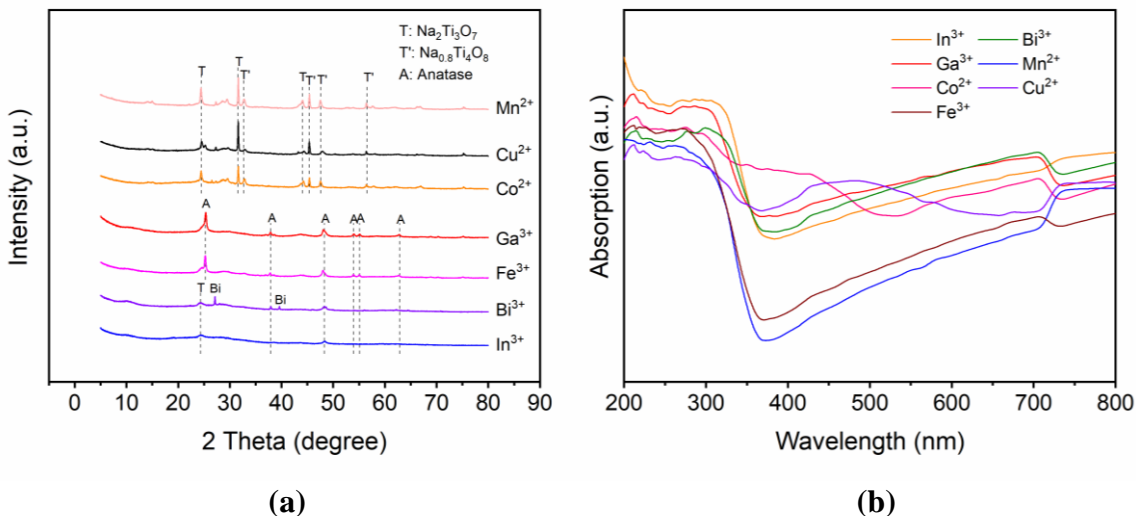
**Figure 2-1.** (a) XRD pattens and (b) UV-DRS spectra of TNTs@AC doped by various metals (2 wt.%). Experimental conditions for material synthesis: F400 mass content = 50%, NaOH concentration = 10 M, hydrothermal treatment temperature = 130 °C, duration = 72 h, calcination duration = 3.5 h, and calcination temperature = 550 °C.



(a)                                        (b)
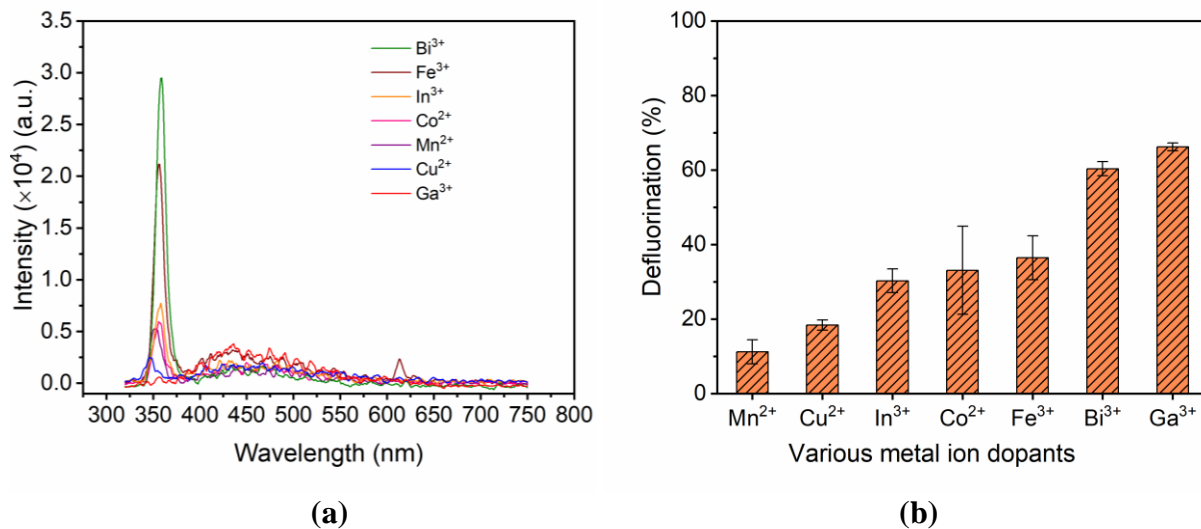
**Figure 2-2.** **(a)** PL spectra **(b)** Defluorination of PFOS under 4-h UV irradiation by TNTs@AC doped by various metal ions (2 wt.%) following the conditions in **Figure 2-1.** Conditions for adsorption: initial PFOS concentration = 100 µg/L, material dosage = 3 g/L, pH = 7 ± 0.1, and adsorption time = 4 h; Conditions for photodegradation: initial PFOS concentration = 100 µg/L, material dosage = 3 g/L, pH = 7 ± 0.1, UV intensity = 210 W/m$^2$, reaction time = 4 h. Data are plotted as mean of duplicates with error bars indicating deviation from the mean.

### 2.3.2. Effect of type of AC on PFOS photodegradation

To investigate the effects of the parent carbon type, a suite of commonly used ACs were employed in the preparation of the Ga/TNTs@AC composites, including F400, GAC D4-12, D20-40, NAC 1240, D60, and HD 820. In all cases, 2 wt.% Ga was doped. **Table 2-1** gives the BET SSAs and particle sizes of these parent carbons. Notably, F400 gives the largest SSA and pore volume of 1012.0 m$^2$/g and 0.570 cm$^3$/g, respectively. In addition, the particle size for F400 (0.25-0.5 mm) was also smaller than most of the other ACs except for D60 (<0.15 mm).

However, 2%Ga/TNTs@F400, 2%Ga/TNTs@NAC1240, 2% Ga/TNTs@HD820, and 2%Ga/TNTs@D60 showed a much decreased SSA of 341.03, 415.95, 407.72, and 366.41 m$^2$/g, respectively, while Ga/TNTs@D4-12 and Ga/TNTs@D20-40 exhibited a similar SSA to that of the parent carbons (**Table 2-2**). The results indicate that the alkaline hydrothermal treatment, the subsequent Ga decomposition, and calcination has negligible effect on SSA of the Darco$^®$ carbon (D4-12 and D20-40) and TiO$_2$, whereas these modifications resulted in notable alteration of the pores and SSA for the other ACs. It can be deduced that the reduction of SSA is attributed to the blockage of the interior sites inside the parent ACs due to the hydrothermal treatment and the conversion of larger pores of TNTs into smaller micropores in composite (Li et al. 2020a; Liu et

al. 2016). As illustrated in **Figure 2-3**, due to the surface phase blending, a layer of mixed AC-TNTs-Ga phases is attached to the exterior of AC, resulting in partial blockage of the core sites inside the AC particle. Consequently, the major adsorption sites are shifted from the pure AC phase to the photoactive mixed phases, with the deep core AC sites largely unused. From a photocatalysis viewpoint, the accumulation of PFAS on the photoactive shell sites is conducive to the subsequent photocatalytic degradation reaction due to easily photon access and facilitated mass/electron transfer.

**Table 2-2.** BET-based specific surface areas and pore volumes of 2%Ga/TNTs@AC with various carbon sources.

| Carbon | BET surface area $(m^2/g)$ | Pore size (nm) |
|---|---|---|
| 2%Ga/TNTs@F400 | 341.03±3.71 | 5.87 |
| 2%Ga/TNTs@D4-12 | 293.21±4.58 | 7.02 |
| 2%Ga/TNTs@D20-40 | 434.78±3.77 | 6.63 |
| 2%Ga/TNTs@NAC1240 | 415.95±10.41 | 5.41 |
| 2%Ga/TNTs@HD820 | 407.72±6.12 | 6.37 |
| 2%Ga/TNTs@D60 | 366.41±7.05 | 7.12 |

**Figure 2-4a** shows that all of the composite materials were able to adsorb >99% of PFOS within 4 h. **Figure 2-4b** shows how the various carbon precursors affected the PFOS mineralization. Evidently, 2%Ga/TNTs@AC prepared with F400 displayed the highest

defluorination of 66.2% after 4 h of the UV irradiation. Overall, the defluorination rates by 2%Ga/TNTs@AC prepared with the different carbonaceous materials follow the sequence of: F400 (66.2%) > D60 (47.2%) > D20-40 (34.9%) > NAC1240 (33.6%) > HD820 (23.9%) > D4-12 (22.6%).

F400 has been known to offer higher adsorption rates for long-chain PFAS than other common ACs (Gagliano et al. 2020). The smaller pore size of 2%Ga/TNTs@F400 can be attributed to the formation of AC-Ga-TNTs mixed phases. Such microscale mixed phases can facilitate a corporative adsorption mode through hydrophobic interactions between the tail of PFOS and carbon particles and electrostatic/complexation interactions between the metal (hydr)oxides and the head group of PFOS (Li et al. 2002; Yuan et al. 2005). Moreover, the smaller particle size of F400 is also beneficial for UV exposure because of elevated absorption and back scattering of the light (Peña et al. 2001). Besides, Smaller particle size gives shorter mass transfer paths for the degradation products to reach the surface, facilitating the subsequent photocatalytic degradation. Moreover, the sharp drop in SSA from parent F400 to 2%Ga/TNTs@F400 indicates the blockage of the interior sites upon the hydrothermal alkaline treatment (**Figure 2-3**) and a major conversion of the adsorption sites from intraparticle pores for the parent AC to the shell of the composite materials, which are not only accessible for PFOS, but also reachable by photons as well as the photo-generated charge carries and reactive oxygen species. Consequently, F400 was considered the most suitable AC, and 2%Ga/TNTs@F400 was employed for further optimization in the subsequent experiments.
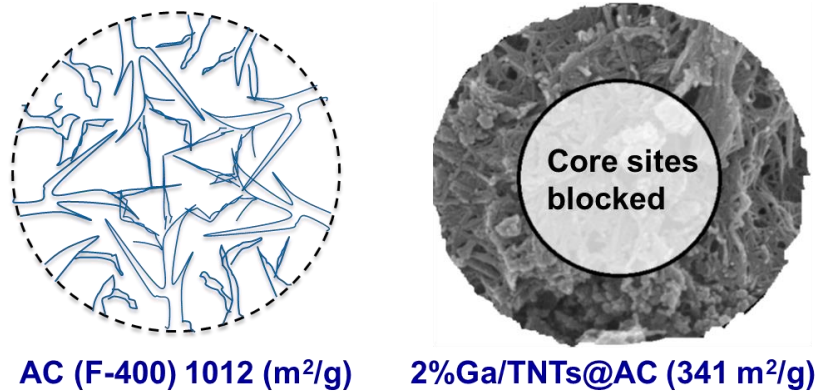
**Figure 2**-**3.** Conceptualized representation of adsorption sites for AC and Ga/TNTs@AC.



**(a)**                 **(b)**
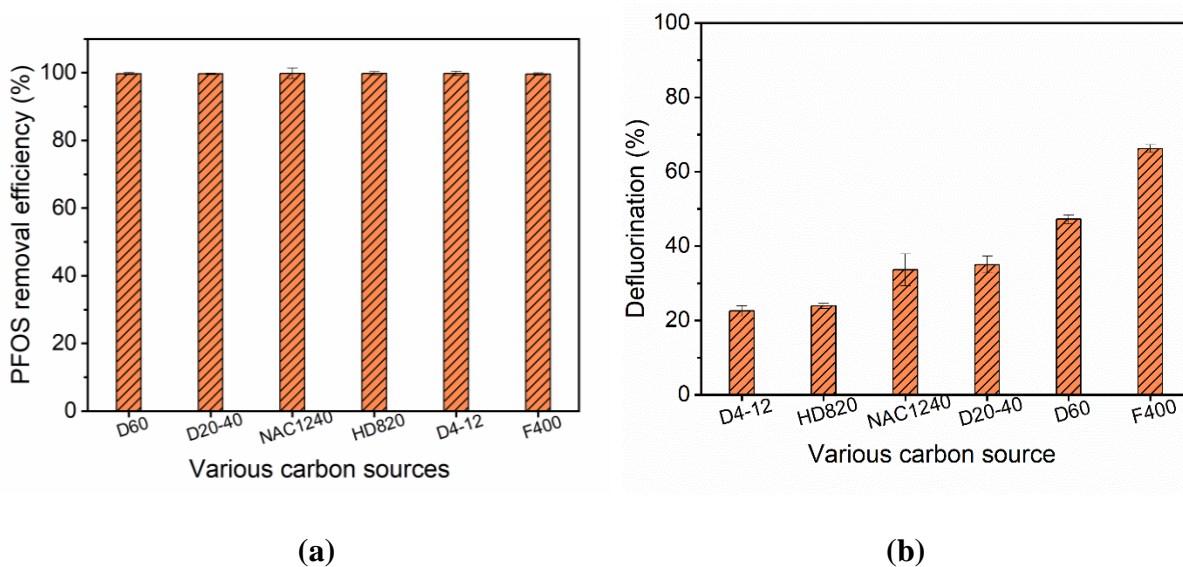
**Figure 2-4.** **(a)** Adsorption and **(b)** defluorination of PFOS under 4-h UV irradiation by 2%Ga/TNTs@AC prepared with various carbons. Experimental conditions for material synthesis: carbon mass content = 50%, hydrothermal treatment time = 72 h, hydrothermal reaction temperature = 130 ℃, NaOH concentration = 10 M, calcination temperature = 550 ℃, and calcination duration = 3.5 h; Conditions for adsorption: initial PFOS concentration = 100 µg/L, material dosage = 3 g/L, pH = 7 ± 0.1, and adsorption time = 4 h. Data are plotted as mean of duplicates with error bars indicating deviation from the mean.

### 2.3.3. Effect of F400 mass content on PFOS adsorption and photoactivity of 2%Ga/TNTs@F400

To examine the effect of the mass content of F400, the composite materials were prepared with five different mass contents of F400Ga/TNTs@33%F400, Ga/TNTs@40%F400, Ga/TNTs@50%F400, Ga/TNTs@60%F400, and Ga/TNTs@67%F400, where the percentiles indicate the mass contents of F400 based on the total mass of F400 and TiO$_2$. **Table 2-3** lists the SSAs of the resulting composites. The SSA increased from 130.91 m$^2$/g for 2%Ga/TNTs@33%F400 to 349.42 m$^2$/g for 2%Ga/TNTs@67%F400, respectively, with increasing F400 content. This suggests that more AC sites were added to the composite materials when more F400 was present.

**Figure 2-5a** compares the XRD patterns of the composite materials prepared by varying the parent F400 mass contents. For Ga/TNTs@50%AC, the peaks observed at 25.3°, 37.8°, 48.0°, 53.9°, 55.0°, 62.7°, 68.8°, 70.3°, and 75.0° are indexed to (101), (004), (200), (105), (211), (204), (116), (220), and (215) planes of tetragonal anatase. However, no apparent anatase peaks emerged in the XRD patterns of Ga/TNTs@60%AC and Ga/TNTs@40%AC, while new peaks appeared at 9.9°, 24,4°, 28.6°, and 48.3°. These new peaks are all ascribed to sodium tri-titanate Na$_2$Ti$_3$O$_7$, suggesting that Na$_2$Ti$_3$O$_7$ in TNTs was not effectively transformed into anatase in Ga/TNTs@60%AC and Ga/TNTs@40%AC. The XRD patterns for Ga/TNTs@33%AC and Ga/TNTs@67%AC nearly resemble that of Ga/TNTs@60%AC, though six distinctive peaks were observed at 27.3°, 31.7°, 45.4°, 56.4°, 66.2°, and 75.3° corresponding to the characteristic peaks of NaCl (JCPDS-ICDD No. 05-0628) (Chen et al. 2012). The observations insinuate that the crystallite growth of anatase was highly dependent on the initial AC content, and the formation of the photoactive anatase phase during the material calcination was suppressed when the F400 mass

37

content deviates from the optimal 50 wt.%. The poorly crystallized phase of anatase predicts a poor photocatalytic activity.

**Table 2-3.** BET-based specific surface areas of 2%Ga/TNTs@F400 prepared with various F400 mass contents.

| Material | BET surface area (m$^2$/g) |
|---|---|
| 2%Ga/TNTs@33%F400 | 130.91±1.20 |
| 2%Ga/TNTs@40%F400 | 264.01±2.33 |
| 2%Ga/TNTs@50% F400 | 341.03±3.71 |
| 2%Ga/TNTs@60% F400 | 347.29±3.89 |
| 2%Ga/TNTs@67% F400 | 349.42±3.64 |



(a)                                           (b)
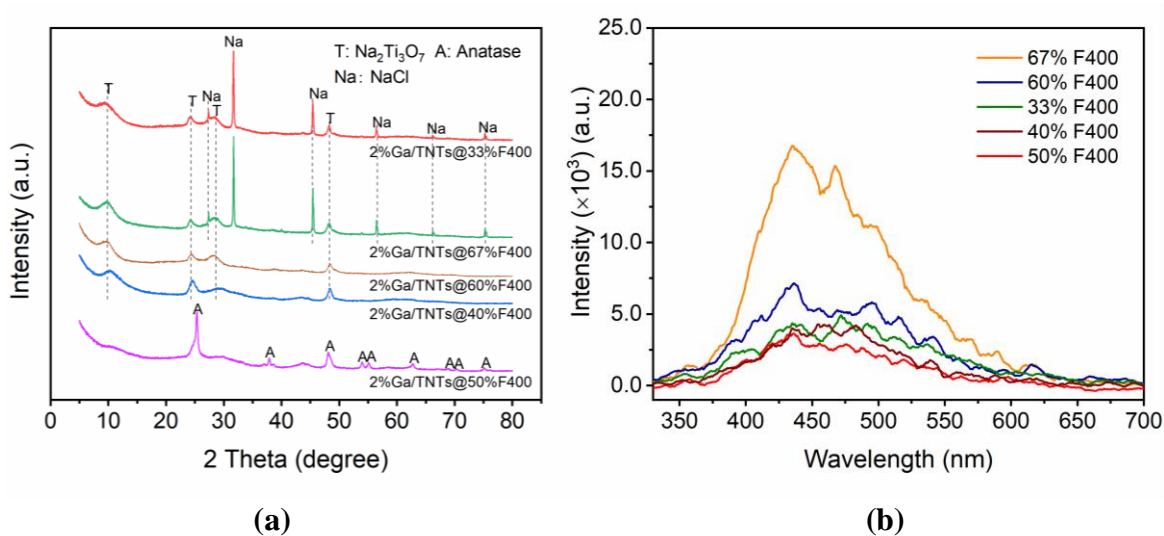
**Figure 2-5. (a)** XRD patterns and **(b)** PL spectra of 2%Ga/TNTs@AC prepared with various AC (F400) mass contents. Experimental conditions for material synthesis: AC = F400, hydrothermal treatment time = 72 h, hydrothermal reaction temperature = 130 °C, NaOH concentration = 10 M, calcination duration = 3.5 h, and calcination temperature = 550 °C.

PL emission spectra were obtained to investigate the separation efficiency of the photoexcited $e^-/h^+$ pairs for Ga/TNTs@AC prepared with various contents of F400 at room temperature under a xenon lamp at 254 nm (**Figure 2-5b**). Generally, a low PL intensity is indicative of a high separation efficiency of $e^-/h^+$ pairs. Notably, all samples exhibited a similar broad peak centered at approximately 434 nm, which can be ascribed to the oxygen vacancies owning to the substitution of $Ti^{4+}$ by $Ga^{3+}$ (Kim and Shim 2007; Lu et al. 2018). The highest emission peak intensity was observed for Ga/TNTs@67%AC, and it decreased sharply when the AC content was decreased to60 wt.%, and further decreased to the lowest level when the AC content was decreased to 50 wt.%. Further decreasing the carbon content to 40 wt.% and 33 wt.% resulted in a slight rebound of the peak intensity. The results indicate that Ga/TNTs@50%AC offered the highest level of oxygen vacancies, which played a critical role in the separation of the $e^-/h^+$ pairs, resulting extended lifetime of the charge carriers (Zhu et al. 2021).

**Figure 2-6** shows the defluorination rates of PFOS pre-sorbed on Ga/TNTs@AC prepared at different F400 mass contents after 4-h UV irradiation. In accord with the levels of the oxygen vacancies, the heist PFOS defluorination (66.2%) was attained at a $TiO_2$/F400 ratio of 1/1. Increasing the AC content to 60 wt.% and 67 wt.% resulted in a sharp drop of the defluorination to 43.3% and 36.0%, respectively. In addition to oxygen vacancy effect of the recombination rate of the $e^-/h^+$ pairs, excessive AC patched on the photocatalysts may partially block the UV light (Ali et al. 2019), and elevated fraction of the pure carbon phase is not photoactive although the SSA of the composite increased with increasing F400 content. Moreover, the observed defluorination rates are also in line with the XRD spectra, which predicted the highest photoactivity for Ga/TNTs@50%F400 based on the content of the pure anatase phase.
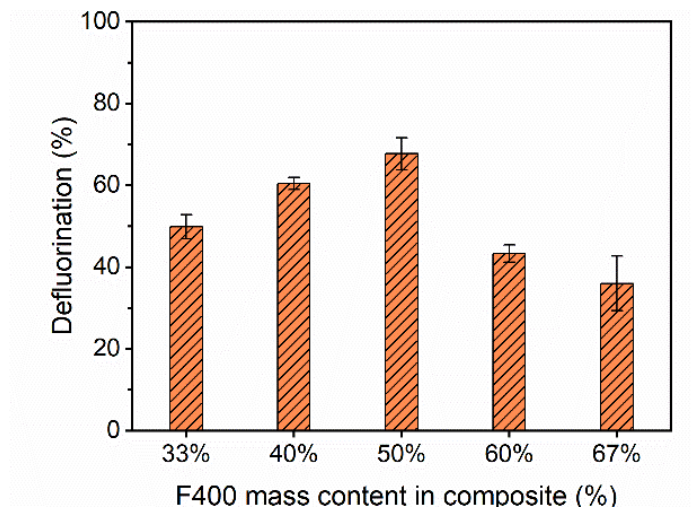
**Figure 2-6.** Photocatalytic defluorination of PFOS pre-sorbed on using 2%Ga/TNTs@AC prepared with various AC (F400) mass contents following the conditions in **Figure 2-5**. Conditions for adsorption: initial PFOS concentration = 100 µg/L, material dosage = 3 g/L, pH = 7 ± 0.1, and adsorption time = 4 h; Conditions for photodegradation: pH = 7 ± 0.1, UV intensity = 210 W/m$^2$, reaction time = 4 h. Data are plotted as mean of duplicates with error bars indicating deviation from the mean.

### 2.3.4. Effects of hydrothermal treatment time and temperature

To explore the effects of hydrothermal treatment time and temperature, Ga/TNTs@AC was prepared by varying the hydrothermal treatment time (24, 48, and 72 h) and temperature (130, 150, 165, 180, and 200 °C), and then characterized the material morphologies and crystalline structures and tested the photoactivities for PFOS defluorination. In all cases, F400 was used at a TiO$_2$/AC ratio of 1/1, and Ga was doped at 2 wt.%. **Figure 2-7** shows the SEM images of Ga/TNTs@AC prepared with various hydrothermal treatment durations and temperatures. **Figure 2-7a** shows that at 130 °C for 24 h, the bulk precursor materials (TiO$_2$) remained nearly intact, and no TNTs and AC nano/microparticles formed. At 150 °C for 24 h (**Figure 2-7b**), a fraction of the TiO$_2$ particles

40

was apparently transformed into broken rods with some AC petals grafted. When the hydrothermal temperature was increased to 165 ℃ and 180 ℃ for 24 h, rod-like structures grew longer, with some nano- or microscale AC particles attached (**Figures 2-7c** and **2-7d**). Moreover, more intensive rod-like tubular structures were formed when the temperature was elevated to 200 ℃ (**Figure 2-8**). The results indicate that elevating the hydrothermal treatment temperature facilitated the conversion of $TiO_2$ into the rod-like structures and particle breakage of AC into flower-like nano- or microparticles.

Comparing the samples prepared at 130 ℃ but with various hydrothermal treatment times (**Figures 2-7a**, **2-7e**, and **2-7i**) reveals that much finer, wool-like nanotubes were developed with prolonged treatment times. Specifically, bundle- or clustered structures were obtained with 48 h treatment, though the AC and TNTs phases appeared largely separate. Increasing the treatment time to 72 h resulted in the nanowire-like nanotubes grafted onto the surface of AC. Meanwhile, some carbon particles are attached on TNTs, forming the TNTs-AC mixed micro-phases. This observation is in accord with the report by Hu et al. (2011) that increasing hydrothermal treatment reaction time may increase the length of the TNTs. The results also agree with the measured change in SSAs and the postulated core-shell structure (**Figure 2-3**).

**Figures 2-7d**, **2-7h**, and **2-7i** show the SEM images of the samples prepared at 180 ℃ and with different hydrothermal treatment times (24, 48 h, and 72 h). By increasing the treatment duration to from 24 h to 48 h, interwoven nanotubes were observed mixed with decomposed AC particles; yet, further increasing the treatment time to 72 h converted the fine nanotubes into larger slabs as separate phases. Similar morphology was also observed in the samples treated at 165 ℃ for 48 h and 72 h (**Figures 2-7g** and **2-7k**), while the mixed-phases of carbona and interwoven TNTs were observed at the lower hydrothermal treatment temperatures (150 ℃ and 130 ℃)

(**Figures 2-7j** and **2-7i**). These results suggest that the transformation from $TiO_2$ to TNTs and further to slabs is dependent on the hydrothermal treatment duration and temperature, which is also related a critical phase-transformation pressure (Elsanousi et al. 2007).
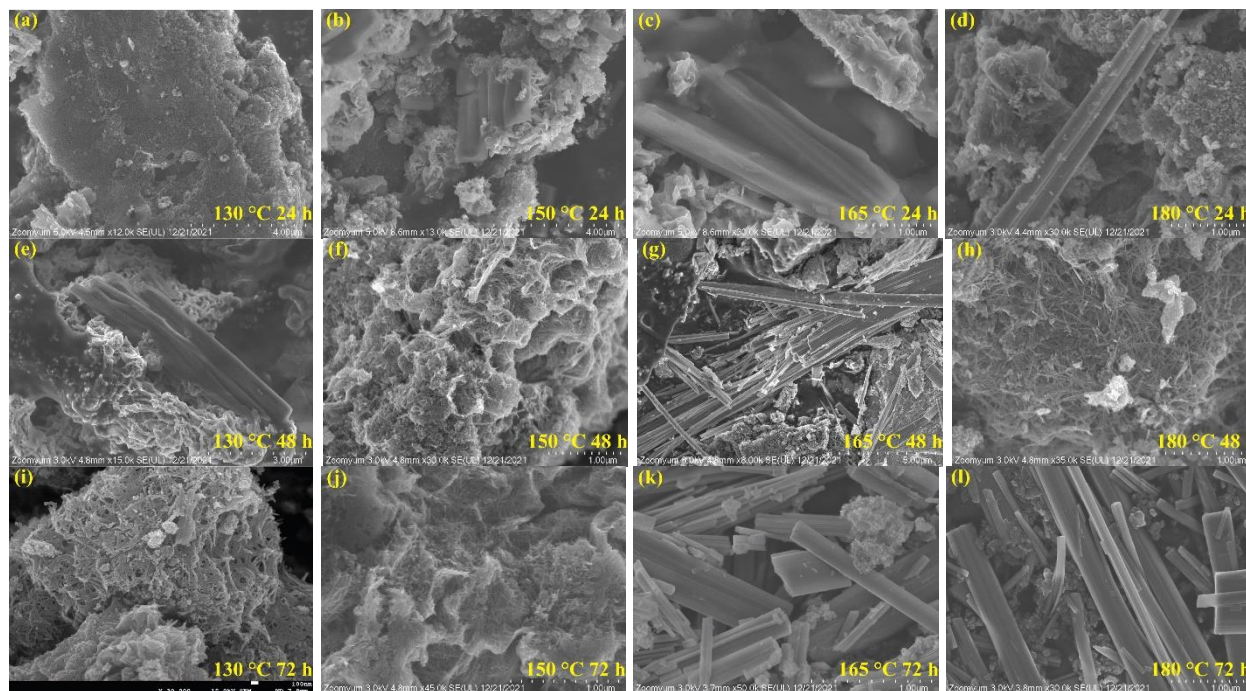


**Figure 2-7.** SEM images of 2%Ga/TNTs@AC under various hydrothermal reaction times and temperatures but otherwise identical conditions. Experimental conditions for material synthesis: mass content of F400 = 50 wt.%, NaOH concentration = 10 M, Ga = 2 wt.%, calcination temperature = 550 ℃, and calcination duration = 3.5 h.
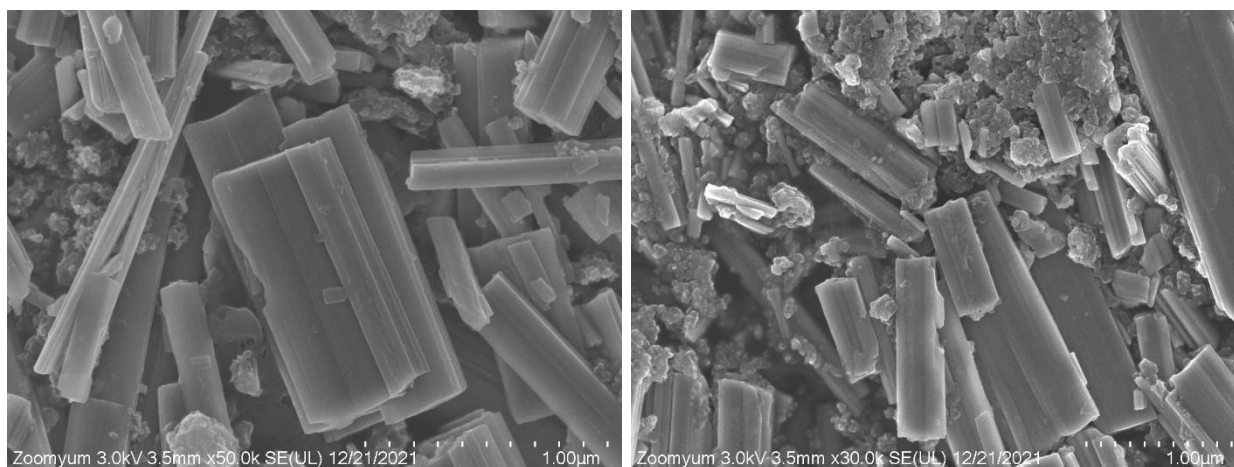
**Figure 2-8.** SEM images of 2%Ga/TNTs@AC under hydrothermal treatment condition at 200 °C for 24 h following the conditions in **Figure 2-7**.

**Figure. 2-9a** shows the XRD patterns of the composites prepared at various hydrothermal treatment temperatures but for fixed a time of 24 h. At 130 ℃, the diffraction peaks at $2\theta$ of 27.3°, 31.7°, 45.4°, 56.4°, 66.2°, and 75.3° belong to crystal NaCl, with only a small XRD peak emerged at 48.6° attributed to $Na_2Ti_3O_7$. This result is in agreement with the observation from SEM image (**Figure 2-7a**), where no obvious TNTs observed after 24 h hydrothermal treatment at 130 ℃. Notably, the peaks of NaCl vanished completely when the temperature was raised to 150 °C, while the peaks for $Na_2Ti_3O_7$ emerged at 9.8°, 24.4°, 28.3°, 48.6°, and 62.9°. Further elevating the temperature to 165 °C led to the similar XRD patterns, though the diffraction peak intensity decreased slightly. At 180 ℃, the diffraction peaks at 25.3°, 37.8°, and 48.1° are indexed to the crystalline anatase phase. However, when the hydrothermal treatment temperature was elevated to 200 ℃, the anatase peak intensity decreased and a new peak emerged at 12.8° corresponding to (101) plane of $Na_2Ti_3O_7$ besides a minor shift in $2\theta$ values (Reddy et al. 2016), indicating excessive temperature could transfer the anatase phase back to $Na_2Ti_3O_7$.

43

**Figure 2-9b** compares the XRD patterns of the samples prepared under various hydrothermal treatment temperatures but at a fixed time of 48 h. At 130 ℃, while the characteristic diffraction peaks due to NaCl still occurred, a new XRD diffraction peak at 53.9° for anatase emerged. The observation is consistent with the SEM images, indicating conversion of $TiO_2$ into TNTs. Moreover, at elevated temperatures (150 ℃-180 ℃), the NaCl peaks disappeared completely and $Na_2Ti_3O_7$ peaks emerged .

**Figure 2-9c** compares the XRD patterns of samples prepared at temperatures from 130 ℃ to 180 ℃ and with a treatment time of 72 h, the diffraction pattern at 130 ℃ was nearly identical to that of pure anatase phase. In contrast, at the higher temperatures, the diffraction peaks for the anatase phase diminished, whereas the tri-titanate phase emerged. This is attributed to the suppression of anatase transformation by the excessive tri-titanate formed during the hydrothermal treatment, due to the low loading of Ga (2 wt.%) (Zhu et al. 2021). Zhu et al. (2021) investigated that the presence of Ga altered the titanate lattice after the calcination, facilitating the transformation of anatase.



| (a) | (b) | (c) |
|-----|-----|-----|
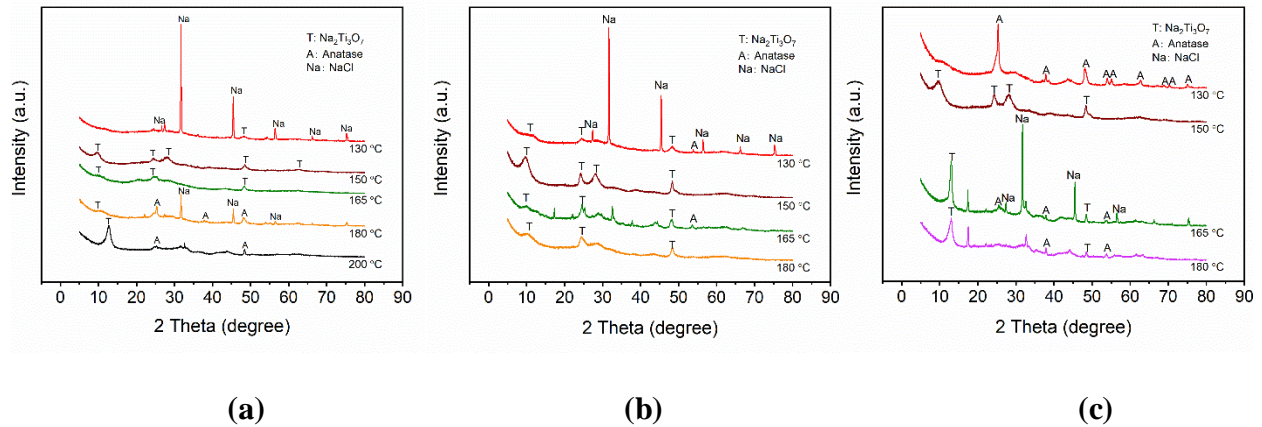
**Figure 2-9.** XRD patterns of 2%Ga/TNTs@F400 under hydrothermal treatment conditions **(a)** for 24 h at various temperature, **(b)** for 48 h at various temperature, and **(c)** for 72 h at various

temperature. Experimental conditions for material synthesis: F400 mass content = 50%, NaOH

concentration = 10 M, calcination duration = 3.5 h, and calcination temperature = 550 °C. Data are

plotted as mean of duplicates with error bars indicating deviation from the mean.
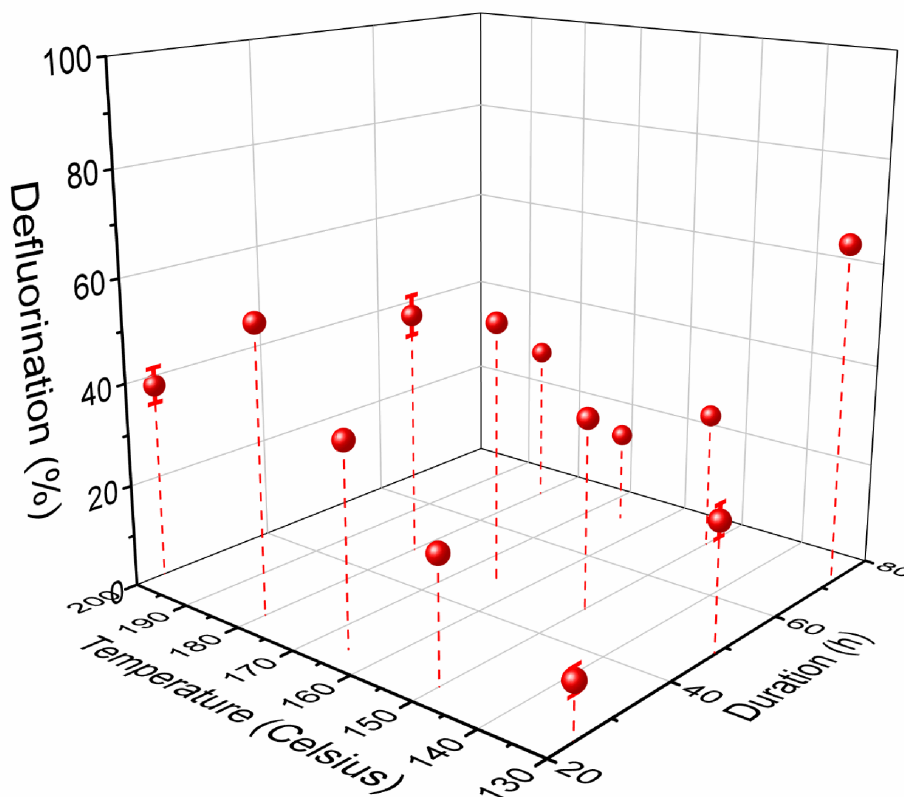


**Figure 2-10.** Defluorination of PFOS under 4-h UV irradiation by 2%Ga/TNTs@AC prepared

with various hydrothermal reaction temperature and duration following the conditions in **Figure**

**2-9**. Conditions for adsorption: initial PFOS concentration = 100 µg/L, material dosage = 3 g/L,

pH = 7 ± 0.1, and adsorption time = 4 h; Conditions for photodegradation: initial PFOS

concentration = 100 µg/L, material dosage = 3 g/L, pH = 7 ± 0.1, UV intensity = 210 W/m$^2$, and

reaction time = 4 h. Data are plotted as mean of duplicates with error bars indicating deviation

from the mean.

**Figure 2-10** compares the 4-h difluorination rates of PFOS pre-sorbed on Ga/TNTs@AC prepared under the various hydrothermal alkaline conditions. For the materials prepared with a hydrothermal treatment duration of 24 h at various temperatures, the photocatalytic performances followed the order of: 130 °C sample (10.8%) < 150 °C sample (24.2%) < 165 °C sample (38.8%) < 180 °C sample (55.5%)> 200 °C (38.1%). Namely, the highest defluorination was observed at 180 °C. However, the defluorination was decreased from 55.5% to 48.4% and 31.8% when the hydrothermal treatment time was increased from 24 h to 48 h and 72 h at 180 °C, respectively. In addition, the defluorination was also lowered when the temperature was decreased to 165 °C and 150 °C regardless of the hydrothermal treatment time (24 h to 72 h). Conversely, extending the hydrothermal treatment duration from 24 h to 48 h and 72 h at 130 °C led to highest PFOS mineralization (10.8% for 24 h, 25.1% for 48 h, and 66.2% for 72 h). Overall, the most photoactive Ga/TNTs@AC was obtained under the hydrothermal conditions of 130 °C for 72 h.

This is in accord with the above characterizations (SEM and XRD) as the composite prepared at 130 °C for 72 h (**Figure 2-7i**) resulted in the most reactive mixed phases of micro-AC particles and flowerlike fine TNTs microstructures. Such micro- or nanoscale carbon-TNTs mixed phases can facilitate cooperative adsorption and boost the subsequent solid-phase photocatalytic degradation of PFOS. Moreover, the higher content of the pure anatase phase (**Figure 2-9c**) further boosts photocatalytic activity.

**2.3.5. Effect of calcination temperature**

Calcination temperature can affect the photoactivity because it may induce phase transformation and alter the material crystallinity and SSA. The anatase phase is more photoactive than the $Na_2Ti_3O_7$ and rutile phases due to the larger band gap or relatively shallower band of the latter (Schulte et al. 2010). The transformation of titania has been known to be temperature-

dependent (Hanaor and Sorrell 2011). Sauvet et al. (2004) reporeted that pure $Na_2Ti_3O_7$ was obtained at 937 K (664 °C), whereas partial $Na_2Ti_3O_7$ decomposed into $Na_2Ti_6O_{13}$ upon sintering at 1373 K (1100 °C). Liu et al. (2005) prepared the $Zn^{2+}$-doped $TiO_2$ nanoparticles through a sol-gel method found that the most photoactive catalyst was obtained with the material calcined at 500 °C and higher calcination temperature resulted in lower photocatalytic activity, which was attributed to the transformation of anatase to rutile at the higher temperature 500 °C. (Huang et al. 2007) reported that the photocatalytic activity of N-doped $TiO_2$ increased when the calcination temperature was elevated from 300 to 500 °C, but decreased when further increased 700 °C, owing to the formation of a mixture of anatase and rutile phases at 600 °C and above.

To test the effect to calcination temperature, Ga/TNTs@AC was prepared at four different calcination temperatures (350 °C, 450 °C, 550 °C, and 650 °C), and upon proper characterization, then tested for the photocatalytic defluorination of PFOS under 4-h UV irradiation.

**Figure 2-11** the $N_2$ adsorption-desorption isotherms by Ga/TNTs@AC prepared at different calcination temperatures. According to the IUPAC classification, all isotherms conform to the Type IV isotherm, typical of mesoporous materials (2-50 nm), with an H3 hysteresis loop. **Figure 2-11b** shows the pore size distribution determined via the BJH method. The predominant pore size for all samples was 4 nm. The pore size distribution displayed a bimodal profile with another minor peak at 7 nm for the samples calcined at 350 °C and 10 nm at 450 °C. However, Ga/TNTs@AC calcined at 550 °C displayed a tri-modal pore-size distribution with three types of mesopores with sizes centered at 4 nm, 5 nm, and 6.5 nm, and the composite showed the highest pore volume at 4 nm among all the photocatalysts (**Table 2-4**). The pore volume for the catalyst calcined at 550 °C (0.50 cm³/g) was 108% and 14% larger than that at 350 °C (0.24 cm³/g) and 450 °C (0.44 cm³/g), respectively, whereas the pore volume at 650 °C (0.43 cm³/g) was similar to that at 450 °C.

47

Moreover, Ga/TNTs@AC prepared at 550 °C not only exhibited the highest SSA (341.03 m$^2$/g), but also showed the smallest pore size (5.87 nm) that at 350, 450, and 650 °C, resulting in the more adsorption sites and hybrid phases.
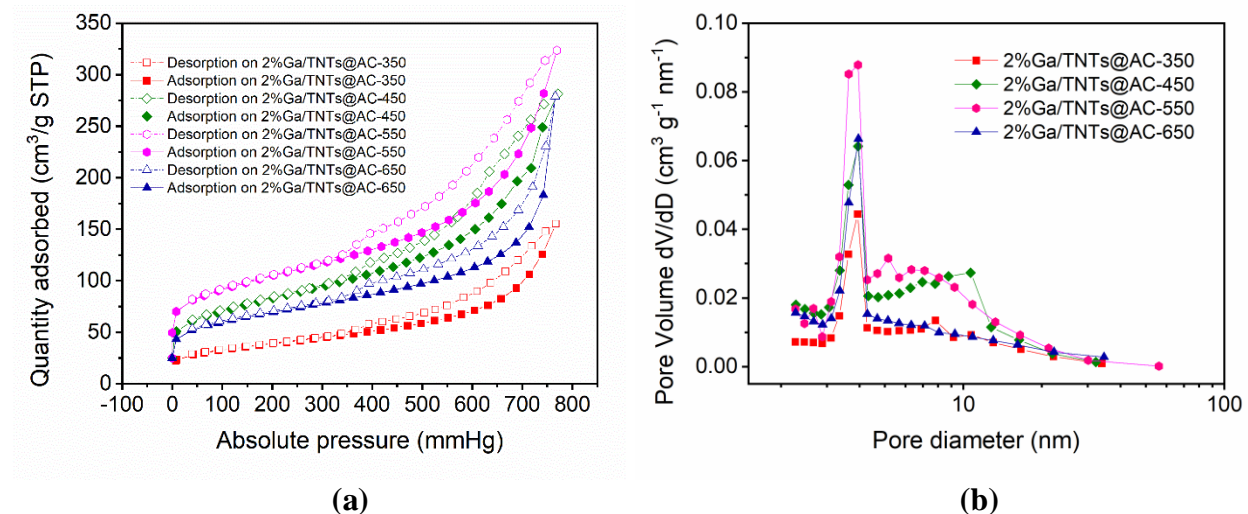


**Figure 2-11. (a)** N$_2$ adsorption-desorption isotherms and **(b)** pore size distributions of 2%Ga/TNTs@AC calcined at various temperatures. Experimental conditions for material synthesis: F400 mass content = 50%, NaOH concentration = 10 M, hydrothermal reaction time = 72 h, hydrothermal reaction temperature = 130 °C, and calcination duration = 3.5 h.

**Table 2-4.** BET-based specific surface areas of 2%Ga/TNTs@AC calcined at various temperatures.

| Carbon | BET surface area (m²/g) | Pore volume (cm³/g) | Pore size (nm) |
|---|---|---|---|
| 2%Ga/TNTs@F400-350 | 127.54±3.71 | 0.24 | 7.52 |
| 2%Ga/TNTs@F400-450 | 272.30±1.98 | 0.44 | 6.39 |
| 2%Ga/TNTs@F400-550 | 341.03±3.71 | 0.50 | 5.87 |
| 2%Ga/TNTs@F400-650 | 226.28±2.35 | 0.43 | 7.63 |

**Figure 2-12a** shows the XRD patterns of the Ga/TNT@AC calcined at various temperatures. The peaks at 9.9°, 24.3°, 28.3°, and 48.3° were observed for the case of 350 °C, which are ascribed to $Na_2Ti_3O_7$. In addition, the characteristics peaks of crystal NaCl at 27.3°, 31.7°, 45.4°, 56.6°, 66.2°, and 75.3° were also observed, indicating the coexistence of NaCl and $Na_2Ti_3O_7$ when calcined at 350 °C. When the calcination temperature was raised to 450 °C, the NaCl phase completely disappeared, while the crystal phase of $Na_2Ti_3O_7$ remained, though the intensity of the $Na_2Ti_3O_7$ peaks decreased notably. In contrast, upon calcination at 550 °C, the sodium tri-titanate phase was transformed into the anatase phase with a tetragonal structure. Our prior study (Zhu et al. 2021) revealed that the doped Ga played a critical role in this phase transformation process . The resulting anatase crystallites can absorb a broader range of light. Further increasing the calcination temperature to 650 °C resulted in the similar XRD pattern to that for 550 °C, while additional seven characteristic peaks emerged belonging to monoclinic sodium tetratitanate

($Na_{0.8}Ti_4O_8$). $Na_{0.8}Ti_4O_8$ is thermally unstable, which can be converted to $Na_2Ti_6O_{13}$ at elevated temperature (Dostanić et al. 2019; Triviño-Bolaños and Camargo-Amado 2019).

**Figure 2-12b** compares the 4-h PFOS mineralization rates by Ga/TNTs@AC prepared at a fixed Ga content of 2 wt.% and various calcination temperatures (350, 450, 550, and 650 °C) under 4-h UV irradiation. Increasing the calcination temperature from 350 °C to 450 °C and 550 °C increased the defluorination rate from 11.1% to 50.7% and 66.2%, respectively. However, further elevating the temperature to 650 °C decreased the PFOS mineralization to 41.9%), which is in accord with the transformation of the more active anatase phase into the sodium titanate phase as well as a significant reduction in the SSA and loss of mesoporous structure. Thus, the optimal calcination temperature for Ga/TNTs@AC was determined to be approximately 550 °C. This observation agrees with the results by(Li et al. 2020a), who found that iron-doped TNTs@AC prepared at a calcination temperature of 550 °C displayed the highest defluorination rate for PFOA.



(a)            (b)
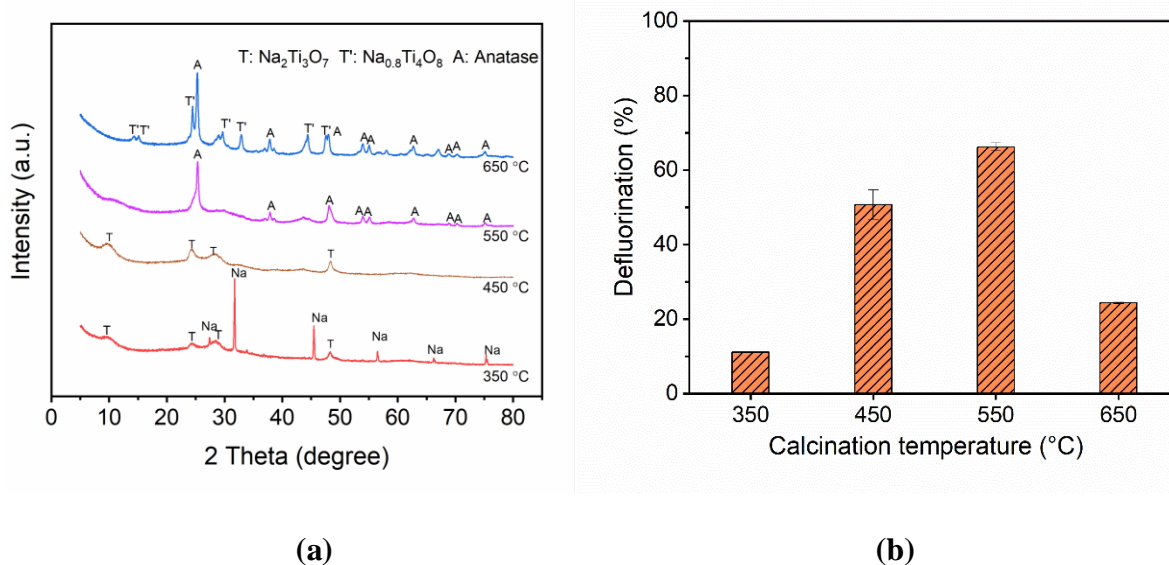
**Figure 2-12. (a)** XRD patterns and **(b)** Defluorination of PFOS under 4-h UV irradiation of 2%Ga/TNTs@F400 prepared with various calcination temperature following the conditions in

**Figure 2-11**. Conditions for adsorption: initial PFOS concentration = 100 µg/L, material dosage = 3 g/L, pH = 7 ± 0.1, and adsorption time = 4 h; Conditions for photodegradation: initial PFOS concentration = 100 µg/L, material dosage = 3 g/L, pH = 7 ± 0.1, UV intensity = 210 W/m$^2$, reaction time = 4 h. Data are plotted as mean of duplicates with error bars indicating deviation from the mean.

### 3.6 Toxicity assessment of by-products

As illustrated by previous study (Zhu et al. 2021), the intermediate products after 4 h of the PFOS photocatalytic process by 2%Ga/TNTs@AC included the shorter chain PFOA (C7F15COOH), PFHpA ($C_6F_{13}COOH$), PFHxA ($C_5F_{11}COOH$), PFPeA ($C_4F_9COOH$), PFBA ($C_3F_7COOH$), PFPA ($C_2F_5COOH$), and TFA ($CF_3COOH$). In this work, the acute and chronic toxicity of PFOS and its intermediate products of photocatalytic degradation towards fish, daphnid, and green algae were predicted by ECOSAR (V2.0), which was issued by US Environmental Protection Agency. According the LC50, EC50, and ChV values, the toxicity of compounds could be classified into four categories, including harmless (>100.0 mg/L), harmful (10.0-100.0 mg/L), toxic (1.0-10 mg/L), and highly toxic (<1.0 mg/L) (Chen et al. 2022; Xu et al. 2017b). As shown in **Figure 2-13**, PFOS was toxic to fish and daphnid when considering its chronic toxicity, while it had harmful effect on the three kinds of test organisms for acute toxicity. As for the PFOA, it was toxic not only to fish, daphnid, and green algae regarding the chronic toxic testing, but also to daphnid for the acute toxicity. Considering the other generated intermediates (from PFHpA to TFA), the overall trend of toxicity decreased with decreasing carbon content. This observation is also confirmed by **Figure 2-13b**, which displays the relationship between intermediate products arranged by increasing carbon numbers and $-\log(1/(EC_{50}$ or $LC_{50}))$. The result shows that the acute

toxicity of intermediate products declined with decrease of the fluorinated carbon-chain length, suggesting that the shorter carbon-chain results in lower toxicity. Alternatively, compared to the parent PFOS, all of the transformation products with reduced carbon numbers showed toxicity reduction. In consideration of impacts of 2%Ga/TNTs@AC upon the aquatic environment, Zhu et al. (2021) reported that no Ti and less than 1.3% of embedded Ga were leached from 2%Ga/TNTs@AC over 4 consecutive adsorption and photodegradation runs. Consequently. 2%Ga/TNTs@AC, based on activated carbon and low-cost $TiO_2$, is an environment-friendly and renewable material. It is ecotoxicologically effective for the treatment of PFOS, transforming to less-toxic shorter chain carboxylic acids during photodegradation process under UV irradiation. Therefore, the 2%Ga/TNTs@AC can be used as an excellent adsorptive photocatalyst for practical implications toward PFOS removal and degradation.



**(a)**                                         **(b)**
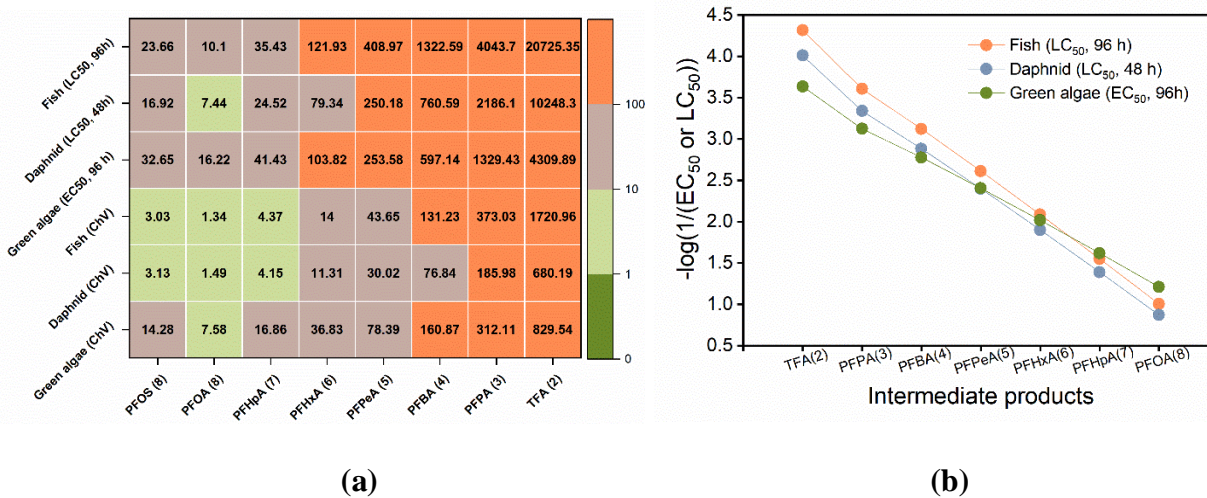
**Figure 2-13. (a)** Acute and chronic toxicity of intermediate products predicted by ECOSAR and **(b)** relationship between intermediate products and $-\log(1/(EC_{50}$ or $LC_{50}))$. $EC_{50}$ = Median effect concentration, $LC_{50}$ = Median lethal concentration, and ChV = Chronic value predicted by ECOSAR V2.0 model.

**2.4. Conclusions**

A series of metal ions-doped TNTs@AC nanocomposites with different carbon (F400) mass contents, carbon sources, hydrothermal treatment conditions (temperature and duration), and calcination temperatures, were prepared and evaluated their photocatalytic performance on the removal of the pre-sorbed PFOS. The major findings are summarized as follows:

1) Comparing with the metal dopants, including $Ga^{3+}$, $In^{3+}$, $Fe^{3+}$, $Bi^{3+}$, $Co^{2+}$, $Mn^{2+}$, and $Cu^{2+}$, $Ga^{3+}$ exhibited highest PFOS defluorination rate. Based on the PL and UV-vis diffuse reflectance spectra, the embedded $Ga^{3+}$ not only facilitated light absorption, but also induced the oxygen vacancies by the substitution of $Ti^{4+}$. Moreover, higher pre-sorbed PFOS mineralization rate was attained with trivalent metal ions than divalent, which is attributed to the presence of anatase phase transformed from the tri-titanate phase upon the calcination from XRD diffraction patterns, while the highest defluorination rate was still remained by the TNTs@F400 doped by 2 wt.% $Ga^{3+}$.

2) 2%Ga/TNTs modified by Filtrosorb-400® granular activated carbon (F400) shows higher pre-sorbed PFOS defluorination efficiency (66.2%) than other carbon sources, which is ascribed to the smaller particle size and larger BET surface area of precursor F400, and smaller pore size for resulting 2%Ga/TNTs@F400. Those parameters may result in higher adsorption, back scattering of the light, shortening the paths for intermediate degradation products, offering more avaible and accessible sites on the shell of material, and increasing the adsorption strength, respectively, which enhances the photoactivity toward PFOS degradation.

3) 2%Ga/TNTs@F400 prepared with 1.2 g $TiO_2$ and 1.2 g F400 as the precursor carbon source exhibited higher pre-sorbed PFOS defluorination (66.2%) under 4-h UV irradiation.

Decreasing or increasing the carbon content in the range of 33% to 67% led to lower PFOS mineralization rates. Based on the XRD and PL results, the superior photoactivity of 2%Ga/TNTs@50%F400 was attributed to the formed anatase phase during the calcination and inhibition of the recombination of the $e^-/h^+$ pairs.

4) The highest PFOS defluorination rate remained at 66.2% under the hydrothermal treatment conditions of 10 M NaOH at 130 °C for 72 h. The nanowire-like nanotubes were observed for 72 h at 130 °C with a flower-like structure grafted onto the surface of AC in SEM image. XRD diffraction pattern displayed apparent anatase phase in the sample of 2%Ga/TNTs@F400 prepared at 130 °C for 72 h.

5) Referring to the calcination temperature, 550 °C was determined to the optimal calcination temperature for the 2%Ga/TNTs@F400 with the 66.2% pre-sorbed PFOS defluorination efficiency, which is due to the pure anatase crystallites from the XRD pattern and the higher SSA from BET data.

Overall, according to the pre-sorbed PFOS mineralization (66.2%) under 4-h UV irradiation, the optimal values of synthesis parameters were obtained as 130 °C, 72 h, 50% carbon mass content, GACF400 as the carbon source, calcination temperature of 550 °C, and $Ga^{3+}$ as the metal dopant.

**Chapter 3. Adsorption and Solid-Phase Photocatalytic Degradation of Perfluorooctane Sulfonate in Water Using Gallium-Doped Carbon-Modified Titanate Nanotubes**

PFOS has drawn increasing attention due to its omnipresence and adverse health effects. We prepared a new adsorptive photocatalyst, Ga/TNTs@AC, based on activated carbon and $TiO_2$, and tested the adsorption and subsequent solid-phase photodegradation of PFOS. Ga/TNTs@AC showed faster adsorption kinetics and higher affinity for PFOS than the parent AC, and could degrade 75.0% and mineralize 66.2% of pre-sorbed PFOS within 4-h UV irradiation. The efficient PFOS photodegradation also regenerates Ga/TNTs@AC, allowing for repeated uses without invoking chemical regenerants. The superior photoactivity is attributed to the oxygen vacancies, which not only suppressed recombination of the $e^-/h^+$ pairs, but also facilitated $O_2^{\bullet-}$ generation. Both $h^+$ and $O_2^{\bullet-}$ played critical roles in the PFOS degradation, which starts with cleavage of the sulfonate group and converts it into PFOA that is then decarboxylated and defluorinated following the stepwise defluorination mechanism. Ga/TNTs@AC holds the potential for more cost-effective PFOS degradation.

## 3.1. Introduction

PFOA and PFOS are the most detected PFAS in drinking water (Li et al. 2019). A recent survey revealed that drinking water supplies for 6 million U.S. residents exceeded the EPA lifetime health advisory (70 ng/L) for the sum of PFOA and PFOS (Hu et al. 2016). Amid mounting health concerns, the EPA further unveiled a PFAS Action Plan in early 2019, which would move forward with developing a nationally enforceable Maximum Contaminant Level (MCL) for PFOA and PFOS in drinking water (Li et al. 2019). In the meanwhile, many US states have established or proposed MCLs and action levels for the PFAS in drinking water. For instance, several states have recommended MCLs in the range of 10-15 ng/L (JDSUPRA 2019). While PFOA and PFOS are both long-chain (C8) PFAS, they bear different head groups (carboxylate vs. sulfonate). As such, PFOS is more hydrophobic (organic carbon partition coefficient = 2.57 for PFOS and 2.06 for PFOA), more bio-accumulative, and more persistent to various degradation processes (EPA 2017b).

Gallium (Ga) is one of the commonly used dopants in photocatalysis, electrocatalysis, and sensors (Manríquez et al. 2009; Mohammadi and Fray 2007). Ga (hydr)oxides are considered non-toxic to the human and environmental health partially due to the low solubility (Schulz et al. 2018) and poor absorbability to biota (Gray et al. 2000; Schulz et al. 2018; Staff et al. 2011). As such, gallium has been widely used for modifying $TiO_2$ (Myilsamy et al. 2018). While relevant toxicity data has been very limited, a recent study revealed the activities of two types of microorganisms were not affected when exposed to up to 500 mg/L of $Ga_2O_3$ nanoparticles (Nguyen et al. 2020). Myilsamy et al. (2018) used Ga to modify $TiO_2$ and observed enhanced photocatalytic degradation of Rhodamine B. They also reported that Ga doping induced oxygen vacancies owing to the substitution of $Ti^{4+}$ by $Ga^{3+}$, facilitating the separation of the $e^-/h^+$ pairs. Guo et al. (2018) reported

that Ga-doped Au/TiO$_2$ nanotubes exhibited superior catalytic activity and stability over plain Au/TiO$_2$ nanotubes, and they also attributed the phenomenon to the defects associated with the Ga-induced oxygen vacancies. Apart from acting as a dopant, gallium oxide (Ga$_2$O$_3$) itself is a photoactive semiconductor. Shao et al. (2013) observed that needle-like β-Ga$_2$O$_3$ exhibited a 16.8-times higher degradation rate for PFOA than TiO$_2$ due to more favorable interactions between Ga$_2$O$_3$ and PFOA. Zhao et al. (2015) reported that synthetic β-Ga$_2$O$_3$ nanorods were able to mineralize 56.2% of PFOA in an anaerobic atmosphere. However, there has been no report on photocatalytic degradation of PFOS using Ga-doped TiO$_2$ or Ga$_2$O$_3$ as a photocatalyst.

Several adsorptive photocatalysts have been studied, including iron-doped AC-supported titanate nanotubes (Fe/TNTs@AC) and carbon-sphere (CS) modified ferrihydrite or bismuth phosphate composites (Li et al. 2020a; Xu et al. 2020a; Xu et al. 2020b). The new adsorptive photocatalysts may enable a new concentrate-and-destroy strategy, where low-concentrations of PFAS are first adsorbed on the photocatalytic sites, and then degraded under UV or solar light. Namely, adsorption is used to treat the bulk water, whereas photodegradation is only applied to the PFAS-laden solid. This arrangement is expected to be more energy-efficient compared to conventional photocatalytic processes that apply the photodegradation directly to the bulk water. However, the effectiveness of these new materials for treating PFOS has not been explored. Moreover, given the different photocatalytic characteristics of Ga from Fe and Bi, especially, its ability to facilitate oxygen vacancies and $e^-/h^+$ separation, we could expect that Ga-doped TNTs@AC (Ga/TNTs@AC) may serve as a promising photocatalyst for enhanced adsorption and degradation of PFOS in contaminated waters.

As such, the overall goal of this study was to fabricate a novel Ga-embedded adsorptive photocatalyst Ga/TNTs@AC and test its performance for PFOS adsorption and subsequent

photodegradation. The specific objectives were to (1) synthesize the desired catalyst through a modified alkaline hydrothermal-calcination method, (2) test the adsorption kinetics and capacity of Ga/TNTs@AC for PFOS, (3) determine the solid-phase photodegradation rate of pre-sorbed PFOS, (4) examine the effects of pH, (5) evaluate the material reusability, and (6) elucidate the underlying reaction mechanisms.

## 3.2. Materials and methods

### 3.2.1. Chemicals

Nano-TiO$_2$ (P25, 80% anatase and 20% rutile) was obtained from Evonik Industries AG, Germany, and Filtrosorb-400® granular activated carbon (F-400 GAC) was acquired from Calgon Carbon Corporation (PA, USA) (density = 2.1 t/m$^3$, size = 0.25-0.5 mm, and specific surface area = 1050-1200 m$^2$/g). PFOS, anhydrous gallium chloride, sodium hydroxide, methanol, ethanol, isopropanol, benzoquinone, and potassium iodide were purchased from VWR International (Radnor, PA, USA). **Table 3-1** provides relevant physical-chemical properties of PFOS Sodium perfluoro-1-[$^{13}$C$_8$] octanesulfonate (M8PFOS) was purchased from Wellington Laboratories Inc. (Guelph, Ontario, Canada Perfluoro) and was used as isotopically labeled internal standard (IS) for PFOS analysis. All chemicals were analytical-grade or higher. All solutions were prepared using deionized (DI) water (18.2 MΩ cm).

**Table 3-1**. Key properties of PFOS.

| Molecular Formula | $C_8F_{17}O_3S$ | 2-D structure |
|---|---|---|
| Molecular Weight (g/mol) | 500.13 | |
| Water solubility (25°C) (mg/L) | 680 |  |
| Organic carbon partition coefficient $K_{oc}$ | 2.57 | 3-D structure |
| Vapor pressure at 25°C (mm Hg) | 0.002 |  |
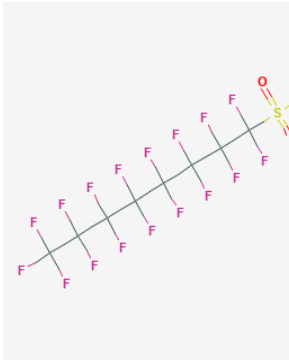
### 3.2.2. Synthesis of Ga/TNTs@AC

First, TNTs@AC was prepared through a modified one-step hydrothermal method (Liu et al. 2016). In brief, 1.2 g of AC and 1.2 g of $TiO_2$ were mixed in 66.7 mL of a 10 M NaOH solution. After magnetic stirring for 12 h, the mixture was transferred into a Teflon reactor with a stainless-steel cover and heated at 130 °C for 72 h. The black precipitate (TNTs@AC) was separated upon gravity settling and washed with DI water until pH reached $7.0 \pm 0.5$, and then dried at 105 °C. No PFOS was detected in the resulting material.

Second, 1 g dried TNTs@AC was dispersed in 80 mL DI water under continuous stirring. Then, 2, 4, 6, or 10 mL of a $GaCl_3$ solution (5 g/L) was added dropwise into the TNTs@AC suspension. After stirring for 3 h, the mixture was separated by removing the supernatant, and then oven-dried at 105 °C. Based on the initial and final concentrations of Ga in the aqueous phase,

59

>99.7% of Ga$^{3+}$ was taken up by TNTs/AC. In addition, <0.01 % of Ti was dissolved in the supernatant during the Ga-doping. Based on the Ga percentage mass content, the resulting composites were denoted as 1%Ga/TNTs@AC, 2%Ga/TNTs@AC, 3%Ga/TNTs@AC, and 5%Ga/TNTs@AC. Finally, the dried particles were subjected to calcination at 550 °C with a temperature ramp of 10 °C/min and at a nitrogen flow of 100 mL/min. For comparison, plain TNTs@AC was also prepared separately via the same procedure but without Ga, and a sample of treated AC was prepared by subjecting the neat AC to the same alkaline hydrothermal and calcination procedures.

### 3.2.3. Characterization

The surface morphology and microstructure were characterized by field emission scanning electron microscopy (FE-SEM, JEOL, JEM-7600F) and high-resolution transmission electron microscopy (HRTEM, TF20, JEOL 2100F). The crystal phases of the materials were identified through X-ray diffraction (XRD) analysis using a Bruker D2 PHASER X-ray diffractometer (Bruker AXS, Germany) with Cu Kα radiation ($\lambda = 1.5418$ Å). The elemental compositions and oxidation states were analyzed via AXIS-Ultra X-ray photoelectron spectroscopy (XPS, Kratos, England) with the AI $K\alpha$ X-ray at 15 kV and 15 mA. The standard C 1s peak (Binding energy, $E_b$=284.80 eV) was used to calibrate all the peaks and eliminate the static charge effects. The Brunauer-Emmett-Teller (BET) surface area was measured on an ASAP 2010 BET surface area analyzer (Micromeritics, USA) in the relative pressure ($P/P_0$) range of 0.06-0.20. The pore size distribution was obtained following the Barret-Joyner-Halender method. Nitrogen adsorption at the relative pressure of 0.99 was performed to determine the pore volumes and the average pore size. Zeta potential of the materials was determined by a Nano-ZS90 Zetasizer (Malvern Instrument, Worcestershire, UK). Electron paramagnetic resonance (EPR) analysis was performed

to monitor surface defects of the materials using a Bruker EPR A300-10/12 spectrometer (center field = 3500 G, sweep width = 1000 G, microwave frequency = 9.82 GHz, field modulation frequency = 100 kHz, and microwave power = 0.63 mW). The optical properties were assessed through photoluminescence (PL) spectroscopy using a Cary Eclipse 100 fluorescence spectrophotometer employing a xenon lamp excitation source at an excitation wavelength of 260 nm. Raman scattering was excited by a 514.5 nm line air-cooled 20 mW argon ion laser using a Renishaw inVia Raman microscope system.

Based on the defluorination performance, the material characterization focused on 2%Ga/TNTs@AC, although Raman, XRD and BET analyses were performed on all the materials to understand the effects of Ga contents on the phase transformation, crystalline composition, and surface area of the composites.

### 3.2.4. Adsorption kinetic and isotherm experiments

Adsorption kinetic experiments were carried out in the dark using 40 mL high-density polypropylene (HDPE) vials. The reaction was initiated by mixing 40 mL of a PFOS solution (100 µg/L) and 0.12 g of a Ga/TNTs@AC, with the pH adjusted to $7.0 \pm 0.1$. The vials were then placed on a rotator (100 rpm) located in an incubator at 25°C. At predetermined times, duplicated samples were taken and centrifuged at 4000 rpm for 3 min. The supernatants were analyzed for PFOS remaining in the aqueous phase. For comparison, adsorption kinetic data for the treated AC and TNTs@AC were also obtained in the same manner. Adsorption isotherms were performed in a similar fashion, where the mixtures were equilibrated for 24 h and the initial PFOS concentration was varied from 5 to 100 mg/L while the Ga/TNTs@AC dosage was kept at 1 g/L. In all cases, equilibrium was reached within a few hours. All experiments were carried out in duplicate to assure data precision.

### 3.2.5. Photodegradation of PFOS

Following the adsorption equilibrium (initial PFOS = 100 µg/L), the mixtures were left still for 1 h to allow the composite material to settle by gravity. Then, ~95% of the supernatant was pipetted out, and the remaining solid-liquid mixture was transferred into a quartz photo-reactor with a quartz cover reactor. Subsequently, 8 mL DI water was added to the mixture so that the total solution volume reached 10 mL. The photoreactor was then subjected to UV irradiation in a Rayonet chamber UV-reactor (Southern New England Ultraviolet CO., Branford, CT, USA) equipped with 16 RPR-2537 Å lamps at the distance of 1.5 in (3.81 cm) and with a light intensity of 210 W/m$^2$. A cooling fan was mounted at the bottom of the photoreactor to keep the temperature inside the chamber in the range of 30-40 °C. The solids in the quartz photo-reactor were manually shaken intermittently to facilitate the UV exposure (for large reactors, the solid-liquid slurry can be stirred continuously as commonly practiced in photocatalytic processes). At predetermined times (*i.e.*, 1, 2, 3, and 4 h), the mixtures were sacrificially filtered through a 0.22 µm polyether sulfone (PES) membrane. Then, the filtrates were analyzed for fluoride and PFOS, and the solids were extracted using 40 mL of methanol at 80 °C for 8 h to determine the remaining PFOS and reaction byproducts in the solid phase. The average method recovery was >90% for PFOS, and thus no surrogate IS was used during the extraction. In all cases, no PFOS was detected in the filtrates.

Defluorination of PFOS was quantified based on the fluoride concentration in the aqueous phase. Fluoride adsorption on the solid phase sample during the photodegradation process was negligible. To confirm, the solid sample after the photodegradation was extracted using 20 mL of a 1 M NaOH solution. The extractant was then neutralized by a 2 M HCl solution to 7.0 ± 0.5 and then filtered with a 0.22 µm PES membrane. No fluoride was detected in the filtrate.

Meanwhile, *in situ* radical scavenging experiments were carried out following the similar experimental procedures, but in the presence of a specific radical scavenger, including 10 mM of potassium iodide (KI), isopropanol (IPA), and benzoquinone (BQ) to probe the roles of the holes ($h^+$), hydroxyl radical ($^\bullet$OH), and superoxide radical ($O_2^{\bullet-}$), respectively.

### 3.2.6. pH effects

The effects of pH on the adsorption and the subsequent photodegradation of PFOS were tested using 2%Ga/TNTs@AC (the most effective material) at a dosage of 3 g/L and an initial PFOS concentration of 100 µg/L. For the adsorption tests, the initial solution pH was varied from 3.5 ± 0.1 to 10.5 ± 0.1. For the photodegradation tests, the same adsorption experimental procedures with initial solution pH of 7.0 ± 0.1 were followed, and then, upon removal of the supernatant, the pH of the remaining mixture was adjusted from 3.5 ± 0.1 to 12.0 ± 0.1 during the photodegradation process.

### 3.2.7. Reusability of Ga/TNTs@AC

Following the photodegradation experiments (**Section 2.5**), the photo-regenerated Ga/TNTs@AC was collected and then reused in another cycle of adsorption and photodegradation experiments following the same protocol and under the same conditions. The reusability was tested in 4 consecutive cycles. In addition, control experiments were carried out by reusing the same Ga/TNTs@AC in four consecutive adsorption runs under the same batch adsorption conditions but without the photo-regeneration after each run. After the fourth adsorption, the solids were collected and then subjected to the same photodegradation protocol to gauge the defluorination rate.

### 3.2.8. Chemical analysis

PFOS in solution was determined using an ultra-performance LC system (UPLC, ACQUITY, Waters Corp., USA) equipped with an electrospray ion source operated in the negative mode and coupled with a quadrupole time-of-flight mass spectrometer (QTOF-MS, Q-TOF Premier, Waters). The instrument detection limit was <1 µg/L. M8PFOS (20 µg/L) was used as the IS. Aqueous $F^-$ was analyzed by ion chromatography (Dionex, CA, USA) equipped with an anion exchange column (Dionex Ionpac AS22) and an anion dynamically regenerated suppressor (ADRS 600, 4mm). The detection limit was $10.00 \pm 0.01$ µg/L. Dissolved Ga and Ti were determined on an inductively coupled plasma-optical emission spectroscopy (ICP-OES, 710-ES, Varian, USA), with a detection limit of 50 µg/L for both elements.

### 3.2.9. Analysis of PFOS by LC-QTOF-MS

PFOS concentration and its photodegradation intermediates were determined using an ultra-performance LC system (UPLC, ACQUITY, Waters Corp., USA) coupled to electrospray ionization (ESI) with a quadrupole time-of-flight mass spectrometer (QTOF-MS, Q-Tof Premier, Waters) in the negative mode. $^{13}C8$ PFOS (20 µg/L) was used as the internal standard for PFOS analysis. Briefly, a sample or standard (10 µL) was injected into a C18 column (Luna C18(2), 3 µm, 100 Å, $2 \times 50$ mm with a $2 \times 4$ mm guard cartridge, Phenomenex). Gradient elution was performed using a mobile phase consisting of a 2 mM ammonium acetate aquesou solution (pH = 4.7) as solvent A and 100% acetonitrile as solvent B. The flowrate of mobile phase was set at 0.2 mL/min. The gradient conditions were: begin with 70% A and 30% B for the first 0.3 min, then change to 95% B for 3.4 min, hold for 0.7 min, back to 30% acetonitrile for 1.2 min, and re-equilibrate for 1.4 min, resulting a total run time of 7 min. The voltages for capillary, sample cone, and extraction cone were set at 2.8 kV, 30 V, and 4.0 V, respectively. The source temperature was performed at

100 °C, and the desolvation temperature was maintained at 300 °C with a gas flowrate of 600 L/h. The TOF/MS scan was 1 s from 150 to 600 m/z with a 0.02 s inter-scan delay using the centroid data format. A 0.2 mg/L solution of Leucine encephalin was used as the lock mass reference standard for instrument tuning and calibration. The ion source parameters such as the source temperature (gas and sample cone), mobile phase flow rate, and cone voltage were kept constant throughout the study.

The calibration of LC-QTOF-MS system was performed each time of analysis using at least five PFOS standards in the linear concentration range of 1 to 90 µg/L. The relative standard deviation (%RSD) of the response factors (RFs) for all analysts must be within ± 20% or the linear regression $R^2$ must be ≥0.99, based on initial calibration (ICAL) criteria and their true values. The second source standard was used after the ICAL for the initial calibration verification. The analyte concentrations were within ± 30% of their true value. After 10 samples each time or at the end of the sequence, two consecutive calibration verification standards were analyzed before next sample analysis with analyte concentrations within ± 30% of their true values from the Limit of Quantitation (LOQ) (5 µg/L) to the mid-level calibration concentration.

### 3.3. Results and discussion

### 3.3.1. Characterization of Ga/TNTs@AC

**Figures 3-1a and 3-1b** show the FE-SEM images of 2%Ga/TNTs@AC calcined at 550 °C. The particle surface appeared as clusters of aggregated particles, with interwoven or interfused TNTs patched with decomposed AC particles. Gallium oxide and/or AC particles were found randomly attached to the sheet-like structure. **Figure 3-1c** presents the EDS mapping of the elements on the surface of 2%Ga/TNTs@AC, indicating that Ti, C, Na, O, and Ga were uniformly distributed on the surface of 2%Ga/TNTs@AC.

**Figures 3-1d-f** present the TEM images of 2%Ga/TNTs@AC, where carbon nanoparticles resulting from the decomposition of the parent AC were blended with TNTs (**Figure 3-1d**). **Figure 3-1e** shows that TNTs had an inner diameter of ~5 nm and an outer diameter of ~12 nm. Moreover, the interlayer distance of TNTs was 0.75 nm, which is assigned to the crystal plane (020) of titanate (Wang et al. 2018). In addition, most of the nanotubes kept their tubular texture after the calcination. The crystal distance of 0.35 nm was also observed, which belongs to the crystal plane of anatase (101) (Zhao et al. 2016b). Besides the nanotubular structure, some partially rolled titanate slabs were also observed (**Figure 3-1f**).

The modifications of TNTs by AC nanoparticles and Ga were expected to induce multiple synergistic interactions with PFOS, including electrostatic and metal-ligand interactions with the head sulfonate group, hydrophobic interactions with the tail group, and anion-$\pi$ or $\pi$-CF interactions between the electron-deficient aromatic skeletons of AC and the $CF_2/CF_3$ and sulfonate groups (Liu et al. 2015b; Wang et al. 2012a; Xu et al. 2020b). In addition, the AC and Ga modifications also facilitate light absorption and electron transfer and inhibit hole-electron recombination.



**(a)**   **(b)**   **(c)**

66

**(d)**   **(e)**   **(f)**
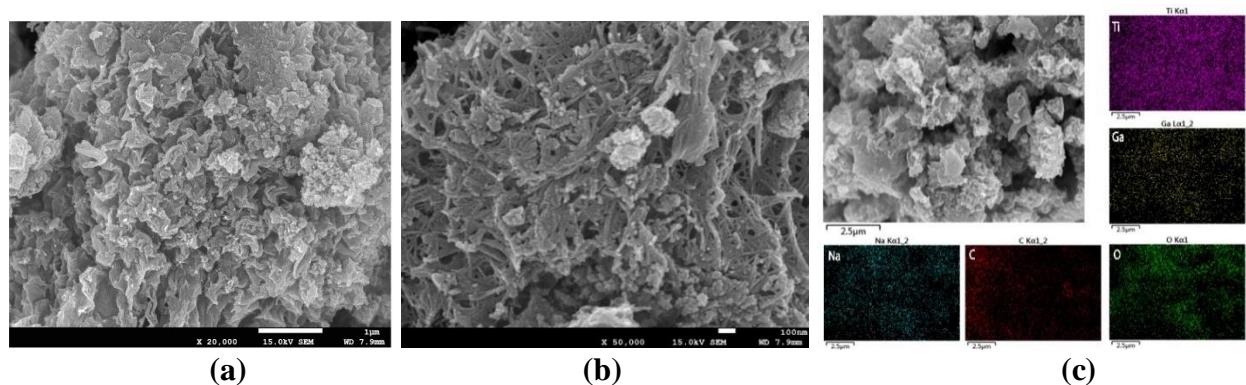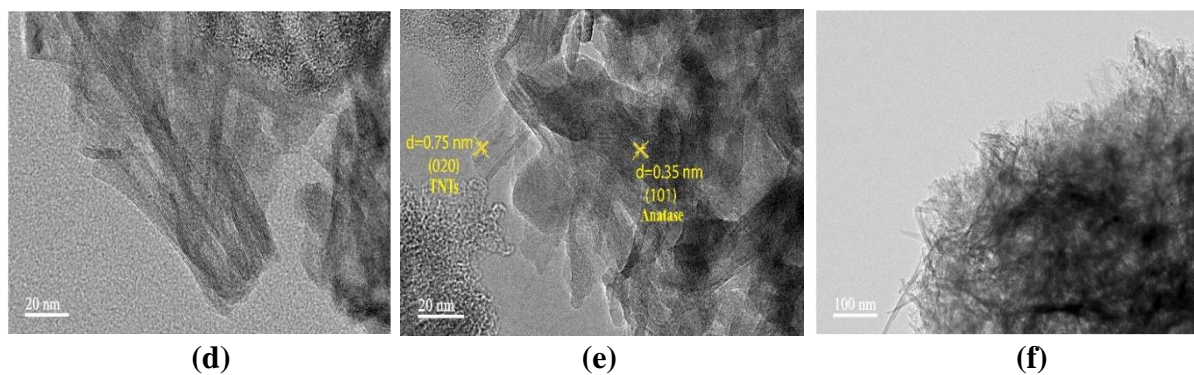
**Figure 3-1. (a, b)** FE-SEM images and **(c)** EDS mapping of 2%Ga/TNTs@AC; and **(d, e, f)** TEM images of 2%Ga/TNTs@AC. 2%Ga/TNTs@AC was calcined at 550 ℃.

**Figure 3-2a** shows the $N_2$ adsorption-desorption isotherms for TNTs@AC and 2%Ga/TNTs@AC. Both isotherms conform to the Type IV isotherm with the H3 hysteresis loop defined by IUPAC, suggesting that the materials are predominantly mesoporous (2-50 nm) (Liu et al. 2016), which was also evident from **Figure 3-2b**. The pore size distribution of 2%Ga/TNTs@AC displayed a bimodal profile with a major peak at ~ 4 nm (**Figure 3-2b**). Compared to TNTs@AC, 2%Ga/TNTs@AC showed a lower peak at ~4 nm and more changes in dV/dD from 4 to 10 nm, indicating that the pore volume distribution of TNTs@AC (0.56 cm$^3$/g) was broader than that of 2%Ga/TNTs@AC (0.52 cm$^3$/g). Furthermore, the specific surface areas of TNTs@AC and 2%Ga/TNTs@AC were 348.54 m$^2$/g and 244.43 m$^2$/g, respectively. The values were much lower than that of the parent AC (1069.2 m$^2$/g) (Walker and Weatherley 1998), but similar to that of neat TNTs (272.3 m$^2$/g) (Liu et al. 2016). Taken together the SEM/TEM data, the surface area change, and the adsorption data (**Section 3.3.2**), it can be deduced that the alkaline hydrothermal treatment of the parent AC and TiO$_2$ and the subsequent Ga deposition and calcination caused a blockage of the interior sites inside the neat AC core, and created a shell of blended TNTs and AC nanoparticles. Compared to the parent AC, these new sites consisting of

67

mixed phases are expected to be more selective towards PFOS due to the synergistic binding mechanisms, easier accessibility owing to the easier mass transfer, and enhanced photoactivity, despite the lower specific surface area. **Table 3-2** compares the specific surface areas and pore volumes of Ga/TNTs@AC with different Ga contents. The BET surface areas for 1%Ga/TNTs@AC and 2%Ga/TNTs@AC were nearly the same; however, increasing the Ga content from 2 wt.% to 3 and 5 wt.% decreased the surface area from 0.52 $cm^3$/g to 0.42 and 0.36 $cm^3$/g, respectively; and moreover, 2%Ga/TNTs@AC exhibited the largest pore volume among the Ga-doped composites. The observation indicates that the Ga-doping caused notable structural changes of the materials, which are further interpreted in the following Raman and XRD analyses.



(a)                                                                 (b)
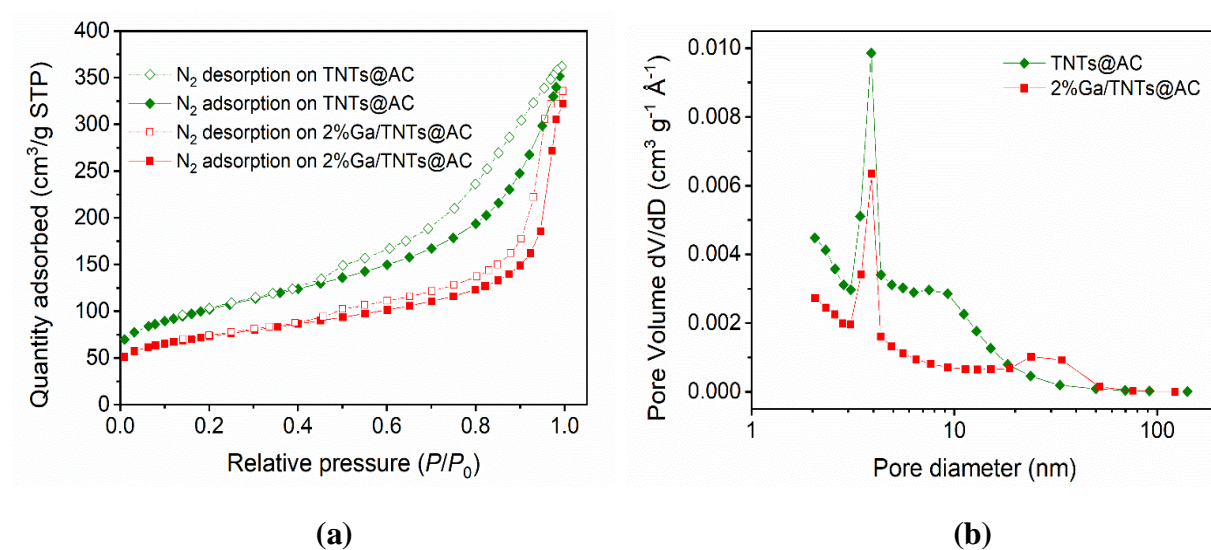
**Figure 3-2. (a)** $N_2$ adsorption-desorption isotherms and **(b)** pore size distributions of TNTs@AC and 2%Ga/TNTs@AC calcined at 550 °C.

68

**Table 3-2.** BET-based specific surface areas and pore volumes of various composite materials.

| Material | BET surface area ($m^2$/g) | Pore Volume ($cm^3$/g) |
| --- | --- | --- |
| TNTs@AC | 348.54 | 0.56 |
| 1%Ga/TNTs@AC | 243.78 | 0.34 |
| 2%Ga/TNTs@AC | 244.43 | 0.52 |
| 3%Ga/TNTs@AC | 269.77 | 0.42 |
| 5%Ga/TNTs@AC | 279.59 | 0.36 |

Raman analysis was carried out to investigate the macrostructural change of TNTs@AC upon the Ga doping. **Figure 3-3a** shows the Raman spectra of uncalcined TNTs@AC (uncal TNTs@AC) and calcined TNTs@AC and Ga/TNTs@AC with various Ga contents. The Raman spectra for uncalcined TNTs@AC displayed four prominent peaks at 197, 284, 442, and 700 cm$^{-1}$, which are attributed to sodium tri-titanate with a chemical formula of $Na_xH_{2-x}Ti_3O_7$ ($x$ depends on the sodium content) (Gajovic et al. 2009). After calcination at 550 $^o$C, no new peaks were observed in the spectra of TNTs@AC, although a broad peak at 700 cm$^{-1}$ was shifted to 680 cm$^{-1}$, which can be associated with the thermal expansion and changes in the population of the vibration energy level at elevated temperature (Gajovic et al. 2009). The observation indicates that the calcination presents little effect on the sodium tri-titanate phase, which agrees with the literature report (2003). In contrast, four new peaks occurred for Ga/TNTs@AC at 198, 398, 519, and 639 cm$^{-1}$, which are assigned to the $E_g$, $B_{1g}$, $A_{1g}$+$B_{1g}$, and $E_g$ modes of the anatase phase, respectively (Ohsaka et al. 1979; Zhang et al. 2008b). In general, the first Raman peak of the $E_g$ mode of anatase occurs at 144 cm$^{-1}$, but the wavenumber for Ga/TNTs@AC was shifted to 150 cm$^{-1}$, which is

attributed to the phonon confinement and internal stress in the photocatalyst (Balaji et al. 2006). Besides, the peak intensity of the anatase phase decreased with increasing Ga content. The observations indicate that the Ga doping facilitates the transformation of the tri-titanate phase into anatase upon the calcination, but excessive Ga ($\geq$2 wt.%) may inhibit the phase transformation.

**Figure 3-3b** shows the XRD spectra of the materials. For uncalcined TNTs@AC, the peaks at ~10°, 24°, 28°, 48°, and 61° are all ascribed to sodium tri-titanate (Wang et al. 2018; Zhao et al. 2016b). The basic skeleton of titanate is composed of triple edge-sharing [$TiO_6$] octahedron with $Na^+$ and $H^+$ attached at the interlayers serving as exchangeable counter ions (Ma et al. 2017); and the peak at 26° is attributed to the crystal plane of graphite (002), confirming that AC nanoparticles were intermingled with TNTs (Liu et al. 2016). The XRD patterns for calcined TNTs@AC nearly resemble those of uncalcined TNTs@AC, though the peaks are significantly weakened and the interlayer peak at 10° was shifted to 11° due to the partial breakage of the tubular and layered structures during the calcination (Zhao et al. 2016b). For Ga/TNTs@AC, there are five peaks at 25.4°, 36.4°,48.1°, 54.2°, and 62.8°, which correspond to the (101), (004), (200), (211) and (213) planes of tetragonal anatase (JCPDS-ICDD 21-1272), respectively, indicating that the presence of Ga altered the titanate lattice after the calcination (Ismail et al. 2018). The increased crystallinity of the anatase phase predicts a greater photocatalytic activity due to improved separation of the photo-generated charge carriers (Haque et al. 2017). The diffraction peak intensities decreased with increasing Ga content, although no significant shift of the anatase peaks was observed; and no evident diffraction for $Ga_2O_3$ was observed. These observations support the notion that Ga existed in the amorphous form, and $Ga^{3+}$ ions were embedded/doped into the lattice of anatase by substituting $Ti^{4+}$ in an octahedral coordination environment partially due to the adjacent ionic

radius (0.62 Å for $Ga^{3+}$ and 0.68 Å for $Ti^{4+}$) (Myilsamy et al. 2018); and more $Ga^{3+}$ ions were incorporated at higher Ga contents.

Both the Raman and XRD data did not show the presence of a rutile phase, indicating no phase transformation of anatase occurred under the calcination conditions (550 °C in $N_2$). This agrees with the general consent that ~600 °C is the region of the onset temperature for the transformation of anatase to rutile in air (Hanaor and Sorrell 2011).



(a)                                  (b)
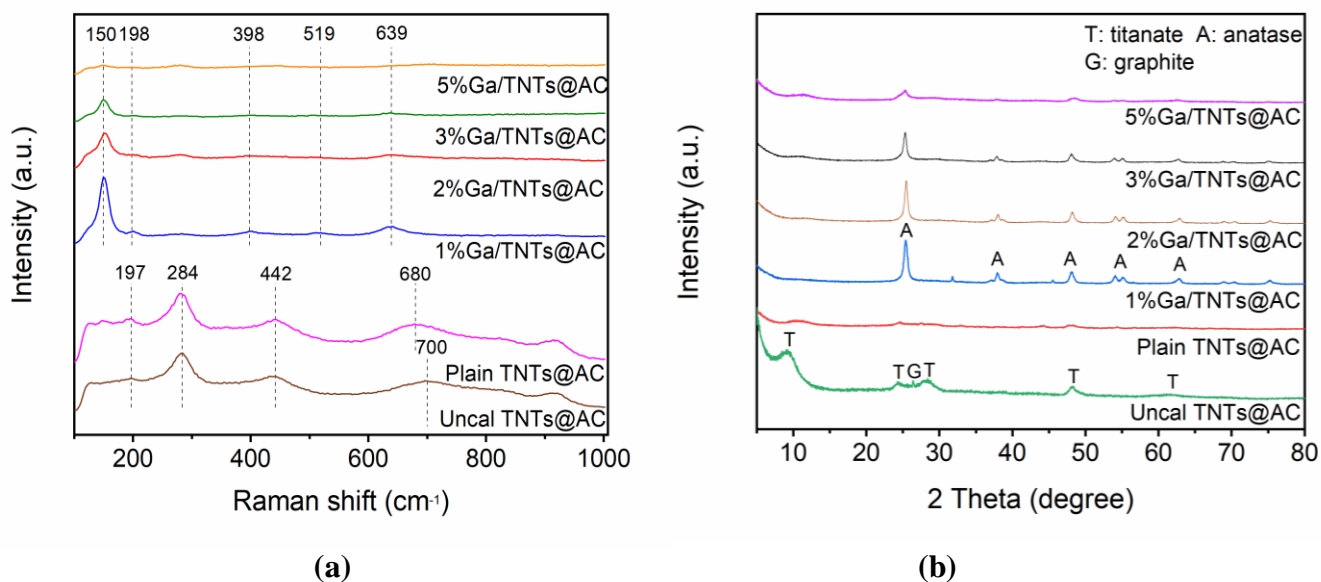
**Figure 3-3. (a)** Raman spectra and **(b)** XRD patterns of uncalcined TNTs@AC, TNTs@AC, and Ga/TNTs@AC prepared at various Ga contents. TNTs@AC and Ga/TNTs@AC were calcined at 550 °C.

### 3.3.2. Adsorption kinetics and isotherms

**Figure 3-4a** shows the adsorption kinetics of PFOS by AC, TNTs@AC, and 2%Ga/TNTs@AC. TNTs@AC and 2%Ga/TNTs@AC were able to adsorb nearly all the PFOS within 10 min. Despite its 3-4 times greater surface area, the AC showed slower kinetics, and the

adsorption equilibrium was not reached until after 120 min. The fast adsorption rate of TNTs@AC and 2%Ga/TNTs@AC is in line with the characterization data where the AC-modified TNTs or Ga/TNTs in the shell of the particles are easily accessible for PFOS. Because 2%Ga/TNTs@AC showed the best defluorination effectiveness (**Section 3.3.3**), it was further tested in the subsequent experiments.



**(a)**                                    **(b)**

**(c)**                                    **(d)**
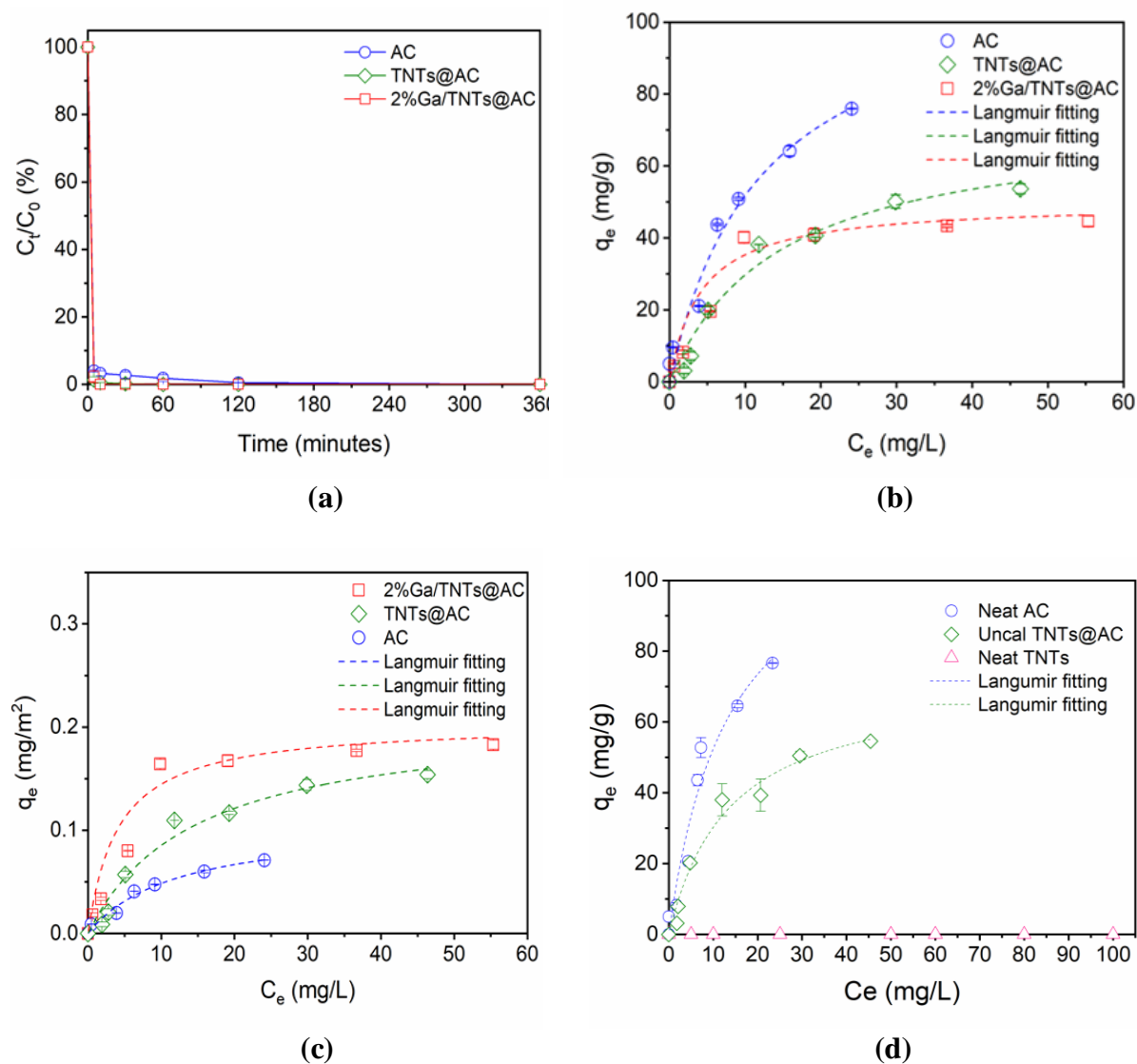
**Figure 3-4. (a)** Adsorption kinetics and isotherms based on **(b)** unit-mass uptake and **(c)** unit-surface-area uptake of PFOS by treated AC, TNTs@AC, and 2%Ga/TNTs@AC, and **(d)**

adsorption isotherms of PFOS by neat AC, uncalcined TNTs@AC, and neat TNTs. Experimental conditions for kinetic tests: initial PFOS concentration = 100 µg/L, material dosage = 3 g/L, pH = 7 ± 0.1; Conditions for isotherm tests: initial PFOS concentration = 5-100 mg/L, material dosage = 1 g/L, pH = 7 ± 0.1. TNTs@AC and 2%Ga/TNTs@AC were calcined at 550 °C. Data are plotted as mean of duplicates with error bars indicating deviation from the mean.

**Figure 3-4b** compares the adsorption isotherms of PFOS for treated AC, TNTs@AC, and 2%Ga/TNTs@AC using the mass-based PFOS uptakes. Because of the different densities (4.23 g/cm$^3$ for TiO$_2$, 2.10 g/cm$^3$ for AC) and specific surface areas of the materials (**Section 3.3.1**), the isotherm data are also plotted based on the specific surface areas (**Figure 3-4c**). In addition, **Figure 3-4d** shows the adsorption isotherms for neat AC, neat TNTs, and uncalcined TNTs@AC The classical Langmuir and Freundlich isotherm models were used to fit the experimental data:

$$q_e = \frac{Q_{max}bC_e}{1+bC_e} \qquad\qquad \text{Langmuir model} \qquad\qquad (1)$$

$$q_e = K_F C_e^{1/n} \qquad\qquad \text{Freundlich model} \qquad\qquad (2)$$

where $Q_{max}$ (mg/g or mg/m$^2$) is the Langmuir maximum adsorption capacity, b (L/mg) is the Langmuir affinity coefficient related to the affinity of binding sites and is also a measure of free energy of adsorption, $K_F$ (mg/g·(L/mg)$^{1/n}$) is the Freundlich capacity coefficient, and n is the heterogeneity factor related to the cumulative measurement of magnitude and distribution of energies associated with various categories of sorption sites.

**Table 3-3**. Best-fitted isotherm model parameters for adsorption of PFOS by neat AC, uncalcined TNTs@AC, treated AC, TNTs@AC, and 2%Ga/TNTs@AC.

| Model | Parameter | Adsorbents | | | | |
|---|---|---|---|---|---|---|
| | | Treated AC | TNTs@AC | 2%Ga/TNTs@AC | Neat AC | Uncalcined TNTs@AC |
| Freundlich model | $K_F$ $(mg/g \cdot (L/mg)^{1/n}$ | 14.51 | 8.11 | 12.44 | 12.51 | 8.27 |
| | n | 1.89 | 1.93 | 2.86 | 1.69 | 1.94 |
| | $R^2$ | 0.97 | 0.93 | 0.87 | 0.93 | 0.95 |
| Langmuir model | $Q_{max}$ (mg/g) | 114.40 | 73.00 | 49.80 | 123.00 | 71.70 |
| | b (L/mg) | 0.08 | 0.07 | 0.24 | 0.07 | 0.07 |
| | b x $Q_{max}$ | 9.50 | 5.04 | 12.15 | 9.10 | 5.23 |
| | $R^2$ | 0.97 | 0.97 | 0.94 | 0.93 | 0.97 |

**Table 3-3** shows the best-fit Langmuir and Freundlich parameters. Based on the coefficient of determination ($R^2$), the Langmuir model better interpreted the adsorption isotherms for TNTs@AC and 2%Ga/TNTs@AC, and both models adequately fitted the isotherm data for AC.

Referring to the mass-based isotherms, neat AC provided a $Q_{max}$ of 123.0 mg/g, which is significantly higher than that for treated AC (114.4 mg/g), indicating the hydrothermal treatment caused some drop in the adsorption capacity. Neat TNTs showed negligible adsorption of PFOS (<15 µg/g), while TNTs@AC offered a $Q_{max}$ of 73.0 mg/g. Noting that TNTs@AC was composed of 50% of TNTs and AC, this capacity value is 28% higher than the average $Q_{max}$ (57.2 mg/g) based on the $Q_{max}$ values of TNTs and AC. This observation indicates that TNTs@AC was not a

simple integration of TNTs and AC, rather, TNTs and AC modified each other, rendering the non-adsorptive TNTs more favorable towards PFOS. Uncalcined TNTs@AC offered a $Q_{max}$ of 71.7 mg/g, which is comparable to that of calcined TNTs@AC, indicating that the calcination had a negligible effect in the adsorption capacity for PFOS by TNTs@AC.

Comparing TNTs@AC and 2%Ga/TNTs@AC, the isotherm for 2%Ga/TNTs@AC appeared much more favorable than that for TNTs@AC, and 2%Ga/TNTs@AC offered higher uptake in the relatively lower concentration range ($C_e$ < 15 mg/L), indicating that the Ga-doping enhanced the affinity of the adsorbent. Given that PFOS in most contaminated waters is in the low ppb or ppt levels, the adsorption capacity in the low concentration range is often of greater practical value than the $Q_{max}$. At a sufficiently low $C_e$ (e.g., < 100 µg/L), the Langmuir model (Eq. 1) reduces to

$$q_e = b \, Q_{max} \, C_e \tag{3}$$

As such, the overall adsorption is governed by the product of b and $Q_{max}$. Based on the b×$Q_{max}$ values (**Table 3-3**), the materials can be ranked in the sequence of: 2%Ga/TNTs@AC (12.15) > AC (9.10-9.50) > TNTs@AC (5.04-5.23).

At elevated PFOS concentrations ($C_e$ > 5 mg/L), AC may adsorb more PFOS than 2%Ga/TNTs@AC, which can be attributed to the decreased specific surface area and pore volume of the latter (**Section 3.3.1**). In addition, because the anatase surface in 2%Ga/TNTs@AC was only partially modified by the AC nanoparticles, it can only take up a limited amount of PFOS as pure anatase is known to be a poor adsorbent for PFOS (Chen et al. 2011).

**Table 3-4.** Isotherm model parameters based on isotherms using surface-area-normalized uptakes of PFOS by treated AC, TNTs@AC, and 2%Ga/TNTs@AC.

| Model | Parameter | Material | | |
|-------|-----------|----------|--|--|
| | | Treated AC | TNTs@AC | 2%Ga/TNTs@AC |
| Langmuir | $Q_{max}$ (mg/m$^2$) | 0.107 | 0.209 | 0.225 |
| | b (L/mg) | 0.083 | 0.069 | 0.244 |
| | $R^2$ | 0.968 | 0.965 | 0.936 |

The much-enhanced affinity of 2%Ga/TNTs@AC for PFOS can be more clearly revealed when the isotherm data are plotted based on the surface-area-normalized uptakes (**Figure 3-4c, Table 3-4**). For instance, the maximum PFOS uptake per surface area by 2%Ga/TNTs@AC (0.225 mg/m$^2$) is 2.1 folds higher than that for AC (0.107 mg/m$^2$). This observation indicates that the mutual modifications in the composite material transformed the predominant adsorption sites from AC to AC-modified Ga/TNTs microstructures and induced multiple adsorption mechanisms such as electrostatic interactions between the metal-oxides and the head group of PFOS and hydrophobic and anion-$\pi$ interactions between AC and the perfluorinated chain of PFOS (Ip et al. 2010; Wibowo et al. 2007; Yu et al. 2009) (See **Section 3.3.6**). Moreover, the pre-accumulation of PFOS on the photoactive sites facilitates the subsequent solid-phase photocatalytic degradation of PFOS.

### 3.3.3. Photodegradation of PFOS

**Figures 3-5a and 3-5b** show the photocatalytic degradation kinetics of PFOS pre-adsorbed on neat AC, TNTs@AC, and Ga/TNTs@AC prepared at various Ga contents. Under the UV

irradiation, neat AC showed almost no degradation of the sorbed PFOS. TNTs@AC exhibited a modest degradation rate and degraded 13.1% and defluorinated 6.2% of the PFOS after 4 h. In contrast, Ga/TNTs@AC in all cases displayed much enhanced photocatalytic activity, with a defluorination rate of 41.2%-66.2%.

2%Ga/TNTs@AC, namely TNTs@AC doped with 2 wt.% of Ga, exhibited the highest photoactivity and was able to degrade 75.0% and defluorinate 66.2% of the pre-sorbed PFOS in 4 h. It is noteworthy that increasing the Ga content from 2 wt.% to 3 and 5 wt.% resulted in the lower PFOS degradation (70.0% and 67.3%) and defluorination (62.0% and 57.0%), respectively. This behavior can be attributed to 1) excessive loading of Ga may result in poorly crystallized phases of anatase, as shown in the XRD results (**Figure 3-3b**), and 2) excessive Ga may act as a recombination center of the charge carriers, impeding the separation of the $e^-/h^+$ pairs (Liu et al. 2013b). **Section 3.3.6** gives details about the important roles of Ga in the photocatalytic degradation of PFOS.



(a)                              (b)
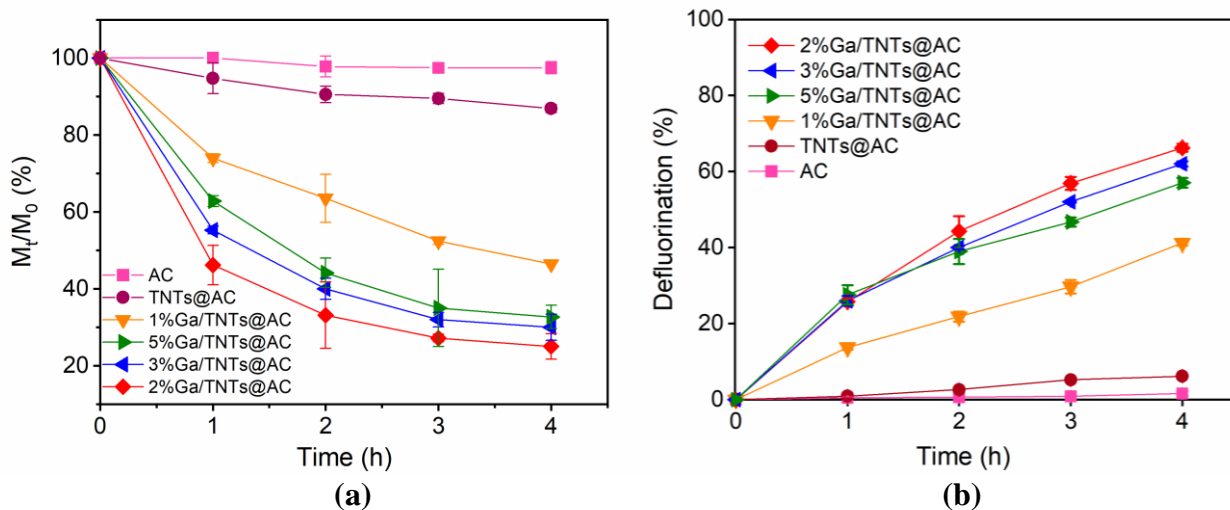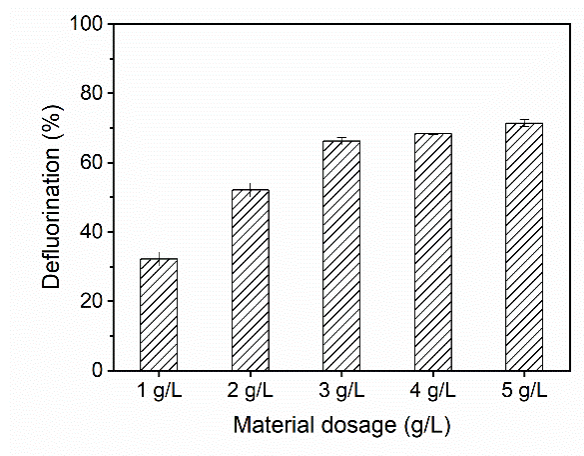
**(c)**

**Figure 3-5. (a)** Photodegradation, **(b)** defluorination kinetics of PFOS pre-adsorbed on neat AC, TNTs@AC, and Ga/TNTs@AC prepared at various Ga contents, and **(c)** defluorination of PFOS pre-sorbed on 2%Ga/TNT@AC at various material dosages during the adsorption stage. Experimental conditions during adsorption: initial PFOS concentration = 100 µg/L, material dosage = 3 g/L, pH = 7.0 ± 0.1; Conditions for photodegradation: UV intensity = 210 W/m², pH = 7.0 ± 0.1. Data are plotted as mean of duplicates with error bars indicating deviation from the mean.

In addition, the catalyst dosage (or the material-to-PFOS ratio) during the adsorption also affected the PFOS photodegradation. **Figure 3-5c** compares the 4-h defluorination of PFOS pre-loaded on 2%Ga/TNTs@AC at various material dosages during the adsorption stage. The mineralization of PFOS was enhanced from 32.2% to 66.2% when the 2%Ga/TNTs@AC dosage was raised from 1 to 3 g/L. At the lower material dosage, more PFOS is adsorbed on the deeper sites, which are less photoactive and less reachable by the photons and photo-generated holes and radicals (**Section 3.3.6**). However, further increasing the material dosage from 3 to 5 g/L gained only 5.2% of additional defluorination, indicating that the reaction was no longer limited by the

78

easily accessible photoactive sites at the higher material dosages. Consequently, the subsequent experiments were carried out using 3 g/L of 2%Ga/TNTs@AC to concentrate PFOS.

### 3.3.4. pH effect

**Figure 3-6a** shows that 2%Ga/TNTs@AC at both 1 and 3 g/L was able to consistently adsorb nearly 99% of PFOS from the solution over a broad pH range of 3.5-10.5 within 2 h. **Figure 3-6b** shows the measured zeta potential of 2%Ga/TNTs@AC, which gives a $pH_{PZC}$ of ~4.6. At pH > $pH_{PZC}$, the negative material surface repels the sulfonate head group of PFOS. As such, PFOS is more likely to be adsorbed through hydrophobic interaction between the carbon particles and the tail of PFOS and the π-anion interactions between the electron-deficient aromatic system on the AC surface and PFOS. Conversely, at lower pH, the adsorption of PFOS becomes favorable for electrostatic interactions between the positively charged surface of Ga/TNTs@AC and PFOS, and surface complexation between PFOS and the surface metals (Ti and Ga) can be also operative.

**Figure 3-6c** shows the photocatalytic defluorination of PFOS on 2%Ga/TNTs@AC at various pH levels during the photodegradation. Compared with the PFOS defluorination of 66.2% at the neutral pH, the 4-h mineralization of PFOS decreased to 48.1% and 50.7% at pH 3.5 and 5.0, respectively; while increased to 73.7%, 73.0%, and 72.5% at pH 9.0, 10.5, and 12.0. Although the higher pH is less favorable for interacting with the head sulfonate group, it may have the following beneficial effects: 1) the more negative catalyst surface at higher pH favors adsorption of molecular oxygen, resulting in more $O_2^{\bullet-}$, which favors PFOS degradation (**Section 3.3.6**) (Fang et al. 2013; Mirkhani et al. 2009), and 2) the higher pH suppresses the protonation of $O_2^{\bullet-}$ to $HO_2^{\bullet}$ and $H_2O_2$ according to Eqs (4) and (5) (Liu et al. 2014; Mirkhani et al. 2009). Taken together, Ga/TNTs@AC can function well in the broad pH range (>7.0), though the adsorption and

photodegradation mechanisms may vary. This presents a superior attribute of the composite material over other photocatalysts that can only adsorb anionic PFAS at acidic pH.

$$O_2^{\bullet-} + H^+ \leftrightarrow HO_2^{\bullet} \tag{4}$$

$$2\,O_2^{\bullet-} + 2\,H^+ \leftrightarrow H_2O_2 + O_2 \tag{5}$$



**(a)**



**(b)**



**(c)**
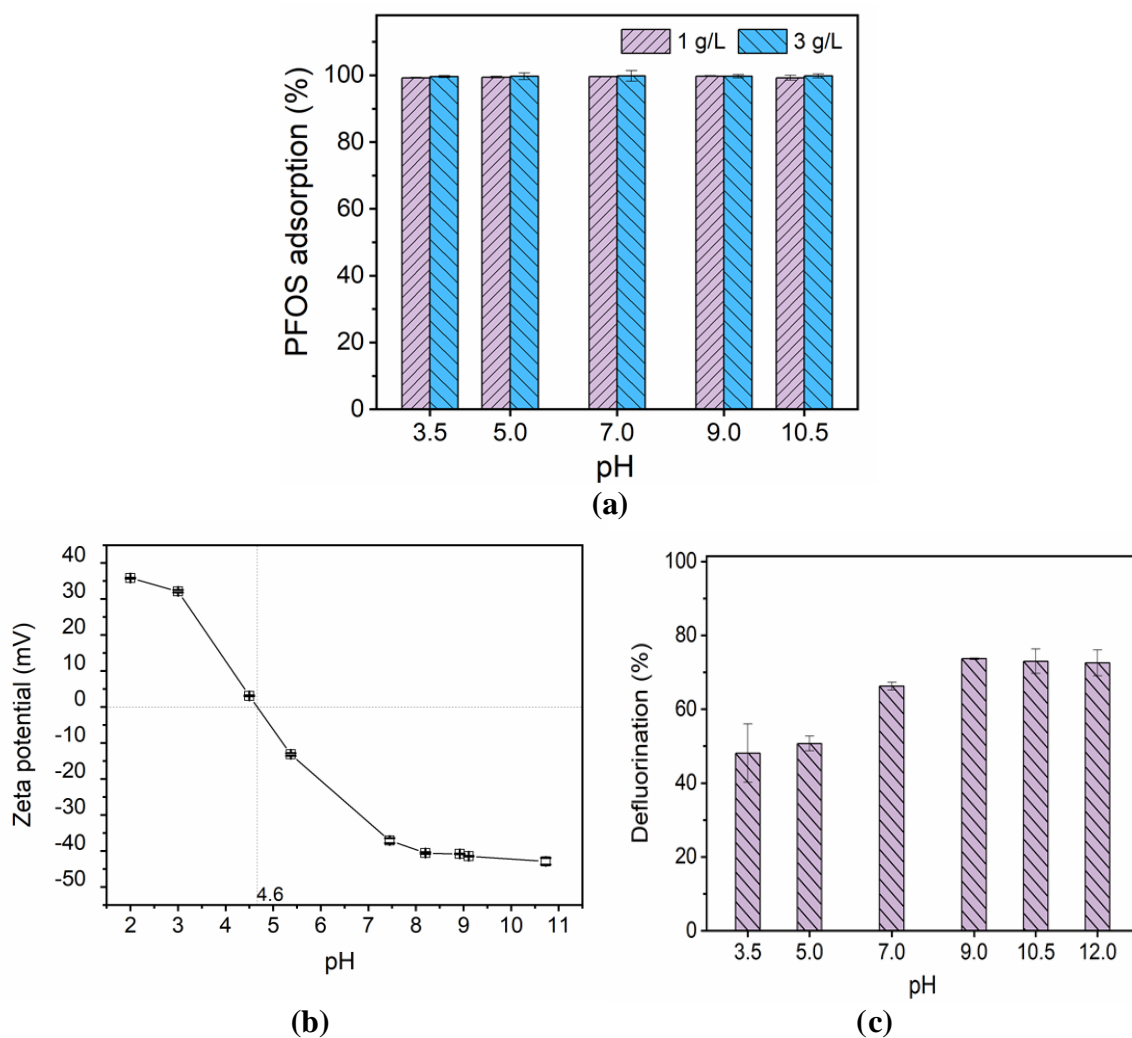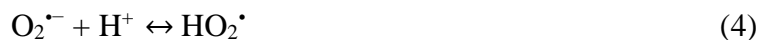
**Figure 3-6. (a)** Effect of pH on PFOS adsorption by 2%Ga/TNTs@AC, **(b)** Zeta potential of 2%Ga/TNTs@AC as a function of pH, and **(c)** effect of pH on photo-defluorination of PFOS presorbed on 2%Ga/TNTs@AC. Experimental conditions (adsorption): initial PFOS concentration = 100 µg/L, material dosage = 1 or 3 g/L in **(a)** = 3 g/L in **(c)**, adsorption time = 2 h, and pH = 7 ±

0.1; Experimental conditions (photodegradation): UV intensity = 210 W/m$^2$, reaction time = 4 h, pH = 3.5 to 12.0. Data are plotted as mean of duplicates with error bars indicating deviation from the mean.

### 3.3.5. Reusability of Ga/TNTs@AC

**Figure 3-7a** shows the adsorption and defluorination of PFOS by 2%Ga/TNTs@AC over 4 consecutive adsorption and photodegradation runs. After 4 cycles of repeated uses, 2%Ga/TNTs@AC remained able to adsorb nearly 99% of the PFOS from the solution, although the PFOS mineralization dropped gradually from 66.2% to 58.3%. This mild decrease in PFOS defluorination may result from the accumulation of short-chain intermediates produced in the previous cycles, which may occupy some of the photoactive sites and compete for the reactive species although PFOS is known to have a higher affinity than its shorter-chain daughter products. It is noted that some of the PFOS and the degradation byproducts pre-sorbed from the previous runs may be further defluorinated in the subsequent photodegradation runs. Cumulatively, about 62% of PFOS was mineralized in the four cyclic runs. No Ti leaching was detected and less than 1.3% of embedded Ga was leached after the 4 cycles. Because of the small fraction of Ga on the material (2 wt.% for 2%Ga/TNTs@AC), the modest bleeding of Ga did not cause significant loss in adsorption and photodegradation of PFOS. While the catalyst activity may drop over prolonged cyclic uses, it can be easily re-doped if needed.

**Figure 3-7b** shows that when the same 2%Ga/TNTs@AC was reused in 4 consecutive adsorption runs without the photo-regeneration after each run, the material was still able to consistently adsorb >99% of PFOS (100 µg/L) in each run. This observation indicates that the adsorption capacity was underused due to the relatively high dosage of 2%Ga/TNTs@AC and

81

more PFOS could be pre-loaded on the material before the photodegradation/regeneration. In terms of defluorination, about 54% of PFOS collected from the four adsorption runs was defluorinated after 4-h UV irradiation, which is ~8% lower than that when photo-degradation was implemented after each adsorption run. The observation suggests that it can be more cost-effective to make best use of the adsorption capacity before the photo-degradation/regeneration is practiced.
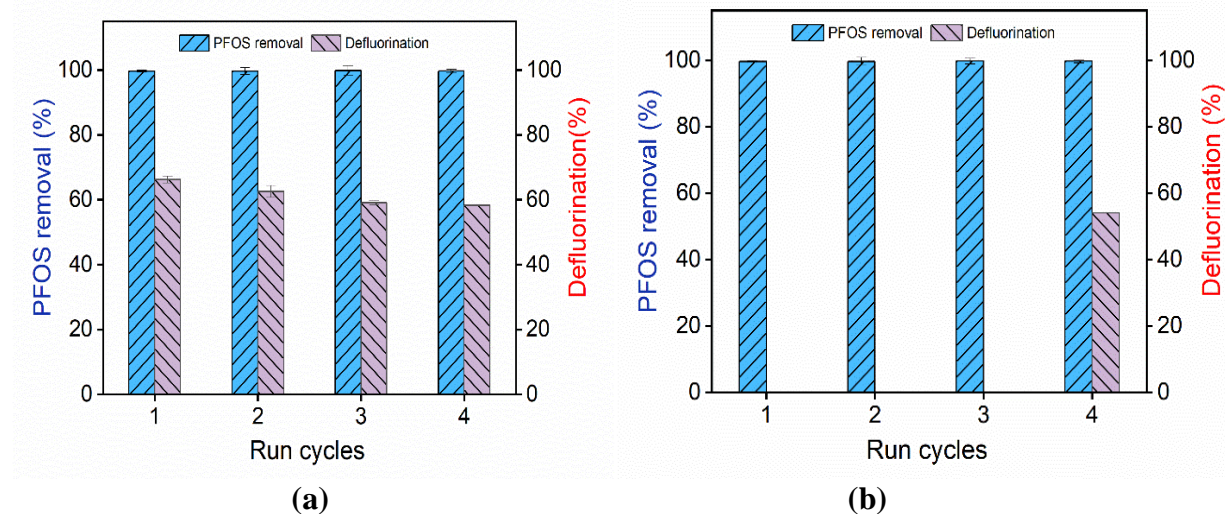


**Figure 3-7. (a)** Adsorption and *solid-phase* defluorination of PFOS during four consecutive runs using the same 2%Ga/TNTs@AC and **(b)** adsorption of PFOS during four consecutive runs without regeneration and defluorination of PFOS after the fourth adsorption run with 2%Ga/TNTs@AC. Experimental conditions for adsorption: initial PFOS concentration = 100 µg/L in each batch adsorption, 2%Ga/TNTs@AC = 3 g/L, pH = 7.0 ± 0.1; Conditions for photodegradation: UV intensity = 210 W/m$^2$, reaction time = 4 h, pH = 7.0 ± 0.1.

### 3.3.6. Mechanisms for enhanced photodegradation of PFOS by Ga/TNTs@AC

To identify roles of various active species in the photodegradation, the photocatalytic degradation of PFOS by 2%Ga/TNTs@AC was carried out in the presence of KI, IPA, and BQ as scavengers of $h^+$ ($k \geq 1.1 \times 10^{10}$ M$^{-1}$s$^{-1}$), $^\bullet$OH ($k = 1.9 \times 10^9$ M$^{-1}$s$^{-1}$), and $O_2^{\bullet-}$ ($k = 1.1 \times 10^9$ M$^{-1}$s$^{-1}$),

respectively (Van Doorslaer et al. 2012; Zhu et al. 2020). As shown in **Figure 3-8,** 75% of adsorbed PFOS was degraded after 4 h when no inhibitor was present, while the 4-h degradation was lowered to 72%, 51%, and 30% in the presence of IPA, KI, and BQ, respectively. The results indicate that both the holes and superoxide radicals played important parts in the PFOS degradation, whereas $^{\bullet}$OH played an insignificant role.
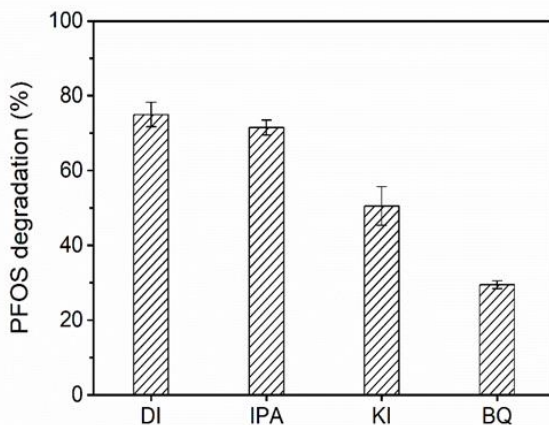


**Figure 3-8.** Photodegradation of PFOS pre-sorbed on 2%Ga/TNTs@AC in the presence of various radical scavengers (IPA, KI, and BQ). Experimental conditions (adsorption): initial PFOS concentration = 100 µg/L, material dosage = 3 g/L, adsorption time = 2 h, and pH = 7 ± 0.1; Experimental conditions (photodegradation): UV intensity = 210 W/m$^2$, reaction time = 4 h, 7.0 ± 0.1; and scavenger concentration = 10 mM. Data are plotted as mean of duplicates with error bars indicating deviation from the mean.

The oxidation states and compositions of TNTs@AC and 2%Ga/TNTs@AC were investigated by XPS (**Figure 3-9**). The XPS survey spectra confirmed the presence of Ti, Ga, and O in the composites (**Figure 3-9a**). For both TNTs@AC and 2%Ga/TNTs@AC, the deconvolution of the Ti 2p spectrum (**Figure 3-9b**) yielded two peaks at binding energies of ~459.4 and 465.2 eV representing the Ti $2p_{3/2}$ and Ti $2p_{1/2}$ orbitals, respectively (Amdeha et al. 2020), which are

characteristic of $Ti^{4+}$. Likewise, the Ga 2p spectrum (**Figure 3-9c**) was deconvoluted into the $2p_{1/2}$ and $2p_{3/2}$ peaks centered at 1145.5 and 1118.6 eV, respectively, which are typical of $Ga^{3+}$ (Myilsamy et al. 2018). The XPS results showed that $Ti^{4+}$ was the dominant oxidation state of Ti and Ga was present as $Ga^{3+}$. Besides, the O 1s peak was deconvoluted into two peaks (**Figure 3-9d**). For TNTs@AC, the peak at ~531.0 eV is attributed to the regular lattice oxygen (Ti−O−Ti), and the other oxygen peak at 533.0 eV is assigned to the surface hydroxyl groups (Ti−OH) (Banerjee et al. 2012). However, for Ga/TNTs@AC, the binding energy of the regular lattice oxygen shifted slightly to ~530.8 eV, suggesting that the doped Ga affected the lattice of TNTs, which is in accord with the results of the Raman and XRD data. In addition, the O 1s peak shifted from 533.0 eV (TNTs@AC) to 532.5 eV (Ga/TNTs@AC), which is attributed to the formation of oxygen vacancies upon the Ga doping (Diak et al. 2017; Qi et al. 2014). The generation of the oxygen vacancies is attributed to the incorporation of $Ga^{3+}$ into the TNTs@AC structure by substituting $Ti^{4+}$, which induced a loss in the local charge neutrality in the lattice (de los Santos et al. 2014). Surface defects can serve as charge carrier traps as well as adsorption sites where the charge transfer to adsorbed species can inhibit the $e^-/h^+$ recombination.
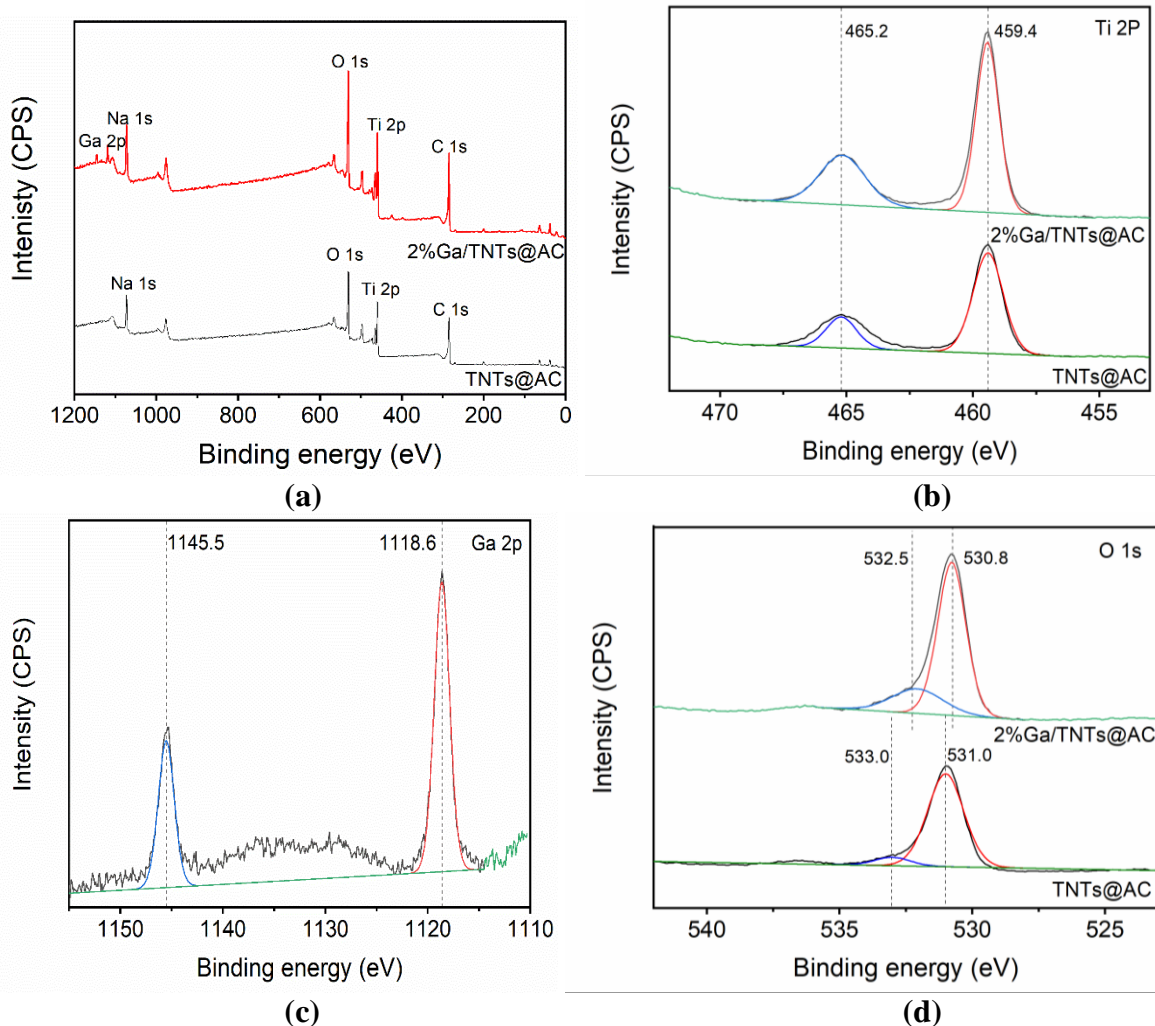
**Figure 3-9. (a)** XPS survey spectra and high-resolution XPS spectra **(b)** of Ti 2p, **(c)** of Ga 2p, and **(d)** O 1s for TNTs@AC and 2%Ga/TNTs@AC.

The EPR measurements were performed to further investigate the presence of surface defects. **Figure 3-10a** shows the EPR results of treated AC, TNTs@AC (TNTs@AC), and 2%Ga/TNTs@AC. No signals were detected in the treated AC and TNTs@AC, while a sharp electron signal was evident at g factor ~2.005 (denoted with an asterisk) for 2%Ga/TNTs@AC, indicating the presence of paramagnetic defects. According to the g value, the defects can be attributed to the oxygen vacancies (Li et al. 2008) rather than $Ti^{3+}$ (g = 1.972) (Zhang et al. 2008a).

85

This observation is in line with those reported for other composite materials. For example, Pan and Xu (Pan and Xu 2013) observed a sharp symmetrical signal at a g factor of 2.004 for Au-TiO$_2$-OV due to oxygen vacancies; and Nakamura et al. (Nakamura et al. 2000) observed a sharp signal at 2.004 for plasma-treated TiO$_2$, which was identified as the electrons trapped on oxygen vacancies. The energy level of the oxygen vacancies was reported to be below the conduction band of titania (Myilsamy et al. 2018; Nakamura et al. 2000). For example, Cronemeyer (Cronemeyer 1959) determined the oxygen vacancy states were located at 0.75–1.18 eV above the valence band for anatase. These newly formed oxygen vacancy states in the anatase band structure are expected to facilitate a new photoexcitation process by actively trapping the electrons excited from the valence band of anatase, which can lead to 1) inhibition of the recombination of the $e^-/h^+$ pairs, 2) generation of reactive oxygen species or atomic oxygen, and 3) extension of the excitation wavelength to the visible light range [31, 66]. Myilsamy et al. (2018) reported a bandgap of 2.98 eV for TiO$_2$ doped with 1.0 wt.% of Ga, which is ~0.19 eV below the conduction band of titania.

To further investigate the effect of Ga, PL emission spectra were obtained (**Figure 3-10b**). The PL spectra reflect the luminescence emitted during the recombination of photo-induced $e^-/h^+$ pairs, i.e., the PL intensity is directly proportional to the rate of electron–hole recombination. All samples exhibited an emission peak at 550 nm, and in all cases, Ga/TNTs@AC displayed weaker peaks than TNTs@AC, indicating the oxygen vacancies enhanced the separation rate of the $e^-/h^+$ pairs, and thus increased the lifetime of the charge carriers. Moreover, the weakest PL intensity was observed for 2%Ga/TNTs@AC, which agrees with the PFOS photodegradation data, where 2%Ga/TNTs@AC was most effective. The data also confirm that when doped at the right amount (i.e., 2 wt.%), Ga acts as a charge carriers separation center; however, excessive Ga would serve as charge carriers recombination center.

86
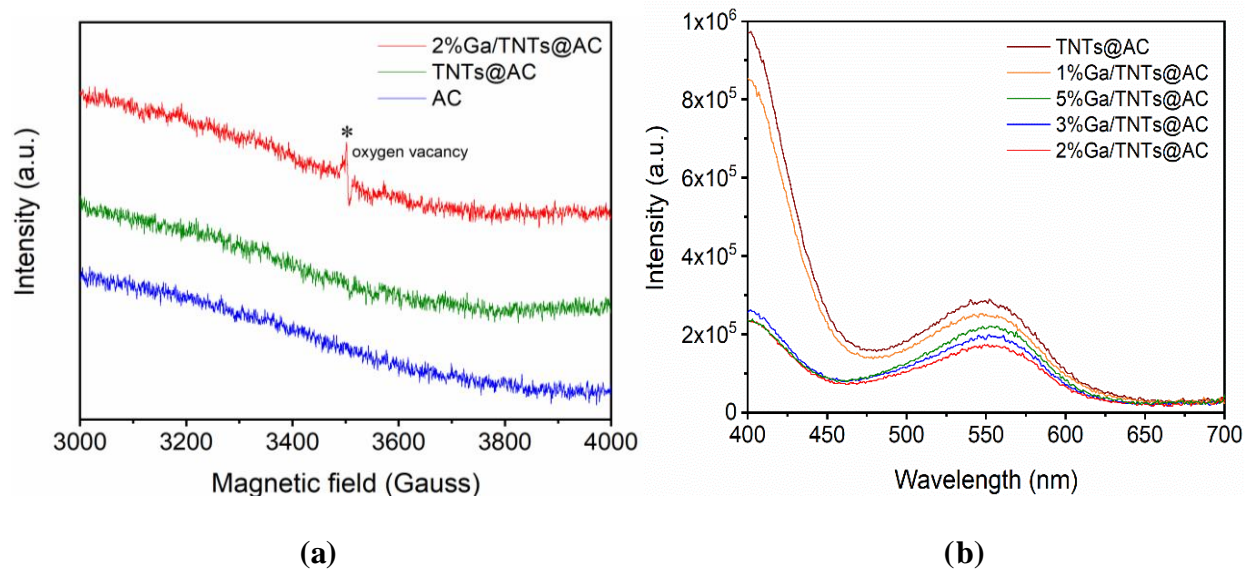
**Figure 3-10. (a)** EPR spectra of treated AC, TNTs@AC, and 2%Ga/TNTs@AC and **(b)** PL spectra of TNTs@AC and Ga/TNTs@AC with various Ga contents. TNTs@AC and 2%Ga/TNTs@AC were calcined at 550 $^\circ$C in all cases.

Based on the forgoing analyses, **Figure 3-11** illustrates the mechanism for the enhanced photodegradation of PFOS by Ga/TNTs@AC and the possible defluorination pathway. First, based on our prior works (Li et al. 2020a; Xu et al. 2020a; Xu et al. 2020b), the integration of metals and carbon particles facilitates multi-point side-on binding of PFOS due to concurrent hydrophobic, ligand exchange, and $\pi$-anion interactions, and such an adsorption mode is conducive to the subsequently electron transfer and redox reactions. Second, the substitution of $Ti^{4+}$ by $Ga^{3+}$ results in oxygen vacancies to maintain charge neutrality. The oxygen vacancies act as electron acceptors, which capture the photoelectrons, thereby suppressing the $e^-/h^+$ recombination and rendering more $h^+$ available for degrading PFOS (Choudhury and Choudhury 2013); on the other hand, the oxygen vacancy defects facilitate adsorption of molecular oxygen, which reacts with the photo-induced electrons and the free electrons on the oxygen vacancies to generate $O_2^{\bullet-}$ ions (Trojanowicz et al.

2018). Both $h^+$ and $O_2{}^{\bullet-}$ were responsible for the solid-phase photocatalytic degradation of PFOS by 2%Ga/TNTs@AC. It is also possible that some of the electrons captured on the oxygen vacancies may be directly involved in the redox reactions.
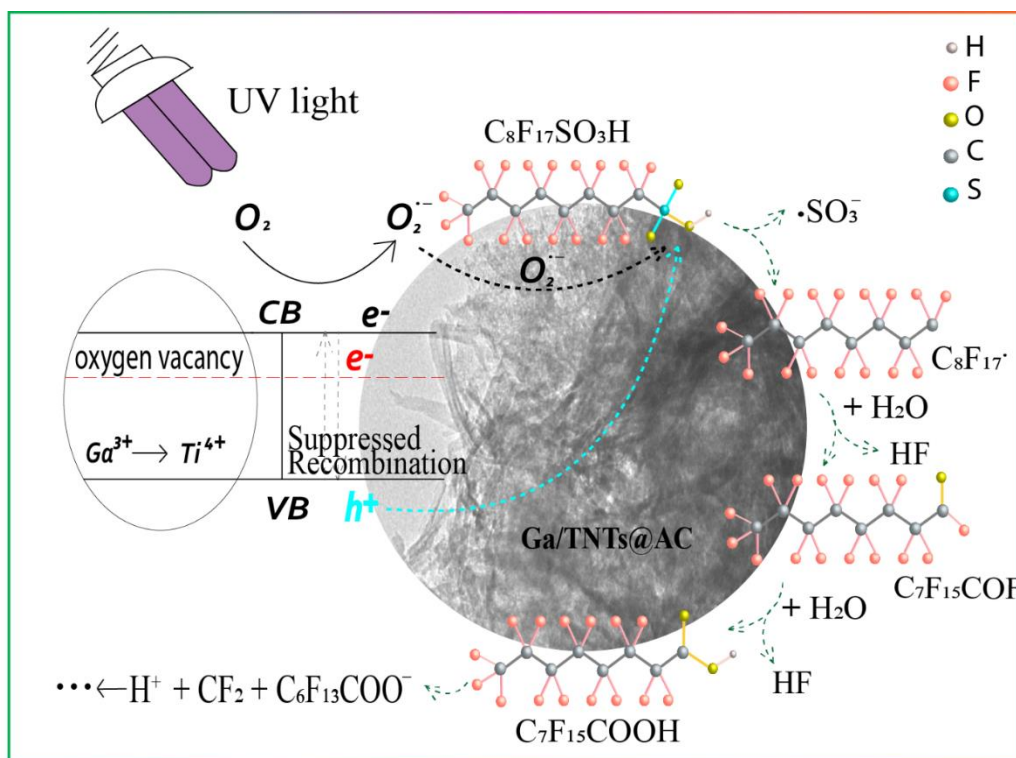


**Figure 3-11.** Proposed mechanism and pathway of enhanced photodegradation of PFOS by Ga/TNTs@AC.

**Figure 3-12** shows the LC-QTOF-MS chromatogram, showing the intermediate products after 4 h of the PFOS photocatalytic process, which included the shorter-chain perfluorooctanoic acid ($C_7F_{15}COOH$), perfluoroheptanoic acid ($C_6F_{13}COOH$), perfluorohexanoic acid ($C_5F_{11}COOH$), perfluoropentanoic acid ($C_4F_9COOH$), perfluorobutanoic acid ($C_3F_7COOH$), pentafluoropropionic acid ($C_2F_5COOH$), and trifluoroacetic acid ($CF_3COOH$). Based on the above analysis and the intermediate products, the photodegradation pathway of PFOS by

88

2%Ga/TNTs@AC is proposed as follows. First, $O_2^{\bullet-}$ and $h^+$ cleave the C−S bond to convert PFOS into $C_8F_{17}\bullet$ (Eq. 6). (Xu et al. 2020b; Yang et al. 2013). Direct oxidation of the C−F bonds by $h^+$ and $O_2^{\bullet-}$ appears unlikely due to the high oxidation potential demand ($E^0 = 3.6$ eV) (Yang et al. 2013). Subsequently, the unstable $C_8F_{17}\bullet$ reacts with $H_2O$ to generate $C_7F_{15}COF$ with one F converted to $F^-$ (Eqs. 7 and 8). Upon further hydrolysis, $C_7F_{15}COF$ converts into PFOA ($C_7F_{15}COOH$) (Eq. 9). The PFOA then undergoes the decarboxylation by $h^+$ or $O_2^{\bullet-}$ to form $C_7F_{15}\bullet$, which is then converted to $C_6F_{13}COF$ (Xu et al. 2020b). The unstable $C_6F_{13}COF$ is then converted into shorter-chain perfluoroheptanoic acid ($C_6F_{13}COOH$) with a $CF_2$ unit eliminated, and the same stepwise defluorination then continues until complete defluorination.

$$C_8F_{17}SO_3^- + h^+ \text{ or } O_2^{\bullet-} \rightarrow C_8F_{17}\bullet + \bullet SO_3^- \tag{6}$$

$$C_8F_{17}\bullet + H_2O \rightarrow C_8F_{17}OH + H^+ \tag{7}$$

$$C_8F_{17}OH \rightarrow C_8F_{15}COF + H^+ + F^- \tag{8}$$

$$C_8F_{15}COF + H_2O \rightarrow C_7F_{15}COOH + H^+ + F^- \tag{9}$$
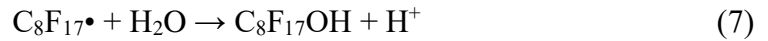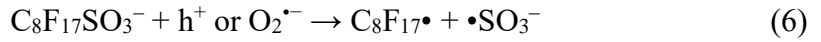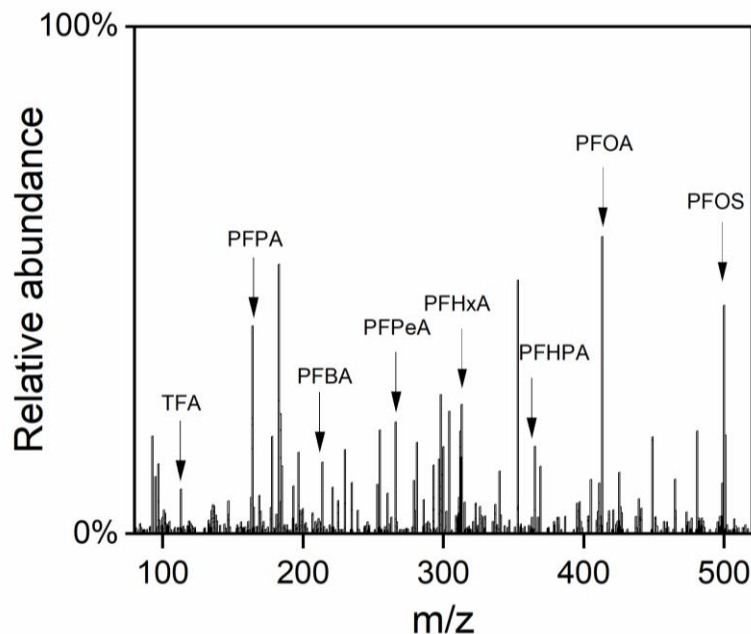
**Figure 3-12.** LC-QTOF-MS chromatogram of ion peaks assigned to the intermediate products of PFOS photodegradation by 2%Ga/TNTs@AC after 4 h UV irradiation. Experimental conditions during adsorption: initial PFOS concentration = 500 µg/L, 2%Ga/TNTs@AC = 3 g/L, pH = 7.0 ± 0.1; Conditions for photodegradation: UV intensity = 210 W/m$^2$, reaction time = 4 h, pH = 7.0 ± 0.1. The intermediates were extracted from the solids after the photodegradation following the same hot-methanol extraction method.

### 3.4. Conclusions

A new adsorptive photocatalyst, Ga/TNTs@AC, was prepared, characterized, and tested for adsorption and subsequent solid-phase photocatalytic degradation of PFOS. The major findings are summarized as follows:

1) Ga/TNTs@AC can be easily prepared based on commercially available TiO$_2$ and activated carbon/charcoal.

2) Ga/TNTs@AC appeared as clusters of aggregated particles, with interwoven TNTs blended or patched with Gallium oxide and AC particles. The modifications of TNTs by AC nanoparticles and Ga induced synergistic interactions with PFOS and facilitated light absorption, electron transfer, and hole-electron separation.

3) The integration of TNTs with AC decreased the specific surface area of the parent AC by >4 times and shifted the adsorption sites from the deep pores of neat AC to the outer shell consisting of AC/Ga-modified TNTs, which are more photoactive and more accessible to PFOS.

4) Raman analysis confirmed that Ga doping facilitated the phase transformation of tri-titanate to anatase upon calcination though excessive Ga inhibited the transformation. XRD spectra provided further evidence that $Ga^{3+}$ ions were embedded in the titanate lattice by substituting $Ti^{4+}$ in an octahedral coordination environment.

5) Ga/TNTs@AC was able to rapidly adsorb PFOS, thereby effectively concentrating PFOS on the photoactive sites. Ga/TNTs@AC showed much higher adsorption capacity and affinity for PFOS than the parent AC. Effective adsorption was observed over a broad pH range of 3.5-10.5.

6) 2%Ga/TNTs@AC exhibited the highest photoactivity and was able to degrade 75.0% and mineralize 66.2% of PFOS pre-sorbed on the solid within 4 h of UV irradiation. The material worked even better at elevated pH.

7) The efficient photodegradation also regenerates the material, allowing for repeated uses of the material without invoking expensive and toxic chemical regenerants. After 4 cycles of repeated uses with or without the photo-regeneration in each cycle, 2%Ga/TNTs@AC remained highly reactive in both adsorption and photodegradation.

8) The superior photoactivity of 2%Ga/TNTs@AC is partially attributed to the oxygen vacancies resulting from the substitution of $Ti^{4+}$ by $Ga^{3+}$. The oxygen vacancies not only suppressed recombination of the $e^-/h^+$ pairs, but also facilitated generation of $O_2^{\bullet-}$. Both holes and $O_2^{\bullet-}$ played critical roles in the PFOS degradation.

9) The photocatalytic degradation of PFOS starts with the cleavage of the sulfonate group by $h^+$ and/or $O_2^{\bullet-}$, which converts PFOS into PFOA that is then decarboxylated and defluorinated following the stepwise defluorination mechanism.

The findings unveil the potential of Ga/TNTs@AC as an adsorptive and photo-regenerable material for removal and degradation of PFOS from contaminated water. The knowledge gained may guide future material development for treating low concentrations of PFAS or other persistent organic pollutants in large volumes of water.

# Chapter 4. Photocatalytic Degradation of PFAS in Field Water Using a 'Concentrate-&-Destroy' Technology

PFAS are ubiquitous in field water, due to their widespread applications in various industrial and consumer products, and health concerns. Yet, a cost-effective technology has been lacking for the degradation of PFAS due to their resistance to conventional treatment. Thus, we developed a novel 'Concentrate-&-Destroy' technology, using adsorptive photocatalyst (Ga/TNTs@AC) for enhanced removal of PFAS from field water. Seven PFAS were detected in the field water, with the most predominant PFAS being PFOS. Ga/TNTs@AC (3 g/L) was able to remove ~98% of PFOS (spiked at 100 µg/L) from filed water within 10 min and offered large adsorption capacity. The spiked cationic ions could enhance the PFOS removal efficiency due to the suppressed repulsive force between PFOS and Ga/TNTs@AC. Moreover, 35.5% of pre-concentrated PFOS (100 µg/L) on Ga/TNTs@AC (3 g/L) was degraded, with the defluorination rate of 25.8%. Compared to the degradation of PFOS in pure water by Ga/TNTs@AC in same manner, the declined degradation efficiency (53% lower) is due to the inhibitory effect of DOM. However, addition $Fe^{3+}$ added in the system increased PFOS degradation to 80.4%, corresponding with the mineralization of 70.0%. The superior photoactivity is attributed to the concurrent complexes, including the $Fe^{3+}$ complex with DOM and the complex between $Fe^{3+}$ and PFOS. Additionally, acidic condition is favorable for not only PFOS adsorption in field water onto Ga/TNTs@AC, but also PFOS degradation in the presence of $Fe^{3+}$. The 'Concentrate-&-Destroy' technology appears promising for more cost-effective removal and degradation of PFAS in field water or PFAS-laden high-strength wastewaters.

## 4.1. Introduction

PFOS and PFOA have been found in surface water in both developed and developing countries around the world including in North America, Europe, and Asia (Lein et al. 2008). For instance, PFOA and PFOS concentrations were measured up to 123 ng/L and 2600 ng/L in surface water of the Yodo River basin, Japan, respectively (Lein et al. 2008). Related to the contaminated European rivers, high PFOA concentrations were found in the River Scheldt in Belgium and The Netherlands (88 and 73 ng/L; flow ~150 $m^3$/s), and River Phone in France (116 ng/L; ~1500 $m^3$/s), whereas the PFOS concentrations were detected in the River Scheldt in Belgium (154 ng/L) and The Netherlands (110 ng/L), and Seine in France (97 ng/L; ~80 $m^3$/s) (Loos et al. 2009). A study reported that Alabama State in USA has the fourth-highest concentration of PFAS in its water supply behind California, New Jersey, and North Caroline (Alabama 2016). The PFAS contamination has been linked to the 3M plant in Decatur, AL, which was the major global manufacturer of PFAS and released the perfluorinated chemical into the Tennessee River (STEEEP 2019; Sunderland et al. 2019). The PFOS concentration measured in the samples collected on the Tennessee River, near Decatur, AL, USA, was in a range from 27.8 ng/L to 106 ng/L, whereas the PFOA concentration varied from non-detectable (< 25 ng/L) to 404 ng/L (Hansen et al. 2002). Moreover, the monitoring data recorded by Alabama Department of Public Health (ADPH) showed that many major water systems in Alabama have concentrations of PFOS and PFOA above the health advisory level, including West Morgan-East Lawrence Water Authority, Gadsden Water Works and Sewer Board, Centre Water and Sewer Board, Vinemont Anon West Point Water Systems Inc., West Lawrence Water Co-op, Northeast Alabama Water District, Rainbow City Utilities Board, and Southside Water Works and Sewer Board, affecting hundreds of thousands of Alabamians (ADPH 2016). For instance, the measurements of drinking

water from 2013-2015 from the EPA's Unregulated Contaminant Monitoring Rule (UMR3) program indicated that the levels of PFOS and PFOA in drinking water from the Wet Morgan-East Lawrence Water Authority reached 130 and 100 ng/L, respectively (EPA 2017a; Newton et al. 2017). Likewise, the Guin Water Works and Sewer Board (GWWSB) in Guin, Alabama measured the PFAS level in unitality's water treatment plant in 2020, which showed that the PFAS levels were above the advisory level of 70 ng/L established by EPA (LAGIAPPE 2022). The Purgatory Creek, as the drinking water source of the water treatment plant, has been contaminated by PFAS leached from 3M Guin facility located upstream from the water plant on Purgatory Creek (AL 2020; LAGIAPPE 2022). Rivers are the source of drinking water, which is one of the important pathways in which PFAS reach humans.

Taking advantage of the high adsorption selectivity and photocatalytic activity of Ga/TNTs@AC, this contribution describes the application of adsorptive photocatalyst to test the technical effectiveness of the 'Concentrate-&-Destroy' technology for removal and degradation of PFAS in realistic field water. The specific objectives were to: 1) characterize filed water, 2) test the effectiveness of Ga/TNT@AC for adsorption and subsequent photocatalytic degradation of PFOS in filed water, 3) evaluate the effects of pH and cationic ions on PFOS adsorption, and 4), examine the impacts of pH and $Fe^{3+}$ on subsequent PFOS photodegradation.

## 4.2. Materials and methods

### 4.2.1. Chemicals

Nano-$TiO_2$ (Degussa P25, 80% wt.% anatase and 20 wt.% rutile) was purchased from Evonik (Worms, Germany). Filtrosorb-400® granular activated carbon (F-400 GAC) was obtained from Calgon Carbon Corporation (Pennsylvania, USA). PFOS, calcium chloride, sodium chloride, potassium chloride, magnesium chloride, iron (III) chloride hexahydrate, anhydrous gallium

chloride, methanol, and sodium hydroxide were acquired from VWR International (Radnor, PA, USA). Sodium perfluoro-1-[$^{13}$C$_8$] octanesulfonate (M8PFOS or $^{13}$C$_8$-PFOS) were purchased from Wellington Laboratories Inc. (Guelph, Ontario, Canada Perfluoro) and were used as isotopically labeled internal standard and surrogate, respectively. All chemicals were analytical-grade or higher. All solutions were prepared using deionized (DI) water (18.2 MΩ-cm).

## 4.2.2. Field water sample collection and characterization

Field water samples were collected below the water surface from Purgatory Creek in Guin Alabama as the river was confirmed to be contaminated by PFAS from the nearby 3M landfill. To remove the suspended solids, the original filed water was filtered through a mixed cellulose easter membrane (pore size = 5 µm), denoted as filtered filed water (FFW).

The filtered samples were kept in sealed high-density polypropylene (HDPE) containers in refrigerator at 4 °C for the future use. To analyze the PFAS in FFW and original filed water (OFW), the samples were shipped, on ice, to University of Maryland Laboratory.

## 4.2.3. Preparation of Ga/TNTs@AC

The adsorptive photocatalyst (Ga/TNTs@AC) was synthesized by integrating a commonly used AC and titanate nanotubes through a modified, one-step, hydrothermal treatment approach (Liu et al. 2016; Zhu et al. 2021). Typically, 1.2 g of F-400 GAC and 1.2 g of TiO$_2$ were added to 66.7 mL of a 10 M NaOH solution. After stirring for 12 h, the mixture was transferred into a 100-mL Teflon reactor enclosed in a stainless-steel cup and heated at 130 °C for 72 h, then cooled down to room temperature. After gravity settling for 1 h, two distinct layers were observed. The upper layer was removed, whereas the bottom black precipitate, i.e., TNTs@AC, was washed with DI water to neutral pH and oven-dried at 105 °C for 8 h. Furthermore, 1 g of dried and prepared TNTs@AC was well dispersed in 80 mL of DI water, and subsequently, 4 mL of a GaCl$_3$ solution

(5 g/L as Ga) was added dropwise into the TNTs@AC suspension. The mass ratio of Ga to TNTs@AC was fixed at 2 wt.%, and the corresponding composite was denoted as 2%Ga/TNTs@AC. The mixture was equilibrated for 3 h, at which >99% of Ga was adsorbed on TNT. Nearly all composite materials were settled and the color of the aqueous solution after 1-h gravity-settling was clear. Upon separation of the solids, the materials were oven-dried at 105 °C for 8 h, and the resulting particles were calcined at 550 °C for 3.5 h in a nitrogen atmosphere with a temperature ramp of 10 °C/min and a nitrogen flow of 2.5 L/min. No fluorine or fluoride was detected in the resulting material.

**4.2.4. Adsorption tests of PFAS in field water by Ga/TNTs@AC**

**4.2.4.1. Adsorption kinetics and isotherm**

To facilitate quick chemical analysis and a rapid preliminary evaluation of various treatment options, the FFW was spiked with 100 µg/L of PFOS and used in the screening stage of the experiments. PFOS was selected as the probe compound because PFOS was the dominant PFAS in the field water.

Given the sufficient material (2%Ga/TNTs@AC), the adsorption tests were conducted using 45 mL HDPE vials and were initiated by adding 0.04 g 2%Ga/TNTs@AC to 40 mL of a filtered field water sample (spiked with 100 µg/L PFOS) with an equilibrium pH of 7.0 ± 0.1. The vials were kept in darkness and rotated at 70 rpm at 25 °C. Duplicate vials were sacrificially sampled at predetermined times. Upon filtering through a 0.22-µm polyether sulfone (PES) membrane (>99% PFOS recovery), the filtrates were analyzed for reaming PFOS. Meanwhile, another 9 mL filtered samples were analyzed for TOC remaining.

Adsorption isotherms were measured in a similar manner, but the mixtures were equilibrated for 24 h to ensure equilibrium. The initial spiked PFOS concentration in field water sample was

varied (i.e., 0.1, 0.5, 1, 5, 10, 15, 20 mg/L), while the dosage of 2%Ga/TNTs@AC was kept at 1 g/L. For comparison, the adsorption isotherm in pure water was also performed via the same procedure but without matrix effect.

### 4.2.4.2. Cationic ions and pH effect

To evaluate effect of cationic ions in FFW toward PFOS removal, experiments were carried out under same procedures, but adding 10 mM NaCl, KCl, CaCl$_2$, and MgCl$_2$. The specific experimental conditions were: dosage of 2%Ga/TNTs@AC = 0.5 g/L, spiked PFOS concentration in FFW = 20 mg/L, pH = $7.0 \pm 0.1$, and individual cationic ion = 10 mM.

The effect of pH on the adsorption of PFOS was tested using 2%Ga/TNTs@AC at a dosage of 0.5 g/L and an initial POFS concentration of 20 mg/L in a same manner. The equilibrium solution pH was $3.0 \pm 0.1$, $5.0 \pm 0.1$, $7.5 \pm 0.1$, and $10 \pm 0.1$.

### 4.2.5. Photocatalytic degradation of PFAS in filed water by Ga/TNTs@AC

### 4.2.5.1. Photodegradation kinetics

Batch photocatalytic degradation experiments were carried out in a Rayonet RPR-100 UV-reactor (Southern New England Ultraviolet CO., Branford, CT, USA) equipped with 16 RPR-2537 Å lamps. The system was fan-cooled and maintained at a temperature of ~35 °C. Following the adsorption equilibrium, the mixtures (PFAS-laden Ga/TNTs@AC) were separated by gravity settling for 1 h (>99% settled). Subsequently, ~99% of the supernatant was removed, and the solid particles were transferred into a quartz tray (ODxH = 6x1.5 cm) with a quartz cover. Then, 10 mL DI water was added into the photo-reactor. The mixture was placed at the center of the photoreactor chamber. The light intensity was 210 W/m$^2$ at the edge (1.5 in or 3.81 cm to the nearest lamp) of the quartz tray and 128 W/m$^2$ at the center. During the photoreaction, the mixture was mixed every 15 min. At each sampling time (i.e., 1, 2, 3, and 4 h), the mixtures were taken from the reactor and

were settled down for 15 min by gravity driven. The supernatants were sacrificially filtered through 0.22-µm PES membrane to determine the fluoride. To measure the residual solid-phase PFOS concentration, the solids were subjected to hot-methanol extraction using 40 mL methanol at 80 °C for 8 h in an oven (Li et al. 2020a). The total PFOS recovery was >95%. No fluoride was detected when the solids were washed with 20 mL of a 1 M NaOH solution. All tests were performed in duplicate.

### 4.2.5.2. pH effect and $Fe^{3+}$ effect on PFOS photodegradation

To determine the effect of pH on PFOS photodegradation in field water, the pH in the adsorption stage was set $7.0 \pm 0.1$ (material dosage = 3 g/L, initial spiked PFOS = 100 µg/L), while the pH during the photodegradation was varied from $4.0 \pm 0.2$ to $9.0 \pm 0.2$.

To examine the impact of $Fe^{3+}$ on PFOS photodegradation in field water, $FeCl_3$ solution was added in the photodegradation stage at various concentrations (25, 40, 50, 60, 80, and 100 µM as $Fe^{3+}$) by varying pH values (3.5, 5.5, 6.5, and $8.0 \pm 0.2$), following the adsorption experiments in same protocol.

### 4.2.6. Chemical analysis

Spiked PFOS (initial concentration = 100 µg/L) in FFW solution was determined using a Vanquish Flex Binary UPLC system (Thermo Fisher, USA) coupled with a quadrupole-Orbitrap mass spectrometer (Orbitrap Exploris TM120, Thermo Fisher) using the negative mode electrospray ionization (ESI). A delay column was placed between the pump and autosampler (HypersilGOLD, 1.9 µm, 175 Å, $3 \times 50$ mm). The instrument detection limit was <1 µg/L. M8PFOS (20 µg/L) was used as the IS. All PFAS in the filed water were analyzed via an ultra-performance liquid chromatography-tandem mass spectrometer (UPLC-MS/MS). Aqueous $F^-$ was analyzed by ion chromatography (Dionex, CA, USA) equipped with an anion exchange column

(Dionex Ionpac AS22) and an anion dynamically regenerated suppressor (ADRS 600, 4 mm). The detection limit was $10.00 \pm 0.01\ \mu g/L$. TOC was analyzed on a TOC analyzer (model TOC-L; Shimadzu, Kyoto, Japan). Leachate pH was determined using a pH meter (PH800 Digital, Apera Instruments, US). Cationic ions and common parameters analyses in FFW were conducted by the Auburn University Soil Testing Lab.

### 4.2.7. PFOS analysis with LC-MS/MS

PFOS concentration and its photodegradation intermediates were determined using a Vanquish Flex Binary UHPLC system (Thermo Fisher) coupled with a quadrupole orbitrap mass spectrometer (Orbitrap Exploris TM120, Thermo Fisher) with electrospray ionization (ESI) in the negative mode and using the Xcalibur software (V4.4.16.14). A delay column was placed between the pump and autosampler (HypersilGOLD, 1.9 µm, 175 Å, 3 x 50 mm) and the system was enabled for PFAS analysis. $^{13}C8$ PFOS (20 µg/L) was used as the internal standard for PFOS analysis. Briefly, a sample or standard (10 µL) was injected into a C18 column (Luna C18(2), 3 µm, 100 Å, $2 \times 50$ mm with a $2 \times 4$ mm guard cartridge, Phenomenex). Gradient elution was performed using a mobile phase consisting of a 2 mM ammonium acetate aquesou solution (pH = 4.7) as solvent A and 100% acetonitrile as solvent B. The flowrate of mobile phase was set at 0.2 mL/min. The gradient conditions were: begin with 70% A and 30% B for the first 0.3 min, then change to 95% B for 3.4 min, hold for 0.7 min, back to 30% acetonitrile for 1.2 min, and re-equilibrate for 1.4 min, resulting a total run time of 7 min. The voltages for capillary, sample cone, and extraction cone were set at 2.8 kV, 30 V, and 4.0 V, respectively. The source temperature was performed at 100 °C, and the desolvation temperature was maintained at 300 °C with a gas flowrate of 600 L/h. The TOF/MS scan was 1 s from 150 to 600 m/z with a 0.02 s inter-scan delay using the centroid data format. A 0.2 mg/L solution of Leucine encephalin was used as the lock mass

reference standard for instrument tuning and calibration. The ion source parameters such as the source temperature (gas and sample cone), mobile phase flow rate, and cone voltage were kept constant throughout the study.

The calibration of LC-QTOF-MS system was performed each time of analysis using at least five PFOS standards in the linear concentration range of 1 to 90 µg/L. The relative standard deviation (%RSD) of the response factors (RFs) for all analysts must be within ± 20% or the linear regression $R^2$ must be ≥0.99, based on initial calibration (ICAL) criteria and their true values. The second source standard was used after the ICAL for the initial calibration verification. The analyte concentrations were within ± 30% of their true value. After 10 samples each time or at the end of the sequence, two consecutive calibration verification standards were analyzed before next sample analysis with analyte concentrations within ± 30% of their true values from the Limit of Quantitation (LOQ) (5 µg/L) to the mid-level calibration concentration.

### 4.3. Results and discussion

### 4.3.1. Filed water characterization

**Table 4-1** summarizes concentrations of PFAS in the original filed water (OFW) and filtered filed water (FFW) through the 5 µm mixed cellulose easter membrane. The results showed that 7 PFAS were detected in the water. The PFAS concentrations in the OFW sample were (mean ± standard deviation): PFOS (60±10 ng/L) > PFHxS (21±3 ng/L) > PFBA (11.5±0.3 ng/L) > PFOA (8.3±1.2ng/L) > HFPO-DA (8.2±0.7 ng/L) > PFBS (5.6±0.8 ng/L) > PFHxA (<5 ng/L). The total PFAS (sum of all the PFAS) amounted to 119.6 ng/L. Upon the filtration, the PFAS levels only slightly decreased (3.5% < absolute relative errors < 16.6%), however, HFPO-DA concentration value detected in FFW was unusually high suggesting an "accident" contamination during filtration process. Namely, PFOS was the dominant compound accounting for ~50% of the total

PFAS in filed water. Moreover, the sum of PFOS and PFOA in filed water was around 68.3 ng/L, slightly lower than EPA lifetime health advisory (70 ng/L). This observation suggests that long-chain PFAS (PFOS and PFOA) have left a legacy of persisting water contamination, even almost ten years after the phase out of 3M company (EPA 2000). Notably, short-chain PFAS accounted for ~23% of the total PFAS in the OFW, which is attributed to 1) the use of short-chain substitutes in the global fluoropolymer industry (Sunderland et al. 2019); (2) the conversion of the longer-chain homologues and/or PFAS precursors following the stepwise chain-shortening process, induced by the biogeochemical process in filed water and chemical and photochemical process under natural field conditions (Li et al. 2019; Tian et al. 2021).

**Table 4-2** shows key compositions in FFW, including cations, anions, and other parameters. As expected, high concentrations of calcium (2.03 mg/L), magnesium (0.67 mg/L), potassium (1.17 mg/L), and sodium (2.47 mg/L) were present in field water, which may facilitate the PFAS adsorption by Ga/TNTs@AC due to the suppressed negative surface potential and cation bridging effects (See **Section 4.3.2**) (Tian et al. 2021). Additionally, chloride was the predominant anion (2.04 mg/L) followed by nitrate (1.40 mg/L) and fluoride (0.03 mg/L) ions. The concentrations of total dissolved solids (TDS, 18 mg/L) and DOM (3.35 mg/L as TOC) were orders of magnitude higher than those of PFAS, which may inhibit the photodegradation of PFAS owing to the competitive photoactive sites on Ga/TNTs@AC (See **Section 4.3.3**).

**Table 4-1.** PFAS analytes and concentrations in original filed water (OFW) and filtered filed water (FFW).

| Analyte | Carbon number | Molecular Ion Formula | Concentration in OFW (mean ± SD, ng/L) | Concentration in FFW (mean ± SD, ng/L) |
|---------|---------------|------------------------|-----------------------------------------|-----------------------------------------|
| PFBA | 4 | $C_4F_7O_2^-$ | 11.5 ± 0.3 | 9.6 ± 1.0 |
| PFBS | 4 | $C_4F_9O_3S^-$ | 5.6 ± 0.8 | 5.4 ± 0.8 |
| PFHxA | 6 | $C_6F_{11}O_2^-$ | <5 | <5 |
| PFHxS | 6 | $C_6F_{13}O_3S^-$ | 21 ± 3 | 18 ± 3 |
| PFOA | 8 | $C_8F_{15}O_2^-$ | 8.3 ± 1.2 | 7.4 ± 1.2 |
| PFOS | 8 | $C_8F_{17}O_3S^-$ | 60 ± 10 | 63 ± 9 |
| HFPO-DA | 6 | $C_6F_{11}O_3^-$ | 8.2 ± 0.7 | 17.0 ± 2.9 |

**Table 4-2.** Key compositions in filtered field water (FFW).

| Cations | Concentration (mean ± SD, mg/L | Anions | Concentration (mean ± SD, µg/L) | Others | Concentration (mean ± SD, mg/L) |
|---------|--------------------------------|--------|----------------------------------|--------|----------------------------------|
| Calcium | 2.03 ± 0.09 | Chloride | 2038.97 ± 1.54 | TDS [a] | 18.00 ± 0.00 |
| Magnesium | 0.67 ± 0.05 | Fluoride | 31.76 ± 0.33 | Hardness [b] | 7.67 ± 0.47 |
| Potassium | 1.17 ± 0.05 | Nitrate | 1398.92 ± 18.08 | Alkalinity [c] | 12.77 ± 0.19 |
| Sodium | 2.47 ± 0.17 | | | TOC [d] | 3.35 ± 0.44 |
| | | | | pH | 4.56 ± 0.02 |

"<" indicates that the concentration was below the limit of quantitation

"a" TDS: Total dissolved solids              "c" Alkalinity as CaCO$_3$ equivalents

"b" Hardness as CaCO$_3$                      "d" TOC: Total organic carbon

### 4.3.2. Adsorption tests

### 4.3.2.1 Adsorption kinetic and isotherms

**Figure 4-1a** shows the time-courses of spiked-PFOS adsorption in FFW by 2%Ga/TNTs@AC. PFOS was rapidly adsorbed within 10 min, with ~98% of PFOS uptake, before a faster approach to equilibrium and about >99% adsorption occurred in 30 mins. While there was a scope for release of labile dissolved organic matter (DOM, served as matrix effect) from natural FFW at neutral pH, which may occupy and compete the adsorption sites against the target spiked PFOS, the instantaneous adsorption and nearly complete removal rate suggest that the matrix had negligible effect on PFOS adsorption on Ga/TNTs@AC, which is also evident from **Figure 4-1b**.

To gain insight into the influence of matrix in field water toward adsorptive photocatalysts adsorption capacity, the adsorption isotherm compares the PFOS uptake in pure water (DI water) and FFW (**Figure 4-1b**), with the initial concentration of spiked PFOS from 0.1 to 20 mg/L. The experimental data were fitted by two classical isotherm models, namely Langmuir and Freundlich isotherms, which are described by Eqs. (1) and (2), respectively.

$$q_e = \frac{Q_{max}bC_e}{1+bC_e} \tag{1}$$

$$q_e = K_F C_e^{1/n} \tag{2}$$

Where, $Q_{max}$ - the Langmuir maximum adsorption capacity (mg/g), b - the Langmuir coefficient related to affinity of binding sites (L/mg), $K_F$ - the Freundlich capacity constant (mg/g·(L/mg)$^{1/n}$), and n -the heterogeneity factor related to the presence and distribution of different sorption sites.

**Table 4-3** summarizes the parameters for two models. With respect to the values of the coefficient of determination ($R^2$), both the Freundlich model and Langmuir model were able to adequately interpret the data obtained in FFW because of the similar $R^2$ ($R^2 = 0.962$ and $0.975$ for Freundlich and Langmuir model, respectively), while the Freundlich model was more consistent with experimental data in pure water ($R^2 = 0.985$). As a consequence, **Figure 4-1b** shows that the fitting lines of the Freundlich adsorption isotherm in both cases nearly coincide. The Freundlich capacity coefficient for the FFW ($29.75$ mg/g·$(L/mg)^{1/n}$) was slightly higher that for pure water ($28.41$ mg/g·$(L/mg)^{1/n}$), indicating that 2%Ga/TNTs@AC performed well with the FFW. Likewise, the Langmuir maximum adsorption capacities ($Q_{max}$) were also comparable for both cases, $18.70$ mg/g for the FFW and $18.12$ mg/g for pure water. The above observation indicates that the matrix effect in real filtered filed water has insignificant impact on the removal of PFOS onto Ga/TNTs@AC, and even increases the adsorption capacity slightly, which is attributed to the concurrent metal ions. Compared to the concentration of cations measured in FFW (**Table 4-2**), the concentrations of divalent cations ($Mg^{2+}$ and $Ca^{2+}$) in FFW after 24-h adsorption by Ga/TNTs@AC were lower than quantitation limit ($< 0.1$ mg/L), whereas the $K^+$ concentration decreased from 1.17 to 0.1 mg/L (**Table 4-4**). It is noteworthy that the unusually high concentration of $Na^+$ (45.67 mg/L) in filed water after 24-h PFOS adsorption by Ga/TNTs@AC was detected, which may be attributed to $Na^+$ leaching from titanate network (Tsiamtsouri et al. 2018). The observations suggest that the cationic ions presented in the natural field water were adsorbed on to the negatively charged adsorbent surfaces at neutral pH due to the low $pH_{pzc}$ value (~4.6), which is favorable for PFOS removal by Ga/TNTs@AC (See **Section 4.3.2.2**). In addition to the cationic ion concentration comparison, nearly all hardness (~99%) was removed from FFW through adsorption, which also confirms that cationic ions were adsorbed onto Ga/TNTs@AC. On the

other hand, the high adsorption capacity of Ga/TNTs@AC is due to: (1) the great specific surface area (244.43 m$^2$/g), offering more adsorption sites for PFOS, (2) the mutual modifications (hydrothermal alkaline treatment, Ga deposition, and calcination) in the composite, resulting in the blockage of the interior sites inside the core, and creating more avaible and accessible adsorption sites for Ga/TNTs@AC on the shell of the particles, and (3) synergistic adsorption interactions, including electrostatic and metal-ligand interactions with the head sulfonate group, hydrophobic interactions with the tail group of PFOS, and anion-$\pi$ or $\pi$-CF interactions between the electron-deficient aromatic skeletons of AC and the CF$_2$/CF$_3$ and sulfonate groups (Zhu et al. 2021).



(a)                                    (b)
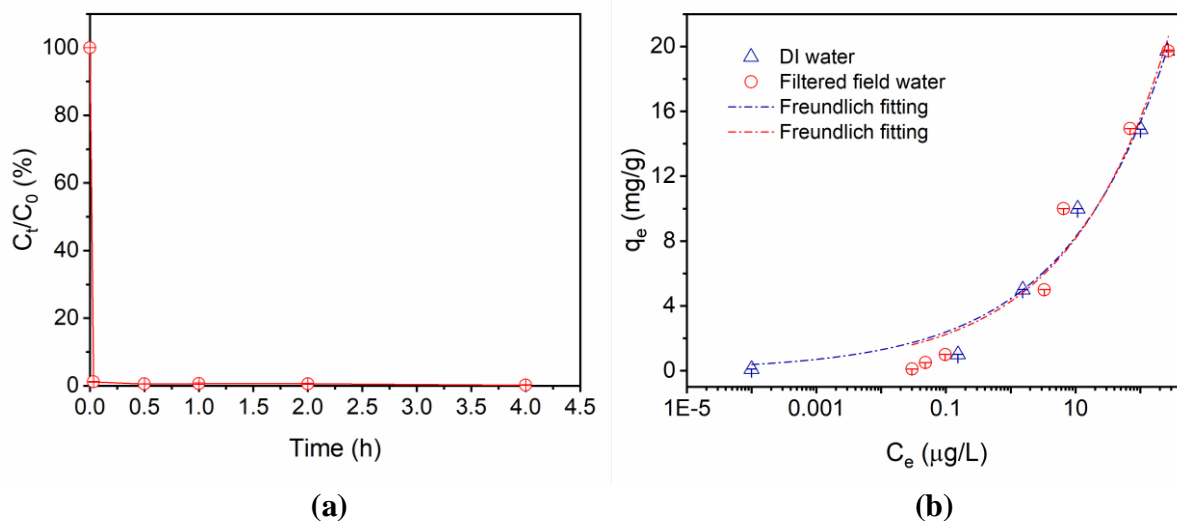
**Figure 4-1. (a)** Adsorption kinetics and **(b)** adsorption isotherm of spiked PFOS in filtered field water and pure water by 2%Ga/TNTs@AC. Experimental conditions for kinetic test: initial spiked PFOS concentration = 100 µg/L, material dosage = 1 g/L, pH = 7.0 ± 0.1; Conditions for isotherm experiments: initial spiked PFOS concentration = 0.1-20 mg/L, material dosage = 1 g/L, pH = 7.0 ± 0.1. Data are plotted as the mean of duplicates with error bars indicating relative deviation from the mean.

**Table 4-3.** Adsorption isotherm model parameters for adsorption of spiked PFOS in FFW by 2%Ga/TNTs@AC.

| Model | Parameter | Solvent | |
|---|---|---|---|
| | | DI water | Filtered field water |
| Freundlich model | $K_F$ (mg/g·(L/mg)$^{1/n}$) | 28.41 | 29.75 |
| | n | 3.72 | 3.56 |
| | $R^2$ | 0.985 | 0.962 |
| Langmuir model | $Q_{max}$ (mg/g) | 18.12 | 18.70 |
| | b (L/mg) | 137.40 | 135.99 |
| | $R^2$ | 0.958 | 0.975 |

**Table 4-4.** Cation analysis in filtered field water after adsorption by Ga/TNTs@AC

| Cations | Concentration (mean ± SD, mg/L) | Others | Concentration (mean ± SD, mg/L) |
|---|---|---|---|
| Calcium | < 0.1 | Hardness [a] | < 0.1 |
| Magnesium | < 0.1 | pH | 7.0 ± 0.1 |
| Potassium | 0.10 ± 0.00 | TOC | 1.04 ± 10.6 |
| Sodium | 45.67 ± 0.47 | | |

### 4.3.2.2 Cations effect on PFOS adsorption

To further investigate the effect of cations on PFOS adsorption in field water, additional 1 mM and 10 mM cations (such as $Na^+$, $K^+$, $Mg^{2+}$, and $Ca^{2+}$) were spiked into the solution, respectively, as shown in **Figure 4-2**. Compared with 77.6% adsorbed PFOS in FFW without additional cations, PFOS uptake increased 80.3%, 80.9%, 88.4%. and 87.8% in the presence of 1 mM $Na^+$, $K^+$, $Ca^{2+}$, and $Mg^{2+}$, respectively, whereas raising cations concentration to 10 mM resulted in higher PFOS removal efficiency (90.3% for $Na^+$, 93.5% for $K^+$, 96.6% for $Ca^{2+}$, and 96.3% $Mg^{2+}$). The above observation suggests that increasing ionic strength promoted PFOS adsorption in field water on Ga/TNTs@AC. Overall, the presence of cations increased PFOS adsorption on Ga/TNTs@AC, while divalent cations spiked in field water caused slight increase of PFOS adsorption than monovalent cations.
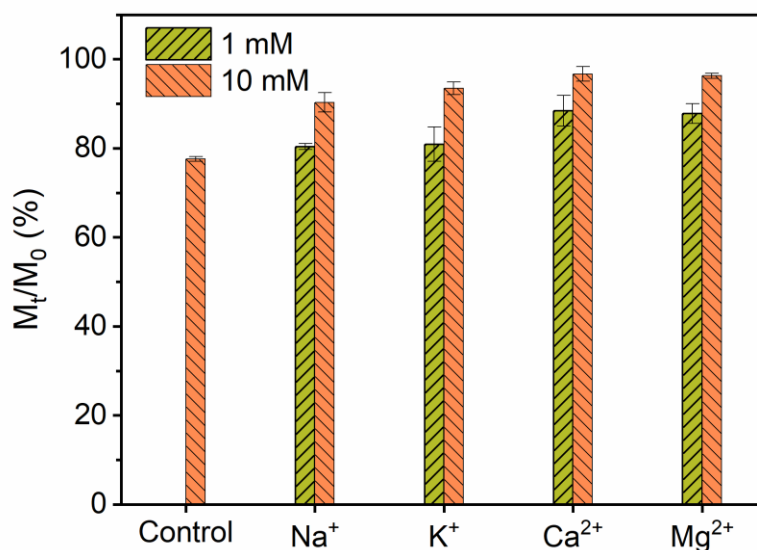


**Figure 4-2.** Effect of additional cations on adsorption of spiked PFOS by Ga/TNTs@AC. Experimental conditions: initial spiked PFOS concentration = 20 mg/L, material dosage = 0.5 g/L, pH = 7.0 ± 0.1, contact time = 24 h, and individual cation concentration = 1M and 10 mM.

At neutral pH, the negative material surface ($pH_{pzc}$ of 2%Ga/TNTs@AC = 4.6) repels the sulfonate head group of PFOS, while the adsorption rate stays high (77.6%) owing to the dominant hydrophobic reaction between the carbon particles and the carbon chain in PFOS (Zhu et al. 2021). Meanwhile, the electrostatic repulsion occurs between PFOS anions and Ga/TNTs@AC, because the adsorbent surface charge is of the same sign as the function group of PFOS ($pK_a$ of PFOS = −3.27) (Brooke et al. 2004). However, the cationic counterions (e.g., $Na^+$, $K^+$) are attracted to the negatively charged adsorbent surface leading to the electric double layer (EDL), which results in the decreased electrostatic repulsion due to the less negatively charged surface of Ga/TNTs@AC in the presence of monovalent cations (Xiao et al. 2011). Additionally, the enhanced PFOS adsorption rate in the presence of divalent cations such as $Ca^{2+}$ and $Mg^{2+}$ is attributed to not only the neutralized surface negative charges of adsorbents and surface complexation, but also the divalent cation-bridging effect between the PFOS anions and 2%Ga/TNTs@AC at neutral pH (Eqs. (3) and (4)) (Wang and Shih 2011). Wang and Shih (2011) reported that the divalent cations ($Mg^{2+}$ and $Ca^{2+}$) could serve as bridge between two PFOS/PFOA molecules and initiate the potential complexes with them, while only PFOS was able to be bridged by $Ca^{2+}$ due to the higher covalent nature of magnesium. Zhao et al. (2016a) speculated that increasing $Mg^{2+}$ concentration in the feed solution (100 PFOS) resulted in higher PFOS rejection rate (from 94.1% to 98.6% at 0.4 MPa), which was owing to the bridge and complex formed between $SO_3^-$ group of PFOS molecule and negatively charged membrane surface (NF270). Besides, Luo et al. (2016) investigated that the $SO_3^-$ group of PFOS was the active site that bound to the positively charged $Na^+$, $Mg^{2+}$, and $Fe^{3+}$, leading to the formation of bridge structures. Moreover, salting-out effect may play a role on enhanced PFOS adsorption on Ga/TNTs@AC, resulting from the lower solubility of PFOS (Cai et al. 2022; Carter and Farrell 2010). For instance, You et al. (2010)

reported that the solubility of PFOS decreased from 680 mg/L in pure water to 25 mg/L in filtered seawater. In light of this study, carbon was a predominant portion (50 wt.%) in Ga/TNTs@AC composite, which was able to attract PFOS via hydrophobic interaction between carbon particles and the C-F chain in PFOS. Thus, the potential reasons contributing to the enhanced PFOS adsorption onto Ga/TNTs@AC in the presence of cations in the filed water solution are: (1) suppressed repulsive force between anionic head group of PFOS and adsorbent; (2) the complex formation between metal ions and PFOS; (3) the formation of bridge between PFOS head group and negatively charged adsorbent surfaces; and (4) a reduction in the solubility of PFOS.

$$CF_3(CF_2)_7SO_3^- + Ca^{2+} = Ca(CF_3(CF_2)_7SO_3)_2 \tag{3}$$

$$CF_3(CF_2)_7SO_3^- + Mg^{2+} = Mg(CF_3(CF_2)_7SO_3)_2 \tag{4}$$
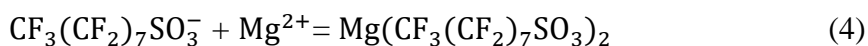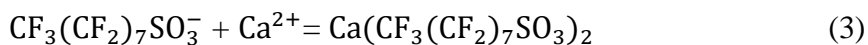
### 4.3.2.3. pH effect on PFOS adsorption

pH is a critical factor in adsorption experiments because it affects the charge characteristics of PFAS molecules and surface properties of adsorbents. **Figure 4-3** shows the PFOS removal efficiency upon adsorption equilibrium from the solution over a broad pH range of 3.0-10.0 by 2%Ga/TNTs@AC at 0.5 g/L. Compared with the PFOS adsorption rate of 77.6% at neutral pH, the PFOS removal efficiency increased to 99.0% and 88.3% at pH 3.0 and 5.0, respectively; while decreased to 60.5% at pH 10.0.

Although $H^+$ may interfere the speciation of solutes in the solution, PFOS mainly exists in the anionic form in the pH values tested in the current study, due to the low $pK_a$ value of PFOS (−3.27) (Brooke et al. 2004). On the contrary, the surface charge of adsorbents is strongly dependent on pH of the solution. The $pH_{pzc}$ of 2%Ga/TNTs@AC was reported at around 4.6 (Zhu et al. 2021); hence, the surface of 2%Ga/TNTs@AC was charged positively at pH < $pH_{pzc}$, while it was negative at pH > 4.6. Thus, lower pH (pH < 5.0) facilitated the PFOS adsorption capacity

110

through multiple synergistic interactions with 2%Ga/TNTs@AC, including electrostatic and metal-ligand interactions between the head sulfonate group and positively charged adsorbents, hydrophobic interactions with the tail group of PFOS and carbon particles, and anion-π or π-CF interactions between the electron-deficient aromatic skeletons of AC and $CF_2/CF_3$ and sulfonate groups. Conversely, at higher pH, the electrostatic interaction was suppressed, while hydrophobic and anion-π interactions were predominant for PFOS adsorption, which may result in lower PFOS removal rate than that in acid condition.
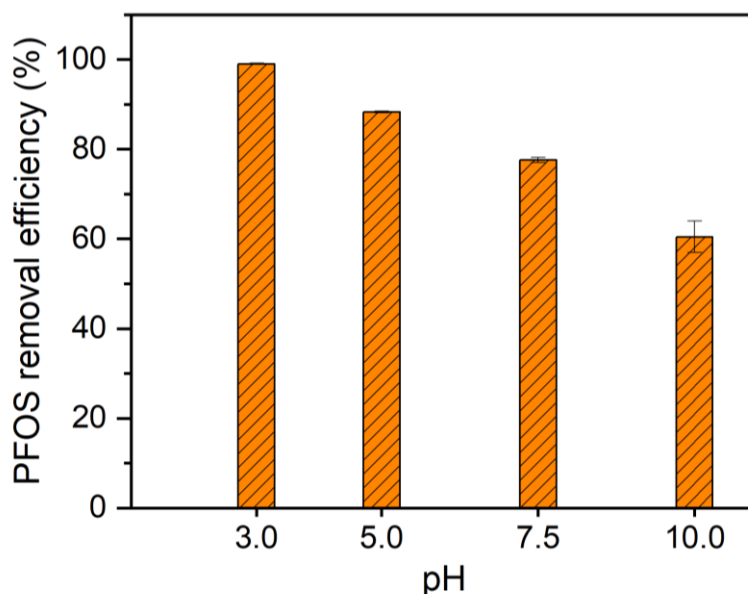


**Figure 4-3.** Effect of pH on adsorption of spiked PFOS by Ga/TNTs@AC. Experimental conditions: initial spiked PFOS concentration = 20 mg/L, material dosage = 0.5 g/L, contact time = 24 h.

### 4.3.3. Photodegradation tests

### 4.3.3.1 Photodegradation kinetics of PFOS in FFW by Ga/TNTs@AC

**Figure 4-4** shows the photodegradation efficiency of spiked PFOS (100 µg/L) in FFW by 2%Ga/TNTs@AC. Under 4-h UV irradiation, 2%Ga/TNTs@AC was able to degrade 35.5%

PFOS, corresponding to 25.8% defluorination rate. However, the values were 53% and 61% lower than PFOS photodegradation (75.0%) and mineralization rates (66.2%) in pure water under same experimental conditions, respectively (Zhu et al. 2021). The above observation is in line with other reports. For example, the degradation of PFOA in the wastewater significantly retarded by the needle-like $Ga_2O_3$ under UV irradiation (~2.67 times longer than pure water), due to high concentration of TOC (18.9 mg/L) in wastewater (Shao et al. 2013). Besides, the presence of HA at 2.0 mg/L in the solution decreased the PFOS decomposition rate constant from ~0.10 $h^{-1}$ to ~ 0.05 $h^{-1}$, which was ascribed to an inhibitory effect of HA (Lyu et al. 2015). Therefore, the significant photoactivity decrease in this study may be attributed to the DOM from FFW.



(a)  (b)
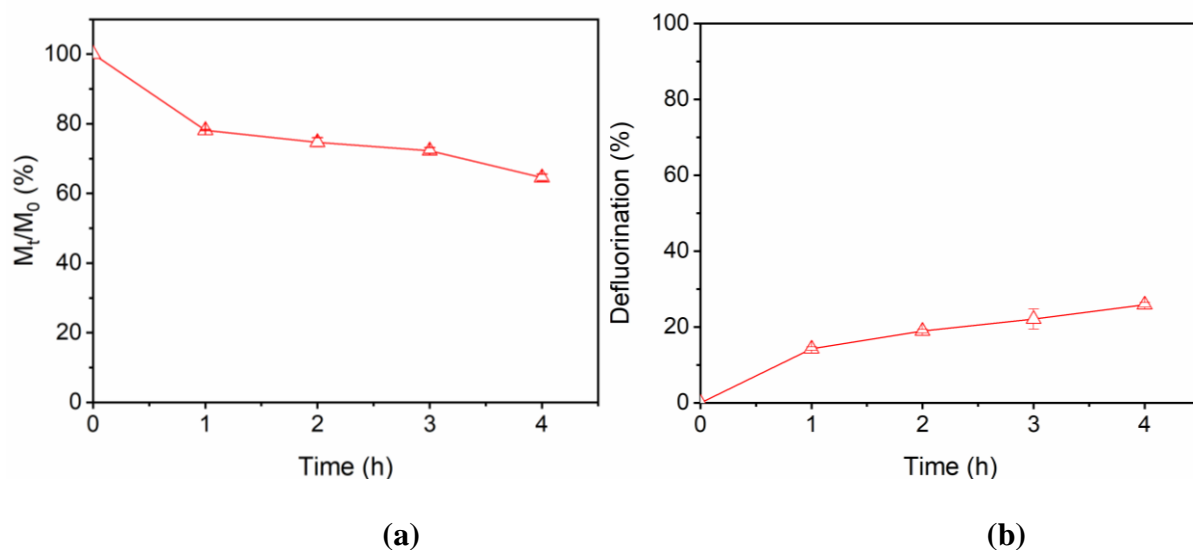
**Figure 4-4. (a)** Photodegradation and **(b)** defluorination kinetics of PFOS in FFW pre-adsorbed on 2%Ga/TNTs@AC. Experimental conditions during adsorption: spiked PFOS concentration = 100 µg/L, material dosage = 3 g/L, pH = 7.0 ± 0.2; Conditions for photodegradation: UV intensity = 210 W/m$^2$, pH = 7.0 ± 0.2. Data are plotted as mean of duplicates with error bars indicating relative deviation from the mean.
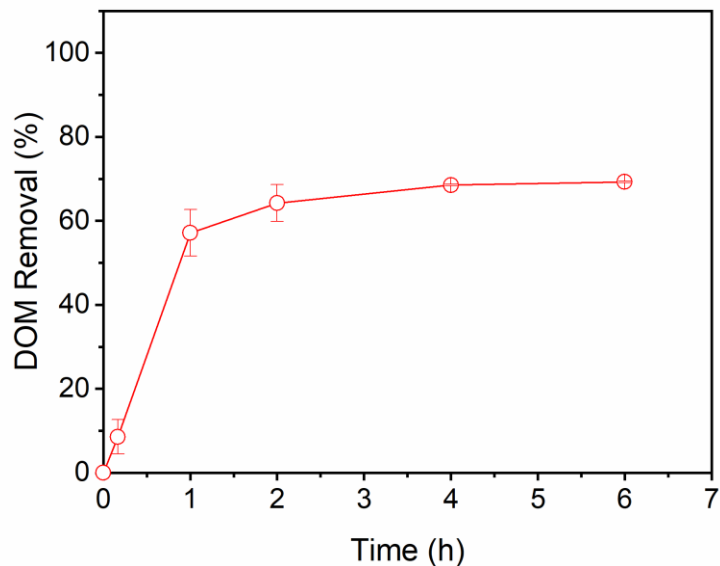
**Figure 4-5.** Adsorption kinetics of DOM (measured as TOC) in FFW by Ga/TNTs@AC. Experimental conditions: initial spiked PFOS concentration = 100 µg/L, material dosage = 1 g/L, pH = 7.0 ± 0.2, and initial TOC = 3.39 mg/L. Data are plotted as the mean of duplicates with error bars indicating relative deviation from the mean.

Generally, DOM is considered to be a critical factor that affects photodegradation process due to the generation of DOM-derived oxidative intermediates, light screening, and their physicochemical quenching effects (Qi et al. 2022; Xu et al. 2017a). **Figure 4-5** shows the adsorption kinetic of DOM (measured as TOC) in FFW spiked with PFOS (100 µg/L) by 2%Ga/TNTs@AC at 1 g/L. Upon adsorption equilibrium, ~60% of DOM was removed by adsorbents via hydrophobic interactions and/or π-interactions with carbon particles in Ga/TNTs@AC (Wang et al. 2021). While it had negligible effect on PFOS adsorption (**Figure 4-1**), the adsorbed DOM occupies the photoactive sites at the surface of the Ga/TNTs@AC, competing with PFOS on the accessible photons, photogenerated charge carries, and reactive

oxygen species, which play important roles on PFOS photodegradation (Konstantinou and Deligiannakis 2013; Zhu et al. 2022; Zhu et al. 2021). Additionally, DOM may interfere with the photolysis of organic contaminants by screening reactive wavelengths of light (Xue et al. 2019). Concretely, Walse et al. (2004) reported that DOM was the variable that decreased fipronil degradation due to competitive light absorption (*i.e.*, attenuation) and the quenching of fipronil*. DOM hindered PFOS photodecomposition not only by absorbing light, but also by acting as photosensitizers to produce reactive species (Lester et al. 2013; Liang et al. 2016). Typically, DOM was transformed to triplet excited states ($^3DOM^*$) by adsorbing light under UV irradiation, which could react with $O_2$ via energy or electron transfer mechanism to generate reactive oxygen species such as singlet oxygen ($^1O_2$), hydroxyl radicals ($^{\bullet}OH$), and hydrogen peroxide ($H_2O_2$) (Lester et al. 2013). However, none of these radicals played a role in PFOS photodegradation by Ga/TNTs@AC, because holes ($h^+$) and $O_2^{\bullet-}$ were responsible for degradation of PFOS in this study (Zhu et al. 2021). The superior PFOS photodegradation by Ga/TNTs@AC in pure water was attributed to the oxygen vacancies, which not only suppressed recombination of the $e^-/h^+$ pairs, but also facilitated $O_2^{\bullet-}$ generation (Zhu et al. 2021). Conversely, pre-adsorbed DOM may compete for the electrons and oxygen, resulting in less $O_2^{\bullet-}$ generation through the reaction between electrons and oxygen. Apart from the transformation from DOM to $^3DOM^*$, the reaction between DOM and $^{\bullet}OH$ could occur at pH = 7.0, which produced reduced DOM ($DOM^{\bullet-}$) by fast one-electron-transfer in the initial stage (Ma et al. 2019). Meanwhile, the unstable $DOM^{\bullet-}$ reacted with $O_2^{\bullet-}$ generating $H_2O_2$ to complete a catalytic dismutation cycle, consuming avaible and accessible $O_2^{\bullet-}$ and further leading to lower PFOS photodegradation by Ga/TNTs@AC (Ma et al. 2019).

**4.3.3.2. pH on PFOS photodegradation**

**Figure 4-6** displays the photodegradation of spiked PFOS in FFW by 2%Ga/TNTs@AC at various pH values. The 4-h PFOS photodegradation efficiency showed an evident decreasing trend with increasing pH, from 61.2% at pH 4.0 to 52.3%, 35,5%, and 23.9% at pH 5.5, 7.0, and 9.0. Interestingly, this result was completely the opposite compared with the one reported by Zhu et al. (2021), where the acidic condition was less favorable for PFOS photodegradation in pure water by Ga/TNTs@AC due to the reactions occurred between $O_2^{\bullet-}$ and $H^+$. In light of pH effect on PFOS degradation in FFW by Ga/TNTs@AC, the matrix effect (DOM) needs to be taken into account. As illustrated in **Section 4.3.3.1**, the pre-adsorbed DOM not only acted as electron trapper producing photo-induced radicals, which played negligible roles on PFOS degradation, but also reacted with $O_2^{\bullet-}$ generating $H_2O_2$ (Ma et al. 2019). However, in addition to $O_2^{\bullet-}$, $h^+$ was also participating in PFOS photodegradation by Ga/TNTs@AC under UV irradiation (Zhu et al. 2021). It is noteworthy that lower pH is favorable for generating $h^+$; thus, $h^+$ is considered to be the predominant oxidizing species in acid condition, which may result in superior PFOS photodegradation at pH < 7.0 (Xu et al. 2017a).
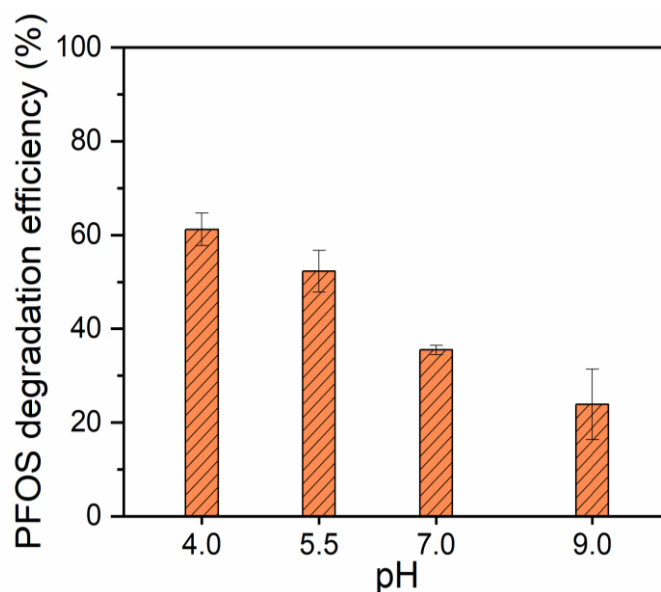
**Figure 4-6.** Effect of pH on spiked PFOS photodegradation by 2%Ga/TNTs@AC. Experimental conditions (adsorption): Spiked PFOS concentration = 100 µg/L, material dosage = 3 g/L, and pH = 7.0 ± 0.1; Experimental conditions (photodegradation): material dosage = 3 g/L during adsorption, UV intensity = 210 W/m², reaction time = 4 h.

### 4.3.3.3. $Fe^{3+}$ effect on PFOS photodegradation

While 2%Ga/TNTs@AC was able to degrade 61.2% of pre-sorbed PFOS in FFW at pH = 4.0 within 4-h UV irradiation, the value was ~18% lower than the highest photodegradation of PFOS in pure water under neutral pH (Zhu et al. 2021). To enhance PFOS degradation by Ga/TNTs@AC and eliminate the negative effect of DOM, $Fe^{3+}$ was added in the system. The beneficial effect of ferric ions in PFAS photochemical degradation has been investigated in recent years. For example, Liang et al. (2016) studied that the addition of 20 µM ferric ions accelerated the PFOA defluorination process, shortening the time from 144 h in the system without ferric ions to 72 h with nearly completed defluorination. Additionally, spectroscopic spectra indicated that PFOA

decomposition reaction was initiated by electron-transfer from PFOA to $Fe^{3+}$; 97.8% ± 1.7% of 50 µM PFOA degraded within 28 days into shorter-chain intermediates and fluoride ($F^-$) in the $Fe^{3+}$ and sunlight system, with an overall defluorination extent of 12.7 ± 0.5% (Liu et al. 2013a).

**Figure 4-7a** shows the pre-sorbed PFOS photodegradation and mineralization by Ga/TNTs@AC in the presence of $Fe^{3+}$ at various concentrations under 4-h UV irradiation. Notably, the presence of $Fe^{3+}$ significantly increased PFOS photodegradation from 61.2% without addition $Fe^{3+}$ to 80.4% at pH = 3.5. Firstly, DOM could form complexes with $Fe^{3+}$, which has a positive effect on the degradation of organic pollutants (Qi et al. 2022). Specifically, the light irradiation of $Fe^{3+}$ complexes with DOM generates both $Fe^{2+}$ via a ligand-to-metal charge transfer (LMCT) reaction and DOM radicals ($DOM^{+\bullet}$) (Eq. 5) (Gaberell et al. 2003). Subsequently, $DOM^{+\bullet}$ reacts with oxygen to generate $O_2^{\bullet-}/HO_2^{\bullet}$ (Eq. 6) (Song et al. 2005), which could attack PFOS anions to decarboxylate and defluorinated PFOS following the stepwise defluorination mechanism. Meanwhile, the redox reactions between $Fe^{2+}/Fe^{3+}$ are initiated. The produced $O_2^{\bullet-}/HO_2^{\bullet}$ radicals could be transformed into $H_2O_2$ either by reaction with $Fe^{2+}$ (Eqs. 7 and 8) or through self-disproportionation (Eqs. 9 and 10); then, $H_2O_2$ reacts with $Fe^{2+}$ to produce $^{\bullet}OH$ radicals (Eq. 11), which causes the generation of $Fe^{3+}$ (Eq. 12) (Song et al. 2005). Therefore, the redox cycle of $Fe^{2+}/Fe^{3+}$ and photo-generated holes/electrons facilitates the production of $O_2^{\bullet-}$ and $^{\bullet}OH$, as well as suppresses electron-hole recombination, resulting in enhanced photodegradation of PFOS (Li et al. 2020a). Secondly, the enhancement of pre-sorbed PFOS photodegradation by Ga/TNTs@AC in the presence of $Fe^{3+}$ might be also ascribed to the generation of complex between PFOS and ferric ion upon UV radiation (Cheng et al. 2014). The $Fe^{3+}$ complex with PFOS could be directly excited by UV light and photolyzed to $Fe^{2+}$ and an organic radical through LMCT. Subsequently, the unstable PFOS radical is subsequently desulfonated to form a perfluoroalkyl radical (Jin et al.

2014). In the meanwhile, $Fe^{2+}$ can be recovered to $Fe^{3+}$ in the presence of oxygen (Jin et al. 2014).

Then, the perfluoroalkyl radical may react with $H_2O$ to generate $C_7F_{15}COF$ with one F converted

to $F^-$ and convert to PFOA that is then decarboxylated and defluorinated following the stepwise

defluorination mechanism (Zhu et al. 2021). Taken together, the presence of $Fe^{3+}$ not only

suppresses the inhibitory effect of DOM, but also forms complex with PFOS, resulting in the

enhanced photocatalytic activity toward pre-sorbed PFOS degradation under UV irradiation.

$$Fe^{3+} - DOM \xrightarrow{hv} Fe^{2+} + DOM^{+\bullet} \tag{5}$$

$$DOM^{+\bullet} + O_2 \rightarrow O_2^{\bullet-}/HO_2^{\bullet} + DOM^{2+} \tag{6}$$

$$Fe^{2+} + O_2^{\bullet-} + 2H^+ \rightarrow Fe^{3+} + H_2O_2 \tag{7}$$

$$Fe^{2+} + HO_2^{\bullet} + H^+ \rightarrow Fe^{3+} + H_2O_2 \tag{8}$$

$$O_2^{\bullet-} + HO_2^{\bullet} + H^+ \rightarrow O_2 + H_2O_2 \tag{9}$$

$$HO_2^{\bullet} + HO_2^{\bullet} \rightarrow O_2 + H_2O_2 \tag{10}$$

$$Fe^{2+} + H_2O_2 \rightarrow Fe^{3+} + {}^{\bullet}OH + OH^- \tag{11}$$

$${}^{\bullet}OH + Fe^{2+} \rightarrow Fe^{3+} + OH^- \tag{12}$$
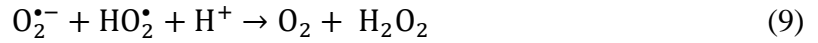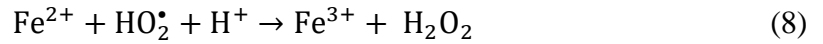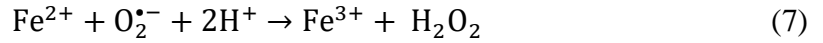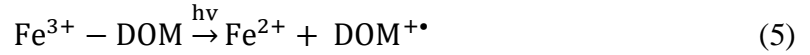
On the other hand, **Figure 4-7a** also displays that increasing $Fe^{3+}$ concentration from 40 µM

to 60 µM resulted in higher PFOS degradation from 57.6% to 80.4%, corresponding to

mineralization rates of 44.% and 70.0%, respectively, while further elevating $Fe^{3+}$ (80 µM) led to

lower PFOS photodegradation rate (68.3%) with 52.6% mineralization efficiency. Moreover, the

defluorination of PFOS decreased to 36.4% and 25.4% when $Fe^{3+}$ concentration was 25 µM and

100 µM, respectively (**Figure 4-7b**). The above observation indicates that 60 µM $Fe^{3+}$ was most

beneficial for enhancing the photodegradation of PFOS. However, excess ferric ion inhibited the

PFOS decomposition efficiency, which is attributed to the photon-limitation phenomenon (Zhang

and Anderson 2013). In this study, photons may be adsorbed by DOM, PFOS, and/or Ga/TNTs@AC, as well as the addition ferric ion, and other reactions influence the consumption rate of the target reactant (Wang et al. 2008; Zhang and Anderson 2013). Therefore, the competition of photons among the components adsorbed onto Ga/TNTs@AC may occur at high ferric ion concentrations, resulting in the reduction of direct photolysis and photocatalytic degradation efficiency (Cheng et al. 2014).



**(a)**                     **(b)**
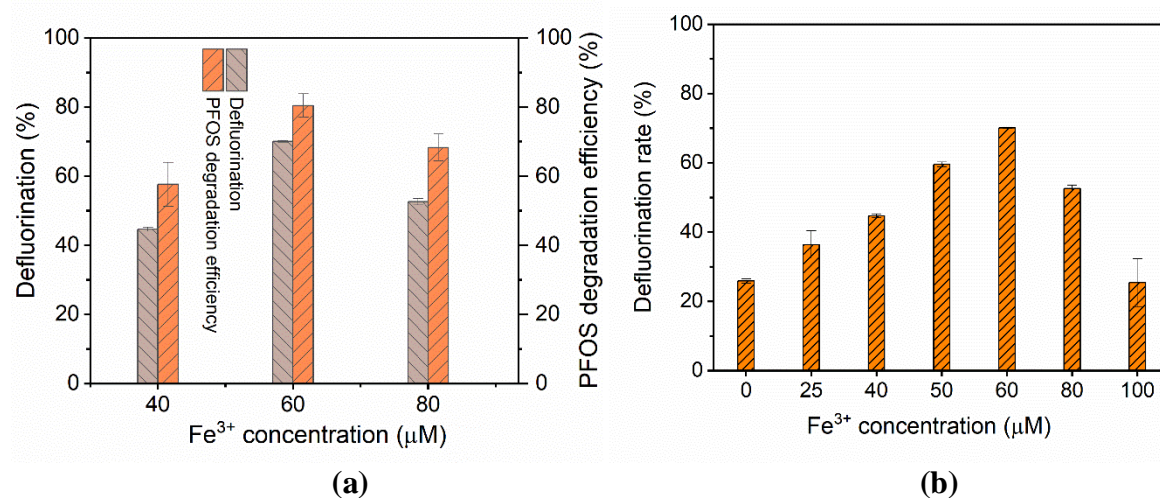
**Figure 4-7. (a)** Photodegradation and **(b)** defluorination and of PFOS pre-sorbed on 2%Ga/TNTs@AC at various $Fe^{3+}$ concentrations during photodegradation. Experimental conditions (adsorption): spiked PFOS concentration = 100 µg/L, material dosage = 3 g/L, adsorption time = 2 h, and pH = 7.0 ± 0.1; Experimental conditions (photodegradation): material dosage = 3 g/L, UV intensity = 210 W/m$^2$, reaction time = 4 h, pH = 3.5 ± 0.2.

In addition to $Fe^{3+}$ dosage, pH effect on PFOS photodegradation in the presence of 60 µM $Fe^{3+}$ (optimized dosage) needs to be taken into consideration, which is an important factor influencing the photocatalytic degradation of PFOS in FFW by Ga/TNTs@AC. **Figure 4-8** shows a clear decreasing trend toward PFOS degradation efficiency as increasing pH. The 4-h PFOS

decomposition rate reduced from 80.4% to 43.2%, 25.9%, to 20.3%, when pH increased from 3.5 to 5.5, 6.5, to 8.0, respectively. The significant decline in PFOS photodegradation rate is ascribed to the complexation efficiency of ferric ion with PFOA and DOM (Cheng et al. 2014; Wang et al. 2008). Due to the low $K_{sp}$ value ($4.0 \times 10^{-38}$) of Fe(OH)$_3$ (Liu et al. 2018), ferric hydroxide precipitation may take place when the pH of the solution is higher than 4, leading to negative effect on both direct photolysis and the photocatalytic degradation efficiency. Thus, the acid condition (pH = 3−4) is favorable for PFOS photodegradation in the presence of Fe$^{3+}$ by Ga/TNTs@AC.
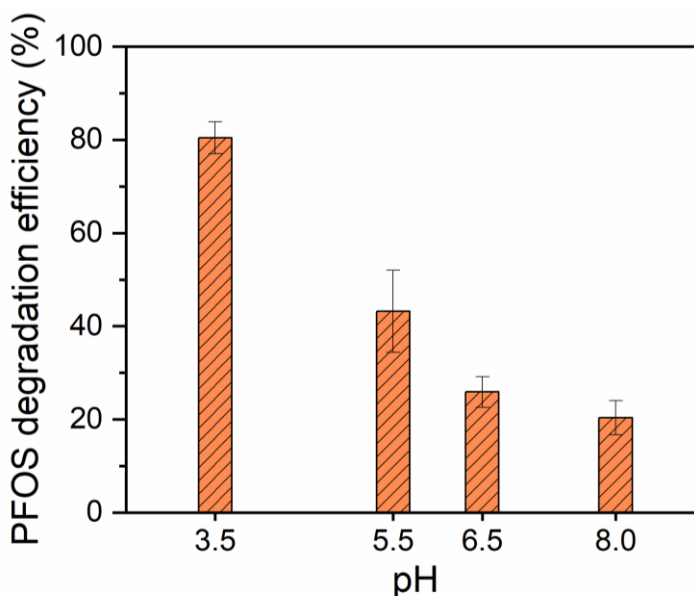


**Figure 4-8**. Effect of pH on PFOS photodegradation 2% Ga/TNTs@AC in the presence of 60 µM Fe$^{3+}$. Experimental conditions (adsorption): spiked PFOS concentration = 100 µg/L, material dosage = 3 g/L, adsorption time = 2 h, and pH = 7.0 ± 0.1; Experimental conditions (photodegradation): material dosage = 3 g/L during adsorption, UV intensity = 210 W/m$^2$, reaction time = 4 h, Fe$^{3+}$ concentration = 60 µM.

**4.4. Conclusions**

A novel 'Concentrate-&-Destroy' technology was investigated, using adsorptive photocatalyst for enhanced removal of PFAS from field water. The major findings are summarized as follow:

1) Seven PFAS were detected in the field water, with the most predominant PFAS being PFOS. Additionally, filed water contained high concentrations of DOM, chloride, nitrate, and metals (*e.g.*, $Na^+$, $K^+$, $Ca^{2+}$, and $Mg^{2+}$).

2) Adsorption experiments using the filtered field water spiked with 100 µg/L PFOS, where 2%Ga/TNTs@AC at a dosage of 1 g/L was able to remove ~98% of PFOS from filed water within 10 min. In addition, 2%Ga/TNTs@AC offered a $Q_{max}$ of 18.70 mg/g of PFOS in field water, slightly higher than the value in pure water, which is attributed to the suppressed negative surface potential by concurrent cationic ions.

3) The addition cations (10 mM $Na^+$, $K^+$, $Ca^{2+}$ and $Mg^{2+}$) added in the system significantly facilitated the PFOS removal efficiency, due to the suppressed repulsive force between anionic head group of PFOS and adsorbent, the complex formation between metal ions and PFOS, the formation of bridge between PFOS head group and negatively charged adsorbent surfaces; and a reduction in the solubility of PFOS.

4) Acidic condition is favorable for PFOS adsorption in field water onto Ga/TNTs@AC, owing to the synergistic reactions, including electrostatic and metal-ligand interactions, hydrophobic interactions, and anion-π or π-CF interactions.

5) The subsequent photodegradation was tested, where 2%Ga/TNTs@AC was able to degrade 35.5% PFOS, corresponding to 25.8% defluorination rate. The reduced PFOS

photodegradation efficiency was ascribed to the inhibitory effect of DOM. However, the material worked better at lower pH.

6) The presence of ferric ion could increase PFOS photodegradation to 80.4% at pH = 3.5 with the defluorination rate of 70.0%, which is due to the concurrent complexes, including the $Fe^{3+}$ complex with PFOS and the complex between $Fe^{3+}$ and DOM. Lower pH was beneficial for PFOS decomposition by Ga/TNTs@AC with $Fe^{3+}$ added.

# Chapter 5. Photocatalytic Degradation of GenX in Water Using a New Adsorptive Photocatalyst

GenX, the ammonium salt of hexafluoropropylene oxide dimer acid, has been used as a replacement for perfluorooctanoic acid. In this study, we developed an adsorptive photocatalyst by depositing a small amount (3 wt.%) of bismuth (Bi) onto activated-carbon supported titanate nanotubes, Bi/TNTs@AC, and tested the material for adsorption and subsequent *solid-phase* photodegradation of GenX. Bi/TNTs@AC at 1 g/L was able to adsorb GenX (100 µg/L, pH 7.0) within 1 h, and then degrade 70.0% and mineralize 42.7% of pre-sorbed GenX under UV (254 nm) in 4 h. The efficient degradation also regenerated the material, allowing for repeated uses without chemical regeneration. Material characterizations revealed that the active components of Bi/TNTs@AC included activated carbon, anatase, and Bi nanoparticles with a metallic Bi core and an amorphous $Bi_2O_3$ shell. Electron paramagnetic resonance spin-trapping, UV-vis diffuse reflectance spectrometry, and photoluminescence analyses indicated the superior photoactivity of Bi/TNTs@AC was attributed to enhanced light harvesting and generation of charge carriers due to the UV-induced surface plasmon resonance effect, which was enabled by the metallic Bi nanoparticles. $^{\bullet}OH$ radicals and photogenerated holes ($h^+$) were responsible for degradation of GenX. Based on the analysis of degradation byproducts and density functional theory calculations, photocatalytic degradation of GenX started with cleavage of the carboxyl group and/or ether group by $^{\bullet}OH$, $h^+$, and/or $e_{aq}^-$, and the resulting intermediates were transformed into shorter-chain fluorochemicals following the stepwise defluorination mechanism. Bi/TNTs@AC holds the potential for more cost-effective degradation of GenX and other per- and polyfluorinated alkyl substances.

## 5.1. Introduction

The health concerns prompted manufacturers in Europe and North America to replace PFOA and PFOS with shorter-chain PFAS in the early 2000s (Sunderland et al. 2019). The most notable substitute is the chemical known as GenX, which is also known as hexafluoropropylene oxide dimer acid (HFPO-DA) or perfluoro-2-propoxypropanoic acid (PFPrOPrA). GenX was introduced in 2009 by DuPont de Nemours, Inc. In addition, from 2003 on, 3M Company replaced PFOS with perfluorobutanesulfonate (PFBS) in several of its major products (Christensen et al. 2019).

GenX has been widely detected in rivers impacted by fluorochemical plants in the Netherlands, Germany, China, and United States, with the highest concentrations at 812, 86.1, 3100, and 4500 ng/L, respectively (Brandsma et al. 2019; Gebbink et al. 2017; Heydebreck et al. 2015; Sun et al. 2016). The GenX concentrations in these drinking water sources far exceeded the US EPA's lifetime health advisory level of 70 ng/L for the sum of PFOA and PFOS in drinking water (EPA 2016a; b). A recent study reported that GenX was detected in 659 out of 837 private wells surrounding a fluorochemical manufacturing facility in North Carolina, with the maximum GenX concentration reaching 4000 ng/L, and GenX in 207 wells exceeded the State's provisional drinking water health goal of 140 ng/L ((North Carolina Department of Environmental Quality DEQ 2018).

Bismuth-based photocatalysts have been found effective for degrading persistent organic pollutants (POPs), including PFAS (Dong et al. 2015; Weng et al. 2013). Song et al. (2017) reported that BiOCl nanosheets were able to defluorinate 59.3% of PFOA after 12 h of UV irradiation, and the degradation rate was 1.7 and 14.6 times faster than that of commercial $In_2O_3$ and $TiO_2$, respectively. Yang et al. (2021) prepared $Bi_5O_7I/ZnO$ heterojunction microspheres and found the material degraded 91% of PFOA after 6 h of visible light irradiation owing to

heterojunction structures formed upon calcination at 400 °C, which also extended the photo-response to the visible light region and increased the separation efficiency of $e^-/h^+$ pairs.

Metallic Bi can also act as an excellent cocatalyst to facilitate charge-carrier separation of $Bi^{3+}$-based photocatalysts (Dong et al. 2014a; Dong et al. 2015), although its role has not been explored for photocatalytic degradation of PFAS. Dong et al. (2015) investigated a semimetal–organic $Bi–g-C_3N_4$ nanohybrid, which showed some unique visible light photocatalytic properties when used for NO removal. The superior photoactivity was ascribed to the surface plasmonic resonance (SPR) endowed by Bi metal to enhance visible light harvesting and charge separation. While these works have revealed the potential of $Bi^0$-$Bi^{3+}$-based photocatalysts, especially the SPR-enhanced photocatalytic activity, these materials have not been explored for treatment of PFAS.

The overall goal of this study was to develop and test an adsorptive photocatalyst, Bi/TNTs@AC, for enhanced adsorption and subsequent degradation of GenX in water. The specific objectives were to (1) synthesize the desired catalyst through a two-step hydrothermal-calcination method, (2) measure the adsorption kinetics and capacity of Bi/TNTs@AC for GenX, (3) evaluate the material stability and reusability, and (4) elucidate the reaction pathway and the underlying mechanisms for the enhanced photocatalytic activity through detailed material characterization and density functional theory (DFT) calculations.

## 5.2. Materials and Methods

### 5.2.1. Chemicals and materials

Nano-$TiO_2$ (Degussa P25) (Evonik, Germany) consisted of anatase (80 wt.%) and rutile (20 wt.%). Filtrosorb-400® granular activated carbon (F-400 GAC) was purchased from Calgon Carbon Corporation (Pennsylvania, USA). Bismuth nitrate pentahydrate ($Bi(NO_3)_3·5H_2O$) (purity

≥ 98%), sodium hydroxide (NaOH) (≥97%), methanol (CH₃OH) (≥99.8%), isopropyl alcohol (ISA) (70%), benzoquinone (BQ) (99%), sodium azide (NaN₃) (≥99.7%), ethylenediaminetetraacetic disodium salt (EDTA) (99%), and GenX in the form of undecafluoro-2-methyl-3-oxahexanoic acid (97%) were acquired from VWR International (Radnor, PA, USA). **Table 5-1** of the Supplementary Material (SM) presents the salient properties of GenX. Analytical standards of HFPO-DA and its mass labeled compound, 2,3,3,3-tetrafluoro-2-(1,1,2,2,3,3,3-hetafluoropropoxy)-$^{13}$C₃-propanoic acid (M3HFPO-DA), which was used as an internal standard (IS), were purchased from Wellington Laboratories Inc. (Guelph, Ontario, Canada). All solutions were prepared using deionized (DI) water (18.2 MΩ-cm).

**Table 5-1.** Key properties of GenX.

| Molecular Formula | $C_6F_{11}O_3^-$ | 2-D structure |
|---|---|---|
| **Molecular Weight (g/mol)** | 329.04 | |
| **Synonyms** | 2,3,3,3-Tetrafluoro-2-(1,1,2,2,3,3,3-hetafluoropropoxy)propanoic acid<br>FRE-903<br>H-28307<br>C3-dimer (acid)<br>GenX Acid |  |
| **p$K_a$** | 2.84 (20 ˚C)(USEPA. 2018) | |
| **p$K_b$** | 8.1 (USEPA. 2018) | 3-D structure |
| **Boiling Point** | 129 ˚C (USEPA. 2018) |  |
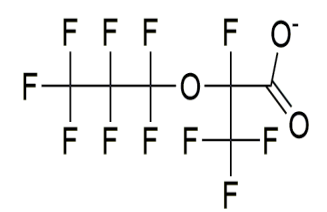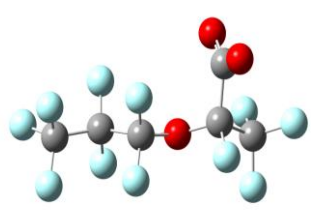
### 5.2.2. Preparation of Bi/TNTs@AC

First, TNTs@AC was synthesized through a modified, one-step, hydrothermal method (Liu et al. 2016; Ma et al. 2017). Typically, 1.2 g of GAC and 1.2 g of $TiO_2$ were added to 66.7 mL of a 10 M NaOH solution and stirred for 12 h. The mixture was transferred into a 100-mL Teflon reactor enclosed in a stainless-steel cup and heated in an oven at 130 °C for 72 h. Two distinct layers were observed after gravity settling for 1 h. The upper layer was removed, whereas the bottom black precipitate (TNTs@AC) was washed with DI water until the water pH reached 7.0 ± 0.5, and then oven-dried at 105 °C for 8 h. Upon proper grinding and sieving, the particles in the size range of 150–425 µm were used in the subsequent experiments. No fluorine or fluoride was detected in the resulting material.

Furthermore, 1 g of the prepared TNTs@AC was dispersed in 80 mL DI water. Separately, 1.16 g $Bi(NO_3)_3·5H_2O$ (5 g/L as Bi) was dissolved in a solution consisting of 20 mL of concentrated $HNO_3$ and 80 mL of DI water. Then, a known volume (*i.e.*, 2, 4, 6, 8, and 10 mL) of the $Bi(NO_3)_3·5H_2O$ solution was added dropwise into the TNTs@AC suspension. The mixtures were equilibrated under stirring for 3 h, at which nearly all $Bi^{3+}$ was adsorbed on TNT ($Ti-O^-$). Upon separation of the solids, the supernatant was analyzed for residual Ti and Bi. In all cases, <0.01% of Ti and <0.01% of Bi were detected in the supernatant. The Bi-loaded TNTs@AC was dried at 105 °C for 8 h, and the resulting particles were calcined at 550 °C for 3.5 h in a nitrogen atmosphere with a temperature ramp of 10 °C/min and a nitrogen flow of 2.5 L/min. The mass ratio of Bi to TNTs@AC was controlled at 1, 2, 3, 4, and 5 wt.%, and the corresponding composites were denoted as 1%Bi/TNTs@AC, 2%Bi/TNTs@AC, 3%Bi/TNTs@AC, 4%Bi/TNTs@AC, and 5%Bi/TNTs@AC, respectively. To inform the performance of the composite materials, treated AC, TNTs@AC, and 3%Bi/TNTs were also prepared via the same procedure.

### 5.2.3. Material characterization

The properties of the crystal phases were analyzed using a Bruker D2 Phaser X-ray diffractometer (XRD) (Bruker AXS, Germany) with Cu Kα radiation (λ, 1.5418 Å). The surface morphology and elemental composition were examined by scanning electron microscopy (SEM, SU8010, Hitachi, Japan) equipped with energy-dispersive X-ray spectroscopy (EDS). The microstructural characteristics were analyzed by high-resolution transmission electron microscopy (HRTEM, JEOL, JEM-2100F, Japan). The elemental compositions and oxidation states were determined via X-ray photoelectron spectroscopy (XPS, Thermo Scientific K-Alpha, UK) with AI $K\alpha$ X-Ray Irradiation at 15 kV and 15 mA. The standard C1s peak (binding energy, 284.80 eV) was used to calibrate the XPS peaks and eliminate static charge effects. An etching technique was used to analyze the depth profile using a monoatomic Ar ion gun (energy: 1000 eV; raster size: 1 × 1 mm). The etching depths were 50 and 150 nm for the XPS analyses, corresponding to an etching time of 250.4 s and 751.2 s, respectively. The $N_2$ Brunauer-Emmett-Teller (BET) specific surface area (SSA) and pore volume of the materials were analyzed through the nitrogen adsorption-desorption procedure (Micromeritics ASAP 2460, USA). The pore size distribution was obtained following the Barret-Joyner-Halender (BJH) method. Zeta potential was determined by a Nano-ZS90 Zetasizer (Malvern Instruments, UK). The electronic properties were measured through the electron paramagnetic resonance (EPR) method using a Bruker EMXPLUS spectrometer. The photoluminescence (PL) spectra were obtained from an FLS1000 photoluminescence spectrometer (Edinburgh Instruments, UK) equipped with a xenon source at an excitation wavelength of 254 nm. The UV-vis diffuse reflectance spectrometry (UV-DRS) analysis was performed on a Shimadzu UV-3600i Plus spectrophotometer.

### 5.2.4. Adsorption kinetic and isotherm tests

Adsorption kinetic experiments were conducted in 45-mL high-density polypropylene (HDPE) vials. To facilitate the chemical analysis and evaluation of material effectiveness, the experimental solutions were prepared with an initial GenX concentration of 100 µg/L. The adsorption was initiated by adding 0.04 g Bi/TNTs@AC to 40 mL of a 100 µg/L GenX solution with an initial pH of 7.0 ± 0.1. The vials were placed on a rotator (70 rpm) at 25 °C in the dark. Duplicate vials were sacrificially sampled at predetermined times. Upon filtering through a 0.22-µm polyether sulfone (PES) membrane, the filtrates were analyzed for GenX remaining.

Adsorption isotherms were measured in a similar manner, but the mixtures were equilibrated for 24 h to ensure equilibrium. The initial GenX concentration was varied (*i.e.*, 0.1, 0.4, 1, 3, 5, 20, 50, 80, 100 mg/L), while the dosage of Bi/TNTs@AC was kept at 1 g/L. For comparison, the kinetic and equilibrium isotherm tests were also carried out with treated AC and TNTs@AC following the same experimental protocols. Note, no Bi was detected in the supernatant during the kinetics and isotherm experiments.

### 5.2.5 Photodegradation of pre-sorbed GenX

The photocatalytic degradation experiments were carried out in a Rayonet RPR-100 UV-reactor (Southern New England Ultraviolet CO., Branford, CT, USA) equipped with 16 RPR-2537 Å lamps. The system was fan-cooled and maintained at a temperature of ~35 °C. Following the adsorption equilibrium, the GenX-laden Bi/TNTs@AC was separated by gravity settling for 1 h (>99% settled). Subsequently, ~95% of the supernatant was removed, and the remaining solid-liquid mixture was transferred into a quartz tray (ODxH = 6x1.5 cm) with a quartz cover. Then, 8 mL DI water was added to the mixture to achieve a total solution volume of 10 mL. The mixture was placed at the center of the photoreactor chamber. The light intensity was 210 W/m$^2$ at the edge

(1.5 in or 3.81 cm to the nearest lamp) of the quartz tray and 128 W/m$^2$ at the center. At predetermined times (*i.e.*, 1, 2, 3, and 4 h), the mixtures were sacrificially filtered through a 0.22-µm PES membrane (>99% GenX recovery), and the filtrates analyzed for GenX and fluoride. To measure the residual solid-phase GenX concentration, the solids were extracted using 20 mL methanol at 80 °C for 4 h in a water bath. After centrifugation at 2500 rpm for 5 min, the supernatant was transferred to a clean vial, and then the solids were extracted with another 20 mL of methanol under the same conditions. The extractants were then combined and analyzed for GenX. The total GenX recovery was >95%, and thus no surrogate IS was used during the extraction. No fluoride was detected when the solids were washed with 20 mL of a 1 M NaOH solution.

The effect of catalyst dosage on the photodegradation effectiveness were carried out following the same experimental protocol, but the material dosage was varied from 1 to 5 g/L.

### 5.2.6. pH effect

To evaluate effect of solution pH on the adsorption process, experiments were conducted with 3%Bi/TNTs@AC (the best performing material) at a dose of 1 g/L and an initial GenX concentration of 100 µg/L. The equilibrium solution pH was 3.5 ± 0.1, 5.0 ± 0.1, 7.0 ± 0.1, 8.5 ± 0.1, and 10.0 ± 0.1. To determine the impact of pH on GenX photodegradation, the pH in the adsorption stage was set at 7.0 ± 0.1 (material dosage = 2 g/L, initial GenX = 100 µg/L), while the pH during the photodegradation was varied from 3.5 ± 0.1 to 10.0 ± 0.1.

### 5.2.7. Material stability and reusability

3%Bi/TNTs@AC was subjected to five consecutive cycles of adsorption and photodegradation. The same experimental protocols for the adsorption and the subsequent

photodegradation were followed, and leaching of Bi and Ti into the aqueous phase was analyzed after each cycle.

**5.2.8. Roles of UV-induced reactive species**

The contribution of common UV-induced reactive species to the photocatalytic degradation of GenX was assessed using various scavengers. In particular, EDTA, ISA, BQ, and NaN$_3$ were added to experimental mixtures to quench photogenerated holes ($h^+$), hydroxyl radicals ($^\bullet$OH), superoxide radicals ($O_2^{\bullet-}$), and singlet oxygen ($^1O_2$), respectively. The same experimental procedures were followed for the adsorption and photodegradation tests except one of the scavengers was present during the photodegradation at various concentrations (0.5, 1.0, 5.0, and 10.0 mmol/L). The use of the molarity units was to facilitate cross-comparison among the scavengers and with literature data for other materials.

**5.2.9. Density functional theory calculations**

The Fukui functions, which are based on the density functional theory (DFT), were employed to predict the attack sites in GenX for different radicals using the Gaussian 16 C.01 package (Ji et al. 2020). The geometry optimization and single-point energy calculations were carried out via the B3LYP method with the 6-31+G(d,p) basis set. The Fukui function based on the density functional theory (DFT) was used to predict the regioselectivity of radicals ($h^+$, $^\bullet$OH) acting on GenX. All of the calculations were performed using the Gaussian 16 C.01 software (Frisch et al. 2003). The geometry optimization and single-point energy calculations were carried out following the B3LYP method with the 6-31+G(d,p) basis set. Fukui function is an important concept in the conceptual density functional theory (CDFT), and it has been widely used in the prediction of reactive sites of electrophilic, nucleophilic, and general radical attacks (Parr and Yang 1984). Specifically, Fukui function is defined as:

$$f(r) = \left[\frac{\partial \rho(r)}{\partial N}\right]_{V(r)} \tag{1}$$

where $\rho(r)$ is the electron density at a point r in space, N is the electron number in the system, and the constant term $v$ in the partial derivative is the external potential. In the condensed version of the Fukui function, the atomic population number was used to represent the electron density distribution around an atom. The condensed Fukui function was calculated as follows:

Electrophilic attack: $\qquad\qquad f_A^- = q_{N-1}^A - q_N^A$ $\qquad\qquad$ (2)

Nucleophilic attack: $\qquad\qquad f_A^+ = q_N^A - q_{N+1}^A$ $\qquad\qquad$ (3)

Radical attack: $\qquad\qquad f_A^0 = \frac{q_{N-1}^A - q_{N+1}^A}{2}$ $\qquad\qquad$ (4)

where $q^A$ is the charge of atom A at the corresponding state. The more reactive sites on a molecule usually have larger values of the Fukui index. $h^+$, $^\bullet OH$, and $O_2^{\bullet-}$ have been classified as electrophilic, which are more likely to attack the sites that can readily lose electrons (De Vleeschouwer et al. 2007). Thus, we calculated the Fukui index of GenX for electrophilic attacks. The natural population analysis (NPA) was used to study the reactive sites, as it has been considered one of the most suitable methods to calculate the Fukui index (Oláh et al. 2002). A color gradient for a set of Fukui values was generated using the conditional formatting tool in Microsoft Excel 2019.

### 5.2.10. Chemical analysis

Aqueous-phase GenX concentrations were analyzed by a Vanquish Flex Binary UPLC system (Thermo Fisher, USA) coupled with a quadrupole-Orbitrap mass spectrometer (Orbitrap

Exploris TM120, Thermo Fisher) using the negative mode electrospray ionization (ESI). A delay column was placed between the pump and autosampler (HypersilGOLD, 1.9 µm, 175 Å, 3 × 50 mm). M3HFPO-DA (20 µg/L) was used as the IS for the analysis. The limit of detection for GenX was 0.5 µg/L. GenX and two potential transformation products, trifluoroacetic acid (TFA) and pentafluoropropionic acid (PFA), were further confirmed by an UltiMate 3000 LC coupled to a Thermo TSQ Quantum Access Max triple quadrupole tandem mass spectrometer. Fluoride was analyzed by ion chromatography (Dionex, CA, USA) equipped with an anion-exchange column (Dionex Ionpac AS22) and an anion dynamically regenerated suppressor (ADRS 600, 4mm). The detection limit was $10.00 \pm 0.01$ µg/L. Dissolved Bi and Ti were measured by inductively coupled plasma-optical emission spectroscopy (ICP-OES, 710-ES, Varian, USA), with a detection limit of 100 µg/L and 50 µg/L, respectively.

### 5.2.11. GenX analysis with LC-MS/MS

GenX analysis was performed on a Vanquish Flex Binary UHPLC system (Thermo Fisher) coupled with a quadrupole orbitrap mass spectrometer (Orbitrap Exploris TM120, Thermo Fisher) with electrospray ionization (ESI) in the negative mode and using the Xcalibur software (V4.4.16.14). A delay column was placed between the pump and autosampler (HypersilGOLD, 1.9 µm, 175 Å, 3 x 50 mm) and the system was enabled for PFAS analysis. Typically, 10 µL of the standard or sample was injected into a C18 column (Luna C18(2), 3 µm, 100 Å, 2 × 50 mm with 2 x 4 mm guard cartridge, Phenomenex) with a 200 µL/min flow rate of mobile phase of solution A (2 mM ammonium acetate in water) and solution B (100% acetonitrile) beginning at 15% B for the first 0.3 minute to 95% B at 9 min, held at 95% B for 2 min, back to 15%B in 1 min, and re-equilibration, resulting a total run time of 15 min. The MS scan range was 100-800 m/z with a resolution of 120,000, standard AGC target, 70% RF lens, maximum injection time auto,

with EASY-IC run-start on. The negative spray voltage was 2500 V, ion transfer tube temperature was 320 °C, and the vaporizer temperature was 275 °C. The C5F11O in source fragment with m/z 284.9779±0.02 and 12C313C2F11O fragment with m/z 286.9846±0.02 were used for quantitation. M3HFPO-DA was used for quantitation analysis M3HFPO-DA (20 µg/L) as internal standard.

The calibration of the system was performed each time of analysis using at least five GenX standards in the linear concentration range of 1 to 90 µg/L. The relative standard deviation (%RSD) of the response factors (RFs) for all analysts must be within ± 20% or the linear regression $R^2$ must be ≥0.99, based on the initial calibration (ICAL) criteria and their true values. The second source standard was used after the ICAL for the initial calibration verification. The analyte concentrations were within ± 30% of their true value. After 10 samples or at the end of the sequence, two consecutive calibration verification standards were analyzed before next sample analysis with analyte concentrations within ± 30% of their true values from the Limit of Quantitation (LOQ) (0.5 µg/L) to the mid-level calibration concentration.

GenX and its photodegradation products, trifluoroacetic acid (TFA) and pentafluoropropionic acid (PFA), were further confirmed by an UltiMate 3000 LC coupled to a Thermo TSQ Quantum Access Max triple quadrupole tandem mass spectrometer. LC separation of GenX, TFA, and PFA was achieved with a Waters XBridge C18 column (2.1×150 mm, 2.5 µm) and a guard column (2.1×10 mm, 3.0 µm) containing the same material. The mobile phase was comprised of (A) LC-MS grade water with 10 mM ammonium acetate (pH 6.9) and (B) methanol with 10 mM ammonium acetate. The mobile phase flow rate was set to 200 µL/min under an isocratic elution with 40% A and 60% B. The column compartment was maintained at 40 °C. The overall method run time was 6 minutes, and 50 µL of sample was injected. The negative ESI mode was applied to GenX, TFA, and PFA. The spray voltage was 2500 V, capillary temperature was 350 °C, vaporizer

temperature was 300 °C, sheath gas pressure was 35 (arbitrary units, nitrogen), auxiliary gas

pressure was 10 (arbitrary units, nitrogen), and collision-induced dissociation pressure was 1.5

mTorr (argon). The precursor ion and at least one characteristic product ion were identified for

each analyte. The optimized detector parameters and ion transitions are summarized in **Table 5-2**.

**Table 5-2.** LC-MS/MS operating parameters and instrument performance.

| Analyte | Ion or Ion transition [a] | Collision energy (V) | Linear range (µg/L) | $R^2$ | LOD [b] (µg/L) |
|---|---|---|---|---|---|
| *LC-MS/MS (orbitrap)* | | | | | |
| GenX | **284.9779 ± 0.02** | - | 1 – 90 | > 0.99 | 0.5 |
| M3HFPO-DA | **286.9846 ± 0.02** | - | - | - | - |
| *LC-MS/MS (tandem)* | | | | | |
| GenX | **284.9 → 168.9** *328.9 → 284.9* | -8 -5 | 1 – 50 | > 0.99 | 0.1 |
| M3HFPO-DA | **286.9 → 168.9** *331.9 → 286.9* | -8 -5 | - | - | - |
| PFA | - *162.9 → 118.9* | -10 | - | - | - |
| TFA | - *112.9 → 68.9* | -10 | - | - | - |

a: the first product ion (**bold**) was used for quantitation, and the second product ion (*italics*) was used for confirmation if available
b: limit of detection

## 5.3. Results and discussion

### 5.3.1. Material phases and chemical composition

**Figure 5-1a** shows the XRD patterns of calcined TNTs@AC and Bi/TNTs@AC loaded with 1-5 wt.% Bi. For TNTs@AC, the diffraction peaks at 10.5°, 24.4°, 28.4°, and 47.8° are assigned to sodium tri-titanate with a chemical formula of $Na_xH_{2-x}Ti_3O_7$ ($x$ depends on the sodium content) (Wang et al. 2018). The basic skeleton of tri-titanate was composed of edge-sharing triple $[TiO_6]$ octahedrons with $Na^+$ and $H^+$ attached at the interlayers as exchangeable counter ions (Ma et al. 2017). The intensity of the diffraction peaks of TNTs@AC were notably decreased compared to those of uncalcined TNTs@AC and uncalcined 3%Bi/TNTs@AC (**Figure 5-1b**), which can be attributed to breakage of the tubular and layered structures during calcination (Razali et al. 2012), partial collapse of polymerized Ti species (Ti-O-Ti species), and/or decrease in isolated Ti species with higher coordination numbers (Yang and Li 2002). Moreover, the XRD diffraction pattern for calcined TNTs@AC showed a red shift compared to that of uncalcined TNTs@AC (*e.g.*, from ~9.8° to 10.5°) (**Figure 5-1b**), indicating a decrease in interlayer distance due to the release of water molecules (Qamar et al. 2008). Compared to calcined TNTs@AC and uncalcined Bi/TNTs@AC, the XRD patterns for calcined Bi/TNTs@AC with different Bi contents displayed five characteristic peaks with $2\theta$ values of 25.3º, 37.8º, 48.1º, 54.2º, and 62.2º corresponding to the (101), (004), (200), (211), and (213) planes of tetragonal anatase (JCPDS-ICDD No. 21-1272), respectively. This result indicates that sodium tri-titanate was transformed into anatase due to Bi doping and calcination. The adsorption of $Bi^{3+}$ ions on TNTs@AC partially replaced $Na^+$ ions, which is conducive to the formation of anatase upon calcination (Cai et al. 2017). In addition, for Bi/TNTs@AC (**Figure 5-1a**), the characteristic peaks at 22.5º, 27.2º, 39.6º, 44.6º, 46.0º, 48.7º, 64.5º, and 70.8º confirmed the existence of the rhombohedral phase of metallic Bi (JCPDS-ICDD

No. 44-1246). In contrast, no evidence of metallic Bi peaks was observed for uncalcined Bi/TNTs@AC (**Figure 5-1b**), indicating that the calcination facilitated the reduction of $Bi^{3+}$ into $Bi^0$. The XPS analysis confirmed that $Bi^{3+}$ on TNTs@AC was reduced into $Bi^0$ with AC as the electron donor at 550 ºC.

**Figure 5-1a** also indicates that increasing the Bi content from 1 wt.% to 3 wt.% enhanced the peak intensities of Bi, whereas further increasing Bi to 4 and 5 wt.% resulted in a lower Bi intensity. Accordingly, 3%Bi/TNTs@AC demonstrated the highest GenX defluorination efficiency (**Section 5.3.4**) and was, therefore, selected for further testing.

XPS spectra were obtained to examine the chemical composition of Bi/TNTs@AC and TNTs@AC. The scans were performed in two ways, one on the pristine material surface and the other after Ar-ion etching at depths of 50 and 150 nm. **Figure 5-2a** confirms the presence of Ti, C, Na, O, and Bi on the 3%Bi/TNTs@AC surface. For the spectra of Bi 4f without etching (**Figure 5-2b**), the peaks centered at 164.0 and 158.7 eV are characteristic of $Bi^{3+}$ in bismuth oxides and are ascribed to Bi $4f_{5/2}$ and Bi $4f_{7/2}$, respectively (Lan et al. 2020). In conjunction with the XRD results, which showed no crystalline $Bi_2O_3$ on Bi/TNTs@AC, the $Bi_2O_3$ identified by XPS was amorphous.

The two Bi 4f peaks in **Figure 5-2b** shifted from 164.0/158.7 eV to lower binding energies of 163.9/158.6 eV with 50 nm etching and 163.6/158.4 eV with 150 nm etching. These results can be attributed to the partial reduction of $Bi^{3-x}$ species (Liu et al. 2017). Two additional peaks were present at 161.6 and 156.3 eV after the 50 nm etching , and these peaks were attributed to Bi-Bi bonds and confirmed the presence of metallic Bi in the composite (Yang et al. 2020). The Bi-Bi peak intensity was stronger for the 150 nm etching, suggesting that more metallic Bi was present

in the particle core. Namely, the Bi particles consisted of a metallic Bi core and a thin amorphous $Bi_2O_3$ shell on the surface of Bi/TNTs@AC.

The binding energies were corrected by the C 1s levels at 284.8 eV as a reference. The C 1s spectra (**Figure 5-2c**) measured at the surface of the pristine sample can be deconvoluted into three peaks corresponding to C-O (286.0 eV), C=O (287.2 eV), and O-C=O (289.6 eV) bonds, which were also present after the 150 nm etching with the exception of O-C=O bonds (Gopiraman et al. 2017). After the 50 nm etching, the oxygenated carbon groups disappeared, and two additional peaks occurred at 284.6 eV and 286.6 eV. The peak at 284.6 eV highlights the existence of C-C groups (Wang et al. 2020), whereas the peak at 286.6 eV was attributed to carbonyl or quinine groups (Ma et al. 2015). In addition, the O 1s XPS spectra (**Figure 5-2d**) highlighted the presence of Bi-O bonds at 529.7 eV and the regular lattice oxygen (Ti-O-Ti) at 531.3 eV (Almeida et al. 1998; Dong et al. 2015). The peaks at 458.2 eV and 464.0 eV in **Figure 5-2e** belong to Ti $2p_{3/2}$ and Ti $2p_{1/2}$, respectively, which are characteristic of $Ti^{4+}$ (Li et al. 2020b).



(a)                                                    (b)
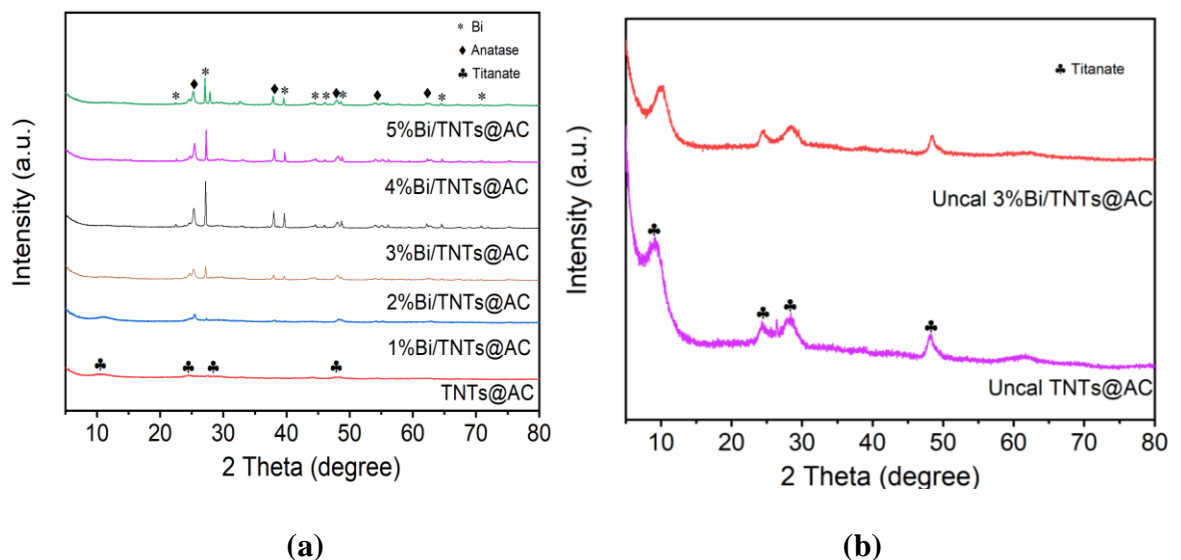
**Figure 5-1.** XRD patterns of **(a)** TNTs@AC and Bi/TNTs@AC prepared with 1-5 wt.% Bi and **(b)** of uncalcined TNTs@AC and uncalcined 3%Bi/TNTs@AC.
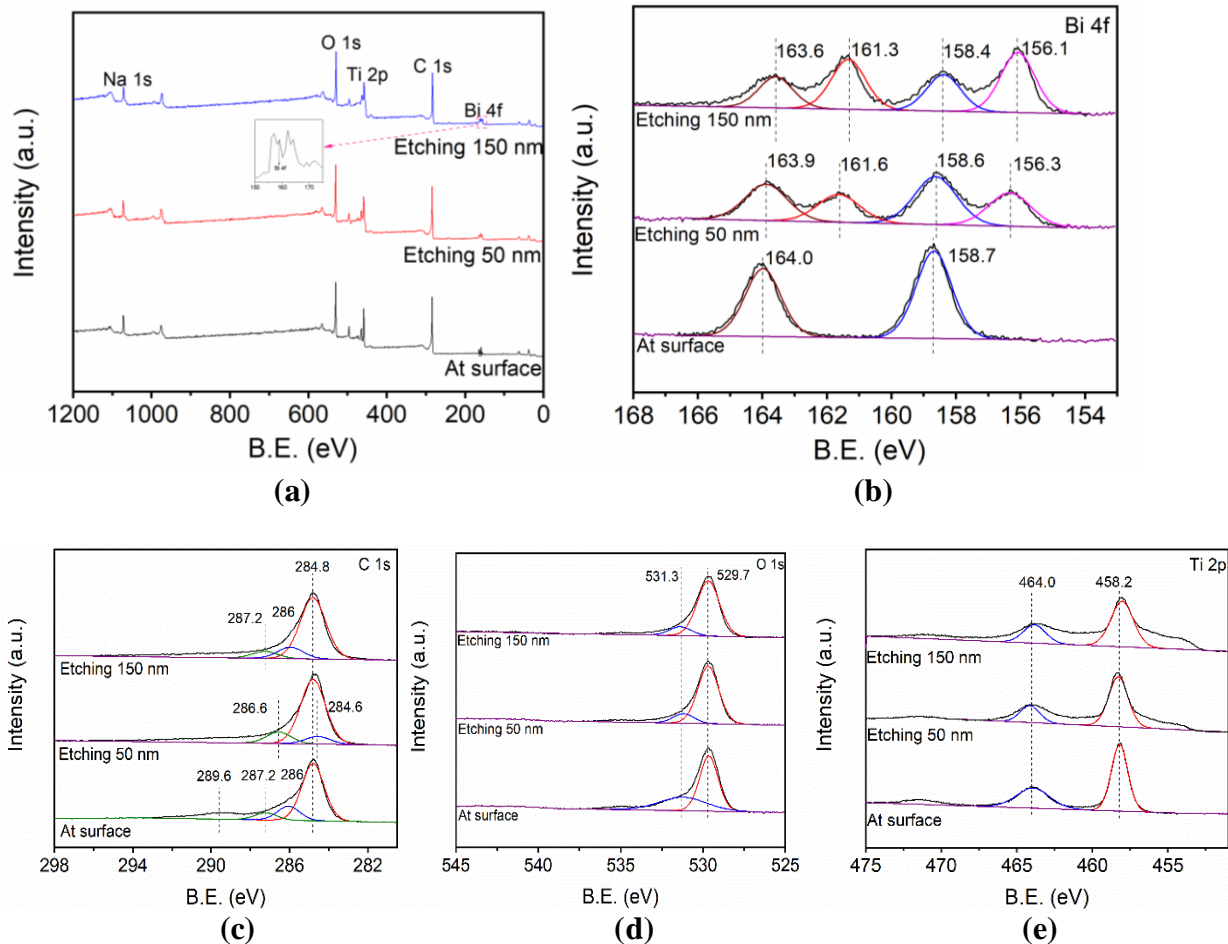
**Figure 5-2.** **(a)** XPS survey spectra and high-resolution XPS spectra of **(b)** Bi 4f, **(c)** C 1s, **(d)** O 1s and **(e)** Ti 2p for 3%Bi/TNTs@AC at the surface before and after etching. 3%Bi/TNTs@AC were calcined at 550 °C in all cases.

### 5.3.2. Morphological characterization

**Figures 5-3a** and **3b** show the SEM images of 3%Bi/TNTs@AC calcined at 550 °C, where the surface displayed a flower-like structure with interwoven TNTs grafted on the AC petals. Micro- or nano-AC particles were attached to well-defined TNTs (**Figures 5-4a** and **Figure 5-3b**). This observation indicates that the hydrothermal treatment under alkaline conditions not only converted $TiO_2$ into TNTs, but also altered the structure of the AC, resulting in mutual

modification of AC and TNTs. The EDS mapping (**Figures 5-3c** and **5-3d**) revealed that five major elements (*i.e.*, C, O, Ti, Na, and Bi) were uniformly distributed on 3%Bi/TNTs@AC, and **Table 5-3** presents the percentile of each element. The high Ti (36.2%), C (19.2%), and Bi (5.2%) contents corroborate the formation of Bi/TNTs@AC.

**Figures 5-4a-c** present the TEM images of 3%Bi/TNTs@AC. **Figure 5-4a** confirms the hybridization of TNTs and AC nanoparticles. The coated carbon particles on TNTs are beneficial and facilitate hydrophobic interactions with GenX and anion-π interactions between GenX and the electron-deficient aromatic skeletons of AC. The interlayer distance of TNTs was 0.75 nm (**Figure 5-4c**), which agrees with the crystal plane (020) of titanate (Wang et al. 2018), whereas the lattice fringe spacing of 0.35 nm (**Figure 5-4b**) conforms to the (101) plane of anatase. Prior work on TNTs@AC showed that no transformation from tri-titanate to anatase would occur upon calcination without a metal dopant (Zhu et al. 2021). This observation suggests that Bi on TNTs facilitated transformation from titanate to anatase, while TNTs retained its nanotube structure with an inner diameter of ~5 nm and an outer diameter of ~12 nm (**Figure 5-4c**). In addition, the lattice spacing (0.328 nm) shown in **Figure 5-4c** corresponds to the (012) lattice plane of metallic Bi (Dong et al. 2015), which is expected to facilitate electron transfer and inhibit recombination of electron-hole pairs (**Section 5.3.4**).

**Table 5-3.** EDS-based distribution of five elements on 3%Bi/TNTs@AC.

| Element | Weight % |
|---------|----------|
| C | 19.2 |
| O | 34.1 |
| Ti | 36.2 |

| | |
|---|---|
| Bi | 5.2 |
| Na | 5.3 |
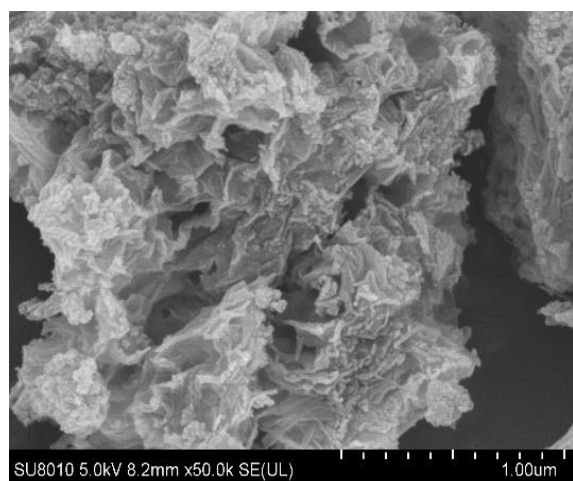


(a)
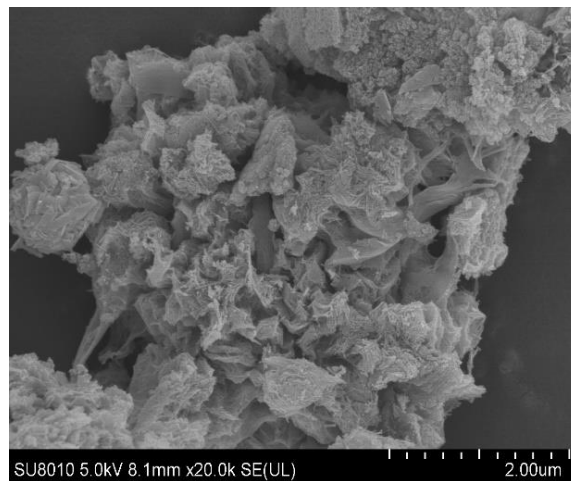
(b)
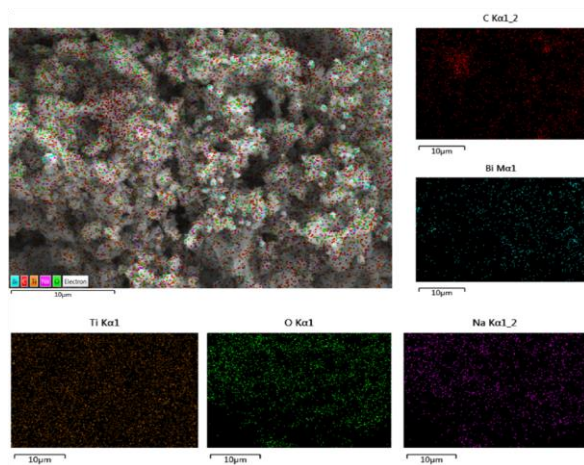
(c)
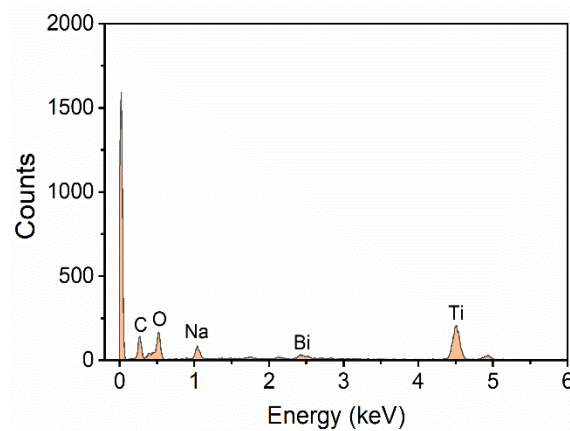
(d)

**Figure 5-3**. (**a, b**) FE-SEM images (scale bars = 1.00 and 2.00 µm, respectively), (**c**) EDS mapping, and (**d**) SEM-EDS spectra of 3%Bi/TNTs@AC.

|          (a)          |          (b)          |          (c)          |
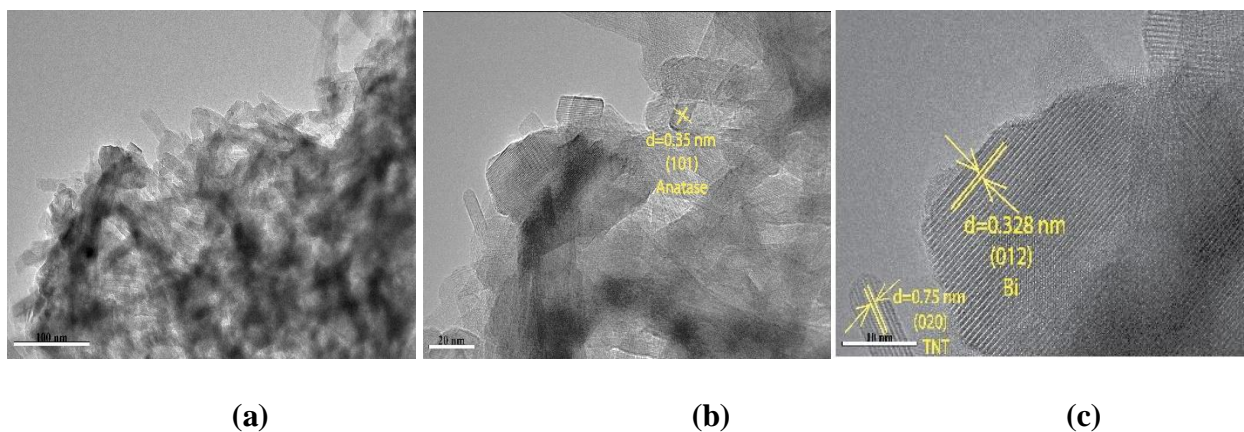
**Figure 5-4.** **(a, b, c)** TEM and HRTEM images of 3%Bi/TNTs@AC calcined at 550 °C. Scale bars are equivalent to 100, 20, and 10 nm, respectively.

**Figure 5-5a** shows the $N_2$ adsorption-desorption isotherms of TNTs@AC and Bi/TNTs@AC with 1-5 wt.% Bi. According to the International Union of Pure and Applied Chemistry (IUPAC) classification system, all isotherms are Type IV and characteristic of mesoporous materials. In the low $P/P_0$ range, the shape of the isotherms conformed to monolayer-multilayer adsorption. Subsequently, the H3 type hysteresis loops appeared at around $P/P_0 = 0.40$, suggesting that another adsorption mechanism, such as capillary condensation, occurred in the nanotubes and/or mesoporous channels (Liu et al. 2016). When the Bi content was increased from 1 to 5 wt.%, the hysteresis loop became larger, which aligns with the capillary condensation mechanism (El-Sheikh et al. 2017). **Figure 5-5b** gives the pore size distribution determined using the BJH method. Except for TNTs@AC and 3%Bi/TNTs@AC, the pore size distributions displayed a bimodal profile with major peaks at 3.7 nm and minor peaks at 8.9-16.0 nm. 3%Bi/TNTs@AC showed the most uniform pore size distribution of the Bi-doped composites. **Table 5-4** summarizes the SSA and pore volume for all materials. The SSA of TNTs@AC was 243.77 m²/g, which is lower than that for the AC by a factor of 2.4, indicating partial blockage of the internal pores (pore volume also decreased by 2.4×) upon the loading of TNTs. When loaded with 1, 2, 3, 4, and 5 wt.% of Bi, the

SSA was increased from 243.77 m$^2$/g for TNTs@AC to 307.50, 279,60, 289.84, 285.26, and 269.78 m$^2$/g, respectively. The increase in SSA stemmed from pore volume increases (**Table 5-4**) resulting from the Bi-mediated phase transformation and restructuring of TNTs and AC (**Figure 5-3**) (Subramaniam et al. 2017). Excessive Bi doping resulted in a slight decrease in SSA due to the increased crystal sizes of anatase and metallic Bi, which partially blocked nanopores (**Table 5-5**) (Zhong et al. 2012). The newly created sites associated with the elevated SSA are expected to not only facilitate GenX adsorption, but also be more photoactive due to the hybridization of Bi, TNTs, and AC.

**Table 5-4.** BET-based specific surface area and pore volume of various composite materials.

| Material | BET surface area[a] (m$^2$/g) | Pore volume[b] (cm$^3$/g) |
|---|---|---|
| AC | 591.38 ± 9.28 | 0.801 |
| TNTs@AC | 243.77 ± 3.77 | 0.330 |
| 1%Bi/TNTs@AC | 307.50 ± 3.75 | 0.462 |
| 2%Bi/TNTs@AC | 279.60 ± 4.60 | 0.347 |
| 3%Bi/TNTs@AC | 289.84 ± 4.48 | 0.463 |
| 4%Bi/TNTs@AC | 285.26 ± 3.48 | 0.554 |
| 5%Bi/TNTs@AC | 269.78 ± 3.89 | 0.408 |

**Notes:** (a) BET surface area was calculated using the BET equation ± relative deviation from the mean; and (b) Pore Volume: total pore volume estimated at a relative pressure of 0.99.

**Table 5-5.** Crystal size and structure for Bi/TNTs@AC prepared at various Bi contents.

| Material | Crystallite size (nm) | Crystal structure (wt.%) |
|---|---|---|
| 1%Bi/TNTs@AC | 10.9 | Anatase (89%) |
| | 2.4 | Metallic Bi (11%) |
| 2%Bi/TNTs@AC | 14.5 | Anatase (69%) |
| | 94.4 | Metallic Bi (31%) |
| 3%Bi/TNTs@AC | 22.8 | Anatase (59%) |
| | >100 | Metallic Bi (41%) |
| 4%Bi/TNTs@AC | 18.7 | Anatase (58%) |
| | >100 | Metallic Bi (42%) |
| 5%Bi/TNTs@AC | 23.1 | Anatase (48%) |
| | >100 | Metallic Bi (52%) |



(a)  (b)
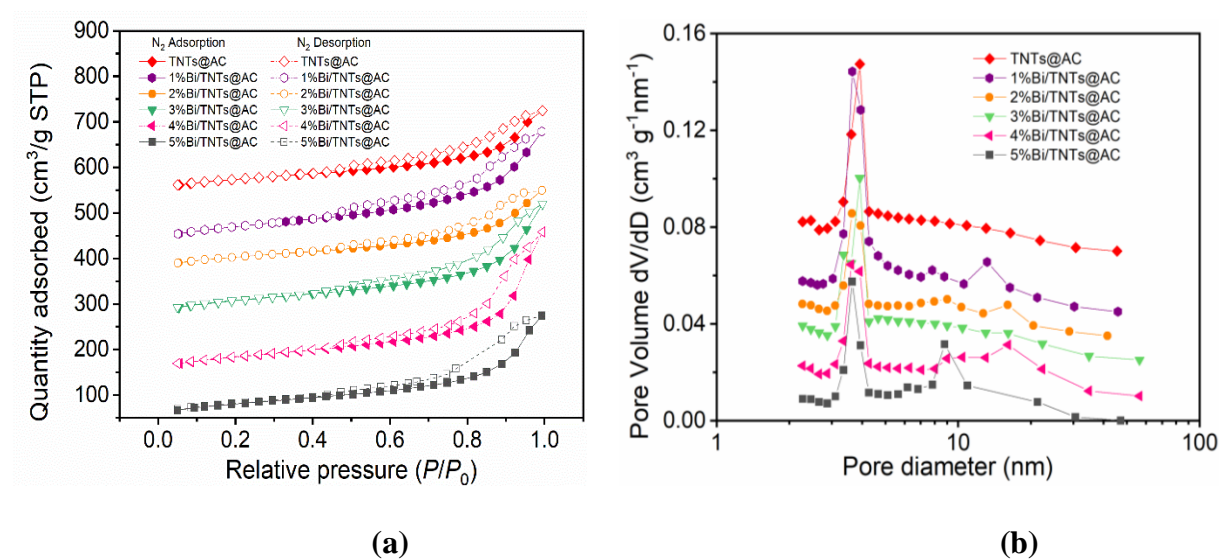
**Figure 5-5. (a)** $N_2$ adsorption-desorption isotherms and **(b)** pore size distributions of TNTs@AC and Bi/TNTs@AC with various Bi contents calcined at 550 °C.

### 5.3.3. GenX adsorption kinetics and isotherms

**Figure 5-6a** compares the GenX adsorption kinetics of 3%Bi/TNTs@AC and its precursor materials, AC and TNTs@AC, which were subjected to the same hydrothermal treatment and calcination process. The rate of GenX adsorption by 3%Bi/TNTs@AC was nearly the same as that of the treated AC on an equal mass basis (40 mg), and >99% of GenX was removed in 1 h with >90% of the removal occurred in the first 10 min. TNTs@AC showed a slower adsorption rate, and equilibrium was not reached until 120 min due to the poor affinity of GenX to the negatively charged TNTs. **Figure 5-6b** shows that when the material dosage was halved to 20 mg, 3%Bi/TNTs@AC displayed clearly faster adsorption rate than the treated AC. The results confirmed that the Bi loading notably improved the adsorption rate of GenX due to (1) suppression of the negative surface potential of TNTs (the $pH_{pzc}$ of TNTs and 3%Bi/TNTs were 2.6 and 6.3, respectively), and (2) Lewis acid-base interactions between Bi and the carboxylate group of GenX.

The pseudo-first-order (Eq. 5) and pseudo-second-order (Eq. 6) kinetic models were utilized to interpret the kinetic data:

$$q_t = q_{e-}q_e \exp(-k_1 t) \tag{5}$$

$$q_t = \frac{k_2 q_e^2 t}{1 + k_2 q_e t} \tag{6}$$

where $q_t$ and $q_e$ (µg/g) are the solid-phase GenX concentrations at time t (min) and equilibrium, respectively, and $k_1$ (min$^{-1}$) and $k_2$ (g/(µg · min)) are the respective rate constants.

**Table 5-6** summarizes the kinetic parameters for both models. The pseudo-second-order model gave a better goodness of fit, as evidence by the $R^2 > 0.99$ for all three materials. However, both models can adequately fit the kinetic data. The different rate constants are in line with the

145

characterization results that the Bi- and TNTs-modifications of the AC, along with the hydrothermal and calcination treatments, altered accessibility of the adsorption sites.

Because GenX concentrations in industrial and contaminated waters can widely vary, detailed isotherms were constructed for AC and 3%Bi/TNTs@AC over a broad range of equilibrium concentrations, namely 0.1-100 mg/L (**Figure 5-6c**). The classical Langmuir (Eq. 7) and Freundlich (Eq. 8) isotherm models were tested to fit the experimental data:

$$q_e = \frac{Q_{max}bC_e}{1+bC_e} \tag{7}$$

$$q_e = K_F C_e^{1/n} \tag{8}$$

where $Q_{max}$ (mg/g) is the Langmuir maximum capacity, b (L/mg) is the Langmuir affinity coefficient, $K_F$ (mg/g·(L/mg)$^{1/n}$) is the Freundlich capacity parameter, and n is the heterogeneity factor related to the presence and distribution of different sorption sites.

**Table 5-7** summarizes the parameters for the models. Based on the coefficients of determination ($R^2$), both models were able to adequately fit the experimental data, though the Freundlich model offered better fitting for AC and TNTs@AC, suggesting a heterogeneous nature in terms of adsorption energy and modes. According to the Langmuir model, the maximum adsorption capacities of GenX on AC, TNTs@AC, and 3%Bi/TNTs@AC were 120.26, 79.96, and 101.77 mg/g, respectively. While the SSA of treated AC was about 2.4 times greater than that of 3%Bi/TNTs@AC, the Langmuir maximum capacity of AC was only ~1.2 times higher. This disproportionality indicates that although the loading of TNTs and Bi on AC resulted in partial loss of the adsorption sites in the core AC, it created a layer of new sites on the AC. The new sites consisted of mixed phases of TNTs, AC particles, and Bi nanoparticles, which enabled a synergized adsorption mechanism and enhanced affinity for GenX. The enhanced affinity of

146

3%Bi/TNTs@AC for GenX can be well revealed when the isotherm data are plotted based on the surface-area-normalized uptake (**Figure 5-6d, Table 5-8**), and **Figure 5-7** shows that the adsorption of GenX by 3%Bi/TNTs@AC was much more favorable in the lower GenX concentration range ($C_e \leq 2$ mg/L) than treated AC and TNTs@AC. The SSA-based $Q_{max}$ values (mg/m$^2$) followed the order of: 3%Bi/TNTs@AC (0.35) > TNTs@AC (0.33) > AC (0.18). Treated AC offered higher GenX uptake only when the GenX concentration is very high ($C_e > 2$ mg/L) (**Figure 5-6c**) due to its much larger SSA (591.38 m$^2$/g). The enhanced performance of 3%Bi/TNTs@AC can be attributed to synergistic adsorptin interactions between anionic GenX and 3%Bi/TNTs@AC (*i.e.,* hydrophobic, Lewis acid-base, and anion-$\pi$ interactions), whereas only hydrophobic interaction was operative for treated AC and TNTs@AC. Thus, the improved affinity of Bi/TNTs@AC for GenX is expected to not only selectively concentrate GenX on the photoactive surface sites, but also facilitate the subsequent solid-phase photocatalytic degradation of GenX.

    **Figure 5-8** shows the measured zeta potential of 3%Bi/TNTs@AC, which exhibited a pH$_{pzc}$ of ~3.8. Hence, in the circumneutral pH range, the adsorption of GenX anions (p$K_a$= 2.8) by 3%Bi/TNTs@AC would not be favorable due to electrostatic repulsion, although the loading of Bi suppressed the surface negative potential (**Figure 5-8**). While the tail group of GenX is not expected to interact with TNTs (pH$_{pzc}$= 2.6), the Bi deposited on the surface of Bi/TNTs@AC may react with GenX through concurrent electrostatic and Lewis acid-base interactions between Bi$^{3+}$ and the hydrophilic head groups ($-COO^-$) of GenX (Khan and Siddiqui 2021; Liu et al. 2015a; Liu et al. 2016), which is in line with the strong adsorption observed at neutral pH. The higher GenX adsorption by 3%Bi/TNTs@AC could also be due to the larger SSA resulting from the mixed phases (**Section 5.3.2**), which enables hydrophobic reactions between the C-F chain of

GenX (except one oxygen atom in the carbon chain) and the AC surface; furthermore, anion-π interactions may also occur between GenX anions and aromatic groups on the AC surface (Xu et al. 2020). The presence of AC and Bi in the composite materials, therefore, enabled cooperative hydrophobic, Lewis acid-base, and anion-π interactions, not only enhanced the adsorption capacity for GenX, but also facilitated a side-on adsorption mode which is conducive to the *in situ* photochemical degradation of pre-adsorbed GenX (Li et al. 2020a).

**Table 5-6.** Kinetic model parameters for adsorption of GenX by treated AC, TNTs@AC, and 3%Bi/TNTs@AC.

| Model | Parameter | Adsorbents | | |
|---|---|---|---|---|
| | | Treated AC | TNTs@AC | 3%Bi/TNTs@AC |
| Pseudo-first-order | $k_1 (\text{min}^{-1})$ | 0.32 | 0.16 | 0.27 |
| | $q_e (\mu g/g)$ | 99.30 | 96.21 | 98.40 |
| | $R^2$ | > 0.99 | 0.98 | 0.99 |
| Pseudo-second-order | $k_2 \times 10^{-3} (\text{g}(\mu g \cdot \text{min})^{-1})$ | 17.82 | 3.46 | 9.20 |
| | $q_e (\mu g/g)$ | 100.33 | 100.47 | 100.46 |
| | $R^2$ | > 0.99 | > 0.99 | > 0.99 |

**Table 5-7.** Best-fitted isotherm model parameters for adsorption of GenX by treated AC, TNTs@AC, and 3%Bi/TNTs@AC.

| Model | Parameter | Adsorbents | | |
|---|---|---|---|---|
| | | Treated AC | TNTs@AC | 3%Bi/TNTs@AC |
| Freundlich model | $K_F$ (mg/g·(L/mg)$^{1/n}$) | 2.88 | 2.00 | 6.38 |
| | n | 0.77 | 1.14 | 1.67 |
| | $R^2$ | 0.988 | 0.997 | 0.973 |
| Langmuir model | $Q_{max}$ (mg/g) | 120.26 | 79.96 | 101.77 |
| | b (L/mg) | 0.007 | 0.028 | 0.033 |
| | $R^2$ | 0.949 | 0.973 | 0.974 |

**Table 5-8.** Isotherm model parameters based on surface-area-normalized uptake of GenX by treated AC, TNTs@AC, and 3%Bi/TNTs@AC.

| Model | Parameter | Material | | |
|---|---|---|---|---|
| | | Treated AC | TNTs@AC | 3%Bi/TNTs@AC |
| Langmuir | $Q_{max}$ (mg/m$^2$) | 0.18 | 0.33 | 0.35 |
| | b (L/mg) | 0.002 | 0.028 | 0.033 |
| | $R^2$ | 0.996 | 0.973 | 0.974 |
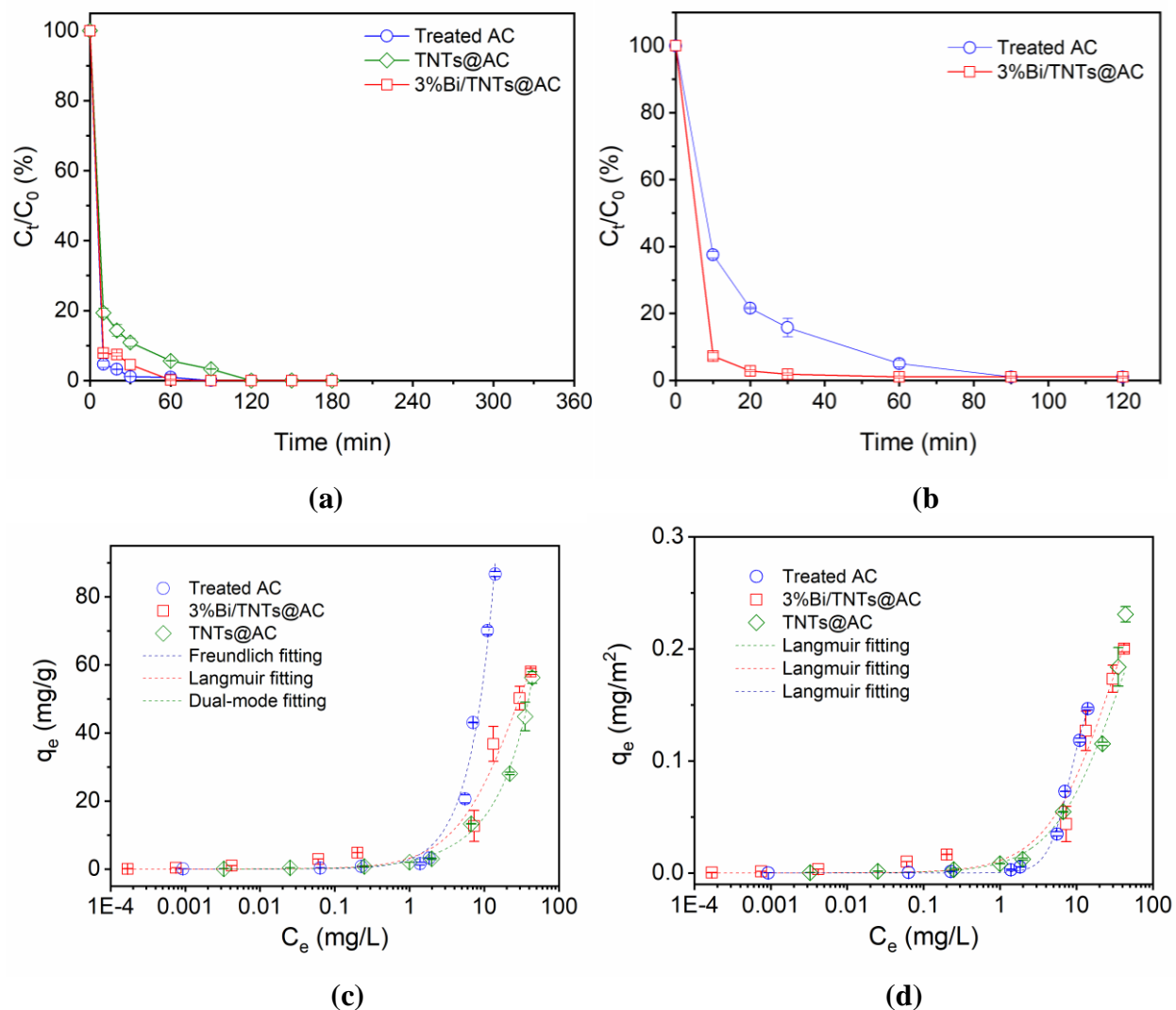
**Figure 5-6.** Adsorption kinetics **(a)** and **(b)** and equilibrium isotherms based on unit-mass uptake **(c)** and unit surface-area uptake **(d)** of GenX by treated AC, TNTs@AC, and 3%Bi/TNTs@AC. Experimental conditions for kinetic tests: initial GenX concentration = 100 µg/L, material dosage = 1 g/L in **(a)** and = 0.5 g/L in **(b)**, pH = 7.0 ± 0.1; Conditions for isotherm experiments: initial GenX concentration = 0.1-100 mg/L, material dosage = 1 g/L, pH = 7.0 ± 0.1. Data are plotted as mean of duplicates with error bars indicating relative deviation from the mean.

150

**(a)**                                                    **(b)**
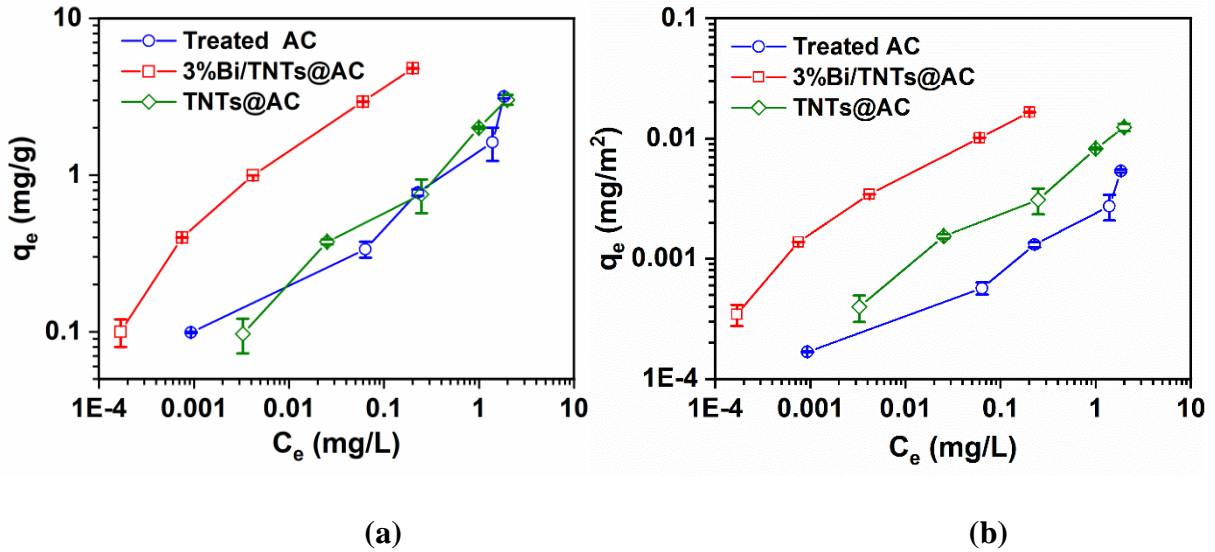
**Figure 5-7.** Adsorption equilibrium isotherms (Ce ≤ 2 mg/L) based on mass uptake **(a)** and unit surface-area uptake **(b)** of GenX by treated AC, TNTs@AC, and 3%Bi/TNTs@AC. Experimental conditions for kinetic tests: initial GenX concentration = 100 µg/L, material dosage = 1 g/L, pH = 7.0 ± 0.1; Conditions for isotherm experiments: initial GenX concentration = 0.1-100 mg/L, material dosage = 1 g/L, pH = 7.0 ± 0.1. Data are plotted as the mean of duplicates with error bars indicating relative deviation from the mean.
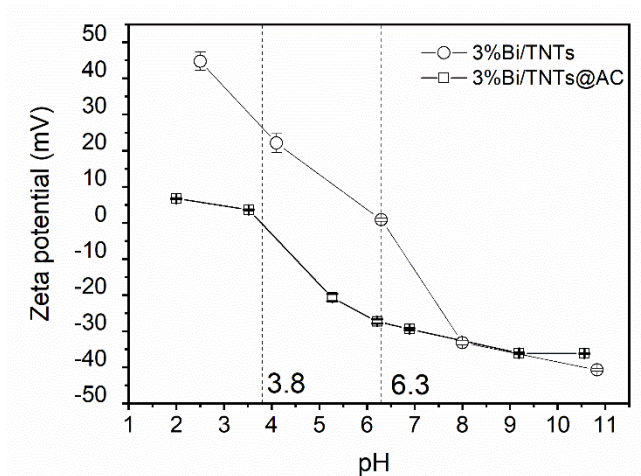


**Figure 5-8.** Zeta potential of 3%Bi/TNTs@AC and 3%Bi/TNTs as a function of pH.

### 5.3.4. Photodegradation of pre-concentrated GenX on Bi/TNTs@AC

**Figure 5-9** shows the photocatalytic degradation rates of pre-adsorbed GenX by treated AC, TNTs@AC, and Bi/TNTs@AC with 1-5 wt.% Bi. After 4 h of the UV irradiation, almost no GenX degradation was observed for AC and TNTs@AC. In contrast, Bi/TNTs@AC degraded up to 70.0% of the pre-concentrated GenX, with up to 42.7% defluorinated (i.e., conversion of fluorine into fluoride). Extending the UV irradiation to 6 and 8 h elevated the GenX photodegradation to 75.1% and 77.2%, and mineralization to 45.3% and 46.1%, respectively (**Figure 5-10**). In accord with the material characterization data, 3%Bi/TNTs@AC exhibited the highest photoactivity for GenX. Excessive Bi (*i.e.*, >3 wt.%) may act as recombination centers of the photo-generated electrons and holes.

**Figure 5-11a** shows the effect of catalyst dosage (1, 2, 3, and 5 g/L) during the adsorption stage on the subsequent photodegradation/defluorination of GenX under UV irradiation. Increasing the photocatalyst dosage from 1 to 2 g/L improved the 4-h GenX degradation and defluorination from 70.0% to 74.1% and from 42.7% to 48.3%, respectively. However, further increasing the dosage to 3 or 5 g/L resulted in lower rates of degradation and defluorination, which can be attributed to diminished light penetration as a result of elevated shading effects from denser suspended particles and aggregation of the particles (Ahmadpour et al. 2020; Mirzaei et al. 2018). Consequently, the dosage of 2 g/L was used in the subsequent studies. In practice, the material dosage should be tuned according to the target water quality conditions.

Different catalyst dosages during the adsorption stage result in adsorption of GenX on sites with different accessibility and photoactivity. Kinetically, GenX will be loaded on the more easily accessible sites at higher material doses. From the photoactivity perspective, the hybrid sites with Bi-TNTs-AC are more photoactive, while the pure AC phase may only adsorb but not degrade

GenX. While most adsorption sites of AC are located inside the particles, the main adsorption sites for 3%Bi/TNTs@AC are likely to be on the outside shell. The differences in adsorption sites were evidenced by the reduced SSA of 3%Bi/TNTs@AC compared to the parent AC (**Table 5-4**). The overall degradation efficiency depends on the fraction of GenX loaded on the more photoactive sites, which are accessible to not only GenX, but also photons, photogenerated charge carriers, and reactive oxygen species (ROS) (Ding et al. 2013) (**Section 5.3.7**). In practice, the low fraction of non-reactive sites should not affect the overall process, because this photo-inert adsorption capacity will remain constant in each treatment cycle and will not affect GenX adsorption and photodegradation on the reactive sites, which are automatically regenerated upon the photodegradation.



(a)  (b)
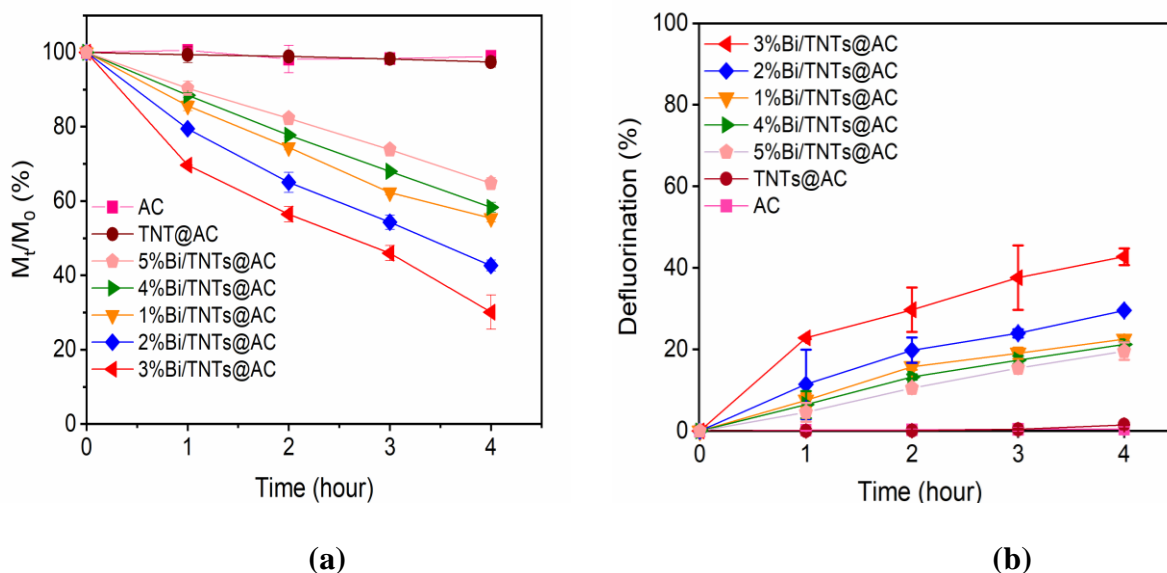
**Figure 5-9. (a)** Photodegradation and **(b)** defluorination kinetics of GenX pre-adsorbed on treated AC, TNTs@AC, and Bi/TNTs@AC prepared with 1-5 wt.% Bi. Experimental conditions during adsorption: initial GenX concentration = 100 µg/L, material dosage = 1 g/L, pH = 7.0 ± 0.1;

153

Conditions for photodegradation: UV intensity = 210 W/m$^2$, pH = 7.0 ± 0.1.  Data are plotted as mean of duplicates with error bars indicating relative deviation from the mean.
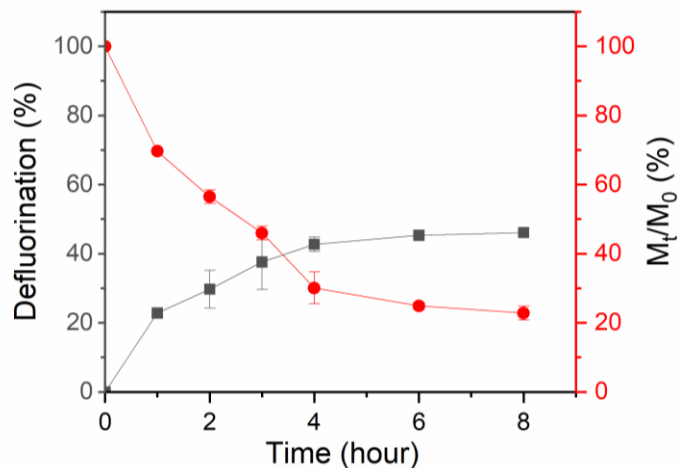


**Figure 5-10.** Photodegradation and defluorination kinetics of GenX pre-adsorbed on 3%Bi/TNTs@AC under 8 h UV irradiation. Experimental conditions during adsorption: initial GenX = 100 µg/L, material dosage = 1 g/L, pH = 7.0 ± 0.1; Conditions for photodegradation: UV intensity = 210 W/m$^2$, pH = 7.0 ± 0.1.  Data are plotted as mean of duplicates with error bars indicating relative deviation from the mean.

**(a)**



**(b)**

**(c)**
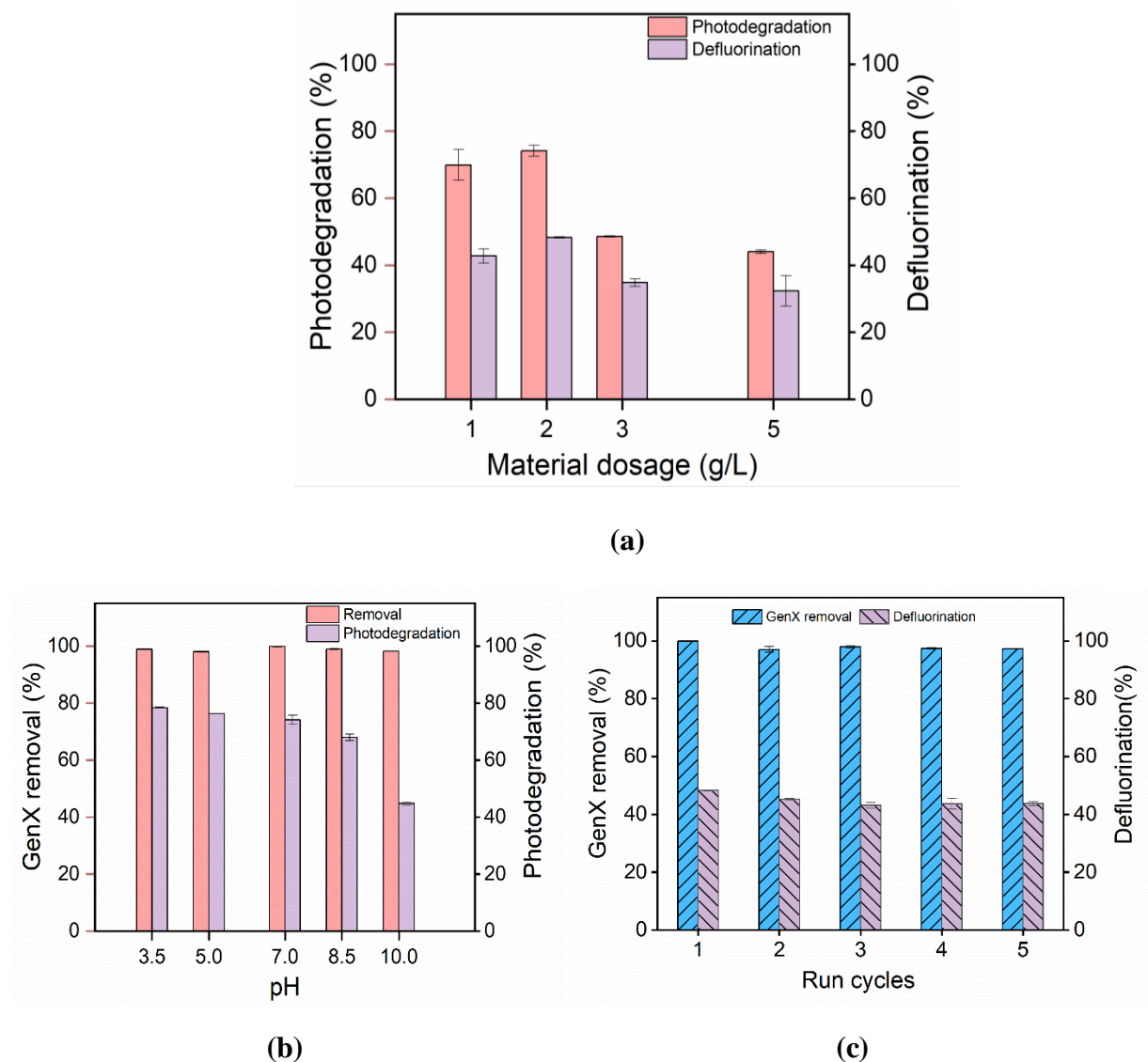
**Figure 5-11.** **(a)** Photodegradation and defluorination of GenX pre-sorbed on 3%Bi/TNTs@AC at various material dosages of 1-5 g/L during adsorption; **(b)** effect of pH on GenX adsorption and photodegradation by 3%Bi/TNTs@AC; and **(c)** adsorption and solid-phase defluorination of GenX during five consecutive cycles using the same 3%Bi/TNTs@AC. Experimental conditions (adsorption): initial GenX concentration = 100 µg/L, material dosage = 2 g/L in **(a)** and **(c)** or 1 g/L in **(b)**, adsorption time = 2 h, and pH = 7.0 ± 0.1 in **(a)** and **(c)**; Experimental conditions

(photodegradation): material dosage $= 2$ g/L during adsorption, UV intensity $= 210$ W/m$^2$, reaction time $= 4$ h, pH $= 7.0 \pm 0.1$.

### 5.3.5. pH effects on GenX adsorption and photodegradation

**Figure 5-11b** shows the effect of pH on GenX adsorption by 3%Bi/TNTs@AC. Nearly all (~99%) of the GenX was consistently adsorbed from the solution over a broad pH range of 3.5-10 upon equilibrium. Due to the low p$K_a$ value (2.8), GenX mainly existed in the anionic form in the pH range tested. In light of the pH$_{pzc}$ of ~3.8 for 3%Bi/TNTs@AC and 6.3 for Bi/TNTs (**Section 5.3.3**), a negative overall surface potential would be expected for 3%Bi/TNTs@AC in the experimental pH range (except for pH 3.5), namely, electrostatic interactions between GenX and 3%Bi/TNTs@AC are unfavorable at neutral or alkaline pH. At more alkaline pH, the surface potential of Bi/TNTs turned more negative (pH$_{pzc} = 6.3$), and thus the interaction with the carboxylate group of GenX became more unfavorable due to electrostatic repulsion and competition of OH$^-$. Consequently, adsorption of GenX would largely rely on the hydrophobic and anion-$\pi$ interactions between GenX and AC, resulting in a vertical tail-on orientation adsorption mode (Li et al. 2020a). Conversely, at more acidic pH, adsorption of GenX becomes more favorable for enhanced electrostatic interaction between the positively charged surface of Bi/TNTs and GenX and Lewis acid-base interaction between GenX and the metals (*i.e.,* Bi, Ti). In this case, GenX tends to be adsorbed in the parallel or side-on mode with both the head and tail of GenX bound to the mixed phases. It is noteworthy that the observed no-effect of pH on adsorption could also be due to the very high removal of GenX in all cases. Our goal here was to show that 3%Bi/TNTs@AC was able to effectively concentrate GenX over a broad pH range at practically relevant dosages.

Thus, the photodegradation efficiency of GenX is evaluated at the five different pH values (**Figure 5-11b**). The 4-h GenX photodegradation showed a clear decreasing trend with increasing pH, from 78.4% at pH 3.5 to 76.4%, 74.1%, 68.0%, and 44.8% at pH 5.0, 7.0, 8.5, and 10.0, respectively. Apparently, the photodegradation effectiveness is associated with the adsorption modes of GenX. As to be illustrated in **Sections 5.3.7** and **5.3.8**, the head group decarboxylation is a critical step in the GenX degradation process. As such, the head-on or side-on adsorption mode is more favorable than the vertical tail-on mode for the photo-generated holes and radicals to attack both the head and tail groups of a GenX molecule. In addition, the production of photogenerated holes and radicals can be suppressed under alkaline conditions. Excessively high $HO^-$ could react with photogenerated holes to produce excessive hydroxyl radicals, which inhibit the direct hole oxidation of GenX (**Section 5.3.7**) (Li et al. 2020a). Moreover, acidic conditions are favorable for formation of $HO_2^{\bullet}$, which is a precursor of $H_2O_2$ and $^{\bullet}OH$ (Eq. 6) (Song et al. 2012).

$$O_2^{\bullet -} + H^+ \leftrightarrow HO_2^{\bullet} \quad pK_a = 4.88 \tag{9}$$
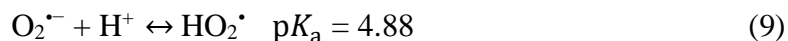
### 5.3.6. Stability and reusability of Bi/TNTs@AC

The efficient photodegradation of sorbed GenX was expected to automatically regenerate the material for repeated uses. To test this hypothesis, 3%Bi/TNTs@AC was subjected to five consecutive cycles of adsorption and photodegradation. After the fifth cycle, 3%Bi/TNTs@AC was still able to adsorb >98% of the GenX from solution (**Figure 5-11c**), indicating that the material retained its adsorption capacity. In addition, the GenX mineralization efficiency only exhibited a modest decrease from 48.3% to 43.7% after the five cycles, potentially due to competition from accumulated short-chain intermediates produced in previous cycles. No loss in Ti content was detected and <1.0 wt.% of the doped Bi leached into the solution after the five cycles.

157

**5.3.7. Mechanisms of enhanced GenX photodegradation by Bi/TNTs@AC**

To understand the roles of common reactive species, photocatalytic degradation experiments were carried out in the presence of radical scavengers, namely ISA for hydroxyl radicals ($^{\bullet}$OH), BQ for superoxide radicals ($O_2^{\bullet-}$), EDTA for the photo-generated holes ($h^+$), and NaN$_3$ for singlet oxygen ($^1O_2$) (Van Doorslaer et al. 2012). **Figure 5-12a** shows the 4-h photodegradation efficiency for GenX in the presence of variable concentrations (0.5, 1, 5, and 10 mM) of ISA, NaN$_3$, BQ, or EDTA. NaN$_3$ and BQ showed only modest or negligible effects on the photodegradation, indicating that neither $O_2^{\bullet-}$ nor $^1O_2$ reacted with GenX. In contrast, the photodegradation decreased from 74.1% without a scavenger to 43.0% in the presence of 0.5 mM ISA, and to < 1.5% when the ISA concentration was increased to 10 mM, indicating that $^{\bullet}$OH played a critical role in the photodegradation process. The addition of 0.5-10 mM of EDTA lowered the GenX degradation to 66.9%-56.2%, suggesting that $h^+$ also played an important role.

**Figure 5-12b** compares the EPR spectra of DMPO-$^{\bullet}$OH adducts generated in the TNTs@AC and 3%Bi/TNTs@AC systems after 10 and 20 min of UV irradiation. A weaker $^{\bullet}$OH signal (four lines with an intensity ratio of nearly 1:2:2:1) was observed for TNTs@AC, while a stronger $^{\bullet}$OH signal was evident after the incorporation of 3 wt.% Bi on TNTs@AC. The $^{\bullet}$OH signal intensity increased with the irradiation time (**Figure 5-12b**) due to the resulting $^{\bullet}$OH. No $O_2^{\bullet-}$ or $^1O_2$ signals were detected for 3%Bi/TNTs@AC (**Figure 5-12c** and **5-12d**). The results confirmed the findings from the radical-quenching experiments (**Figure 5-12a**).

**Figure 5-13a** compares the optical properties of TNTs@AC and Bi/TNTs@AC with 1-5 wt.% Bi. As shown in, Bi/TNTs@AC exhibited greater light absorption than TNTs@AC throughout the UV and visible ranges (200-800 nm), though TNTs@AC did demonstrate notable light absorbance due to the carbon (Kakavandi et al. 2019; Velasco-Arias et al. 2012). In particular,

the maximum absorbance (285 nm) for 3%Bi/TNTs@AC was 14% higher than that (310 nm) for TNTs@AC. These results confirmed that the Bi particles on the surface enhanced light harvesting, leading to enhanced photogeneration of electrons and holes.

This phenomenon is attributed to the SPR effect endowed by the metallic Bi on TNTs@AC. Dong et al. (2015) showed that the electromagnetic field distribution of Bi spheres reached its maximum at the surface of metallic Bi particles, and they observed that the SPR property of Bi could markedly enhance visible light harvesting and charge separation. When the surface plasmon wave interacts with a local particle or rough surface, some of the energy can be re-emitted as light. Other studies have also demonstrated that Bi particles display strong SPR effects in the UV range (228-280 nm), depending on their particle size and shape (Dong et al. 2014b; Ma et al. 2013; Wang et al. 2005). For instance, Ma et al. (2013) determined two SPR absorption peaks at 228 nm and 256 nm for mixed plate-like (40-70 nm) and polyhedral (500 nm) Bi nanocrystals. Wang et al. (2005) synthesized stabilized bismuth nanoparticles (~10 nm) that showed a surface plasmon absorption peak at 281 nm. Moreover, 3%Bi/TNTs@AC also exhibited enhanced visible light absorption, which is in agreement with previous reports that Bi displayed SPR effect in both ultraviolet and visible light domains (Sun et al. 2015; Sun et al. 2017).

PL emission intensity has been used to measure the recombination of photo-induced electrons and holes. **Figure 5-13b** shows the PL emission spectra of TNTs@AC and 3%Bi/TNTs@AC. While the PL intensity for TNTs@AC included two large peaks, the spectra for 3%Bi/TNTs@AC was almost flat, indicating that deposition of Bi resulted in a remarkable decline in the recombination of electron-hole pairs. This observation agrees with the notion that metallic Bi can serve as an effective electron trap and, thus, facilitate electron-hole separation (Dong et al. 2014a). Chen et al. (2017) prepared $Bi@Bi_2O_3$ core-shell nanoparticles and found that metallic Bi

159

nanoparticles can generate charge carriers due to the SPR effect, while the amorphous $Bi_2O_3$ surface layer serves as an efficient electron and hole acceptor to guide the directional transfer of photo-charges and enhance the separation of electron-hole pairs. The $Bi_2O_3$ shell could also protect the metallic Bi core from oxidation, which not only preserves the reactive lifetime, but also provides a safe environment for photocatalytic reactions (Chen et al. 2017).
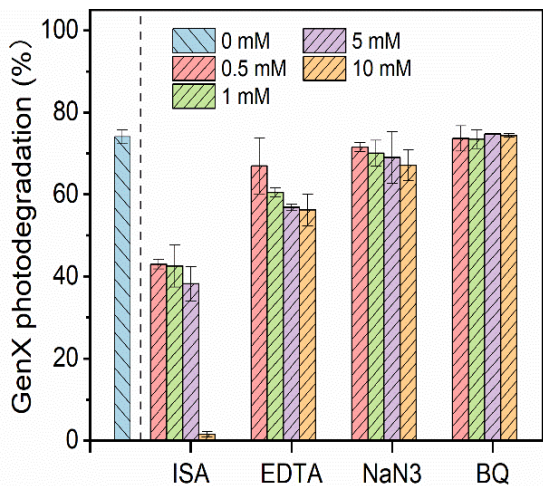
**(a)**
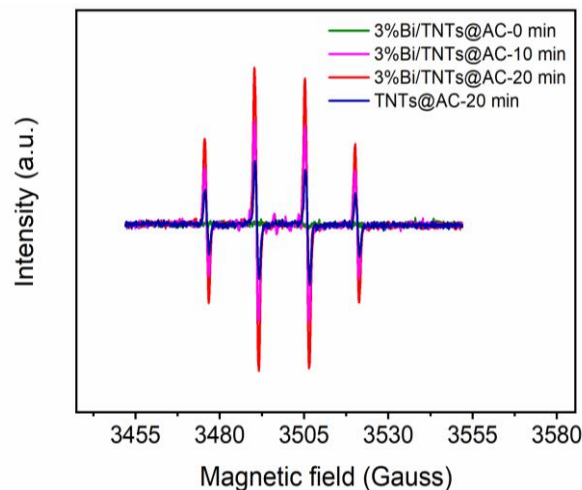
**(b)**
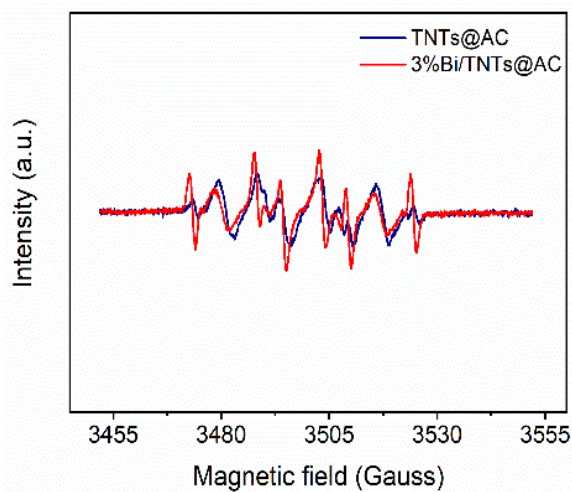
**(c)**
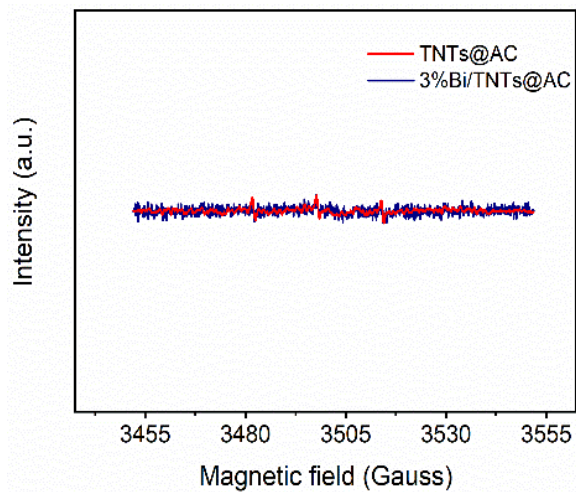
**(d)**

**Figure 5-12.** **(a)** Photodegradation of GenX pre-sorbed on 3%Bi/TNTs@AC in the presence of a scavenger (*i.e.*, ISA, EDTA, NaN$_3$, or BQ), **(b)** EPR spectra of DMPO−·OH adducts produced by TNTs@AC upon UV irradiation for 20 min and by 3%Bi/TNTs@AC after variable UV irradiation times, **(c)** EPR spectra of DMPO−O$_2$$^{·−}$ adducts produced by TNTs@AC and 3%Bi/TNTs@AC upon UV irradiation for 20 min, and **(d)** EPR spectra of TEMP−$^1$O$_2$ adducts produced by TNTs@AC and 3%Bi/TNTs@AC upon UV irradiation for 20 min. Experimental conditions (adsorption): initial GenX = 100 μg/L, material dosage = 2 g/L, adsorption time = 2 h, and pH = 7.0 ± 0.1; Experimental conditions (photodegradation): UV intensity = 210 W/m$^2$, reaction time = 4 h, pH = 7.0 ± 0.1, scavenger = 0.5, 1, 5, and 10 mM in **(a)**, DMPO = 20 mM in **(b)**.
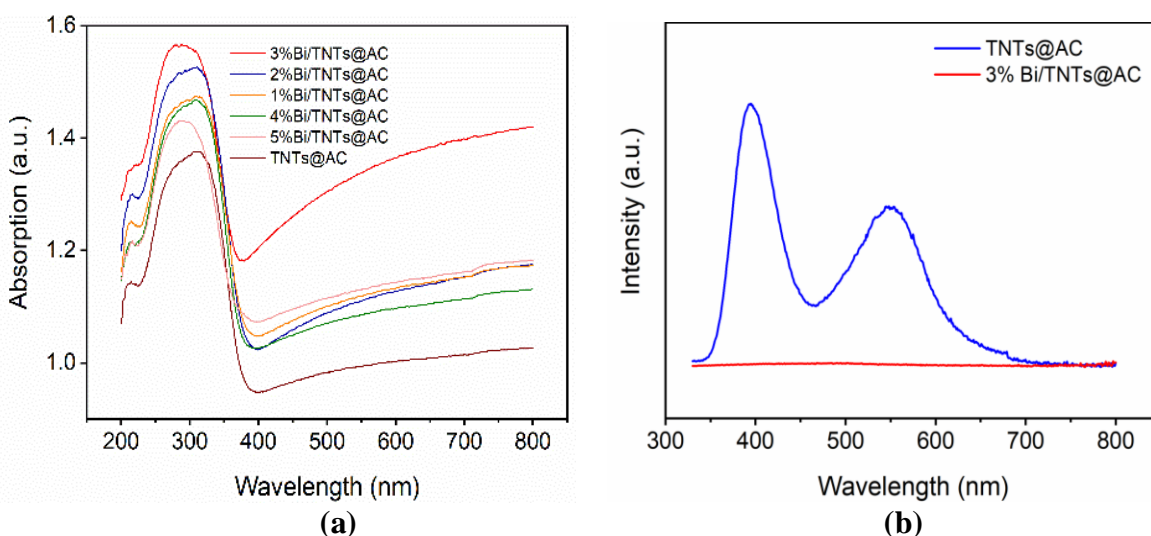


**Figure 5-13.** **(a)** UV-DRS spectra and **(b)** photoluminescence spectra of TNTs@AC and 3%Bi/TNTs@AC.

Based on the experimental results and material characterization, **Figure 5-14** illustrates the key mechanisms governing the enhanced adsorption and photocatalytic degradation of GenX by Bi/TNTs@AC. First, the incorporation of Bi nanoparticles on Bi/TNTs@AC creates a more favorable environment for adsorption due to suppression of the surface negative potential. The

surface Bi along with Ti also serves as a Lewis acid to bind with the carboxylate group of GenX anions, which is conducive to the decarboxylation reaction that is often an essential step for PFAS degradation (Zhu et al. 2021). Second, the Bi nanoparticles enhance light absorbance (**Figure 5-13a**), favoring the production of photogenerated electrons and holes. Third, due to photo-induced SPR, the metallic Bi is photoexcited and promotes excitation of surface electrons, generation of more charge carriers, and interfacial electron transfer (Chen et al. 2017). Fourth, because the Fermi level (vs NHE) of metallic Bi (-0.17 eV) (Dong et al. 2015) is lower than the conduction band (CB) level of TNTs@AC (0.12 eV) (Dang et al. 2020), the photoexcited electrons tend to flow from Bi to TNTs@AC, decreasing the recombination rate of electron-hole pairs and increasing the lifetime of charge-carriers in TNTs@AC. Fifth, the electron release results in positively charged $Bi^{n+}$, which attract and trap photoexcited electrons from the valence band (VB) of TNTs@AC to maintain charge neutrality (Dong et al. 2014a), further inhibiting $e^-/h^+$ recombination and leaving more holes available for reacting with GenX. Lastly, the local electromagnetic field representing the SPR effects of Bi metal can also enhance the generation of electron-hole pairs and subsequent separation of the charge carriers (Tu et al. 2015). Afterwards, the separated electrons will reduce $O_2$ to $H_2O_2$ because the redox potential of $O_2/H_2O_2$ (0.695 eV) (Moon et al. 2017) is more positive than that of the CB of TNTs@AC, and subsequently, $H_2O_2$ is transformed into $^\bullet OH$ by trapping an electron (Dong et al. 2014a). Given the redox potential of $O_2/O_2^{\bullet-}$ (−0.33 eV), the CB electrons are less likely to react with $O_2$ (Dong et al. 2014a). Conversely, the holes with a redox potential of 3.85 eV can facilitate decarboxylation of GenX and oxidation of $HO^-$ into $^\bullet OH$ radicals ($E^0 = 1.99$ eV for $OH^-/^\bullet OH$) (Dong et al. 2014a). As $^\bullet OH$ radicals and $h^+$ are the major reactive species, the photocatalytic degradation of GenX adsorbed on Bi/TNTs@AC was enhanced.

**Figure 5-15a** shows the molecular structure of GenX with labeled sites. **Figures 5-15b** and **5-15c** show the highest occupied molecule orbital (HOMO) and the lowest unoccupied molecular orbital (LUMO) of GenX, respectively, and indicate that the carboxylate group is a favorable attack site for photogenerated holes and radicals. While the gain or loss of electrons on each GenX molecule site cannot be accurately obtained (Ji et al. 2020), the condensed Fukui functions were calculated based on the natural population analysis (NPA) scheme to identify the electrophilic ($f^-$), nucleophilic ($f^+$), and radical ($f^0$) reactive sites in GenX (**Figure 5-15d**). Based on the condensed Fukui function values of 0.3309 and 0.3273, the most reactive sites for electrophilic attack are O19 and O20, respectively, of the carboxylate group. The same sites also exhibit the highest $f^0$ values, namely 0.1906 and 0.1981, respectively. Therefore, the carboxylate group of GenX is most prone to the attack by the photogenerated radicals, which is in agreement with previous reports of photocatalytic degradation of long-chain PFAS (Xu et al. 2020; Zhu et al. 2021). The surface contour of $f^+$ for GenX indicates that C1 (0.1084) and C2 (0.1188) in the $CF_3CF_2CF_2-$ end group are most vulnerable to nucleophilic attack. This observation agrees with the report by Bao et al. (2018). However, Bao et al. (2018) also proposed that the optimal trajectory for radicals to attack the carboxyl group of GenX is blocked by $-CF_3$ due to steric hindrance. Pica et al. (2019) asserted that $^\bullet OH$ attack on the ether bond of GenX is kinetically unfavorable because of the high activation barrier (321 kJ/mol), though the attack can result in concurrent decarboxylation. While the initial oxidative attack does not break the ether bond, stepwise mineralization can occur along the acidic side chain. Moreover, the ether bond introduces a weak point in the perfluorinated carbon chain, facilitating degradation by hydrated electrons.
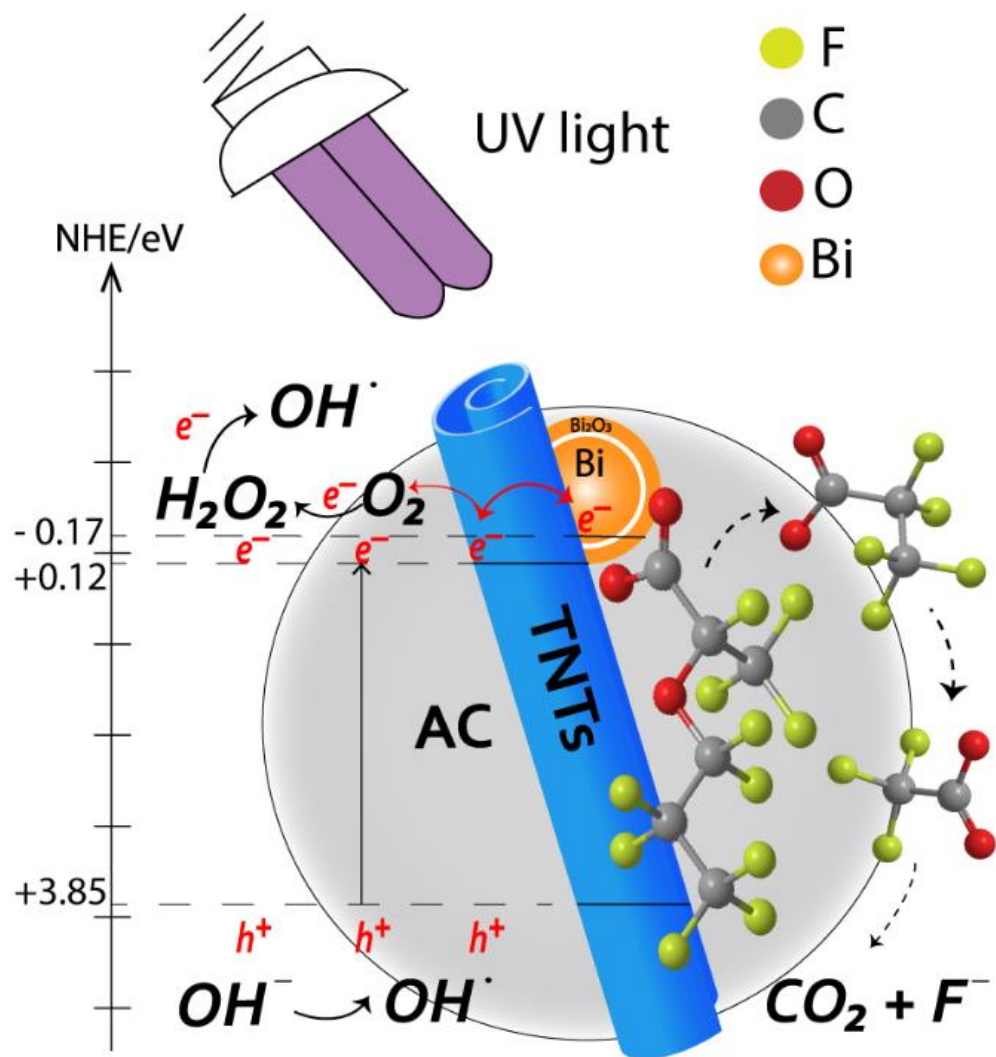
**Figure 5-14.** Conceptualized representation of the adsorptive photocatalysis mechanism with Bi/TNTs@AC for GenX degradation under UV irradiation.

**(a)**

**(b)**

**(c)**

HO

MO

LUMO

**(d)**

| Atom | No | Charge (0)(e/Å³) | Charge (+1)(e/Å³) | Charge (-1)(e/Å³) | $f^-$ | $f^+$ | $f^0$ |
|---|---|---|---|---|---|---|---|
| C | 1 | 1.0685 | 1.0720 | 0.9600 | 0.0035 | 0.1084 | 0.0560 |
| C | 2 | 0.6440 | 0.6451 | 0.5252 | 0.0011 | 0.1188 | 0.0599 |
| C | 3 | 0.9901 | 0.9829 | 0.9220 | -0.0072 | 0.0681 | 0.0305 |
| F | 4 | -0.3597 | -0.3449 | -0.4126 | 0.0147 | 0.0529 | 0.0338 |
| F | 5 | -0.3538 | -0.3445 | -0.3887 | 0.0093 | 0.0349 | 0.0221 |
| F | 6 | -0.3505 | -0.3465 | -0.3950 | 0.0040 | 0.0445 | 0.0242 |
| F | 7 | -0.3406 | -0.3380 | -0.3799 | 0.0026 | 0.0393 | 0.0209 |
| F | 8 | -0.3536 | -0.3414 | -0.4261 | 0.0122 | 0.0725 | 0.0424 |
| F | 9 | -0.3469 | -0.3429 | -0.3881 | 0.0040 | 0.0412 | 0.0226 |
| F | 10 | -0.3782 | -0.3537 | -0.4106 | 0.0245 | 0.0324 | 0.0284 |
| O | 11 | -0.5976 | -0.5532 | -0.6477 | 0.0444 | 0.0501 | 0.0473 |
| C | 12 | 0.4656 | 0.5586 | 0.4031 | 0.0930 | 0.0625 | 0.0778 |
| C | 13 | 1.0879 | 1.0952 | 1.0528 | 0.0073 | 0.0352 | 0.0212 |
| F | 14 | -0.3686 | -0.3072 | -0.3975 | 0.0615 | 0.0289 | 0.0452 |
| F | 15 | -0.3626 | -0.3428 | -0.3933 | 0.0198 | 0.0307 | 0.0252 |
| F | 16 | -0.3532 | -0.3298 | -0.3716 | 0.0233 | 0.0184 | 0.0209 |
| F | 17 | -0.3768 | -0.3344 | -0.3991 | 0.0424 | 0.0223 | 0.0324 |
| C | 18 | 0.7369 | 0.7183 | 0.7170 | -0.0186 | 0.0199 | 0.0006 |
| O | 19 | -0.7355 | -0.4046 | -0.7858 | 0.3309 | 0.0503 | 0.1906 |
| O | 20 | -0.7154 | -0.3881 | -0.7843 | 0.3273 | 0.0688 | 0.1981 |

**Figure 5-15. (a)** NPA analysis of reactive sites in a GenX molecule at the B3LYP/6−31+G(d,p) level; molecular orbitals of GenX structure showing the **(b)** HOMO and **(c)** LUMO; and **(d)** condensed Fukui index distribution of active sites on GenX. Green: negative phase; Purple: positive phase; Blue: F; Deep grey: C; Red: O.

### 5.3.8. Pathways of GenX photodegradation by Bi/TNTs@AC

**Figure 5-16** shows the chromatograms of two major stable intermediate products, TFA ($CF_3COOH$) and PFA ($C_2F_5COOH$), detected after the 4-h photocatalytic degradation of GenX by 3%Bi/TNTs@AC. Other intermediates were either unstable or unidentifiable. Taken together the

165

mechanism analysis, reactive species quenching data, DFT calculations, intermediates, and findings from recent studies (Bao et al. 2018; Pica et al. 2019; Vakili et al. 2021), the photodegradation of GenX by 3%Bi/TNTs@AC may occur along two possible pathways (**Figure 5-17**). The first pathway starts with decarboxylation by $^\bullet OH$ and/or $h^+$ to generate an activated intermediate ($C_5F_{11}O\bullet$). Then, the $C_5F_{11}O\bullet$ radical interacts with $^\bullet OH$ and/or $H_2O$ to form unstable $C_3F_7OCF_3CFOH$, which subsequently transforms into $C_3F_7OCOF$ after elimination of a $CF_3$ moiety on the α carbon (Pica et al. 2019). Upon further reaction with $^\bullet OH$, $C_3F_7OCOF$ converts into $C_4F_8HO_3\bullet$ and subsequently generates $CF_3CF_2CF_2O\bullet$ through cleavage of the FCOOH moiety. Finally, $CF_3CF_2CF_2O\bullet$ continues to lose the $CF_2O$ groups until complete mineralization (Pica et al. 2019; Vakili et al. 2021).

The second pathway is initiated by reduction of the ether group by photogenerated electrons to form $C_3F_7\bullet$ and $\bullet C_3F_4O_3^-$ fragments. The carboxylate fragment ($\bullet C_3F_4O_3^-$) is degraded in a similar manner as pathway (1). Specifically, the carboxylate group is cleaved, and the active intermediate reacts with $^\bullet OH$ and/or $H_2O$ to form the unstable $C_2F_4OOH^-$, which is converted to $C_2F_4O$ after one $H_2O$ molecule is eliminated. Then, $C_2F_4O$ is hydrolyzed to $CF_3COO^-$ (TFA) with the expulsion of $H^+$ and $F^-$. The $C_3F_7\bullet$ fragment may react with $^\bullet OH$ or $H_2O$ to generate unstable $C_3F_7OH$, which further transforms into $CF_3CF_2COF$. Upon hydrolysis, $CF_3CF_2COF$ converts into $C_2F_5COO^-$ (PFA), which is converted into $C_2F_5OH$ upon decarboxylation by $^\bullet OH$ and $h^+$ (Niu et al. 2012). The unstable alcohol undergoes intramolecular rearrangement to form $CF_3COF$ and converts into $CF_3COO^-$ (Niu et al. 2012). In addition, electrons may attack other fluorine atoms in the fluorocarbon tail (Park et al. 2009; Song et al. 2013), resulting in an alternative pathway for PFA photodegradation, where PFA is transformed into $CF_3CH_2COO^-$ via $H^\bullet/F$ exchange and subsequently converted into $CF_3COO^-$ upon elimination of a $\bullet CH_2$ moiety (Bao et al. 2018; Park

et al. 2009; Song et al. 2013). The TFA generated from decomposition of the two GenX fragments may be further degraded to $\cdot CF_3$ and $\cdot COO^-$. The resulting $\cdot CF_3$ may combine with other radicals (e.g., $\cdot CF_3$ or $H\cdot$) to form gaseous products (e.g., $CF_3H$, $C_2F_6$) (Bao et al. 2018).
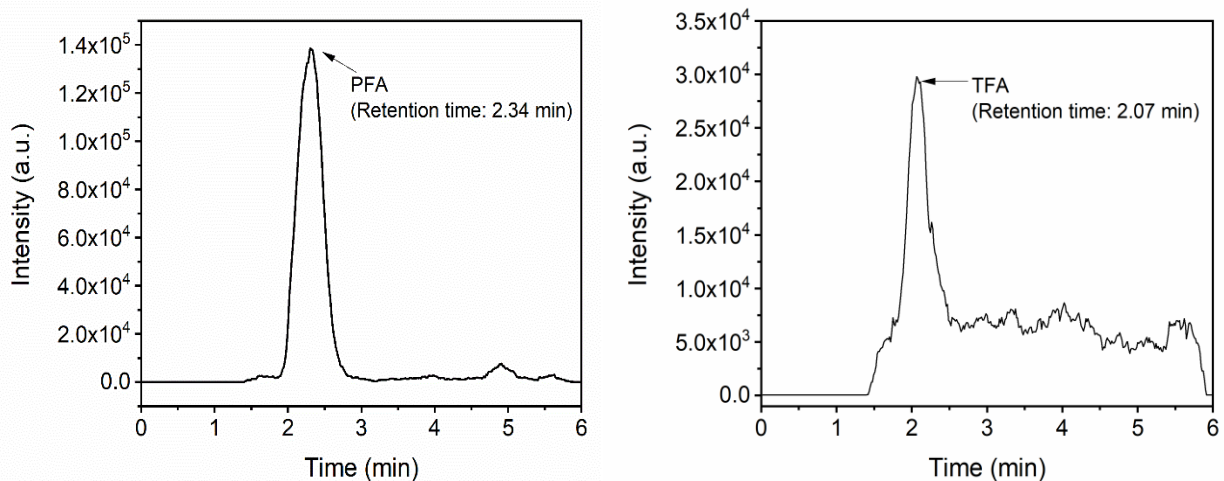


**Figure 5-16.** LC-MS/MS chromatograms showing two major intermediate products (PFA ($C_2F_5COOH$) and TFA ($CF_3COOH$)) after 4 h of GenX photodegradation on 3%Bi/TNTs@AC. Experimental conditions during adsorption: initial GenX = 1 mg/L, 3%Bi/TNTs@AC = 2 g/L, pH = 7.0 ± 0.1; Conditions for photodegradation: UV intensity = 210 W/m$^2$, reaction time = 4 h, pH = 7.0 ± 0.1.
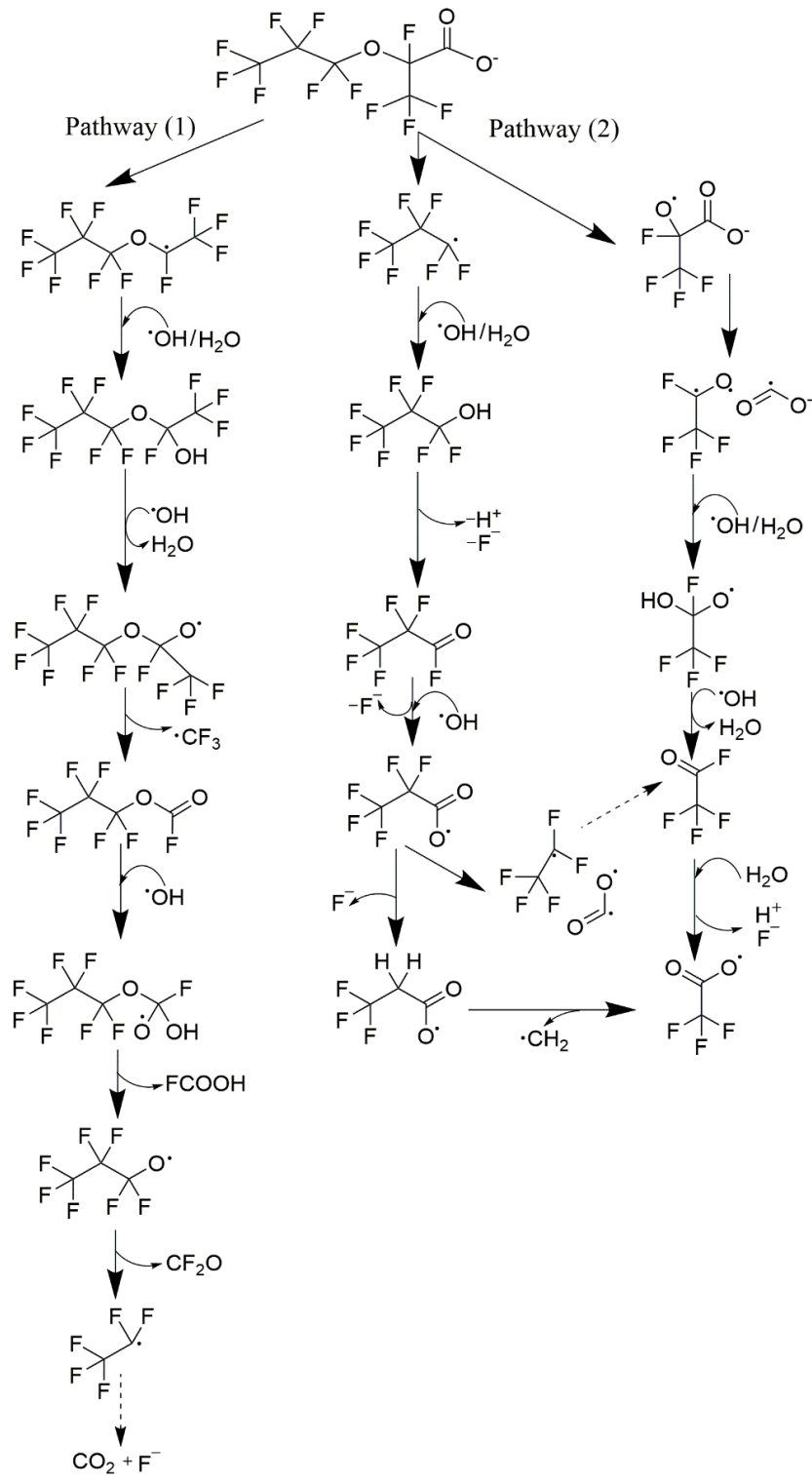
**Figure 5-17.** Proposed photodegradation pathways of GenX by 3%Bi/TNTs@AC under UV irradiation.

## 5.4. Conclusions

A new adsorptive photocatalyst was prepared, characterized, and tested for degradation of GenX as a model emerging PFAS. The major findings are summarized as follows:

1) The most reactive Bi/TNTs@AC was prepared by depositing 3 wt.% Bi on AC-supported titanate nanotubes constructed with commercially available AC and P25.

2) Material characterization indicated that Bi was deposited on the material surface as nanoparticles with a metallic Bi core and amorphous $Bi_2O_3$ shell. In addition, micro- or nanoscale AC particles were also observed on TNTs.

3) Bi/TNTs@AC was able to adsorb nearly all GenX in 1 h, effectively concentrating GenX on the photoactive sites. Subsequently, 70.0% of the pre-sorbed GenX was degraded, including 42.7% defluorinated, after 4 h of UV irradiation. The photodegradation process also regenerated the material, enabling repeated uses without additional chemical regeneration.

4) The hybrid Bi, anatase, and AC phases at the microscale or nanoscale facilitated enhanced adsorption of GenX through concurrent and synergistic hydrophobic, Lewis acid-base, and anion-$\pi$ interactions.

5) The SPR effect enabled by the metallic Bi nanoparticles greatly enhanced light harvesting, generation of charge carriers, and separation of $e^-/h^+$ pairs.

6) While DFT findings suggested that the carboxylate group was the prone to the radical attack in the UV system, the ether bond was a favorable attack site for photogenerated electrons.

7) $^{\bullet}$OH radicals and photogenerated $h^+$ were the main reactive species for the photocatalytic degradation of GenX by Bi/TNTs@AC, which starts with cleavage of the carboxylate

169

group, conversion to $CF_3CF_2CF_2O\bullet$ via decarboxylation and $CF_3$ elimination, and continues through sequential loss of $CF_2O$ groups until complete mineralization. In addition, the ether bond in the GenX molecule may be attacked by photogenerated electrons, opening up another degradation pathway.

Given the widespread use of GenX as a substitute for legacy PFAS and the growing health concerns, Bi/TNTs@AC and the concentrate-and-destroy concept may serve as an important technology for cost-effective treatment of GenX-contaminated waters.

# Chapter 6. Future Research

The follow-on studies are recommended in the future:

1) Explore a new strategy in preparing gallium-doped carbon-modified titanium dioxide and test the material for enhanced adsorption and photodegradation rate of pre-sorbed GenX.

2) Further elucidate the insight mechanisms for PFAS photodegradation by adsorptive photocatalysts, such as quantum yield and energy efficiency calculations.

3) Composite materials that are more reactive and effective under solar light should be further explore.

4) The carbon-based adsorptive photocatalysts may be further improved to enhance the adsorption selectivity and the photocatalytic activity for PFAS in field water. Additional treatment methods should be explored to enhance the photodegradation of the pre-sorbed by manipulating the treatment chemistry and by addition of some strong oxidizing reagents and/or photosensitizers.

5) More experimental and water chemistry conditions could be optimized to promote photocatalytic degradation of more persistent PFAS, such as various light wavelengths, reaction temperature, and different liquid : solid ratios.

6) Further investigations are needed to evaluate the effectiveness under landfill leachate to identify potential inhibitions of the strong matrix and find out ways to overcome these inhibitive effects.

7) Pilot-scale experiments should be performed to facilitate more realistic assessment of the technical and economic effectiveness and to guide field application design.

## References

ADPH 2016. Health department responds to EPA health advisorie impacting north Alabama water systems http://www.adph.org/news/assets/160520.pdf

Ahmadpour, N., Sayadi, M.H. and Homaeigohar, S. 2020. A hierarchical Ca/TiO 2/NH 2-MIL-125 nanocomposite photocatalyst for solar visible light induced photodegradation of organic dye pollutants in water. Rsc Adv 10(50), 29808-29820

AL 2020. Another Alabama utility sues 3M over water pollution.https://www.al.com/news/2020/09/another-alabama-utility-sues-3m-over-water-pollution.html

Alabama, M.A.i. 2016. Water study: Alabama has 4th highest level of PFAS contaminants.https://www.montgomeryadvertiser.com/story/news/local/alabama/2016/08/20/water-study-alabama-has-4th-highest-level-pfas-contaminants/88997602/

Ali, S., Li, Z., Chen, S., Zada, A., Khan, I., Khan, I., Ali, W., Shaheen, S., Qu, Y. and Jing, L. 2019. Synthesis of activated carbon-supported $TiO_2$-based nano-photocatalysts with well recycling for efficiently degrading high-concentration pollutants. Catal Today 335, 557-564

Almeida, R.M., Vasconcelos, H.C., Goncalves, M.C. and Santos, L.s.F. 1998. XPS and NEXAFS studies of rare-earth doped amorphous sol–gel films. J Non-Cryst Solids 232, 65-71

Amdeha, E., El-Salamony, R.A. and Al-Sabagh, A.M. 2020. Enhancing the photocatalytic activity of Ga2O3–TiO2 nanocomposites using sonication amplitudes for the degradation of Rhodamine B dye. Appl Organomet Chem 34(2), e5336

Balaji, S., Djaoued, Y. and Robichaud, J. 2006. Phonon confinement studies in nanocrystalline anatase-TiO2 thin films by micro Raman spectroscopy. Journal of Raman Spectroscopy: An

International Journal for Original Work in all Aspects of Raman Spectroscopy, Including Higher Order Processes, and also Brillouin and Rayleigh Scattering 37(12), 1416-1422

Banerjee, A.N., Joo, S.W. and Min, B.-K. 2012. Photocatalytic degradation of organic dye by sol-gel-derived gallium-doped anatase titanium oxide nanoparticles for environmental remediation. Journal of Nanomaterials 2012

Bao, Y.X., Deng, S.S., Jiang, X.S., Qu, Y.X., He, Y., Liu, L.Q., Chai, Q.W., Mumtaz, M., Huang, J., Cagnetta, G. and Yu, G. 2018. Degradation of PFOA substitute: GenX (HFPO-DA ammonium salt): oxidation with UV/persulfate or reduction with UV/sulfite? Environ. Sci. Technol. 52(20), 11728-11734

Brandsma, S., Koekkoek, J., van Velzen, M. and de Boer, J. 2019. The PFOA substitute GenX detected in the environment near a fluoropolymer manufacturing plant in the Netherlands. Chemosphere 220, 493-500

Brooke, D., Footitt, A. and Nwaogu, T. 2004. Environmental risk evaluation report: Perfluorooctanesulphonate (PFOS). UK Environment Agency

Buck, R.C., Korzeniowski, S.H., Laganis, E. and Adamsky, F. 2021. Identification and classification of commercially relevant per- and poly-fluoroalkyl substances (PFAS). Integrated Environmental Assessment and Management 17(5), 1045-1055

Cai, W., Navarro, D.A., Du, J., Ying, G., Yang, B., McLaughlin, M.J. and Kookana, R.S. 2022. Increasing ionic strength and valency of cations enhance sorption through hydrophobic interactions of PFAS with soil surfaces. Sci Total Environ 817, 152975

Cai, Z., Zhao, X., Wang, T., Liu, W. and Zhao, D. 2017. Reusable platinum-deposited anatase/hexa-titanate nanotubes: roles of reduced and oxidized platinum on enhanced solar-light-driven photocatalytic activity. Acs Sustain Chem Eng 5(1), 547-555

Cambié, D., Bottecchia, C., Straathof, N.J., Hessel, V. and Noel, T. 2016. Applications of continuous-flow photochemistry in organic synthesis, material science, and water treatment. Chemical reviews 116(17), 10276-10341

Carter, K.E. and Farrell, J. 2010. Removal of perfluorooctane and perfluorobutane sulfonate from water via carbon adsorption and ion exchange. Separ Sci Technol 45(6), 762-767

Chen, M., Li, Y., Wang, Z., Gao, Y., Huang, Y., Cao, J., Ho, W. and Lee, S. 2017. Controllable synthesis of core–shell Bi@amorphous $Bi_2O_3$ nanospheres with tunable optical and photocatalytic activity for NO removal. Ind Eng Chem Res 56(37), 10251-10258

Chen, X., Cao, S., Weng, X., Wang, H. and Wu, Z. 2012. Effects of morphology and structure of titanate supports on the performance of ceria in selective catalytic reduction of NO. Catalysis Communications 26, 178-182

Chen, Y.-C., Lo, S.-L. and Kuo, J. 2011. Effects of titanate nanotubes synthesized by a microwave hydrothermal method on photocatalytic decomposition of perfluorooctanoic acid. Water Res. 45(14), 4131-4140

Chen, Z., Chen, W., Liao, G., Li, X., Wang, J., Tang, Y. and Li, L. 2022. Flexible construct of N vacancies and hydrophobic sites on g-C3N4 by F doping and their contribution to PFOA degradation in photocatalytic ozonation. J Hazard Mater, 128222

Cheng, J.-h., Liang, X.-y., Yang, S.-w. and Hu, Y.-y. 2014. Photochemical defluorination of aqueous perfluorooctanoic acid (PFOA) by VUV/$Fe^{3+}$ system. Chem. Eng. J. 239, 242-249

Choudhury, B. and Choudhury, A. 2013. Oxygen vacancy and dopant concentration dependent magnetic properties of Mn doped TiO2 nanoparticle. Curr Appl Phys 13(6), 1025-1031

Christensen, E.R., Zhang, R., Codling, G., Giesy, J.P. and Li, A. 2019. Poly-and per-fluoroalkyl compounds in sediments of the Laurentian Great Lakes: Loadings, temporal trends, and sources determined by positive matrix factorization. Environ. Pollut. 255, 113166

Cronemeyer, D. 1959. Infrared absorption of reduced rutile Ti O 2 single crystals. Physical review 113(5), 1222

Dang, C., Sun, F., Jiang, H., Huang, T., Liu, W., Chen, X. and Ji, H. 2020. Pre-accumulation and in-situ destruction of diclofenac by a photo-regenerable activated carbon fiber supported titanate nanotubes composite material: Intermediates, DFT calculation, and ecotoxicity. J Hazard Mater 400, 123225

de los Santos, D.M., Aguilar, T., Sánchez-Coronilla, A., Navas, J., Cruz Hernandez, N., Alcantara, R., Fernández-Lorenzo, C. and Martín-Calleja, J. 2014. Electronic and structural properties of highly aluminum ion doped TiO2 nanoparticles: A combined experimental and theoretical study. Chemphyschem 15(11), 2267-2280

De Vleeschouwer, F., Van Speybroeck, V., Waroquier, M., Geerlings, P. and De Proft, F. 2007. Electrophilicity and nucleophilicity index for radicals. Org Lett 9(14), 2721-2724

DEQ, N. 2018. Select Committee on North Carolina River Quality. https://www.ncleg.gov/documentsites/committees/house2017-185/Meetings/7%20-%20April%2026%202018/DEQ%20Update%20on%20GenX.pdf.

Diak, M., Klein, M., Klimczuk, T., Lisowski, W., Remita, H., Zaleska-Medynska, A. and Grabowska, E. 2017. Photoactivity of decahedral TiO2 loaded with bimetallic nanoparticles: degradation pathway of phenol-1-13C and hydroxyl radical formation. Applied Catalysis B: Environmental 200, 56-71

Ding, S., Niu, J., Bao, Y. and Hu, L.  2013.  Evidence of superoxide radical contribution to demineralization of sulfamethoxazole by visible-light-driven $Bi_2O_3/Bi_2O_2CO_3/Sr_6Bi_2O_9$ photocatalyst. J Hazard Mater 262, 812-818

Dong, F., Li, Q., Sun, Y. and Ho, W.-K.  2014a.  Noble metal-like behavior of plasmonic Bi particles as a cocatalyst deposited on $(BiO)_2CO_3$ microspheres for efficient visible light photocatalysis. Acs Catal 4(12), 4341-4350

Dong, F., Xiong, T., Sun, Y., Zhao, Z., Zhou, Y., Feng, X. and Wu, Z.  2014b.  A semimetal bismuth element as a direct plasmonic photocatalyst. Chem Commun 50(72), 10386-10389

Dong, F., Zhao, Z.W., Sun, Y.J., Zhang, Y.X., Yan, S. and Wu, Z.B.  2015.  An advanced semimetal-organic Bi spheres-g-$C_3N_4$ nanohybrid with SPR-enhanced visible-light photocatalytic performance for NO purification. Environ. Sci. Technol. 49(20), 12432-12440

Dostanić, J., Lončarević, D., Pavlović, V.B., Papan, J. and Nedeljković, J.M.  2019.  Efficient photocatalytic hydrogen production over titanate/titania nanostructures modified with nickel. Ceram Int 45(15), 19447-19455

El-Sheikh, S.M., Khedr, T.M., Hakki, A., Ismail, A.A., Badawy, W.A. and Bahnemann, D.W. 2017.  Visible light activated carbon and nitrogen co-doped mesoporous $TiO_2$ as efficient photocatalyst for degradation of ibuprofen. Sep Purif Technol 173, 258-268

Elsanousi, A., Elssfah, E., Zhang, J., Lin, J., Song, H. and Tang, C.  2007.  Hydrothermal treatment duration effect on the transformation of titanate nanotubes into nanoribbons. The Journal of Physical Chemistry C 111(39), 14353-14357

EPA 2016a. Drinking water health advisory for perfluorooctane sulfonate (PFOS). https://www.epa.gov/sites/default/files/2016-05/documents/pfos_health_advisory_final-plain.pdf.

EPA 2016b. Drinking water health advisory for perfluorooctanoic acid (PFOA). https://www.epa.gov/sites/default/files/2016-05/documents/pfoa_health_advisory_final-plain.pdf.

EPA 2017a. Occurrence data for the unregulated contaminant monitoring rule: UCMR 3 (2013−2015) occurrence data In 2013−2015.

EPA, E.P.A. 2017b Technical Fact Sheet – Perfluorooctane Sulfonate (PFOS) and Perfluorooctanoic Acid (PFOA). Agency, E.P. (ed), Washington, DC: U.S. Environmental Protection Agency.

EPA, U. 2000 EPA and 3M announce phase out of PFOS, US Environmental Protection Agency Press Release Washington DC.

Fang, G.D., Dionysiou, D.D., Al-Abed, S.R. and Zhou, D.M. 2013. Superoxide radical driving the activation of persulfate by magnetite nanoparticles: Implications for the degradation of PCBs. Appl Catal B-Environ 129, 325-332

Frisch, M.J., Trucks, G.W., Schlegel, H.B., Scuseria, G.E., Robb, M.A. and Cheeseman, J.R. (2003) Gaussian 03, Revision C.02,

Gaberell, M., Chin, Y.-P., Hug, S.J. and Sulzberger, B. 2003. Role of dissolved organic matter composition on the photoreduction of Cr(VI) to Cr(III) in the presence of iron. Environ. Sci. Technol. 37(19), 4403-4409

Gagliano, E., Sgroi, M., Falciglia, P.P., Vagliasindi, F.G. and Roccaro, P. 2020. Removal of poly- and perfluoroalkyl substances (PFAS) from water by adsorption: Role of PFAS chain length, effect of organic matter and challenges in adsorbent regeneration. Water Res. 171, 115381

Gajovic, A., Friscic, I., Plodinec, M. and Ivekovic, D. 2009. High temperature Raman spectroscopy of titanate nanotubes. J Mol Struct 924, 183-191

Gebbink, W.A., van Asseldonk, L. and van Leeuwen, S.P.J. 2017. Presence of emerging per- and polyfluoroalkyl substances (PFASs) in river and drinking water near a fluorochemical production plant in the Netherlands. Environ. Sci. Technol. 51(19), 11057-11065

Gopiraman, M., Saravanamoorthy, S., Kim, S.-H. and Chung, I.-M. 2017. Interconnected meso/microporous carbon derived from pumpkin seeds as an efficient electrode material for supercapacitors. Carbon letters 24, 73-81

Gray, F., Kramer, D.A. and Bliss, J.D. 2000. Gallium and gallium compounds. Kirk-Othmer Encyclopedia of Chemical Technology

Guo, J., Han, Q., Zhong, S., Zhu, B., Huang, W. and Zhang, S. 2018. Au/M-TiO 2 nanotube catalysts (M= Ce, Ga, Co, Y): preparation, characterization and their catalytic activity for CO oxidation. J Sol-Gel Sci Techn 86(3), 699-710

Hanaor, D.A.H. and Sorrell, C.C. 2011. Review of the anatase to rutile phase transformation. J Mater Sci 46(4), 855-874.

Hansen, K.J., Johnson, H., Eldridge, J., Butenhoff, J. and Dick, L. 2002. Quantitative characterization of trace levels of PFOS and PFOA in the Tennessee River. Environ. Sci. Technol. 36(8), 1681-1685

Haque, F.Z., Nandanwar, R. and Singh, P. 2017. Evaluating photodegradation properties of anatase and rutile $TiO_2$ nanoparticles for organic compounds. Optik 128, 191-200

Heydebreck, F., Tang, J.H., Xie, Z.Y. and Ebinghaus, R. 2015. Alternative and legacy perfluoroalkyl substances: differences between European and Chinese river/estuary systems Environ. Sci. Technol. 49(24), 14742-14743

Hori, H., Yamamoto, A., Hayakawa, E., Taniyasu, S., Yamashita, N., Kutsuna, S., Kiatagawa, H., Arakawa, R.J.E.S. and Technology 2005. Efficient decomposition of environmentally

persistent perfluorocarboxylic acids by use of persulfate as a photochemical oxidant. 39(7), 2383-2388

Hu, K., Xiao, X., Cao, X., Hao, R., Zuo, X., Zhang, X. and Nan, J. 2011. Adsorptive separation and photocatalytic degradation of methylene blue dye on titanate nanotube powders prepared by hydrothermal process using metal Ti particles as a precursor. J Hazard Mater 192(2), 514-520

Hu, X.D.C., Andrews, D.Q., Lindstrom, A.B., Bruton, T.A., Schaider, L.A., Grandjean, P., Lohmann, R., Carignan, C.C., Blum, A., Balan, S.A., Higgins, C.P. and Sunderland, E.M. 2016. Detection of Poly- and Perfluoroalkyl Substances (PFASs) in US Drinking Water Linked to Industrial Sites, Military Fire Training Areas, and Wastewater Treatment Plants. Environ Sci Tech Let 3(10), 344-350.

Huang, Y., Zheng, X., Zhongyi, Y., Feng, T., Beibei, F. and Keshan, H. 2007. Preparation of nitrogen-doped $TiO_2$ nanoparticle catalyst and its catalytic activity under visible light. Chinese Journal of Chemical Engineering 15(6), 802-807

Hurum, D.C., Agrios, A.G., Gray, K.A., Rajh, T. and Thurnauer, M.C. 2003. Explaining the enhanced photocatalytic activity of degussa P25 mixed-phase $TiO_2$ using EPR. The Journal of Physical Chemistry B 107(19), 4545-4549

Ip, A.W., Barford, J.P. and McKay, G. 2010. A comparative study on the kinetics and mechanisms of removal of Reactive Black 5 by adsorption onto activated carbons and bone char. Chem. Eng. J. 157(2-3), 434-442

Ismail, A.A., Abdelfattah, I., Faisal, M. and Helal, A. 2018. Efficient photodecomposition of herbicide imazapyr over mesoporous $Ga_2O_3$-$TiO_2$ nanocomposites. J Hazard Mater 342, 519-526

Jamila, G.S., Sajjad, S., Leghari, S.A.K. and Mahmood, T. 2020. Role of nitrogen doped carbon quantum dots on CuO nano-leaves as solar induced photo catalyst. Journal of Physics and Chemistry of Solids 138, 109233

JDSUPRA (2019) State-by-State Regulation of Per- and Polyfluoroalkyl Substances (PFAS) in Drinking Water, https://www.jdsupra.com/legalnews/state-by-state-regulation-of-per-and-82542/

Ji, H., Du, P., Zhao, D., Li, S., Sun, F., Duin, E.C. and Liu, W. 2020. 2D/1D graphitic carbon nitride/titanate nanotubes heterostructure for efficient photocatalysis of sulfamethazine under solar light: Catalytic "hot spots" at the rutile–anatase–titanate interfaces. Applied Catalysis B: Environmental 263, 118357

Jin, L., Zhang, P.Y., Shao, T. and Zhao, S.L. 2014. Ferric ion mediated photodecomposition of aqueous perfluorooctane sulfonate (PFOS) under UV irradiation and its mechanism. J Hazard Mater 271, 9-15

Kakavandi, B., Bahari, N., Kalantary, R.R. and Fard, E.D. 2019. Enhanced sono-photocatalysis of tetracycline antibiotic using $TiO_2$ decorated on magnetic activated carbon (MAC@T) coupled with US and UV: a new hybrid system. Ultrason Sonochem 55, 75-85

Khan, M.U. and Siddiqui, Z.N. 2021. Niobia supported sulfated bismuth oxide nanorods (S-$Bi_2O_3$@$Nb_2O_5$): acidic properties, catalytic activity and green metrics analysis. Sustainable Chemistry and Pharmacy 24, 100542

Kim, H.W. and Shim, S.H. 2007. Bicrystalline gallium oxide nanobelts. Thin Solid Films 515(12), 5158-5162

Konstantinou, I. and Deligiannakis, Y. (2013) Functions of Natural Organic Matter in Changing Environment, pp. 633-636, Springer.

LAGIAPPE 2022. Class Action filed against 3M Guin for water contamination.https://lagniappemobile.com/class-action-filed-against-3m-guin-for-water-contamination/

Lan, Y., Li, Z., Li, D., Xie, W., Yan, G. and Guo, S. 2020. Visible-light responsive Z-scheme Bi@β-Bi$_2$O$_3$/g-C$_3$N$_4$ heterojunction for efficient photocatalytic degradation of 2, 3-dihydroxynaphthalene. Chem. Eng. J. 392, 123686

Land, m.W., C.A.,;Cousins, L.T.; Herzke, D; Johansson, J.; Martin, J.W. 2015. What is the effect of phasing out long-chain per- and polyfluoroalkyl substances on the concentrations of perfluoroalkyl acids and their precursors in the environment? A systematic review protocol. Environ Evid 3

Lein, N.P.H., Fujii, S., Tanaka, S., Nozoe, M. and Tanaka, H. 2008. Contamination of perfluorooctane sulfonate (PFOS) and perfluorooctanoate (PFOA) in surface water of the Yodo River basin (Japan). Desalination 226(1-3), 338-347

Lester, Y., Sharpless, C.M., Mamane, H. and Linden, K.G. 2013. Production of photo-oxidants by dissolved organic matter during UV water treatment. Environ. Sci. Technol. 47(20), 11726-11733

Li, F., Duan, J., Tian, S., Ji, H., Zhu, Y., Wei, Z. and Zhao, D. 2019. Short-chain per-and polyfluoroalkyl substances in aquatic systems: occurrence, impacts and treatment. Chem. Eng. J., 122506

Li, F., Wei, Z., He, K., Blaney, L., Cheng, X., Xu, T., Liu, W. and Zhao, D. 2020a. A concentrate-&-destroy technique for degradation of perfluorooctanoic acid in water using a new adsorptive photocatalyst. Water Res., 116219

Li, G., Dimitrijevic, N.M., Chen, L., Rajh, T. and Gray, K.A. 2008. Role of surface/interfacial Cu2+ sites in the photocatalytic activity of coupled CuO− TiO2 nanocomposites. The Journal of Physical Chemistry C 112(48), 19040-19044

Li, L., Quinlivan, P.A. and Knappe, D.R. 2002. Effects of activated carbon surface chemistry and pore structure on the adsorption of organic contaminants from aqueous solution. Carbon 40(12), 2085-2100

Li, Y., Ding, L., Liang, Z., Xue, Y., Cui, H. and Tian, J. 2020b. Synergetic effect of defects rich $MoS_2$ and $Ti_3C_2$ MXene as cocatalysts for enhanced photocatalytic $H_2$ production activity of $TiO_2$. Chem. Eng. J. 383, 123178

Liang, X., Cheng, J., Yang, C. and Yang, S. 2016. Factors influencing aqueous perfluorooctanoic acid (PFOA) photodecomposition by VUV irradiation in the presence of ferric ions. Chem. Eng. J. 298, 291-299

Liu, D., Xiu, Z., Liu, F., Wu, G., Adamson, D., Newell, C., Vikesland, P., Tsai, A.-L. and Alvarez, P.J. 2013a. Perfluorooctanoic acid degradation in the presence of Fe (III) under natural sunlight. J Hazard Mater 262, 456-463

Liu, G., Zhang, X., Xu, Y., Niu, X., Zheng, L. and Ding, X. 2005. The preparation of $Zn^{2+}$-doped $TiO_2$ nanoparticles by sol–gel and solid phase reaction methods respectively and their photocatalytic activities. Chemosphere 59(9), 1367-1371

Liu, J., Wu, R., Gu, R., Qiu, F. and Pan, J. 2018. Simple formation of chitosan tablet with self-supporting blocks: $Fe^{3+}$-mediated supramolecular coordination. Chem. Eng. J. 341, 648-657

Liu, J., Zou, S., Wang, H., Xiao, L., Zhao, H. and Fan, J. 2017. Synergistic effect between $Pt^0$ and $Bi_2O_{3-x}$ for efficient room-temperature alcohol oxidation under base-free aqueous conditions. Catal Sci Technol 7(5), 1203-1210

Liu, K., Zhang, S., Hu, X., Zhang, K., Roy, A. and Yu, G. 2015a. Understanding the adsorption of PFOA on MIL-101 (Cr)-based anionic-exchange metal–organic frameworks: comparing DFT calculations with aqueous sorption experiments. Environ. Sci. Technol. 49(14), 8657-8665

Liu, K., Zhang, S.Y., Hu, X.Y., Zhang, K.Y., Roy, A. and Yu, G. 2015b. Understanding the Adsorption of PFOA on MIL-101(Cr)-Based Anionic-Exchange Metal-Organic Frameworks: Comparing DFT Calculations with Aqueous Sorption Experiments. Environ. Sci. Technol. 49(14), 8657-8665.

Liu, W., Cai, Z.Q., Zhao, X., Wang, T., Li, F. and Zhao, D.Y. 2016. High-capacity and photoregenerable composite material for efficient adsorption and degradation of phenanthrene in water. Environ. Sci. Technol. 50(20), 11174-11183

Liu, Y., Fang, P.F., Cheng, Y.L., Gao, Y.P., Chen, F.T., Liu, Z. and Dai, Y.Q. 2013b. Study on enhanced photocatalytic performance of cerium doped TiO2-based nanosheets. Chem. Eng. J. 219, 478-485

Liu, Y., Wu, H., Li, M., Yin, J.-J. and Nie, Z. 2014. pH dependent catalytic activities of platinum nanoparticles with respect to the decomposition of hydrogen peroxide and scavenging of superoxide and singlet oxygen. Nanoscale 6(20), 11904-11910.https://pubs.rsc.org/en/content/articlepdf/2014/nr/c4nr03848g

Loos, R., Gawlik, B.M., Locoro, G., Rimaviciute, E., Contini, S. and Bidoglio, G. 2009. EU-wide survey of polar organic persistent pollutants in European river waters. Environ. Pollut. 157(2), 561-568

Lu, Y., Huang, Y., Zhang, Y., Cao, J.-j., Li, H., Bian, C. and Lee, S.C. 2018. Oxygen vacancy engineering of $Bi_2O_3/Bi_2O_2CO_3$ heterojunctions: implications of the interfacial charge transfer, NO adsorption and removal. Applied Catalysis B: Environmental 231, 357-367

Luo, Q., Zhao, C., Liu, G. and Ren, H. 2016. A porous aromatic framework constructed from benzene rings has a high adsorption capacity for perfluorooctane sulfonate. Sci Rep-Uk 6(1), 1-9

Lyu, X.-J., Li, W.-W., Lam, P.K. and Yu, H.-Q. 2015. Photodegradation of perfluorooctane sulfonate in environmental matrices. Sep Purif Technol 151, 172-176

Ma, D., Zhao, J., Chu, R., Yang, S., Zhao, Y., Hao, X., Li, L., Zhang, L., Lu, Y. and Yu, C. 2013. Novel synthesis and characterization of bismuth nano/microcrystals with sodium hypophosphite as reductant. Advanced Powder Technology 24(1), 79-85

Ma, J., Li, F., Qian, T.W., Liu, H.F., Liu, W. and Zhao, D.Y. 2017. Natural organic matter resistant powder activated charcoal supported titanate nanotubes for adsorption of Pb(II). Chem. Eng. J. 315, 191-200

Ma, J., Zhou, H., Yan, S. and Song, W. 2019. Kinetics studies and mechanistic considerations on the reactions of superoxide radical ions with dissolved organic matter. Water Res. 149, 56-64

Ma, X., Zhang, F. and Wei, L. 2015. Effect of wood charcoal contents on the adsorption property, structure, and morphology of mesoporous activated carbon fibers derived from wood liquefaction process. J Mater Sci 50(4), 1908-1914

Manríquez, M.E., Sánchez-Mora, E., Hernández-Cortez, J., Moreno-Rodriguez, A. and García, T.H. 2009 Effect of Ga in the photocatalytic properties of TiO2, p. 012048, IOP Publishing.

Mirkhani, V., Tangestaninejad, S., Moghadam, M., Habibi, M. and Rostami-Vartooni, A. 2009. Photocatalytic degradation of azo dyes alyzed by Ag doped TiO 2 photocatalyst. J Iran Chem Soc 6(3), 578-587

Mirzaei, A., Yerushalmi, L., Chen, Z., Haghighat, F. and Guo, J. 2018. Enhanced photocatalytic degradation of sulfamethoxazole by zinc oxide photocatalyst in the presence of fluoride ions: optimization of parameters and toxicological evaluation. Water Res. 132, 241-251

Mohammadi, M. and Fray, D. 2007. Semiconductor $TiO_2$–$Ga_2O_3$ thin film gas sensors derived from particulate sol–gel route. Acta materialia 55(13), 4455-4466

Moon, G.-h., Fujitsuka, M., Kim, S., Majima, T., Wang, X. and Choi, W. 2017. Eco-friendly photochemical production of $H_2O_2$ through $O_2$ reduction over carbon nitride frameworks incorporated with multiple heteroelements. Acs Catal 7(4), 2886-2895

Morlay, C., Quivet, E., Pilshofer, M., Faure, R. and Joly, J.-P. 2012. Adsorption of Imazamox herbicide onto Filtrasorb 400 activated carbon. Journal of Porous Materials 19(1), 79-86

Myilsamy, M., Mahalakshmi, M., Subha, N. and Murugesan, V. 2018. Mesoporous Ga–TiO2: Role of Oxygen Vacancies for the Photocatalytic Degradation Under Visible Light. J Nanosci Nanotechno 18(2), 925-935.

Nakamura, I., Negishi, N., Kutsuna, S., Ihara, T., Sugihara, S. and Takeuchi, K. 2000. Role of oxygen vacancy in the plasma-treated TiO2 photocatalyst with visible light activity for NO removal. Journal of Molecular Catalysis A: Chemical 161(1-2), 205-212

Newton, S., McMahen, R., Stoeckel, J.A., Chislock, M., Lindstrom, A. and Strynar, M. 2017. Novel polyfluorinated compounds identified using high resolution mass spectrometry downstream of manufacturing facilities near Decatur, Alabama. Environ. Sci. Technol. 51(3), 1544-1552

Nguyen, C.H., Field, J.A. and Sierra-Alvarez, R. 2020. Microbial toxicity of gallium-and indium-based oxide and arsenide nanoparticles. Journal of Environmental Science and Health, Part A 55(2), 168-178

Niu, J., Lin, H., Xu, J., Wu, H. and Li, Y. 2012. Electrochemical mineralization of perfluorocarboxylic acids (PFCAs) by Ce-doped modified porous nanocrystalline $PbO_2$ film electrode. Environ. Sci. Technol. 46(18), 10191-10198

OECD 2018. (the organisation for economic co-operation and development)toward a new comprehensive global database of per- and polyfluoroalkyl substances (pfass): Summary report on updating the oecd 2007 list of per and polyfluoroalkyl substances (pfass).https://www.oecd.org/officialdocuments/publicdisplaydocumentpdf/?cote=ENV-JM-MONO(2018)7&doclanguage=en

Ohsaka, T., Yamaoka, S. and Shimomura, O. 1979. Effect of Hydrostatic-Pressure on the Raman-Spectrum of Anatase ($TiO_2$). Solid State Commun 30(6), 345-347.

Oláh, J., Van Alsenoy, C. and Sannigrahi, A. 2002. Condensed Fukui functions derived from stockholder charges: assessment of their performance as local reactivity descriptors. The Journal of Physical Chemistry A 106(15), 3885-3890

Pan, X. and Xu, Y.-J. 2013. Fast and spontaneous reduction of gold ions over oxygen-vacancy-rich TiO2: A novel strategy to design defect-based composite photocatalyst. Applied Catalysis A: General 459, 34-40

Park, H., Vecitis, C.D., Cheng, J., Choi, W., Mader, B.T. and Hoffmann, M.R. 2009. Reductive defluorination of aqueous perfluorinated alkyl surfactants: effects of ionic headgroup and chain length. The Journal of Physical Chemistry A 113(4), 690-696.

Parr, R.G. and Yang, W. 1984. Density functional approach to the frontier-electron theory of chemical reactivity. J Am Chem Soc 106(14), 4049-4050

Peña, J., Allen, N., Edge, M., Liauw, C. and Valange, B. 2001. Studies of synergism between carbon black and stabilisers in LDPE photodegradation. Polymer degradation and stability 72(2), 259-270

Pica, N.E., Funkhouser, J., Yin, Y.M., Zhang, Z.Y., Ceres, D.M., Tong, T.Z. and Blotevogel, J. 2019. Electrochemical oxidation of hexafluoropropylene oxide dimer acid (GenX): mechanistic insights and efficient treatment train with nanofiltration. Environ. Sci. Technol. 53(21), 12602-12609

Qamar, M., Yoon, C.R., Oh, H.J., Lee, N.H., Park, K., Kim, D.H., Lee, K.S., Lee, W.J. and Kim, S.J. 2008. Preparation and photocatalytic activity of nanotubes obtained from titanium dioxide. Catal Today 131(1-4), 3-14.

Qi, D., Lu, L., Xi, Z., Wang, L. and Zhang, J. 2014. Enhanced photocatalytic performance of TiO2 based on synergistic effect of Ti3+ self-doping and slow light effect. Applied Catalysis B: Environmental 160, 621-628

Qi, Y., Cao, H., Pan, W., Wang, C. and Liang, Y. 2022. The role of dissolved organic matter during per-and polyfluorinated Substance (PFAS) adsorption, degradation, and plant uptake: A review. J Hazard Mater, 129139

Rahman, M.F., Peldszus, S. and Anderson, W.B. 2014. Behaviour and fate of perfluoroalkyl and polyfluoroalkyl substances (PFASs) in drinking water treatment: A review. Water Res. 50, 318-340

Razali, M.H., Mohd Noor, A.-F., Mohamed, A.R. and Sreekantan, S. 2012. Morphological and structural studies of titanate and titania nanostructured materials obtained after heat treatments of hydrothermally produced layered titanate. Journal of Nanomaterials 2012

Reddy, N.L., Kumar, D.P. and Shankar, M. 2016. Co-catalyst free titanate nanorods for improved hydrogen production under solar light irradiation. Journal of Chemical Sciences 128(4), 649-656

Ross, I., McDonough, J., Miles, J., Storch, P., Thelakkat Kochunarayanan, P., Kalve, E., Hurst, J., S. Dasgupta, S. and Burdick, J.J.R.J. 2018. A review of emerging technologies for remediation of PFASs. 28(2), 101-126

Roth, K., Yang, Z., Agarwal, M., Liu, W., Peng, Z.Y., Long, Z., Birbeck, J., Westrick, J., Liu, W.Q. and Petriello, M.C. 2021. Exposure to a mixture of legacy, alternative, and replacement per- and polyfluoroalkyl substances (PFAS) results in sex-dependent modulation of cholesterol metabolism and liver injury. Environ Int 157.

Schneider, J., Matsuoka, M., Takeuchi, M., Zhang, J., Horiuchi, Y., Anpo, M. and Bahnemann, D.W. 2014. Understanding TiO2 photocatalysis: mechanisms and materials. Chemical reviews 114(19), 9919-9986

Schulte, K.L., DeSario, P.A. and Gray, K.A. 2010. Effect of crystal phase composition on the reductive and oxidative abilities of $TiO_2$ nanotubes under UV and visible light. Applied Catalysis B: Environmental 97(3-4), 354-360

Schulz, K.J., DeYoung, J.H., Seal, R.R. and Bradley, D.C. (2018) Critical mineral resources of the United States: economic and environmental geology and prospects for future supply, Geological Survey.

Shao, T., Zhang, P., Li, Z. and Jin, L. 2013. Photocatalytic decomposition of perfluorooctanoic acid in pure water and wastewater by needle-like nanostructured gallium oxide. Chinese J Catal 34(8), 1551-1559

Song, C., Chen, P., Wang, C. and Zhu, L. 2012. Photodegradation of perfluorooctanoic acid by synthesized $TiO_2$–MWCNT composites under 365 nm UV irradiation. Chemosphere 86(8), 853-859

Song, W., Ma, W., Ma, J., Chen, C., Zhao, J., Huang, Y. and Xu, Y. 2005. Photochemical oscillation of Fe(II)/Fe(III) ratio induced by periodic flux of dissolved organic matter. Environ. Sci. Technol. 39(9), 3121-3127

Song, Z., Dong, X., Wang, N., Zhu, L., Luo, Z., Fang, J. and Xiong, C. 2017. Efficient photocatalytic defluorination of perfluorooctanoic acid over BiOCl nanosheets via a hole direct oxidation mechanism. Chem. Eng. J. 317, 925-934

Song, Z., Tang, H., Wang, N. and Zhu, L. 2013. Reductive defluorination of perfluorooctanoic acid by hydrated electrons in a sulfite-mediated UV photochemical system. J Hazard Mater 262, 332-338

Staff, K., Brown, M.B., Chilcott, R.P., Hider, R.C., Jones, S.A. and Kong, X.L. 2011. Ga (III) complexes—the effect of metal coordination on potential systemic absorption after topical exposure. Toxicol Lett 202(3), 155-160

STEEEP 2019. 3M admits to unlawful release of PFAS in Alabama. https://web.uri.edu/steep/3m-admits-to-unlawful-release-of-pfas-in-alabama/#:~:text=Chemical%20structure%20of%20perfluorobutane.&text=American%20multinational%20manufacturing%20company%203M,illegally%20into%20the%20Tennessee%20River.

Subramaniam, M., Goh, P., Abdullah, N., Lau, W., Ng, B. and Ismail, A. 2017. Adsorption and photocatalytic degradation of methylene blue using high surface area titanate nanotubes (TNT) synthesized via hydrothermal method. J Nanopart Res 19(6), 1-13

Sun, M., Arevalo, E., Strynar, M., Lindstrom, A., Richardson, M., Kearns, B., Pickett, A., Smith, C. and Knappe, D.R.U. 2016. Legacy and emerging perfluoroalkyl substances are important drinking water contaminants in the cape fear river watershed of North Carolina. Environ Sci Tech Let 3(12), 415-419

Sun, X.M. and Li, Y.D. 2003. Synthesis and characterization of ion-exchangeable titanate nanotubes. Chem-Eur J 9(10), 2229-2238

Sun, Y., Zhao, Z., Dong, F. and Zhang, W. 2015. Mechanism of visible light photocatalytic $NO_x$ oxidation with plasmonic Bi cocatalyst-enhanced $(BiO)_2CO_3$ hierarchical microspheres. Phys Chem Chem Phys 17(16), 10383-10390

Sun, Y., Zhao, Z., Zhang, W., Gao, C., Zhang, Y. and Dong, F. 2017. Plasmonic Bi metal as cocatalyst and photocatalyst: the case of $Bi/(BiO)_2CO_3$ and Bi particles. J Colloid Interf Sci 485, 1-10

Sunderland, E.M., Hu, X.C., Dassuncao, C., Tokranov, A.K., Wagner, C.C. and Allen, J.G. 2019. A review of the pathways of human exposure to poly-and perfluoroalkyl substances (PFASs) and present understanding of health effects. Journal of exposure science & environmental epidemiology 29(2), 131-147

Sydney Evans, D.A., Tasha Stoiber, Olga Naidenko. 2020 PFAS contamination of drinking water far more prevalent than previously reported, EWG, EWG Home.

Taieb, S.B., Assaker, I.B., Bardaoui, A., Gannouni, M., Souissi, A., Nowak, S., Mouton, L., Ammar, S. and Chtourou, R. 2016. Correlation between Titanium foil substrate purity and

TiO2 NTs; physical and electrochemical properties for enhanced photoelectrochemical applications. Int J Hydrogen Energ 41(15), 6230-6239

Tian, S., Xu, T., Fang, L., Zhu, Y., Li, F., Leary III, R.N., Zhang, M., Zhao, D., Soong, T.-Y. and Shi, H. 2021. A 'Concentrate-&-Destroy'technology for enhanced removal and destruction of per-and polyfluoroalkyl substances in municipal landfill leachate. Sci Total Environ 791, 148124

Triviño-Bolaños, D.F. and Camargo-Amado, R.J. 2019. Synthesis and characterization of porous structures of rutile $TiO_2/Na_{0.8}Ti_4O_8/Na_2Ti_6O_{13}$ for biomedical applications. MethodsX 6, 1114-1123

Trojanowicz, M., Bojanowska-Czajka, A., Bartosiewicz, I. and Kulisa, K. 2018. Advanced oxidation/reduction processes treatment for aqueous perfluorooctanoate (PFOA) and perfluorooctanesulfonate (PFOS)–a review of recent advances. Chem. Eng. J. 336, 170-199

Tsiamtsouri, M.A., Allan, P.K., Pell, A.J., Stratford, J.M., Kim, G., Kerber, R.N., Magusin, P.C., Jefferson, D.A. and Grey, C.P. 2018. Exfoliation of layered Na-ion anode material $Na_2Ti_3O_7$ for enhanced capacity and cyclability. Chem Mater 30(5), 1505-1516

Tu, W., Zhou, Y., Li, H., Li, P. and Zou, Z. 2015. $Au@TiO_2$ yolk–shell hollow spheres for plasmon-induced photocatalytic reduction of $CO_2$ to solar fuel via a local electromagnetic field. Nanoscale 7(34), 14232-14236

USEPA. (2018) Human health toxicity values for hexafluoropropylene oxide (HFPO) dimer acid and its ammonium salt (CASRN 13252-13-6 and CASRN 62037-89-3): Also known as "GenX Chemicals", https://www.epa.gov/sites/default/files/2018-11/documents/genx_public_comment_draft_toxicity_assessment_nov2018-508.pdf

Vakili, M., Bao, Y., Gholami, F., Gholami, Z., Deng, S., Wang, W., Awasthi, A.K., Rafatullah, M., Cagnetta, G. and Yu, G. 2021. Removal of HFPO-DA (GenX) from aqueous solutions: A mini-review. Chem. Eng. J. 424, 130266

Van Doorslaer, X., Heynderickx, P.M., Demeestere, K., Debevere, K., Van Langenhove, H. and Dewulf, J. 2012. $TiO_2$ mediated heterogeneous photocatalytic degradation of moxifloxacin: operational variables and scavenger study. Applied Catalysis B: Environmental 111, 150-156

Vasanthi, V., Kottaisamy, M. and Ramakrishnan, V. 2019. Near UV excitable warm white light emitting Zn doped $\gamma$-$Ga_2O_3$ nanoparticles for phosphor-converted white light emitting diode. Ceram Int 45(2), 2079-2087

Vecitis, C.D., Park, H., Cheng, J., Mader, B.T. and Hoffmann, M.R. 2008. Kinetics and mechanism of the sonolytic conversion of the aqueous perfluorinated surfactants, perfluorooctanoate (PFOA), and perfluorooctane sulfonate (PFOS) into inorganic products. The Journal of Physical Chemistry A 112(18), 4261-4270

Velasco-Arias, D., Zumeta-Dube, I., Díaz, D., Santiago-Jacinto, P., Ruiz-Ruiz, V.-F., Castillo-Blum, S.-E. and Rendon, L. 2012. Stabilization of strong quantum confined colloidal bismuth nanoparticles, one-pot synthesized at room conditions. The Journal of Physical Chemistry C 116(27), 14717-14727

Vithal, M., Krishna, S.R., Ravi, G., Palla, S., Velchuri, R. and Pola, S. 2013. Synthesis of $Cu^{2+}$ and $Ag^+$ doped $Na_2Ti_3O_7$ by a facile ion-exchange method as visible-light-driven photocatalysts. Ceram Int 39(7), 8429-8439

Walker, G.M. and Weatherley, L.R. 1998. Bacterial regeneration in biological activated carbon systems. Process Saf Environ 76(B2), 177-182

Walse, S.S., Morgan, S.L., Kong, L. and Ferry, J.L. 2004. Role of dissolved organic matter, nitrate, and bicarbonate in the photolysis of aqueous fipronil. Environ. Sci. Technol. 38(14), 3908-3915

Wang, F., Liu, C.S. and Shih, K.M. 2012a. Adsorption behavior of perfluorooctanesulfonate (PFOS) and perfluorooctanoate (PFOA) on boehmite. Chemosphere 89(8), 1009-1014.<Go to ISI>://WOS:000308844800015

Wang, F. and Shih, K. 2011. Adsorption of perfluorooctanesulfonate (PFOS) and perfluorooctanoate (PFOA) on alumina: Influence of solution pH and cations. Water Res. 45(9), 2925-2930

Wang, N., Li, X., Yang, Y., Zhou, Z., Shang, Y., Zhuang, X. and Zhang, T. 2020. Two-stage calcination composite of $Bi_2O_3$-$TiO_2$ supported on powdered activated carbon for enhanced degradation of sulfamethazine under solar irradiation. Journal of Water Process Engineering 35, 101220

Wang, Q., Mitchell, R.-L., Hofman, R., Yu, J., Yang, M., Rietveld, L.C. and Zietzschmann, F. 2021. How properties of low molecular weight model competitors impact organic micropollutant adsorption onto activated carbon at realistically asymmetric concentrations. Water Res. 202, 117443

Wang, Q.R., Lei, X.M., Pan, F., Xia, D.S., Shang, Y.J., Sun, W.L. and Liu, W. 2018. A new type of activated carbon fibre supported titanate nanotubes for high-capacity adsorption and degradation of methylene blue. Colloid Surface A 555, 605-614

Wang, S., Yang, Q., Chen, F., Sun, J., Luo, K., Yao, F., Wang, X., Wang, D., Li, X. and Zeng, G. 2017. Photocatalytic degradation of perfluorooctanoic acid and perfluorooctane sulfonate in water: A critical review. Chem. Eng. J. 328, 927-942

Wang, Y., Hong, B.H. and Kim, K.S. 2005. Size control of semimetal bismuth nanoparticles and the UV−visible and IR absorption spectra. The Journal of Physical Chemistry B 109(15), 7067-7072

Wang, Y., Sun, T., Yang, D., Liu, H., Zhang, H., Yao, X. and Zhao, H. 2012b. Structure, reactivity, photoactivity and stability of Ti–O based materials: a theoretical comparison. Phys Chem Chem Phys 14(7), 2333-2338

Wang, Y., Zhang, P., Pan, G. and Chen, H. 2008. Ferric ion mediated photochemical decomposition of perfluorooctanoic acid (PFOA) by 254 nm UV light. J Hazard Mater 160(1), 181-186

Wang, Z., Cousins, I.T., Scheringer, M. and Hungerbühler, K. 2013. Fluorinated alternatives to long-chain perfluoroalkyl carboxylic acids (PFCAs), perfluoroalkane sulfonic acids (PFSAs) and their potential precursors. Environ Int 60, 242-248

Weng, S., Chen, B., Xie, L., Zheng, Z. and Liu, P. 2013. Facile in situ synthesis of a Bi/BiOCl nanocomposite with high photocatalytic activity. J Mater Chem A 1(9), 3068-3075

Wibowo, N., Setyadhi, L., Wibowo, D., Setiawan, J. and Ismadji, S. 2007. Adsorption of benzene and toluene from aqueous solutions onto activated carbon and its acid and heat treated forms: influence of surface chemistry on adsorption. J Hazard Mater 146(1-2), 237-242

Xiao, F., Zhang, X., Penn, L., Gulliver, J.S. and Simcik, M.F. 2011. Effects of monovalent cations on the competitive adsorption of perfluoroalkyl acids by kaolinite: experimental studies and modeling. Environ. Sci. Technol. 45(23), 10028-10035

Xu, B., Ahmed, M.B., Zhou, J.L., Altaee, A., Wu, M. and Xu, G. 2017a. Photocatalytic removal of perfluoroalkyl substances from water and wastewater: Mechanism, kinetics and controlling factors. Chemosphere 189, 717-729

Xu, J., Zhang, H., Liu, T. and Zhang, J. 2014. Fabrication and characterization of potassium and sodium titanate via a hydrothermal method. J. Chem. Soc. Pak. 36(3), 388

Xu, T., Ji, H., Gu, Y., Tong, T., Xia, Y., Zhang, L. and Zhao, D. 2020a. Enhanced adsorption and photocatalytic degradation of perfluorooctanoic acid in water using iron (hydr) oxides/carbon sphere composite. Chem. Eng. J., 124230

Xu, T., Zhu, Y., Duan, J., Xia, Y., Tong, T., Zhang, L. and Zhao, D. 2020. Enhanced photocatalytic degradation of perfluorooctanoic acid using carbon-modified bismuth phosphate composite: effectiveness, material synergy and roles of carbon. Chem. Eng. J., 124991

Xu, T., Zhu, Y., Duan, J., Xia, Y., Tong, T., Zhang, L. and Zhao, D. 2020b. Enhanced photocatalytic degradation of perfluorooctanoic acid using carbon-modified bismuth phosphate composite: Effectiveness, material synergy and roles of carbon. Chem. Eng. J., 124991

Xu, X., Chen, J., Qu, R. and Wang, Z. 2017b. Oxidation of Tris (2-chloroethyl) phosphate in aqueous solution by UV-activated peroxymonosulfate: kinetics, water matrix effects, degradation products and reaction pathways. Chemosphere 185, 833-843

Xue, S., Sun, J., Liu, Y., Zhang, Z., Lin, Y. and Liu, Q. 2019. Effect of dissolved organic matter fractions on photodegradation of phenanthrene in ice. J Hazard Mater 361, 30-36

Yang, C. and Li, X. (2002) Studies in Surface Science and Catalysis, pp. 173-182, Elsevier.

Yang, Q., Wu, Q., Liu, Y., Luo, S., Wu, X., Zhao, X., Zou, H., Long, B., Chen, W. and Liao, Y. 2020. Novel Bi-doped amorphous $SnO_x$ nanoshells for efficient electrochemical $CO_2$ reduction into formate at low overpotentials. Adv Mater 32(36), 2002822

Yang, S., Cheng, J., Sun, J., Hu, Y. and Liang, X. 2013. Defluorination of aqueous perfluorooctanesulfonate by activated persulfate oxidation. Plos One 8(10)

Yang, Y., Ji, W., Li, X., Zheng, Z., Bi, F., Yang, M., Xu, J. and Zhang, X. 2021. Insights into the degradation mechanism of perfluorooctanoic acid under visible-light irradiation through fabricating flower-shaped $Bi_5O_7I/ZnO$ nn heterojunction microspheres. Chem. Eng. J. 420, 129934

You, C., Jia, C. and Pan, G. 2010. Effect of salinity and sediment characteristics on the sorption and desorption of perfluorooctane sulfonate at sediment-water interface. Environ. Pollut. 158(5), 1343-1347

Yu, Q., Zhang, R.Q., Deng, S.B., Huang, J. and Yu, G. 2009. Sorption of perfluorooctane sulfonate and perfluorooctanoate on activated carbons and resin: Kinetic and isotherm study. Water Res. 43(4), 1150-1158

Yuan, R., Guan, R. and Zheng, J. 2005. Effect of the pore size of $TiO_2$-loaded activated carbon fiber on its photocatalytic activity. Scripta Materialia 52(12), 1329-1334

Zhang, J.W., Wang, Y., Jin, Z.S., Wu, Z.S. and Zhang, Z.J. 2008a. Visible-light photocatalytic behavior of two different N-doped $TiO_2$. Appl Surf Sci 254(15), 4462-4466

Zhang, L. and Anderson, W.A. 2013. Kinetic analysis of the photochemical decomposition of gas-phase chlorobenzene in a UV reactor: Quantum yield and photonic efficiency. Chem. Eng. J. 218, 247-252

Zhang, L.W., Fu, H.B. and Zhu, Y.F. 2008b. Efficient TiO2 photocatalysts from surface hybridization of TiO2 particles with graphite-like carbon. Adv Funct Mater 18(15), 2180-2189.

Zhang, Y.Y., Jiang, Z.L., Huang, J.Y., Lim, L.Y., Li, W.L., Deng, J.Y., Gong, D.G., Tang, Y.X., Lai, Y.K. and Chen, Z. 2015. Titanate and titania nanostructured materials for environmental and energy applications: a review. Rsc Adv 5(101), 82632-82632.

Zhao, B., Li, X., Yang, L., Wang, F., Li, J., Xia, W., Li, W., Zhou, L. and Zhao, C. 2015. ß-$Ga_2O_3$ Nanorod Synthesis with a One-step Microwave Irradiation Hydrothermal Method and its Efficient Photocatalytic Degradation for Perfluorooctanoic Acid. Photochemistry and photobiology 91(1), 42-47

Zhao, C., Tang, C.Y., Li, P., Adrian, P. and Hu, G. 2016a. Perfluorooctane sulfonate removal by nanofiltration membrane—the effect and interaction of magnesium ion/humic acid. J Membrane Sci 503, 31-41

Zhao, X., Cai, Z.Q., Wang, T., O'Reilly, S.E., Liu, W. and Zhao, D.Y. 2016b. A new type of cobalt-deposited titanate nanotubes for enhanced photocatalytic degradation of phenanthrene. Appl Catal B-Environ 187, 134-143

Zhao, X., Du, P., Cai, Z., Wang, T., Fu, J. and Liu, W. 2018. Photocatalysis of bisphenol A by an easy-settling titania/titanate composite: Effects of water chemistry factors, degradation pathway and theoretical calculation. Environ. Pollut. 232, 580-590.

Zhong, b.J., Li, J.z., Lu, Y., He, X.y., Zeng, J., Hu, W. and cheng Shen, Y. 2012. Fabrication of $Bi^{3+}$-doped ZnO with enhanced photocatalytic performance. Appl Surf Sci 258(11), 4929 4933

Zhu, M., Lu, J., Hu, Y., Liu, Y., Hu, S. and Zhu, C. 2020. Photochemical reactions between 1, 4-benzoquinone and O2•−. Environmental Science and Pollution Research International

Zhu, Y., Ji, H., He, K., Blaney, L., Xu, T. and Zhao, D. 2022. Photocatalytic degradation of GenX in water using a new adsorptive photocatalyst. Water Res., 118650

Zhu, Y., Xu, T., Zhao, D., Li, F., Liu, W., Wang, B. and An, B.  2021.  Adsorption and solid-phase photocatalytic degradation of perfluorooctane sulfonate in water using gallium-doped carbon-modified titanate nanotubes. Chem. Eng. J. 421, 129676